Draft 4.00 9-Dec-1988

CDF/ANAL/JET/GROUP/805

Dijet Angular Distributions in Proton–Antiproton Collisions at the Fermilab Tevatron

A thesis presented

by

Richard Dante St. Denis

to

The Department of Physics

in partial fulfillment of the requirements

for the degree of

Doctor of Philosophy

in the subject of

Physics

Harvard University

Cambridge, Massachusetts

December, 1988

Dijet Angular Distributions in Proton–Antiproton Collisions at the Fermilab Tevatron

A thesis presented

by

Richard Dante St. Denis

to

The Department of Physics

in partial fulfillment of the requirements

for the degree of

Doctor of Philosophy

in the subject of

Physics

Harvard University

Cambridge, Massachusetts

December, 1988

Copyright © 1988 by Richard Dante St. Denis

All Rights Reserved

Abstract

A measurement of dijet angular distributions is made at $\sqrt{s} = 1.8$ TeV in proton-antiproton collisions at the Fermilab Tevatron using the Collider Detector at Fermilab (CDF). Results are presented for three minimum values of the dijet invariant mass and compared to QCD predictions for various choices of scale and parton momentum distribution functions.

Contents

Acknowledgements **xiii**

1 Introduction **1**

2 The Parton Model and QCD **4**

2.1 Hadron Collisions 4

2.2 The Parton Model and Hadronic Jets 5

2.3 Partons to Quarks and Gluons 8

2.4 Features of the Lowest Order Perturbative QCD Solution 11

2.4.1 Fundamental scattering 11

2.4.2 The Running Coupling Constant 13

2.4.3 Parton Momentum Distribution Function Evolution 13

3 The Collider Detector at Fermilab **14**

3.1 CDF 14

3.1.1 Tracking 15

3.1.2 Calorimetry 17

3.1.3 Forward Calorimetry 22

3.1.4 Muon Detection 23

3.1.5 Trigger 23

3.1.6 Data Acquisition and Online Control 25

3.2 The 1987 Collider Run 26

4 Detector Calibration **29**

4.1 Test beams and Carrying Calibrations to CDF. 30

4.1.1 Calibration of the Central Electromagnetic Detector 31

4.1.2 Calibration of the Central Hadron Detector 31

4.1.3 Endwall Calorimeter 33

4.1.4 Gas Calorimeters 33

4.2 The Role of Electronics 35

5 Event Sample and Jet Reconstruction **37**

5.1 Data Sample 37

5.1.1 Minimum Bias Trigger 38

5.1.2 Jet Trigger 38

5.1.3 Events Collected and Integrated Luminosity 39

5.2 Offline Processing: Raw Data to Jet 4-Vectors 41

5.2.1 Cosmic Ray Bremstrahhlung and Main Ring Event Removal . . . 43

5.2.2 Gas spike removal 44

5.2.3 Jet Reconstruction 46

5.3 Properties of the Central Dijet sample 49

6 Central Jet Energy Resolution **55**

6.1 Dijet k_t Description 56

6.1.1 The Components of the Dijet k_t 56

6.2 Measured behavior of the dijet k_t 58

7 Measurement of $\frac{dN}{d\cos\theta^*}$ 61

7.1 Acceptance Issues 62

7.1.1 The Event Sample 62

7.1.2 Description of the Acceptance Geometry 63

7.1.3 Variables Affecting Acceptance 66

7.2 Phase I: Preliminary Measurement of $dN/d\cos\theta^*$ 68

7.2.1 Uniform Acceptance Measurement of $dN/d\cos\theta^*$ 68

7.2.2 Extension of the Angular distribution 71

7.3 Phase II: Sophisticated Measurement of $dN/d\cos\theta^*$ 74

7.3.1 Tests of the Monte Carlos 74

7.3.2 Determination of the Acceptance 75

7.3.3 Systematic error calculations 80

7.3.4 Results 87

8 Summary 93

A RABBIT calibrations 96

A.1 The RABBIT System 96

A.2 EWE Behavior and Calibration 99

A.2.1 Overview of EWE operations 99

A.2.2 ADC counts in the EWE from the circuit diagram 101

A.2.3 Application of the EWE Equation to Calibrations 104

A.2.4 Threshold circuit equations in the EWE 107

A.2.5 Summary of EWE calibration choices 112

A.3 Amplifier Gain Determination 113

A.3.1 EWE ADC and BAT VCAL Calibrations 113

A.3.2 Charge injection 114

A.4 CDF Database Considerations 117

B Multiple Collision Estimate **119**

C Central Jet Energy Resolution **122**

C.1 Dijet k_t Description 122

C.1.1 Calculating Dijet k_t 123

C.1.2 Relating k_t to energies 124

C.1.3 Distributions of Dijet k_t 126

C.1.4 Origin of the Dijet k_t Components 127

C.2 Central Detector Resolution Study 135

C.2.1 Effective Resolution and Extraction of the Causes 135

C.2.2 Dijet k_t Dependence on the Presence of Third Jets 138

D Energy Scale Probing **147**

D.1 Investigation of the $\theta = 90^o$ Region 149

D.2 Probing Gas Calorimetry 150

D.2.1 The Data Sample 151

D.2.2 Distributions in the Gas Calorimetry 151

D.2.3 Extraction of Gas Calorimeter Resolutions 155

D.2.4 Changing the Gas Calorimetry Scale 167

E Phase I Acceptance Calculations **170**

E.1 The Simple Monte Carlo 170

E.2 Calculation of Acceptance 172

F Tests of QFL **175**

G Theoretical calculations of $dN/\cos\theta^*$ **180**

G.1 The Quantity that is Calculated 181

G.1.1 Overview of the Procedure 181

G.1.2 Parton Distribution Functions 183

G.1.3 Evolution of α_s 185

G.1.4 Parton Subprocess Matrix Elements 185

G.1.5 Summing the Cross Sections and Weighting with Distribution Functions 189

G.2 Application to $dN/d\cos\theta^*$ 189

G.2.1 Transformation of Variables 190

G.2.2 Results of the Calculation 191

Bibliography **194**

List of Tables

3.1 Summary of CDF central calorimeter properties 19

3.2 Summary of CDF gas calorimeter properties 20

5.1 Events per Trigger after downloading constants 40

5.2 Events per Trigger after removing bad runs 41

5.3 Number of dead/hot channels 42

7.1 Cuts on Phase I $dN/d\cos\theta^*$ analysis 74

7.2 Cuts on Phase II $dN/d\cos\theta^*$ analysis 80

B.1 Estimation of double jet events 121

C.1 Sources of dijet k_t components 134

C.2 Cuts on the various samples of data 144

C.3 Effective jet resolution 144

C.4 Calorimeter resolution derived from σ' for various cuts 145

C.5 Calorimeter resolution for various cuts 146

D.1 Probing the ninety degree boundary 149

D.2 Trigger - Probe Distribution Summary 153

D.3 Gas Calorimetry Resolution Coefficients 166

D.4 Gas Calorimetry Correction factors 168

D.5 Gas Calorimetry Resolution Coefficients 169

G.1 Four basic parton subprocess cross sections 187

G.2 Seven basic parton subprocess cross sections for $a + b \rightarrow X$ 188

List of Figures

1.1 Dijet Event at CDF 2

2.1 Initial Parton phase space configuration 6

2.2 Parton phase space configuration at the moment of collision 7

2.3 Final parton phase space configuration 7

2.4 UA2 jet evidence 9

2.5 Illustration of a $\bar{p}p$ collision 10

3.1 The CDF Detector 16

3.2 Calorimeter Tower segmentation 21

3.3 Luminosity vs. time for 1987 collider run 27

3.4 Peak Luminosity vs. time for 1987 collider run 28

5.1 JETCLU flow chart 48

5.2 p_t and E_t jet spectrum 52

5.3 Jet mass spectrum 53

5.4 η-ϕ distribution of jets 53

5.5 EM fraction of jets 54

5.6 Z-vertex distribution 54

6.1 Dijet k_t components 56

6.2 k_{t_ξ} interpretation 57

6.3 k_{t_η} interpretation 58

6.4 σ_ξ vs $E_t^{\frac{1}{2}}$ 59

6.5 σ_η vs $E_t^{\frac{1}{2}}$ 60

7.1 Lab to COM Transformation 64

7.2 Mapping of η_1-η_2 to η^*-η_{boost} 65

7.3 Population of data in η_{boost}-η^* plane 69

7.4 Population of data in the p^*-η^* plane 70

7.5 Dijet Angular distribution in uniform acceptance region 70

7.6 Acceptance corrected dijet angular distributions 72

7.7 Distributions of $dN/d\chi$ 73

7.8 Phase II p^* spectra in bins of $\cos\theta^*$ 76

7.9 k_{t_ξ} distribution for ISAJET/QFL and data. 77

7.10 k_{t_η} distribution for ISAJET/QFL and data. 77

7.11 Z-vertex distribution in ISAJET/QFL and data. 78

7.12 Relation of parton p^* to jet p^* 79

7.13 Phase II acceptance corrections for $dN/d\cos\theta^*$ 81

7.14 Phase II acceptance corrections for $dN/d\chi$ 82

7.15 Pseudorapidity resolution of the trigger and probe jets 83

7.16 Azimuthal resolution of the trigger and probe jets 84

7.17 Phase II result for the η_{boost} and η^* parton-jet relation 85

7.18 Phase II determination of the reasonable choice of parameters 88

7.19 Phase II calculation of the systematic variation of acceptance 89

7.20 Phase II results for $dN/d\cos\theta^*$ 91

7.21 Phase II results for $dN/d\chi$ 92

A.1 RABBIT front-end amplifier 98

A.2 EWE operational schematic 100

A.3 Charge injection schematic 115

C.1 Dijet k_t vs ϕ_{jj} 128

C.2 k_{t_ξ} vs $E_{t_{sum}}$ 128

C.3 k_{t_ξ} for various bins of $E_{t_{sum}}$ 129

C.4 k_{t_ξ} for various bins of $E_{t_{sum}}$ 130

C.5 Jet E_t vs $E_{t_{sum}}$ 131

C.6 Jet E_t for slices of $E_{t_{sum}}$ 132

C.7 Jet E_t for slices of $E_{t_{sum}}$ 133

C.8 k_{t_η} vs $E_{t_{sum}}$ 139

C.9 Distributions in k_{t_η} 140

C.10 Distributions in k_{t_η} 141

C.11 σ_ξ, σ_η, σ^t, vs $E_t^{\frac{1}{2}}$ 142

C.12 k_t components for cone size = 0.6, min tower = 0.1 GeV 143

C.13 k_t components for cone size = 1.0, min tower = 0.1 GeV 143

D.1 Trigger and Probe jet definition 148

D.2 k_{t_ℓ} component for 90° crack 150

D.3 Central and East Plug η-ϕ distribution of jets 156

D.4 Central and West Plug η-ϕ distribution of jets 157

D.5 Central and East Forward η-ϕ distribution of jets 158

D.6 Central and West Forward η-ϕ distribution of jets 159

D.7 East and West plug Cluster Electromagnetic fractions 160

D.8 East and West Forward Cluster Electromagnetic fractions 161

D.9 σ_ξ vs $E_{t_{sum}}$ for the East and West Plugs 162

D.10 σ_ξ vs $E_{t_{sum}}$ for the East and West Forward 163

D.11 σ_ξ distribution for the Plug 164

D.12 σ_ξ distribution for the Forward 165

E.1 p_t spectra of the simple Monte Carlo and Data 171

E.2 Acceptance functions for various pseudorapidity cuts 174

F.1 Jet p_t distributions for ISAJET/QFL and data. 177

F.2 Jet electromagnetic fraction distributions for ISAJET/QFL and data. . . 178

F.3 Single jet mass distributions for ISAJET/QFL and data. 179

G.1 Up and Gluon distribution function evolution 184

G.2 Four QCD Feynman Diagrams 186

G.3 $dN/d\cos\theta^*$ for various theoretical input 193

This thesis is dedicated to my father and mother

Acknowledgements

With the hundreds of people on CDF, it is an awesome task to properly thank all the people with whom I have interacted.

I begin with my advisor, Roy Schwitters, who guided me in the general direction I needed to head, but left me free to choose what I wanted to do. Pointing me at the 1985 run and Hans Jensen as well as discussing the physics of jets in simple terms and suggesting I pursue the dijet balancing were particularly wise recommendations.

The group at Harvard provided intellectual and social support through the early phases. Craig Blocker taught me the ancient history (pre-1982) of high energy physics. Rob Carey, Ed Kearns, and Tiku Majumder provided invaluable support and companionship. George Brandenburg, and Mark Eaton lead us through the early development of chambers from the 5 inch by 5 inch to the 2 by 5 foot to the 5 by 5 foot and eventually to the first 20 chamber quadrant of the forward electromagnetic calorimeter we tested and toasted in June of 1984.

My Fermilab phase was dominated by a number of people, but the a particularly outstanding pair was Marge Shapiro and Hans Jensen. Marge has been a constant guide since her arrival and we have both grown up together on CDF. Hans got me involved in the RABBIT installation and suggested the dijet angular distribution as a topic for my thesis. His methodical habits were valuable to me and essential for understanding the electronics on one hand and the physics on the other.

I was able to take what I had learned from Hans and under the wise management of Dennis Theriot, the undaunted enthusiasm of the B0 technical support fellows, Bill

Wickenburg, Rich Krull, and Mark Knapp, and the trust of the Fermilab PIG group, get the gas calorimeter electronics installed and tested.

And the testing went on. Kathy Turner and her renowned band, Kevin Kuk, Paul Csiszer, and Fred Lewis, worked with me at 6:00 AM every morning for months curing the ills of the bunnies and debugging the MX's that failed to launch. Their excitement was inspiring. The rest of the pedestal gang included Jimmy Proudfoot, a man who taught me to separate the dung (central detector) from the junk (gas calorimeters – or was it the other way around?), and Steve Kuhlmann, who lent a bit of sanity to the exercise.

Surrounding the whole effort has been the CDF online group, with Dave Quarrie as gang leader. They taught me how to code and use tools that saved time in the end. Cathy Van Ingen taught me about FASTBUS, software, when I was being stupid, and when I was not. Dave listened to my suggestions and let me beat on his work. Chris Day, the man who knows all, taught some of it to me. Mark Anderson supported my efforts to use YHIST and was always open to suggestions for improving it. Geri Goeransson's good humor and sharp technical knowledge of FASTBUS was crucial to the online family.

And then, in another dimension, was the Argonne group, lead by the sophisticated, fashion-conscious, Larry Nodulman. Larry's uncanny physical intuition kept me from leaving the mass shell on several occasions. Bob Blair and Barry Wicklund have been helpful in teaching me basic points when I got confused. Jim Proudfoot's rather intense reaction to things going slightly wrong was happy to be a sounding board for my complaints.

Analyzing the jet data took a tremendous amount of coordination, and John Huth

provided the vision to keep the forty members of the jet group going in a similar direction. Jim Siegrist was always eager to discuss how to get there from here as we sat under a pile of data tapes and was willing to try to recall that there was even physics involved. Dave Brown took on the pedestal task, wrote the jet algorithm and worked with Melissa Franklin on the data cleanup. Taking on these dirty tasks allowed me to spend time studying the dijet k_t and I am grateful for what they have done.

Finally I thank my family and friends, who provided a reference point for (in)sanity, Budapest, mystery, the suburban camping style and pointers on cleaning swimming pool filters.

THE CDF COLLABORATION

F.Abe[p], D.Amidei[e], G.Apollinari[k], G.Ascoli[g], M.Atac[d], P.Auchincloss[n], A.R.Baden[f], A. Barbaro-Galtieri[i], V.E.Barnes[l], F.Bedeschi[k], S.Belforte[k], G.Bellettini[k], J.Bellinger[q], J.Bensinger[b], A.Beretvas[n], P.Berge[d], S.Bertolucci[e], S.Bhadra[g], M.Binkley[d], R.Blair[a], C.Blocker[b], J.Bofill[d], A.W.Booth[d], G.Brandenburg[f], D.Brown[f], A.Byon[l], K. L. Byrum[q], M. Campbell[c], R.Carey[f], W.Carithers[i], D.Carlsmith[q], J.T.Carroll[d], R.Cashmore[d], F.Cervelli[k], K.Chadwick[d,l], T.Chapin[m], G.Chiarelli[k], W.Chinowsky[i], S.Cihangir[o], D.Cline[q], D.Connor[j], M. Contreras[b], J.Cooper[d], M.Cordelli[e], M.Curatolo[e], C.Day[d], R.DelFabbro[k], M.Dell'Orso[k], L.DeMortier[b], T.Devlin[n], D.DiBitonto[o], R. Diebold[a], F.Dittus[d], A.DiVirgilio[k], J.E.Elias[d], R.Ely[i], S.Errede[g], B.Esposito[e], A. Feldman[f], B.Flaugher[n], E.Focardi[k], G.W.Foster[d], M.Franklin[f,g], J.Freeman[d], H.Frisch[c], Y.Fukui[h], A.F.Garfinkel[l], P.Giannetti[k], N.Giokaris[m], P.Giromini[e], L.Gladney[j], M.Gold[i], K.Goulianos[m], C.Grosso-Pilcher[c], C.Haber[i], S.R.Hahn[j], R.Handler[q], R.M.Harris[i], J.Hauser[c], T.Hessing[o], R.Hollebeek[j], L.Holloway[g], P.Hu[n], B.Hubbard[i], P.Hurst[g], J.Huth[d], H.Jensen[d], R.P.Johnson[d], U.Joshi[n], R.W.Kadel[d], T.Kamon[o], S.Kanda[p], D.A.Kardelis[g], I.Karliner[g], E.Kearns[f], R.Kephart[d], P.Kesten[b], H.Keutelian[g], S.Kim[p], L.Kirsch[b], K.Kondo[p], U. Kruse[g], S.E.Kuhlmann[l], A.T.Laasanen[l], W.Li[a], T.Liss[c], N.Lockyer[j], F.Marchetto[o], R.Markeloff[q], L. A. Markosky[q], P.McIntyre[o], A.Menzione[k], T.Meyer[o], S.Mikamo[h], M.Miller[j], T.Mimashi[p], S.Miscetti[e], M.Mishina[h], S.Miyashita[p], N.Mondal[q], S.Mori[p], Y.Morita[p], A.Mukherjee[d], C.Newman-Holmes[d], J. Ng[f], L.Nodulman[a], R.Paoletti[k], A.Para[d], J.Patrick[d], T.J.Phillips[f], H.Piekarz[b], R.Plunkett[m], L.Pondrom[q], J.Proudfoot[a], G.Punzi[k], D.Quarrie[d], K.Ragan[j], G.Redlinger[c], J.Rhoades[q], F.Rimondi[d], L.Ristori[k], T.Rohaly[j], A.Roodman[c], A.Sansoni[e], R.Sard[g], V.Scarpine[g], P.Schlabach[g], E.E.Schmidt[d], P.Schoessow[a], M.H.Schub[l], R.Schwitters[f], A.Scribano[k], S.Segler[d], M.Sekiguchi[p], P.Sestini[k], M.Shapiro[f], M.Sheaff[q], M.Shibata[p], M.Shochet[c], J.Siegrist[i], P.Sinervo[j], J.Skarha[q], D.A.Smith[g], F.D.Snider[c], R.St.Denis[f], A.Stefanini[k], Y.Takaiwa[p], K.Takikawa[p], D.Theriot[d], A.Tollestrup[d], G.Tonelli[k], W. Trischuk[f], Y.Tsay[c], F.Ukegawa[p], D.Underwood[a], R.Vidal[d], R.G.Wagner[a], R.L.Wagner[d], J.Walsh[j], T.Watts[n], R.Webb[o], T.Westhusing[g], S.White[m], A.Wicklund[a], H.H.Williams[j], T.Yamanouchi[d], A.Yamashita[p], K.Yasuoka[p], G.P.Yeh[d], J.Yoh[d], F.Zetti[k]

[a] Argonne National Laboratory- [b] Brandeis University- [c] University of Chicago
[d] Fermi National Accelerator Laboratory- [e] INFN, Laboratori Nazionali di Frascati, Italy
[f] Harvard University- [g] University of Illinois- [h] KEK, Japan
[i] Lawrence Berkeley Laboratory- [j] University of Pennsylvania
[k] INFN, University and Scuola Normale Superiore of Pisa, Italy- [l] Purdue University
[m] Rockefeller University- [n] Rutgers University- [o] Texas A&M University
[p] University of Tsukuba, Japan- [q] University of Wisconsin

Work supported by the U.S. Department of Energy, Division of High Energy Physics,

Contract W-31-109-ENG-38, and Harvard University, Contract DE-AC02-76ER03064.

Chapter 1

Introduction

Hadron physics has been revolutionized by the existence of jet events such as the one shown in Figure 1.1. These events contain large depositions of energy in small regions of solid angle and are commonly observed at the energies available at the proton-antiproton colliders at CERN and Fermilab where the center of mass energies ($\sqrt{s}$) are 630 and 1800 GeV respectively. They permit quantitative experimental tests of the theory of strong interactions, quantum chromodynamics (QCD) to be conducted at hadron colliders.

In this thesis two jet events produced in the reaction $\bar{p}p \rightarrow \text{jet1} + \text{jet2} + \text{X}$ are used to probe QCD. The Collider Detector at Fermilab (CDF) is used to measure the energies and angles of the jets. The calculated value of the angular distribution in the center of mass of the partons of which the protons consist is compared to that for the jets observed at CDF. The data are shown to fit the QCD prediction that $dN/d\cos\theta^* \sim \sin^{-4}\theta^*/2$ as in Rutherford scattering.

Jet energy resolution and the transverse momentum of the dijet system introduce systematic errors that must be controlled in order to distinguish between QCD and

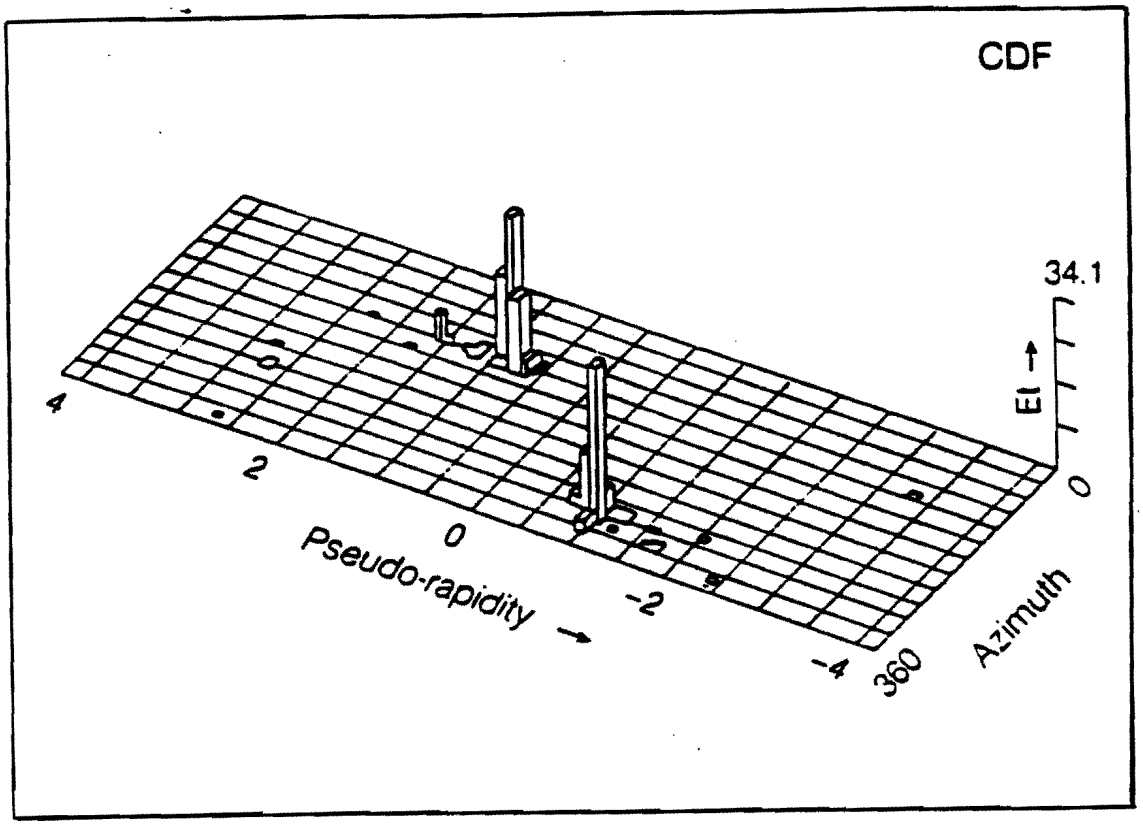

Figure 1.1: Example of a dijet event at the Collider Detector at Fermilab. The plot shows pseudorapidity($\eta \equiv -ln(\tan\theta/2)$) vs. phi in the plane and transverse energy on the vertical scale. The two jets are characterized by the deposition of large amounts of transverse energy in two localized clusters approximately 180 degrees apart in azimuth.

composite models. For this reason, a detailed study of the transverse momentum balance of the jets is made. The resolution (σ) of jets having transverse energies ($E_t \equiv E \sin\theta$) between 30 and 100 GeV is shown to go like $\sigma/E = A/\sqrt{(E)}$, where the constant, A, depends on the algorithm used to define the jet and has values ranging from 0.83 to 1.20 $GeV^{1/2}$.

The thesis is organized as as follows. Chapter 2 motivates the parton model from the history of the theory and experiment of hadron collision. A description of QCD follows with emphasis placed on the prediction of the scattering behavior of dijets. Chapter 3 describes the Fermilab Collider and the CDF experiment. Chapter 4 outlines the calibration and performance of the CDF calorimeters. In Chapter 5 the collection of events in the CDF online system and offline reconstruction of jets is described. The characteristics of these events are presented. Chapter 6 describes the behavior of the transverse momentum of the dijet system and the extraction of the calorimeter jet resolution. The analysis of the dijet angular distribution is given in Chapter 7, with an emphasis on the kinematics and acceptance corrections. The work is summarized in Chapter 8.

Chapter 2

The Parton Model and QCD

This chapter begins with a description of the general properties of hadron collisions and the experimental and theoretical history that lead to the parton model. The linkage of quarks to partons is discussed. The field theory of the strong interaction, quantum chromodynamics, is described with particular attention paid to its experimental predictions concerning the angular distribution in the scattering of partons.

2.1 Hadron Collisions

Particles produced in a majority of hadron collision events have an average transverse momentum relative to the collision axis that varies from 0.350 to 0.500 GeV/c as the center of mass energy increases from 63 to 1800 GeV [1]. This scale is set by that of the size of the hadrons, 1 fm or 0.200 GeV. The transverse momentum spectrum of final state charged particles integrated over all events at $\sqrt{s} = 1800$ GeV behaves like $Ap_0^n/(p_t + p_0)^n$ where $p_0 = 1.29 \pm 0.2$ GeV/c, $A = 0.45 \pm 0.01$, and $n = 8.26 \pm 0.08$ [1].

The distribution of particles is uniform in rapidity, a kinematic variable defined as

$$y = \frac{1}{2} \log \frac{E + p_z}{E - p_z}, \tag{2.1}$$

where the energy of the particle is E and the momentum along the axis of the colliding hadrons is p_z [2]. The average rapidity density, $\bar{n}$, can be expressed as $\bar{n} \equiv \langle dn/dy \rangle dy$ and rises logarithmically with energy, from $\langle dn/dy \rangle |_{y=0} = 1.4$ at $\sqrt{s} = 20$ GeV to $\langle dn/dy \rangle |_{y=0} = 3.3$ at $\sqrt{s} = 540$ GeV [2]. The rapidity distribution remains approximately flat, but grows wider with increasing energy in a manner consistent with conservation of energy and the observed behavior of the rapidity density and transverse momentum spectra.

2.2 The Parton Model and Hadronic Jets

The history of hadronic jets has roots in the physics of deep inelastic electron-proton scattering. Bjorken showed scaling behavior in electroproduction measurements in the deep inelastic region [3]. Feynman proposed this scaling could be predicted from a parton model which viewed the hadrons as being made of pointlike constituents which interacted very weakly with one another [4]. This concept seems self-contradictory in the sense that it is clear that the partons are bound tightly within the scattering nucleons, but as described below, they interact as though they were free, point particles.

Berman, Bjorken and Kogut [5] were able to make a number of powerful predictions about hadronic collisions using the parton model with some simple assumptions based on experimental observations of the soft hadronic processes described in Section 2.1. They described the hard scattering interaction in hadronic collisions as occurring in three

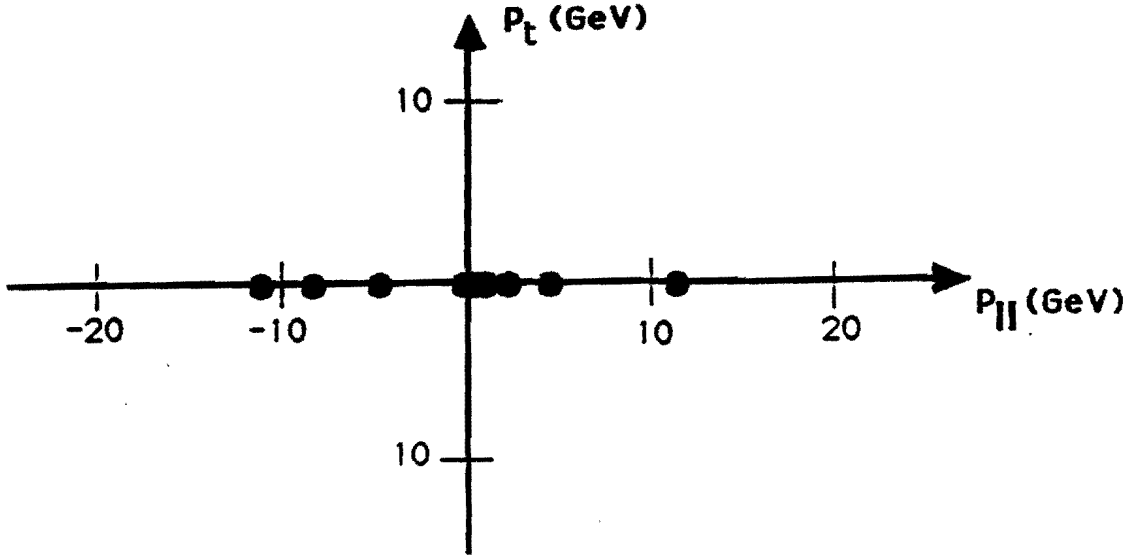

Figure 2.1: Initial Parton phase space configuration.

stages characterized by the time scale for each stage and the momentum phase space configuration of the partons. First, the partons have some distribution, f(x), which partitions the hadron momentum among the partons (Figure 2.1). The partons are confined within the hadron and have a time and energy scale set by that size. Second, the hard scattering occurs, separating the pair of interacting partons from the remaining set (Figure 2.2). Finally, the partons *fragment*, forming a cascade as they dress themselves into the final state hadrons (Figure 2.3). Once again the time scale of the final state cascade is on the order of the confinement size of a hadron.

Since it is rare for hard scattering processes to occur, the final state cascade is characterized by the properties of the "normal" soft interactions described in Section 2.1: flat rapidity distributions of particles that grow logarithmically in width and height and limited momentum transverse to the direction of the scattered partons; one would not expect further hard processes to occur. Furthermore, interference between these three

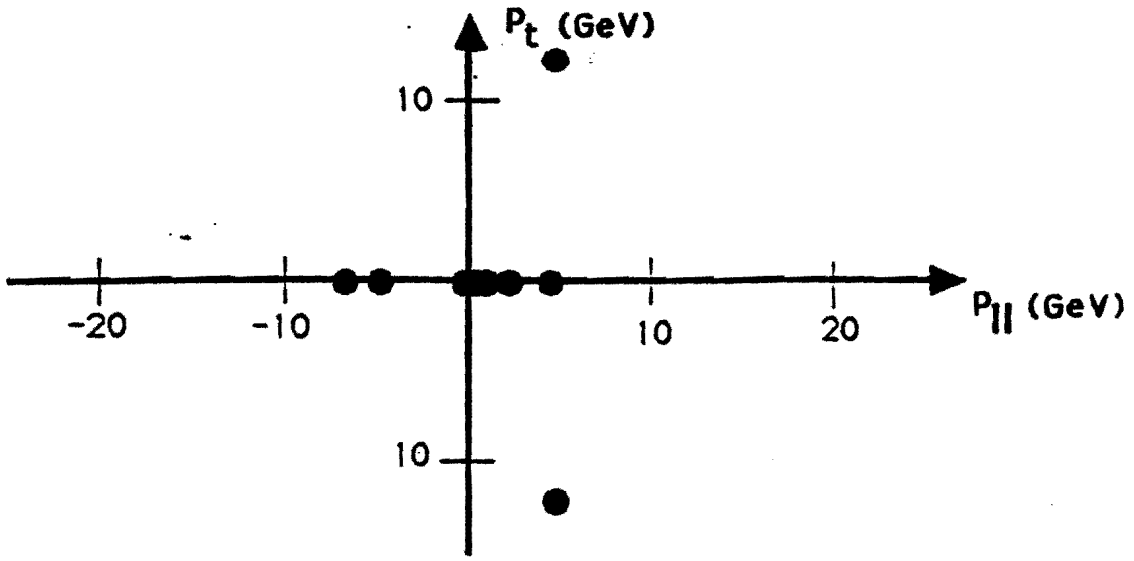

Figure 2.2: Parton phase space configuration at the moment of collision.

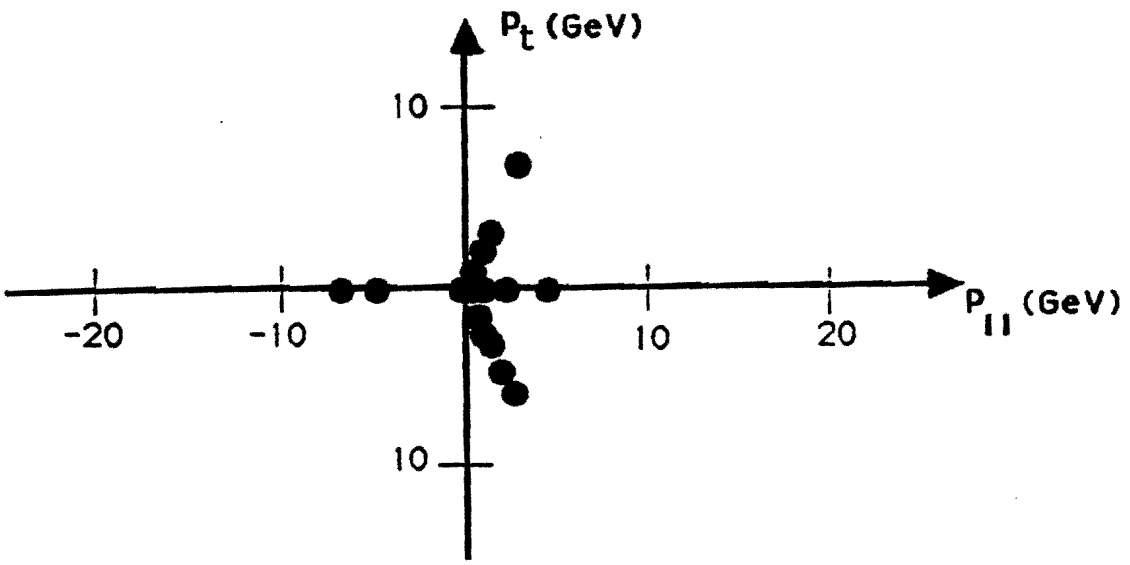

Figure 2.3: Final parton phase space configuration.

stages would be suppressed by the large differences in the time scales. With this final state picture, the scattered parton partitions its energy among the observed hadrons in such a way that the hadrons have most of their momentum along the same direction as the parton. That is to say, there will be a tight bundle of collimated particles emerging from the collision: jets.

Clear evidence of such hadronic jet events was seen in the UA2 experiment at the CERN $Sp\bar{p}S$ collider at $\sqrt{s} = 540$ GeV. The detector was constructed in projective calorimeter towers of $\Delta\eta \times \Delta\phi = 0.1 \times 15^o$, where the pseudorapidity is $\eta = -\ln(\tan\theta/2)$. The transverse energy, $E_{t_i} \equiv E_i \sin\theta_i$, was formed in each of the calorimeter cells. The total transverse energy was calculated by summing over the transverse energies of all the cells. A simple algorithm found clusters of energy with $\sqrt{\Delta\eta^2 + \Delta\phi^2} \leq 1.0$ and computed the transverse energy for each cluster. The fraction of the total transverse energy contained in the highest transverse energy cluster was computed (h_1) as well as the fraction of transverse energy contained in both the first and second highest clusters (h_2). It can be seen (Figure 2.4) that as the total transverse energy increases, the majority of the energy is seen in these two localized regions of the calorimeter, demonstrating the emergence of jet structure in hadron collisions.

2.3 Partons to Quarks and Gluons

The parton model motivated by deep inelastic lepton-proton and hadron-hadron hard scattering experiments is currently described by a renormalizable non-abelian gauge theory: quantum chromodynamics (QCD) [6,7,8]. The main features of the parton model

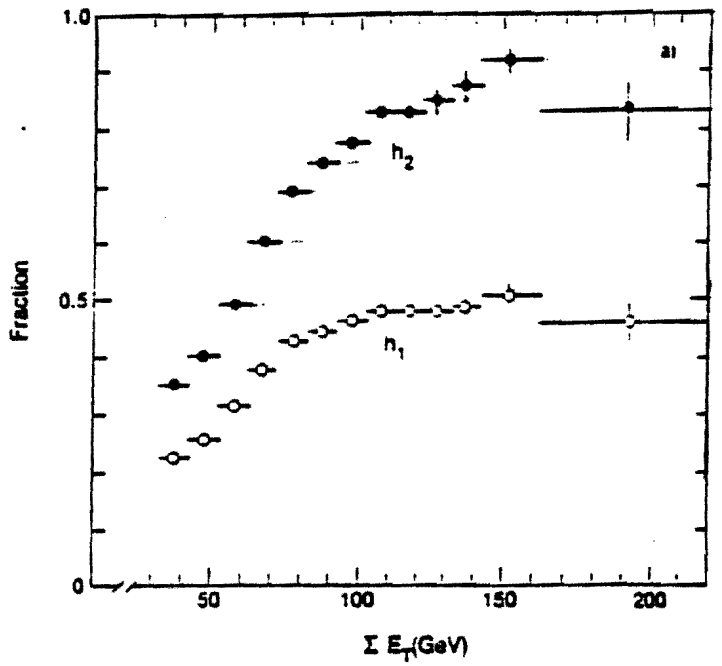

Figure 2.4: Evidence for Jets at UA2. h_1 corresponds to the fraction of total transverse energy in the highest E_t cluster, h_2 is the fraction of total transverse energy in the first and second highest E_t clusters. These quantities and are plotted as a function of the total transverse energy in the detector.

described by Berman, Bjorken, and Kogut remain but are cast in a slightly different language. There are two types of partons: the quarks, originally postulated as a mathematical construct to describe hadron spectroscopy [9,10], and gluons that mediate the parton interactions. The distribution functions of parton momenta, f(x), are related to the momentum distributions for each of the flavors of quarks, the gluons, and the anti-quarks. The dynamics of the hard scattering of the partons are described in detail by perturbative calculations of the equations of motion of the QCD Lagrangian[11]. The two are tied together with the theorem of factorization which states that since the initial and final distributions of partons interact on time scales that are vastly different from that of the hard scattering (Figure 2.5), the interference between the hard scattering and the initial and final states should be small; therefore one may sum up over the individual momentum densities of the incoming constituents and add the cross sections [12]. The

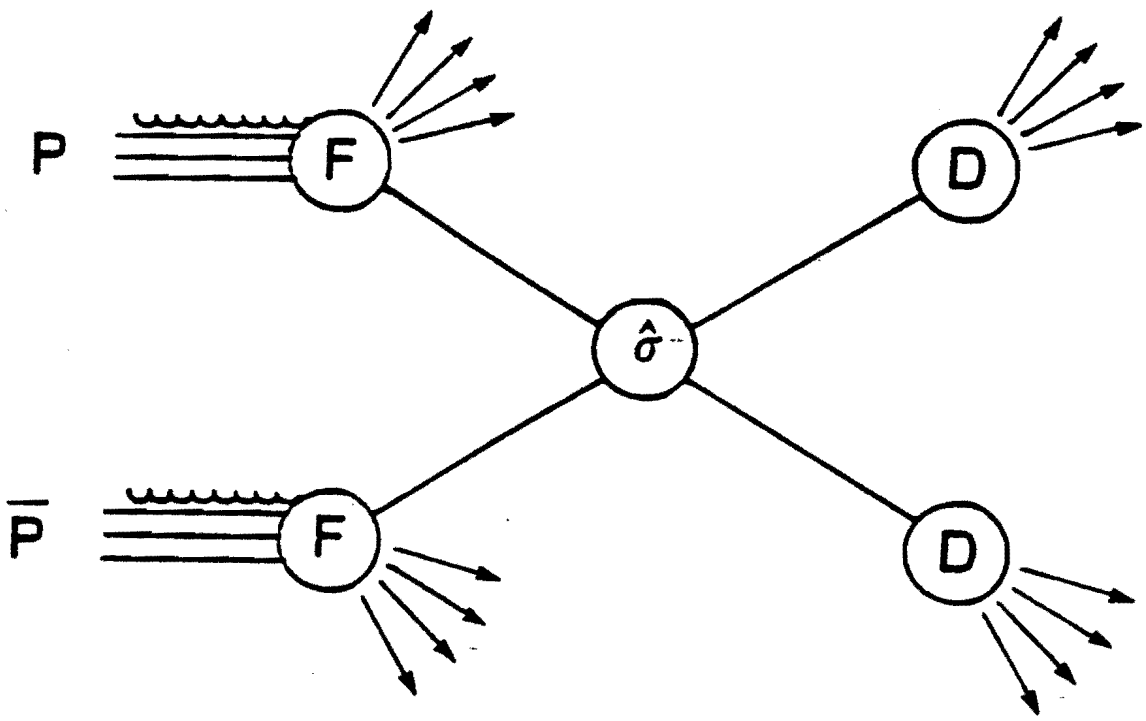

Figure 2.5: Illustration of a $\bar{p}p$ collision. The partons participating in the hard scattering are chosen according to their momentum distribution functions of the incoming proton and antiproton. The scattering occurs according to perturbative QCD. The final state fragments into hadrons according to a fragmentation function $D(z)$, where z is the momentum fraction of the observed hadrons. The observed cross section is an incoherent sum of all possible subprocesses weighted by the strength of the interaction, α_s and the probability of finding the initial state partons, f(x).

expression for the production of two jets may be written schematically as (see Section G.1 for exact expression):

$$\frac{d\sigma(\bar{p}p \to jet_1 + jet_2 + X)}{dy_1 dy_2 dp_t^2} = \sum_{ij} f_i\left(x_i, Q^2\right) f_j\left(x_j, Q^2\right) \frac{d\sigma\left(ij \to kl\right)}{d\hat{t}}. \tag{2.2}$$

The parton flavors are denoted by i,j,k and l. The hadron momentum fractions of each parton flavor has been indicated by $f\left(x, Q^2\right)$. The hard scattering parton cross section is given by $\sigma\left(ij \to kl\right)$ and the scale at which the interaction occurs is given by Q. The variables $\hat{s}$, $\hat{t}$, and $\hat{u}$ are defined in Section 2.4.1.

2.4 Features of the Lowest Order Perturbative QCD Solution

The perturbative solution of the equations of motion can be discussed in terms of three main features: the form of the fundamental cross sections, the strength and behaviour of the coupling, and the behaviour of the parton momentum distribution functions.

2.4.1 Fundamental scattering

There are three kinds of parton subprocess interactions: quark-quark (qq), quark-gluon (qg), and gluon-gluon (gg). The expressions for the individual subprocess scattering cross sections and the angular distributions are shown in Tables G.1 and G.2. They may be written in terms of the variable,

$$\chi = \frac{\hat{u}}{\hat{t}},$$

where

$$\hat{t} = \left(p_1^\mu - p_3^\mu\right)^2 = -p_t\sqrt{s}\tan\frac{\theta}{2} = -\frac{\hat{s}}{2}\left(1 - \cos\theta^*\right),$$

$$\hat{u} = (p_2^\mu - p_3^\mu)^2 = -p_t\sqrt{s}\cot\frac{\theta}{2} = -\frac{\hat{s}}{2}(1+\cos\theta^*),$$

and, for completeness,

$$\hat{s} = (p_1^\mu + p_2^\mu)^2 = x_1 x_2 s = p_t\sqrt{s}\left(x_1\tan\frac{\theta}{2} + x_2\cot\frac{\theta}{2}\right).$$

The four-momenta of the incoming partons are given by p_1, p_2, p_3, and p_4. The scattering angle in the center of mass is given by θ^*, the square of the center of mass energy of the proton and antiproton is s, the momentum fractions of the incoming partons are x_1 and x_2, the transverse momentum of the outgoing partons is p_t. The square of the invariant mass of the two-parton system is $\hat{s}$.

The various subprocesses may be approximated by single effective subprocess (SES) [13] so that the hard scattering cross section may be written:

$$\frac{d\hat{\sigma}}{d\chi} = \frac{\pi\alpha_s^2}{\hat{s}}\left[\frac{\chi^2+\chi+1+\chi^{-1}+\chi^{-2}}{(1+\chi)^2}\right], \tag{2.3}$$

where α_s is the QCD coupling constant. An estimate of the two jet cross section is obtained by multiplying the SES by an effective quark and gluon momentum distribution function.

This fact makes salient features of the dynamics of QCD easier to grasp. For a fixed invariant mass ($\sqrt{\hat{s}}$) and for large χ (≥ 2), the cross section, $d\sigma/d\chi$, goes to a constant value. Upon conversion back to the center of mass scattering angle, θ^*, where $\chi = (1+\cos\theta^*)/(1-\cos\theta^*)$, one finds that the cross section, $d\sigma/d\Omega \sim d\sigma/d\cos\theta^*$, goes as $\sin^{-4}(\theta^*/2)$. Testing this prediction of the behavior of the parton scattering is the simple result that is a main goal of this thesis.

2.4.2 The Running Coupling Constant

Perturbative QCD calculations indicate that the coupling constant varies with the energy scale at which the interaction occurs (See Section G.1.3). Since this energy scale is taken as the transverse momentum of the scattered parton, the coupling constant is logarithmically χ-dependent and Equation 2.3 is modified.

2.4.3 Parton Momentum Distribution Function Evolution

As shown in Equation 2.2, the individual parton subprocesses must be convoluted with the parton momentum distribution functions when the cross section is calculated. Two uncertainties arise from these operations. First, since proton structure functions are determined using lepton probes, the gluon distribution functions cannot be measured directly and must be inferred. The distribution functions are measured at an energy scale different from the hard scattering and must be evolved to the proper choice of scale [14]. Second, there is uncertainty in the proper scale choice(see Section G.2.2).

To address these problems, the standard parameterizations of the momentum distribution functions come in sets that are intended to bracket the uncertainty in the gluon distribution function. Also, the calculations are performed for various choices of Q^2 scale. These calculations have been done for the dijet angular distribution and are described in Section G.2.2. The main observation is that the form of the angular distribution is insensitive to these theoretical uncertainties at $\sqrt{s} = 1800$ GeV.

Chapter 3

The Collider Detector at Fermilab

In order to study the physics of two jets, one must have a large sample of unambiguously defined jet events and a detector capable of measuring the kinematic variables of interest. The Fermilab collider, the highest energy collider in the world, provides hadronic collisions at a center of mass energy of 1800 GeV. The Collider Detector at Fermilab (CDF) is a multipurpose detector operating at the FNAL collider. It provides tracking and calorimetry information over 98% of the solid angle, and can provide the kinematic data necessary to measure two jet physics.

3.1 CDF

CDF [15] was constructed to provide tracking information, electromagnetic and hadronic energy data, and muon detection for particles created from collisions of protons with

antiprotons. The apparatus,shown in Figure 3.1, is described in some detail here.

3.1.1 Tracking

CDF has four tracking systems. These are the Vertex Time Projection Chamber, (VTPC) the Central Tracking Chamber (CTC), the Central Drift Tubes (CDT), and the Forward Tracking Chamber (FTC). The VTPC, CTC and CDT are contained within a 1.5 Tesla superconducting solenoid.

3.1.1.1 VTPC

The Vertex Time Projection Chamber consists of eight modules mounted end-to-end along the beam direction. It is 2.8 meters in length and contains a total of 3072 sense wires that measure track coordinates in R-Z (R is the radial distance from the beam, and Z is the distance along the beam). This is used to determine the position of the interaction to within 3 millimeters. The VTPC is used in jet analysis for two reasons. First, since the interaction vertices are gaussian distributed with $\sigma = 35$ cm, it is necessary to make event by event determination of the z component of the vertex position so that the correct values of the jet pseudorapidities may be evaluated. Second, the VTPC is used to distinguish events due to $\bar{p}p$ collisions from collisions of either beam with the residual gas in the vacuum pipe of the accelerator.

3.1.1.2 CTC, CDT, FTC

The Central Tracking Chamber (CTC) is a 1.3 m-radius 3.2 m-long cylindrical drift chamber which gives precise momentum measurements in the angular region $40^o \leq \theta \leq$

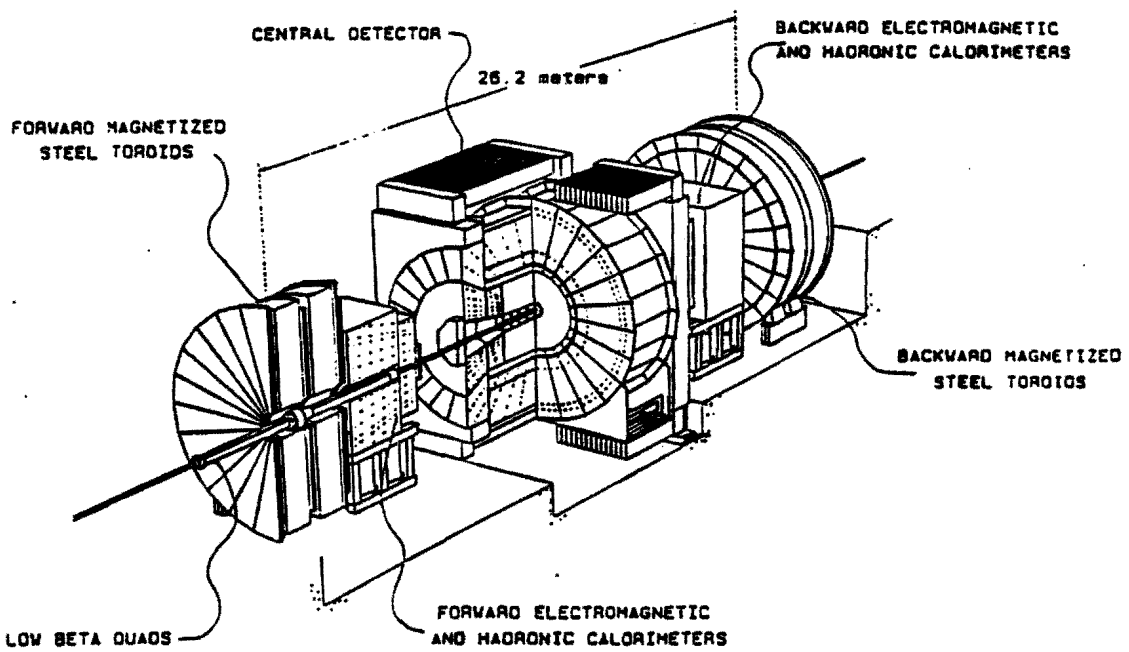

Figure 3.1: Major systems of the CDF detector are shown here. Tracking includes the vertex time projection chambers (VTPC), the central tracking chamber (CTC), forward tracking chamber (FTC), and central muon drift tubes (CDT). Calorimeters include the central electromagnetic (CEM), central hadron (CHA), wall hadron (WHA), plug electromagnetic (PEM), plug hadron (PHA), forward electromagnetic (FEM) and forward hadron (FHA).

140°. It has 84 wire layers arranged in nine superlayers, with small angle stereo in some layers to provide for Z position measurement. The resolution in r-ϕ is about 200 microns, and the total number of wires is 36000. It is able to measure the momenta of tracks to an accuracy of $\delta p_t/p_t^2 \leq 0.002(GeV/c)^{-1}$.

The Central Drift Tubes (CDT) consist of three layers of 3 m-long, 1.27 cm-diameter stainless steel tubes mounted on the outer perimeter of the CTC. A correlated space point measurement is made by using drift-time and charge division measurements. Typical resolutions are 2.5 mm in the beam direction and 200 microns in azimuth.

The Forward Tracking Chamber (FTC) is a radial drift chamber which covers the small angular regions ($2^o \leq \theta \leq 10^o$ and $170^o \leq \theta \leq 178^o$). These chambers have 20 wires/$\Delta\phi$=5°, and a resolution of 120 microns.

The CTC, CDT, and FTC are not used in the analysis presented here.

3.1.2 Calorimetry

The most important part of the detector for the measurement of the two jet angular distributions is the calorimetry. In CDF, there are three systems of calorimetry, the Central, Plug and Forward systems. All of these systems measure the energies of ensembles of particles by sampling the electromagnetic and hadron energies. The electromagnetic portions sample the showers of electrons and photons in a sandwich of lead and detector. The hadronic portions sample the showers of pions in a sandwich of steel and detector. The calorimeters are segmented in cells of pseudorapidity and azimuth. These cells form projective towers that point back to the nominal interaction vertex. The parameters of the CDF calorimeters are shown in Tables 3.1 and 3.2. One quadrant of calorimeter

tower segmentation is illustrated in Figure 3.2.

3.1.2.1 Central Calorimeter

The central calorimeter consists of the *arches* and *endwalls*. There are four arches that form a barrel that surrounds the superconducting solenoid. These arches are built out of individual wedge-shaped modules. Each wedge contains a portion of the electromagnetic and hadronic calorimeters as well as part of the muon system. The electromagnetic calorimeter consists of a stack of 31 layers of lead and scintillator. Wave-shifter and light guides attached to photomultiplier tubes are positioned along two sides of the stack. They provide redundant readout of each projective tower so that high voltage breakdown in a single photomultiplier tube may be easily recognized. They also give a better determination of the azimuthal energy centroid of showers. There is a strip chamber placed at layer nine of the electromagnetic calorimeter for aiding in the identification of electrons. In the wedges, the hadronic calorimeter consists of 32 layers of scintillator and steel also read out via wave-shifters and light pipes that are attached to two photomultiplier tubes, one on each side of every tower. Hadronic coverage of projective towers that overlap the return yoke of the magnet is handled by 15 layers of steel and scintillator in the endwall calorimeters. Taken together, the central arches and the endwall cover the central two units of pseudorapidity with both electromagnetic and hadronic compartments.

	Central		Endwall
	Electromagnetic	Hadronic	Hadronic
$\|\eta\|$ coverage	0-1.1	0-0.9	0.7-1.3
Tower size ($\Delta\eta \times \Delta\phi$)	0.1 x 0.26	0.1 x 0.26	0.1 x 0.26
Longitudinal samples in tower	1†	1	1
Active medium	polystyrene scintillator	acrylic scintillator	acrylic scintillator
Scintillator thickness	0.5 cm	1.0 cm	1.0 cm
Number of Layers	31	32	15
Absorber	Pb	Fe	Fe
Absorber Thickness	0.32 cm	2.5 cm	5.1 cm
Typical phototube high voltage	-1100 V	-1500 V	-1100 V
Typical phototube gain	1.2×10^5	6×10^5	1.0×10^6
Typical tower signal	-4 pC/GeV	-4 pC/GeV	-4 pC/GeV
Energy resolution (σ/E at 50 GeV)	2%	11%	14%
Typical position resolution at 50 GeV	0.2x0.2 cm^2†	10x5 cm^2	10x5 cm^2
Characteristic total width of azimuthal boundary region	3.5 cm	4.1 cm	3.8 cm, 8.9 cm alternating

† An imbedded proportional tube chamber at shower maximum gives additional information. The quoted position resolution is measured with this chamber

Table 3.1: Summary of CDF central calorimeter properties

	Endplug		Forward	
	Electromagnetic	Hadronic	Electromagnetic	Hadronic
$\|\eta\|$ coverage	1.1-2.4	1.3-2.4	2.2-4.2	2.3-4.2
Tower size ($\Delta\eta \times \Delta\phi$)	0.09 x 0.09	0.09 x 0.09	0.1 x 0.09	0.1 x 0.09
Longitudinal samples in tower	3	1	2	1
Active medium	Proportional tube chambers with cathode pad readout			
proportional tube size (cm^2)	0.7 x 0.7	1.4 x 0.8	1.0 x 0.7	1.5 x 1.0
Number of Layers	34	20	30	27
Absorber	Pb	Fe	94%Pb,6%Sb	Fe
Absorber Thickness	0.27 cm	5.1 cm	0.48 cm	5.1 cm
Typical wire high voltage	+1700 V	+2120 V	+1900 V	+2200 V
Typical wire gain	2×10^3	2×10^4	5×10^3	1×10^4
Typical tower signal (pc/GeV)	+1.25	+1.3	+2	+0.7
Energy resolution (σ/E at 50 GeV)	3%	20%	4.5%	23%
Typical position resolution at 50 GeV	0.2x0.2 cm^2	2x2 cm^2	0.2x0.2 cm^2	3x3 cm^2
Characteristic total width of azimuthal boundary region (cm)	0.9	0.8	0.7;3.2†	1.3;3.2†

† The first number is for the vertical boundary.
The second number is for the horizontal boundary.

Table 3.2: Summary of CDF gas calorimeter properties

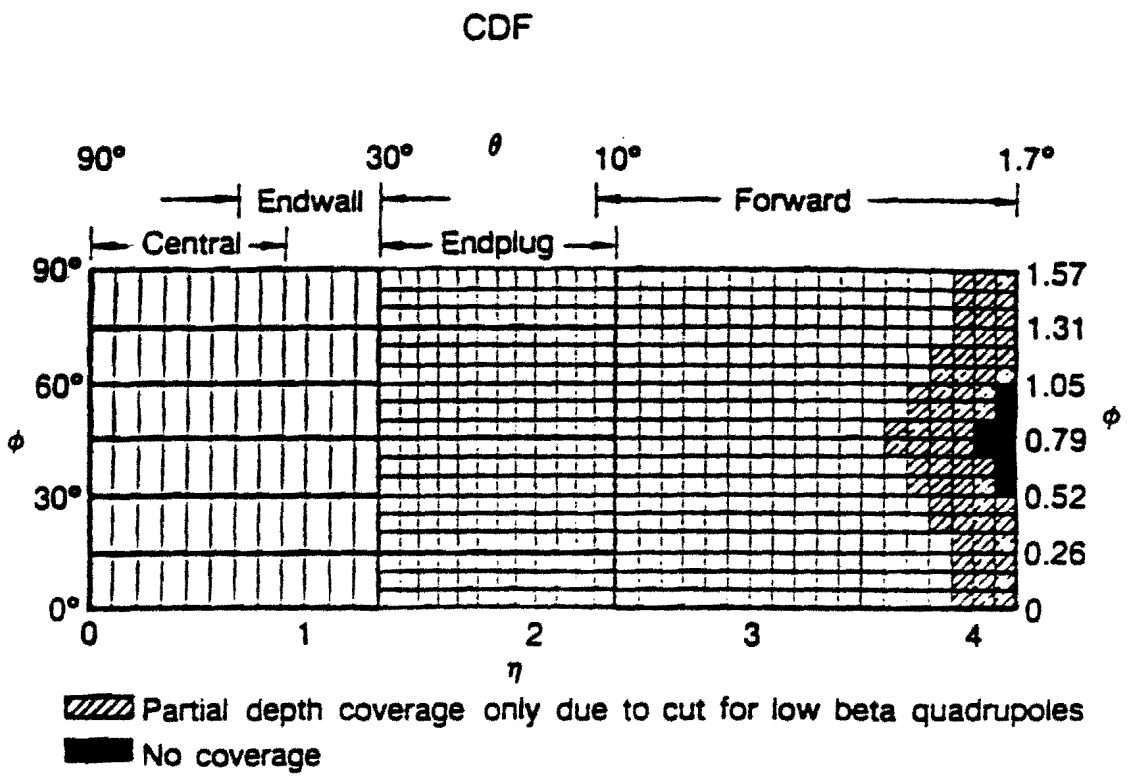

Figure 3.2: One quadrant of the CDF calorimeter coverage showing the η-ϕ segmentation

3.1.2.2 Plug Calorimetry

The endplug electromagnetic calorimeter consists of 34 layers of 0.27 cm lead sandwiched with gas proportional chambers. The chambers use cathode pad readout which maintains the projective geometry. The electromagnetic towers are divided into three compartments. These divisions in depth sample 3.8, 14.2, and 3.0 radiation lengths each. The wires in each plane are ganged in ninety degree sections for readout. The chambers in the middle portion are instrumented with pads on both sides, one side forming the projective towers, and the other providing x-y strip information across the face of the calorimeter for better electron identification. Each of the chambers provides either an x or y view.

The endplug hadron calorimeter consists of 20 layers of 5.1 cm steel sandwiched with gas proportional chambers. As in the electromagnetic compartment, the chambers utilize cathode pad readout to maintain projective geometry. The wire planes are ganged in 30 degree sections and are read out individually to provide longitudinal shower profile data.

The endplug calorimeters cover the pseudorapidity region $1.1 \leq |\eta| \leq 2.4$.

3.1.3 Forward Calorimetry

The forward electromagnetic calorimeter consists of 30 layers of 0.48 cm lead sandwiched with gas proportional chambers which are read out via cathode pads. The detector is constructed in a wall consisting of ninety degree *quadrants*. This calorimeter is read out in two depths for each tower, the separation occurring after layer 15. The wire information is ganged in five sections across the face of each layer of each quadrant and read out to provide longitudinal profile information for identification of isolated electrons.

The forward hadron calorimeter consists of 27 layers of 5.1 cm steel sandwiched with gas proportional chambers. For the period of data taking used here, only half of the chambers were in place, giving an segmentation of 14 layers of 10.2 cm steel sandwiched with the chambers. They are read out via cathode pads ganged in towers. They are also constructed in ninety degree sections, but wire readout is summed over the whole layer.

The forward/backward detectors cover the pseudorapidity range $2.2 \leq |\eta| \leq 4.2$.

3.1.4 Muon Detection

There are two separate muons systems covering two regions of space. The central muon system lies behind the central hadron calorimeter and consists of four layers of drift chambers. These chambers measure the azimuthal location of a muon to 250 microns and the location along the beam to 1.2 mm (using charge division). They cover polar angles from $56^o \leq \theta \leq 124^o$.

The forward muon system consists of three layers of electrodeless drift chambers and two layers of scintillator (used for triggering) placed around a system of two toriods in each of the forward and backward regions. The toriods run at a magnetic field that varies from 2.0 Telsa at the inner radius to 1.6 Tesla at the outer radius. The angular coverage is between 3° and 16° relative to the beam pipe.

These systems are not used in the analysis presented here.

3.1.5 Trigger

The proton-antiproton collisions produced by the Tevatron can occur up to every seven microseconds as three bunches of circulating protons intersect with three bunches of

antiprotons moving in the opposite direction. The collision rate per second is given by $dN/dt = L\sigma$, where σ is the cross section for a collision and L is the luminosity given by

$$L = \frac{N_p N_{\bar{p}} M f_r}{4\pi^2 \sigma_{beam}^2}, \tag{3.4}$$

where N_p, $N_{\bar{p}}$ are the number of protons and and antiprotons in a bunch, M is the number of bunches and σ_{beam} is the gaussian half-width of the beam. For luminosities of order 10^{29} $cm^{-2}s^{-1}$, 3 bunches and beam half-widths of 0.27 mm, and a cross section of 42 mb, approximately 5000 interactions occur each second. Since only one event may be recorded each second, this requires a sophisticated trigger selection.

For the 1987 collider run, the triggering of CDF was done using a combination of two systems. The first, the Beam-Beam Counters (BBC's), consists of a scintillator hodoscope in front of each of the forward calorimeters. These planes provide a *minimum bias* trigger for the detector and are used as a luminosity monitor. The counters have a timing accuracy of better than 200 psec. They are arranged in a rectangle around the beam pipe and cover the angular region from 0.32^o to 4.47^o corresponding to $3.24 \leq |\eta| \leq 5.90$. The minimum bias trigger requires at least one counter in each plane to fire within a 15 nsec window centered on the beam crossing time.

The second system exploits the projective geometry of the calorimetry towers. Both electromagnetic and hadronic calorimeter towers are summed into *trigger towers* with a width in $\Delta\eta \times \Delta\phi = 0.2 \times 15^o$. This results in a representation of the entire detector as a 42 (in pseudorapidity) by 24 (in azimuth) array for the electromagnetic and hadronic calorimeters. For the case of the central detector, the analog output of the photomultiplier tubes are brought to the counting room individually and summed into the trigger

towers. All gas calorimetry pad signals are summed at the detector into trigger towers. The analog calorimeter signals are weighted by $\sin\theta$ to form the transverse energy for the tower and compared to the set trigger tower threshold. All trigger towers above this threshold (typically 1 GeV) are summed and compared to the total transverse energy trigger level. If the total exceeds this level, the event is read out of the detector by the data acquisition system. Further details of the triggers for the 1987 run are given in Section 5.1.2.

3.1.6 Data Acquisition and Online Control

The CDF Data Acquisition system (DAQ) has three major components: the analog front end system, RABBIT, the digital control system, FASTBUS, and the VAX computers that accumulate the data and write them to tape.

The RABBIT (Redundant Analog Bus-Based Information Transfer) system, together with microprocessors, digitize and store the calorimeter data. The main features are:

- Analog electronics attached to the active detector elements are multiplexed for digitization to a single analog to digital convertor (ADC). (There are approximately 500 channels/crate in 120 crates);
- Comparison of the signal before and after beam crossing allowing for removal of baseline shifts;
- Analog pedestal subtraction and threshold comparison;
- Digital processing to do linear and quadratic channel by channel corrections that incorporate calibration constants.

The FASTBUS system at CDF consists of over 50 crates and one thousand modules. It coordinates the timing and transfer of events from the RABBIT and trigger systems into the VAX and it contains the digital electronics for readout of the tracking systems.

The DAQ system is configured, controlled, and diagnosed by a large body of software (over 250000 lines of code) that resides on the VAX. The hardware is automatically configured in about ten minute's time. Calibrations are performed periodically (see Chapter 4). The results are stored in databases and the information is downloaded to the scanners so that the data are corrected online.

3.2 The 1987 Collider Run

The data taking period extended from February through May, 1987. Most of the time was used to test out the accelerator and detector systems. The luminosity of the machine grew exponentially during that time as shown in Figures 3.3 and 3.4.

The efficiency of data taking grew to a maximum of 83%. An important limitation during data taking was the need to disable triggering during injection of protons into the Fermilab main ring. This accelerator passes over the top of the detector and is used for antiproton production at the same time that colliding beam data are being recorded. The detector triggers on particles lost during main ring injection; main ring protons lost during other times constitute a background to jet events (see Chapter 5). Although access to the detector was extremely limited (a few hours every couple of weeks), fewer than one percent of the calorimeter channels failed during the running period. The luminosity recorded on tape is shown in Figure 3.3.

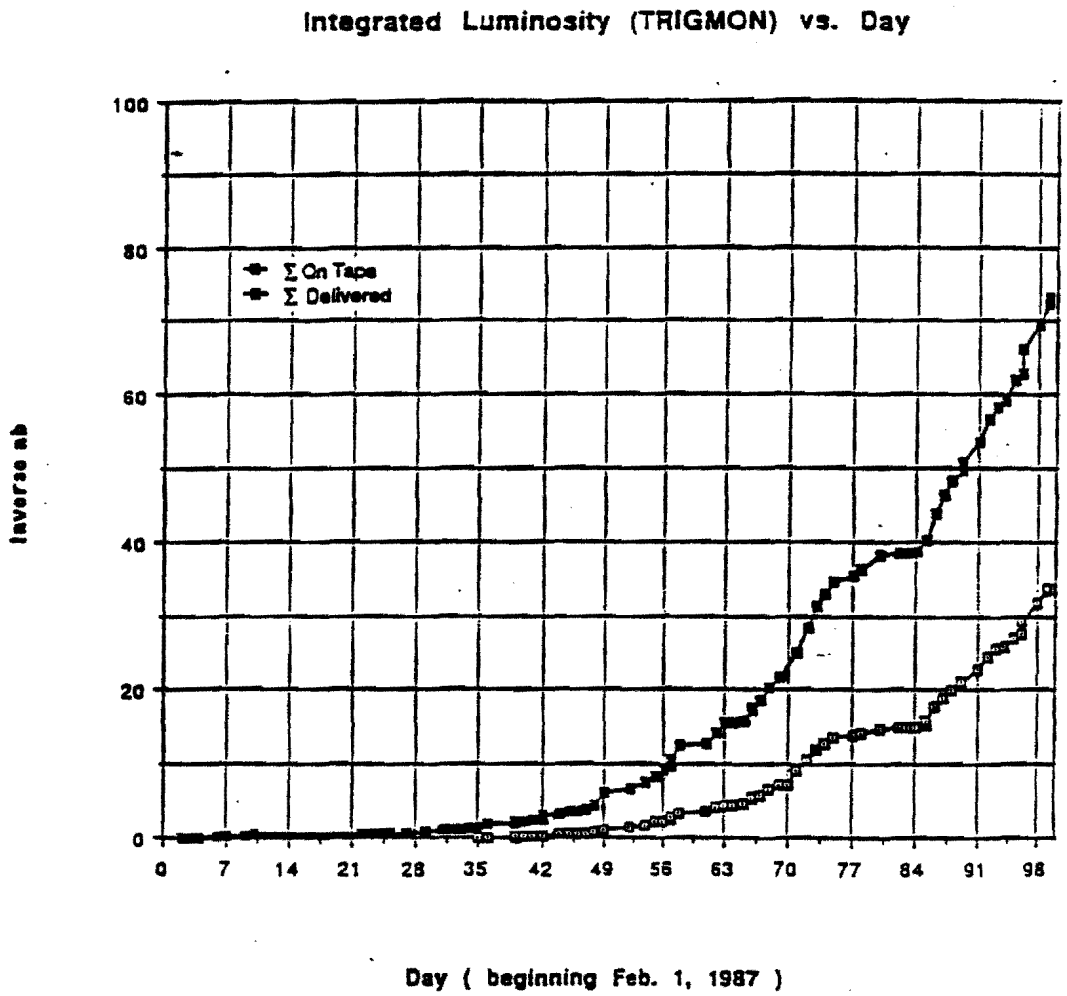

Figure 3.3: The accumulation of luminosity as a function of time is shown in terms of that delivered as well as that recorded on tape for 1987.

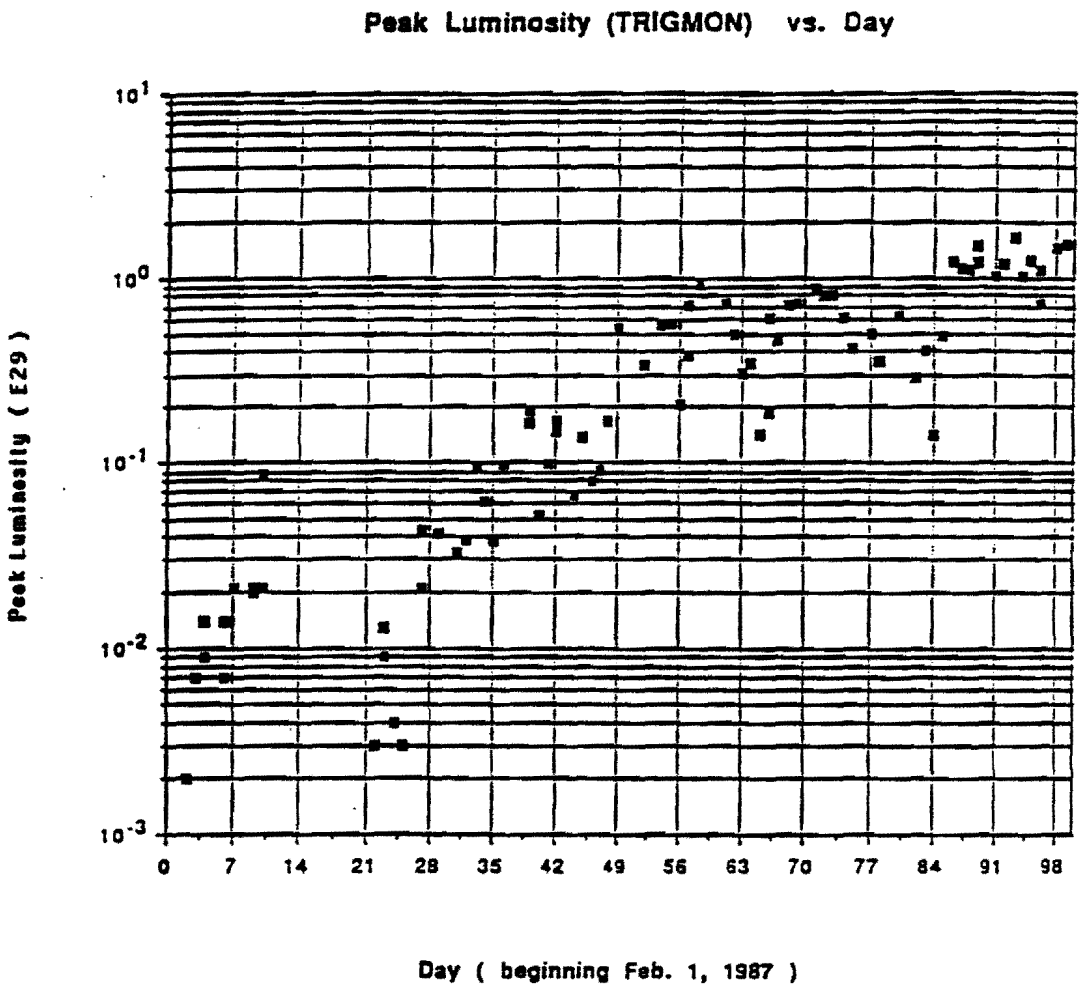

Figure 3.4: The peak luminosity is shown as a function of time for the 1987 run. It shows an exponential growth as the machine was tuned.

Chapter 4

Detector Calibration

In this chapter, the response of the various calorimeters to single particles is described. The relationship of this response to the energy response to jets will be considered in Chapter 7. This response is best understood in the central detector and has been connected to the jet energy response in the measurement of the single jet inclusive cross section in the central detector [16]. For this reason, jet energy scales are obtained from the central detector for the analysis of the dijet angular distributions. The jet energy scale in the gas calorimeters has not been determined as accurately and is used minimally here.

In CDF, there are a number of methods that have been used to provide the basic calibration numbers and check that the detector responds uniformly in both space and time. In this chapter the following will be described:

- Test beam calibration results for the calorimeters;
- The linking of those calibrations between the test beam and the experimental hall;

- Minimizing the role of the electronic variations.

4.1 Test beams and Carrying Calibrations to CDF.

The calorimeters have been tested in beams of pions, muons and electrons in order to provide sets of basic parameters for each system. The identity of the particles of each beam was controlled and the momentum of those particles was measured by passing the beam through a series of multiwire proportional chambers and magnetic spectrometers. These tests provided information on the following items:

- **Relation of charge collected to energy deposited** - The absolute energy scale of each calorimeter was determined so that the digitized value could be translated into energy units. (See Tables 3.1 and 3.2 in Chapter 3.)

- **Energy resolution** - The ability of the calorimeters to distinguish particles of one energy from that of another was measured as a function of the energy and identity of the particle.

- **Mappings** - The response of the calorimeter as a function of the location of the particle on the face of the calorimeter as well as the variation from one module to the next was measured.

- **Stability and calibration monitoring** - The ability to reproduce the above measurements with the aid of a system that monitors the calibration without the need of a test beam was examined.

- **Pathologies** - There are defects in each calorimeter system that needed to be understood. Measurement at a test beam is the first step in understanding such defects. The defects studied in CDF included leakage of energy, energy lost in cracks, hot spots and sensitivity to neutrons.

4.1.1 Calibration of the Central Electromagnetic Detector

The central electromagnetic detector was calibrated with a beam of electrons. The energy resolution of the detector is $\sigma/E = 0.135\ GeV^{1/2}/\sqrt{E \sin\theta}$[17]. Mapping of five wedge modules with 50 GeV electrons indicates that a common response map (one for each of the ten towers in the modules) describes the module response to about 1.5% rms. The calibration is monitored by a Cs^{137} source system which moves a source on a wire through one layer of the electromagnetic calorimeter. This calibration is done weekly. To carry the calibration from day to day, there are light emitting diodes attached to optical fibers that carry the light pulses to the photomultiplier tubes. Also, Xenon flash tubes direct light through another series of quartz fibers to a transition piece in front of each photomultiplier tube. The comparison of the calibration to the test beam after 35 days for four wedges [17] indicated that the wedges maintained their calibration over this time and from module to module to 0.7% [18].

4.1.2 Calibration of the Central Hadron Detector

The Central hadron detector was calibrated with a beam of pions at energies of 10 through 150 GeV. The calibration is defined by requiring that the pion be minimum ionizing in the electromagnetic compartment and deposit all of its energy in the hadronic

compartment. Then the sum of the charge collected in each of the compartments is related to the energy of the beam. Pions typically begin to deposit energy in the electromagnetic calorimeter. The response of the electromagnetic calorimeter to pions is lower that that of the hadronic calorimeter. As a result, a sample of all 50 GeV pions will have a mean sum pulse height that is lower than 50 GeV. The resolution of the hadron calorimeter is 11% for 50 GeV charged pions. The systematic error in the absolute calibration of the hadron calorimeter is estimated in the same way as that for the electromagnetic calorimeter and is determined to be 2% [19].

A problem that arises is the nonlinearity of the response for pions with energies between 1 and 10 Gev, where the charge collected drops by 25% from the linear expectation. This has been measured by using the momenta of low energy tracks in minimum bias events as measured in the central tracking chamber and looking at the calorimeter response to these tracks [20].

The calibration is monitored by a Cs^{137} source system which moves a source on a wire through a layer of the hadron calorimeter. This is the same source that runs through the electromagnetic calorimeter. This system is only operated once per week, so to monitor the calibration over periods of two or three days, a laser flasher system is employed. Light is carried by fibers to the transition piece in front of the photomultiplier tubes and a laser is flashed to all parts of the detector. Over a period of a few months, this procedure shows systematic variations less than 2%.

The response near the boundary between two wedge modules is not uniform. The boundary area consists of the wedge steel cover plates and the wave shifters and light guides of the calorimeters. Electrons and photons that strike this crack will cause *hot*

spots in the response of the hadron calorimeter. To reduce this effect, there are uranium bars placed in front of each boundary between modules. These serve to attenuate electromagnetic showers in this area. In addition, there is a crack between the arches. This crack runs along the top and bottom of the barrel, as well as around the center. Since there are no light guides where the arches butt against each other, there will be some loss of energy response. This response has been measured for use in Monte Carlo simulations of the detector so that corrections can be made to the data [19].

4.1.3 Endwall Calorimeter

The endwall calorimeter has a resolution of 14% for 50 GeV charged pions. It is calibrated by inserting line sources of Cs^{137} into tubes orthogonal to the layers of the steel and scintillator sandwich. This is done by hand every few months. The calibration between these times is done by using the laser flasher system described above for the central hadron calorimeter. Only two endwall modules were calibrated in the test beam. The module to module variation in response to sources is used to estimate the systematic error in the absolute energy scale and found to be 4%[19].

4.1.4 Gas Calorimeters

The gas calorimeters have been calibrated in a fashion similar to the central calorimeter. In this case, however, the monitor system that maintains the calibration from the test beam to the experimental hall and through time consists of a separate data acquisition system based on CAMAC. Since the gains of these calorimeters change rapidly with pressure, temperature and the composition of the gas, continuous monitoring of the

detectors must be done. This is accomplished by distributing a number of proportional tubes throughout the gas calorimetry such that they share the same environment as the calorimeters. These tubes have Fe^{55} sources attached to them and the characteristic spectrum provides a monitor of the gain of the calorimeters. The various monitors track with one another to better than 2%. The systematic errors in the absolute energy scales of the gas calorimeters have not been measured. After completion of the 1988 collider run, this will be checked by recalibrating portions of the gas calorimeters and examining the changes. Since this number is not known for the 1987 collider run, the only central detector measurement of jet energies will be used.

The energy resolution of the plug electromagnetic calorimeter to high energy electrons was $\sigma/E = (0.28\ GeV^{1/2})/\sqrt{E}$ and the position resolution is 0.2 cm*. The plug hadronic calorimeter had an energy resolution of $\sigma/E = 0.869\ GeV^{1/2}/\sqrt{E} + 0.041$ [21]. The forward electromagnetic calorimeter has a test beam resolution for electrons that is $\sigma/E = (0.254 \pm 0.007\ GeV^{1/2})/\sqrt{E} + (0.0047 \pm 0.0001)$ [22]. It has a position resolution for electrons that varies between 0.1 and 0.4 cm depending on the location in the calorimeter. The forward hadron calorimeter had an energy resolution of $\sigma/E = (1.41\ GeV^{1/2})/\sqrt{E}$ for 200 GeV pions [23]. It had a position resolution of about 3 cm.

A particular problem with the response of the gas calorimeter is that neutrons produced in hadronic showers can travel a long distance and scatter elastically with free protons in some other part of the calorimeter. The protons deposit large amounts of ionizing energy that are interpreted as real energy depositions by pions. The signature is quite clear: a large amount of hadronic energy is deposited in one pad in a single

*Throughout the energy resolution discussion, E is assumed to be expressed in GeV

layer of the detector. The rate of these neutrons in the colliding beam environment was so large that gas hadron calorimeters had to be removed from the trigger. The work that has been done to understand the characteristics of the neutrons in gas calorimeters is described in Section 5.2.2. For the jet physics, the clear signal makes these easy to remove from the data. In subsequent collider runs, this will be removed in the online trigger.

4.2 The Role of Electronics

The goal in CDF has been to design the electronics so that they have a gain that is stable to 0.1%, known absolutely to 0.5% and has a large dynamic range.

The amplifiers in the central detector have all been tested with the same digitizer and charge injection circuit. The RABBIT electronics all have charge injection circuits such that there is one such system on each card, servicing between 24 and 48 channels. For the central detector, this circuit was used to monitor the gain of the amplifiers at one time relative to the next. For the gas calorimetry, these circuits were used to determine the absolute gain of the amplifiers. A description of the gain determination is given in Appendix A. The stability and reliability of these channels has been very good. They did meet the design goal stated above. Also, for the 40000 channels involved in calorimetry (including 20000 strip chamber and wire plane channels) only a few were dead at any given time (see Chapter 5.)

The pedestal determination was done each day before the beams were stored. The noise levels varied for different parts of the detector, the worst case being in the plug.

Typical pedestals had an rms of 0.03 GeV. There were a few hundred channels in the forward electromagnetic detector whose pedestals had a very long relaxation time (~ 45 minutes). These channels would drift during a data taking run and were corrected offline.

Chapter 5

Event Sample and Jet Reconstruction

This chapter describes the raw event sample obtained in the 1987 CDF data run. A description of the hardware triggers is given. The luminosities and numbers of events recorded for each trigger are presented. A description of the general offline processing of jets follows. This includes a summary of the various algorithms used to remove hardware defects that provide background to the jet signal. The algorithm used to reconstruct jets is described. The properties of the central dijet sample are shown.

5.1 Data Sample

The hardware trigger was described in Section 3.1.5. For an event to be recorded on magnetic tape, it had to pass at least one of four triggers. These triggers were the minimum bias, jet, electron/central muon, and forward muon triggers. Only the minium

bias and jet triggers are relevant to this analysis. The are described in the next two sections.

5.1.1 Minimum Bias Trigger

The minimum bias trigger used the beam-beam counters (see Section 3.1.5), requiring at least one counter in each of the hodoscope planes to fire within a 15 ns window centered on the beam crossing time. This trigger was automatically limited to 0.05 Hz. It was used as a monitor of the detector hardware.

5.1.2 Jet Trigger

The jet trigger required a minimum bias trigger and a total transverse energy, or sum-E_t, above a threshold. The transverse energy is defined as $E_t \equiv E \sin\theta$, where θ is the polar angle of the center of the calorimeter tower taken with respect to the *nominal* event vertex. Since the event vertex is a gaussian with $\sigma = 35$ cm, is important to note that the trigger assumes all events to have vertices at the nominal center of the detector. The transverse energy was calculated in towers of $\Delta\eta \times \Delta\phi = 0.2 \times 15^o$.

The jet trigger consisted of a sum of the electromagnetic total transverse energy with the central and wall hadronic total transverse energy. The total electromagnetic energy sum was formed by adding the transverse energies in electromagnetic calorimeter towers above a 1 GeV threshold. The total central and wall hadronic energy was formed by adding the transverse energies in the hadronic calorimeter towers above a 1 GeV threshold. The hadronic gas calorimeters were not included in the trigger because of noise problems and a large trigger rate hypothesized to be due to neutron sensitivity.

This phenomenon has been studied and is discussed in Section 5.2.2.

The jet trigger sums were compared to a threshold value. During the 1987 data taking period, the values of the jet trigger total transverse energy thresholds were set to 20, 30, 40 or 45 GeV. The specific value was chosen for each run after the instantaneous luminosity was known. The threshold choice was made to be certain that the total trigger rate would be approximately 1 Hz. This was chosen so that the time during which the detector was inactive because it was being read out amounted to 10% of the total time.

Approximately half of the jet triggers were due to high voltage breakdown in the plug electromagnetic calorimeter. For this reason, for part of the run, the plug electromagnetic detector was excluded from the trigger. Because of this and the absence of the hadronic gas calorimeters from the trigger, the jet analysis here will use only those events satisfying a central jet trigger.

5.1.3 Events Collected and Integrated Luminosity

The performance of the accelerator and the CDF data taking, as well as the integrated luminosity have been described in Section 3.2. During the first part of the 1987 data taking cycle, the detector hardware was unstable as calibration procedures were being debugged. Once these procedures produced reliable results for all systems and variations of the calorimeter calibrations could be compensated for in the online processors, the data were considered suitable for analysis. After this point, a total of 446347 events were recorded. The corresponding integrated luminosity is $30.8 \pm 4.6\ nb^{-1}$. Table 5.1 shows the number of events that passed each of the four triggers. Since an event can satisfy more than one trigger, the sum of the events passing the triggers exceeds the

Trigger	Jet	Minimum Bias	Electron/Central Muon	Forward Muon
Events	156376	189709	87695	52492

Table 5.1: The number of events for each trigger is given. This is the number taken for runs after calibration constants were downloaded to the data acquisition hardware.

total number of events recorded.

There were a number of runs in which severe and obvious hardware failures were identified. These failures included the failure of large portions of the detector electronics and high voltage turned off in some portion of the detector. These runs were removed from consideration in the final analysis of the jet sample.

In order to facilitate the analysis of jets, the raw calorimeter data and the reconstructed event vertex were taken from the 350 raw data tapes and stored on a separate set of 26 tapes for events passing the jet trigger. The vertex was determined from the VTPC and the tracking information was abandoned. A total of 147365 events remain after this selection. This corresponds to a total integrated luminosity of $29.0 \pm 4.4\ nb^{-1}$ and constitutes the main starting point of the jet calorimeter based-analysis. At the same time, all trigger information from all events was taken from the raw data tapes and stored on five data tapes for analysis of luminosity. In a separate exercise, the calorimeter data for 60000 minimum bias events were removed from the raw data and placed on to seven data tapes. These events were used in the jet analysis in the sense that they were the basis upon which pedestal and bad channel determinations were made.

As was described in Section 5.1.2, in each run, the central jet trigger had to satisfy one of four thresholds. The total number of events and the integrated luminosities corresponding to each of these thresholds are given in Table 5.2. This constitutes the

Threshold	20 GeV	30 GeV	40 GeV	45 GeV
Events	15885	98034	17946	15500
Integrated Luminosity	0.419 nb^{-1}	14.9 nb^{-1}	6.30 nb^{-1}	7.24 nb^{-1}

Table 5.2: The number of events and integrated luminosity for each central jet trigger threshold is given. There is a 15% error on the luminosity numbers.

starting point for offline processing of the data and jet reconstruction.

5.2 Offline Processing: Raw Data to Jet 4-Vectors

The events selected in Table 5.2 were analyzed with a number of reconstruction algorithms and filters. The steps are described below; expanded descriptions of the jet background filters and the jet reconstruction modules are given in subsequent sections.

1. **First event after pause** - As the events were removed from the raw data tapes, the times were checked and if more than 20 seconds had elapsed, the next event was discarded. This was done because the first event after a pause always contained unphysically large amounts of energy due to the shifts of all pedestals during the pause. This filter removed 630 events from the 141173 sample.

2. **Vertex Reconstruction** - The event vertex was reconstructed using the wire data from the vertex time projection chamber (VTPC). The vertex distribution has a gaussian shape with a width of 35 cm and an offset of 3 cm from the center of the detector. There is no background from beam-gas interactions. Calculations of multiple interactions (see Appendix B) indicate that there should be no overlapping jet events and about a 1-3% rate of minimum bias events overlapping jet events.

Detector region	Central	Endwall	Plug	Forward
Electromagnetic Component	0 (960)	X	21 (6912)	34 (5760)
Hadronic Component	2 (768)	0 (576)	4 (1728)	13 (2880)

Table 5.3: The number of dead/hot channels in each of the calorimeter systems for the entire data sample. The total number of channels is in parenthesis.

The minimum bias/jet event overlap will cause some deterioration in jet energy resolution and will be considered as part of the measurement made in Chapter 6.

3. **Calorimeter analysis** - Some hardware defects were corrected and the raw data were turned into energy quantities to prepare for further analysis. A few events with garbled raw data banks were rejected. The specific functions of this analysis are listed here:

   (a) **Pedestal centering** - The minimum bias data were used to determine channels with significant shifts in pedestal value. Approximately 200 of the 19584 calorimeter channels had their raw data values shifted back to the correct pedestal. All but two of these channels were in the gas calorimeters.

   (b) **Bad channel suppression** - The minimum bias data were used to remove channels with excessive noise (more than a few GeV in width). The number of dead/hot channels and the total number of channels are listed by calorimeter element in Table 5.3.

   (c) **Hot phototube suppression** - Photomultiplier tubes in the central electromagnetic detector were subject to high voltage discharge. These spurious signals were easily removed by comparing the signals in the two photomultiplier tubes that instrument each central calorimeter tower.

(d) **Data reformatting** - The raw data were reformatted into an η-ϕ grid appropriate for jet reconstruction using clustering algorithms. The ADC counts were converted into energy units (GeV) using the nominal calibration values.

4. **Plug hadron noise** - Noise in the plug hadron calorimeter appeared as square patches in $\eta - \phi$ space. These channels were zeroed.

5. **Cosmic ray and Main ring Removal** - This event filter used the timing information from the central and endwall hadron TDC's to determine if an event was due to cosmic rays or particles from the Fermilab main ring. The filter is 95% efficient and rejects less than 1% of good central jets. Further details of this algorithm are given in Section 5.2.1.

6. **Gas spike removal** - Plug electromagnetic breakdown and neutron sensitivity are referred to as gas spikes. These were removed from each event by zeroing the energy in the identified spikes. The algorithm is between 80 and 95% efficient and rejects no clusters above ~30 GeV. Further details of this algorithm are given in Section 5.2.2.

7. **Jet reconstruction** - A clustering algorithm was applied to each event and jets were reconstructed. Further details of this algorithm are given in Section 5.2.3.

5.2.1 Cosmic Ray Bremstrahhlung and Main Ring Event Removal

After the events have been reformatted, those events that are caused by cosmic ray bremstrahhlung or particles from the Fermilab main ring are removed. These are identified using the TDC's in the central and endwall hadron calorimeters. Since the main ring

passes over these calorimeters, the particles will deposit energy that is out of time with the beam crossing. Cosmic rays constantly shower on the detector; on occasion, they can bremstrahhlung [24] and cause a shower of energy. These showers will be out of time with the beam crossing as well.

The TDC filter algorithm looks at two quantities. First it looks a the total energy out of time with the beam crossing. If there is more than 8 GeV of energy that was deposited between -10 and 25 ns relative to the beam crossing in the central detector or between -15 and 55 ns for the endwall detector, the event is rejected. The negative times are needed to compensate for particles emitting light directly into the light guide. The second quantity is the total energy for channels that have no signal in the TDC's. This energy must be deposited just before the TDC's are activated, during a time in which no energy from the crossing may have been deposited. These events are also rejected if the total energy is above 8 GeV.

This algorithm is 95% efficient at rejecting cosmic ray bremstrahhlung [24]. The removal of main ring events has been studied by looking at a sample of events taken when the main ring was known to have triggered the detector. It is fully efficient at removing these events because there is always a considerable amount of energy out of time with the beam crossing [25]. The rejection of good events is less than 1%.

5.2.2 Gas spike removal

The most problematic sources of background to jets are the gas spikes. There are two kinds of gas spikes. The first is due to high voltage breakdown in the plug electromagnetic detector. It is characterized by clusters that are typically only one tower wide with only

electromagnetic energy. In addition, these spikes occur in a few specific towers. In principle, they are not a problem to identify and remove; however, they can be mixed with the other kind of gas spike.

The second kind of gas spike is hypothesized to be caused by a neutron that deposits a large amount of ionization in a single chamber and across one or two towers of the gas calorimeters [21]. Although this is a rather clear signal, difficulty in identifying this noise source arises because the gas calorimeters have different segmentations in the way that the single planes of chambers are read out and because these neutrons can be buried within a hadronic shower. The problem of segmentation means that one must use only the small lateral extent and small or large electromagnetic energy fraction to identify the spurious clusters. This is used for low energy clusters (typically under 30 GeV), but for high energy cases, one must use the depth information.

The low energy algorithm can be validated by choosing a sample of well-defined gas spikes, using events which have isolated clusters of energy that can be easily associated with a deposition in a single wire plane. These clusters are found by requiring all towers decrease monotonically from a seed tower (above 1.5 GeV in energy in the endplug, above 5 GeV in energy in the forward) and that the towers be above half the energy of the seed tower. Using this technique, one finds for cluster energies between 10 and 30 GeV, the efficiencies are 80% in the plug hadron, 100% in the plug electromagnetic, 95% in the forward hadron, and 80% in the forward electromagnetic. For the higher energy clusters, the efficiencies are all on the order of 99% with the exception of the plug electromagnetic which stands at 96%.

The main concern of this algorithm lies with its ability to remove signals from the

event. This has been checked by looking for events with a cluster in the central detector only. No such events are found in the jet sample used in the analysis of the dijet angular distributions.

5.2.3 Jet Reconstruction

After the best estimate of the calorimeter energies is made, an energy clustering algorithm is applied in order to search for jet events. The jet algorithm, JETCLU uses a cone of a fixed radius in η-ϕ space to define a jet. In this sense, it is closely related to previous algorithms used on $Sp\bar{p}S$ [26,27] experiments and corresponds most closely to the cut-offs used in calculating QCD cross sections. The next few sections describe the action of this algorithm. A flow chart of the algorithm is shown in Figure 5.1.

5.2.3.1 Preclustering

Candidate and seed lists are formed. The candidate list consists of towers above a fixed E_t threshold set to 0.1 GeV. The seed list consists of towers with an E_t threshold, $E_{t_{seed}}$, set to 1.0 GeV. The gas calorimeter towers are ganged together in groups of three in azimuth to correspond to the central segmentation. After the seed and candidate towers have been found, preclusters are formed. In this additional step, JETCLU differs from other algorithms. Preclusters are by definition an unbroken chain of adjacent seed towers with a continuously decreasing tower E_t. If the total E_t of a precluster is larger than 2 GeV, it is used as a starting point for clustering.

5.2.3.2 Clustering

The preclusters are grown into clusters using the true tower segmentation (*ie* no ganging). The E_t weighted centroid of the precluster is found. A fixed cone in η - ϕ space of radius R, set to 1.0, is formed around the centroid and candidate towers inside this cone are merged into the cluster.

A new centroid is calculated from this new set of towers. Again, all candidate towers inside the cone around the new centroid are merged into the cluster. The process of recomputing a centroid and finding new or deleting old towers is iterated until the tower list remains unchanged.

5.2.3.3 Overlap Conditions

For many jet studies, it is important to have overlap conditions handled correctly. This is particularly true for multijet studies in the case of final state gluon emission where the gluon can merge into the jet. If calorimeter towers appear in two clusters, then an overlap fraction is computed as the sum of the E_t of the common towers divided by the E_t of the smaller cluster. If the fraction is above a cutoff of 0.5 then the two clusters are combined. If the fraction is less that the cut, the clusters are kept intact, the energy is divided up between the clusters based on the proximity of the towers to the centroid, and the centroids are recomputed. The original overlapping towers are then reallocated according to the new centroids. As with the original cluster finding, the process of centroid computation and tower reshuffling is iterative and ends when the tower lists remain fixed.

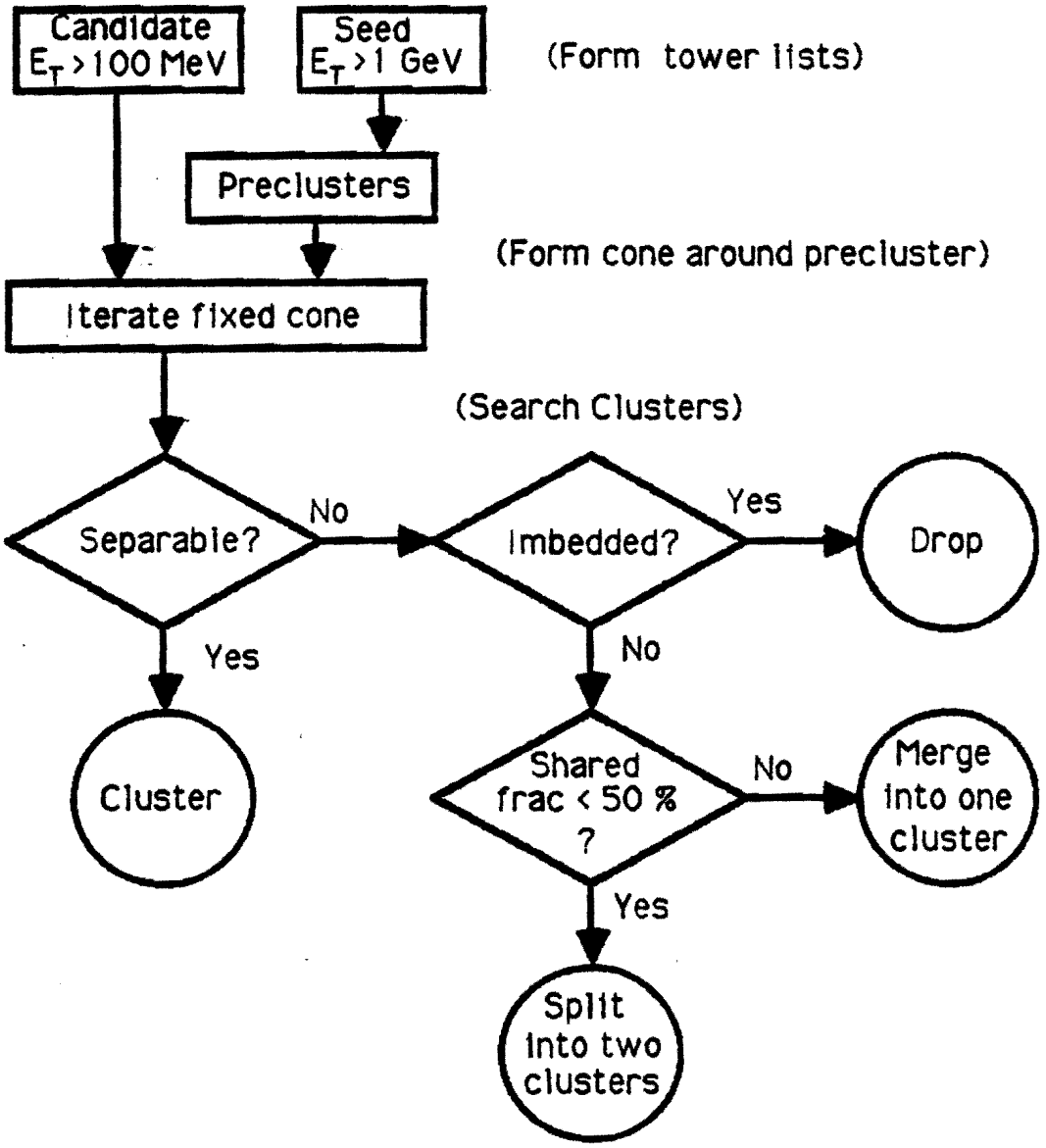

Figure 5.1: Flow chart of the algorithm JETCLU. Seed towers and candidate towers are found. Preclusters are found from combining all touching seed towers. A fixed cone in η-ϕ space is drawn around the preclusters. A centroid is computed for the candidate towers in this cone. A cone is drawn around the centroid; new candidate towers are added and subtracted, and the centroid is recomputed. This process is iterated on until a stable set of clusters is formed. Finally, overlap conditions are resolved.

5.2.3.4 Jet 4-Vectors

The algorithm produces the 4-vectors of the jets, the fraction of energy deposited in the electromagnetic compartment of the detector for the cluster, and the width of the jets in η-ϕ space. The 4-vectors are calculated by assuming that each tower in the cluster is a massless particle with the energy of the cell equal to its momentum. The sum of the individual 4-vectors yields the jet 4-vector. As a result of this, the jets have a finite mass and therefore the transverse energy and momenta may exhibit some differences. (See Section 5.3.) The individual calorimeter cell energy is calculated from a simple sum of electromagnetic and hadronic energies defined in the calibrations of Chapter 4. Although this may not be the optimum way to combine the energies of the jets [27], there is no evidence to suggest that an improvement in the CDF jet resolution can be obtained by changing the algorithm. (See Appendix D.)

5.3 Properties of the Central Dijet sample

In this section, the characteristics of the reconstructed events are studied. Two jet events were selected by requiring two clusters in the central detector with the sum of the magnitudes of their transverse momentum greater than 60 GeV. This requirement ensured that the events passed all hardware trigger levels. The jets had a cone size of 0.6 and a minimum tower energy of 0.2 GeV. Both clusters had to be *well-contained*, having their axis no closer than 0.2 units of pseudorapidity to the plug boundary after accounting for the vertex in the calculation of θ. A cut was placed on the relative phi of the two jets such that the second was within 180 ± 20° of the first. A number of features

of these events are noted here:

1. **p_t, E_t, and mass spectra** - These spectra are shown in Figures 5.2 and 5.3. The transverse momentum and energy spectra show a rise due to the total energy cut of 60 GeV and then fall rapidly, roughly as a sixth power of p_t or E_t. The jet mass is sufficiently small so that the difference between p_t and E_t is negligible.

2. **Electromagnetic Fraction** - The fraction of the cluster energy that was deposited in the electromagnetic calorimeter is shown in Figure 5.5. The first thing to observe is that the spectrum does not indicate any unusual features that would imply detector malfunction. Next, one notes that 61% of the energy is electromagnetic. This is consistent with being due to the neutral content of the jet plus the large fraction of low energy charged pions that shower in the electromagnetic detector. The energy calculation is done by simply adding the electromagnetic and hadronic energies using the test beam calibration described in Chapter 3. This may not be the best algorithm for determining jet energies, especially since the response of a pion is lower in the electromagnetic compartment (see Section 4.1.2).

3. **η-ϕ distribution** - A two dimensional histogram of azimuth and pseudorapidity of the jets is shown in Figure 5.4. The pseudorapidity is measured relative to the vertex as determined by the VTPC. Except at the center of the detector, the jet axes are distributed evenly in pseudorapidity out to about 0.7 and in the full range of azimuth. There is indication of a 30% rate change where the calorimeter arches meet. This is studied in Appendix D. Since Figure 5.2 shows a rapid decline of jet rate with energy, variations in mapping response correspond to a sixth power

increase or decrease in trigger rate and therefore to variations in in the population of events in Figure 5.4. The observed change of rate corresponds to a change in energy response of a few per cent.

4. **z-vertex** - The distribution of the z component of the vertex of the interaction is shown in Figure 5.6. It has a mean of 3.25 cm and a sigma of 32.4 cm. It can be seen that some vertices extend to large distances that put the interaction into the end plug.

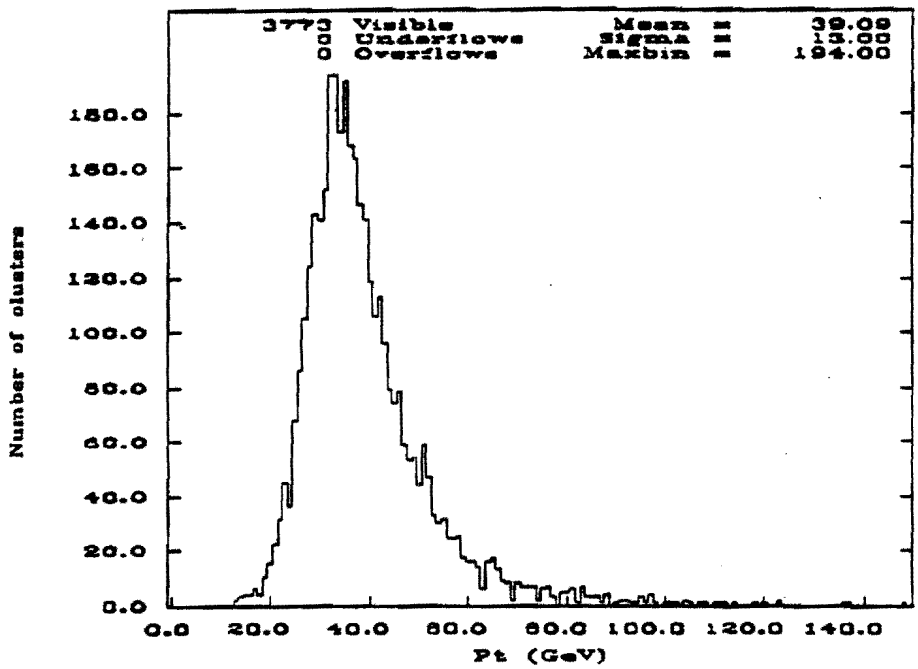

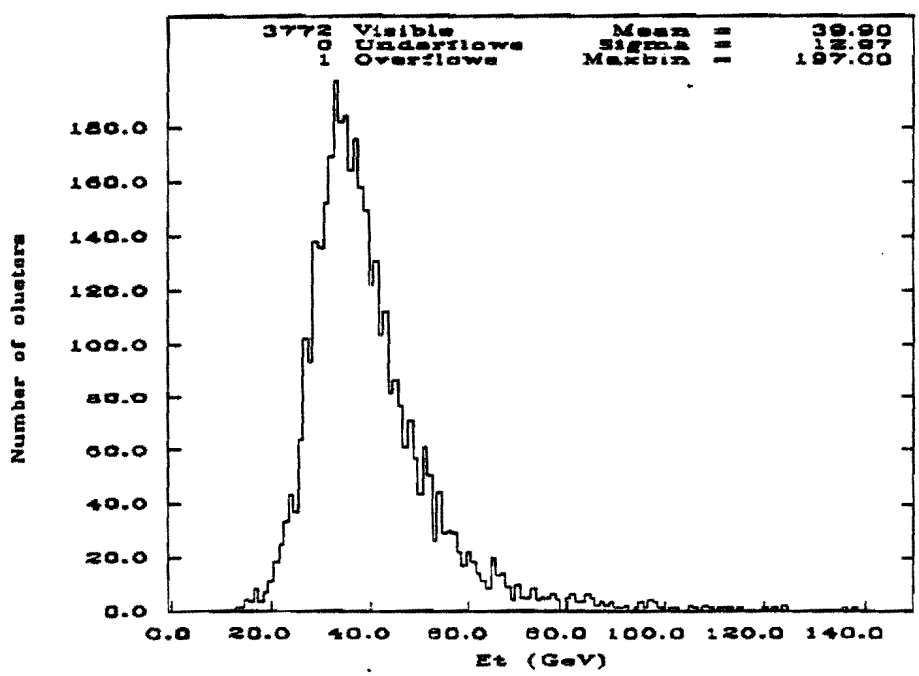

Figure 5.2: Jet p_t and E_t spectra. There are no acceptance corrections and the energy is calculated from the sum of the response of the electromagnetic an hadronic calorimeters

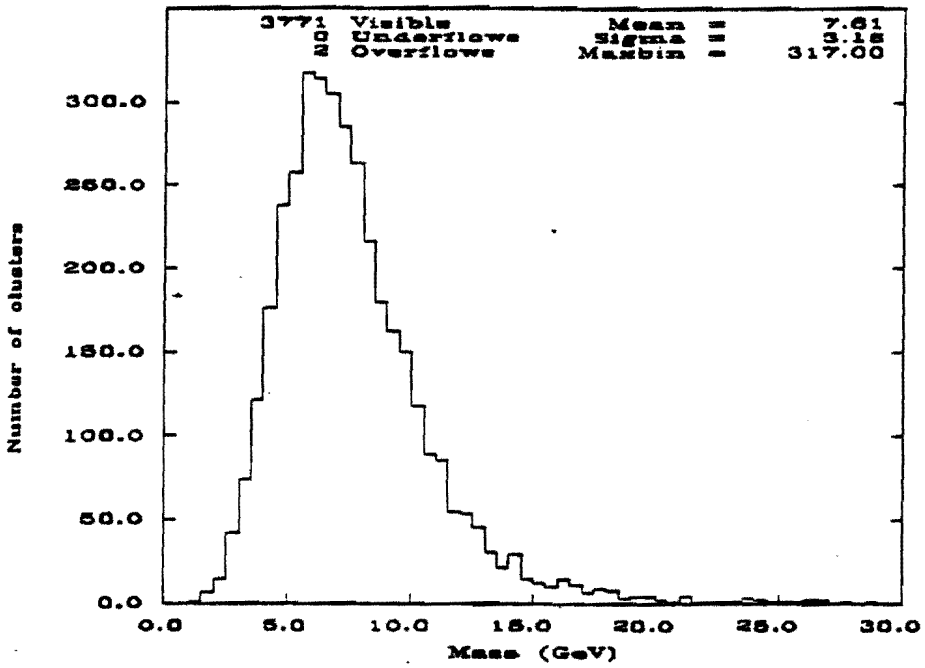

Figure 5.3: Jet mass spectrum. There are no acceptance corrections and the mass calculation is based on the sum of the response of the electromagnetic an hadronic calorimeters.

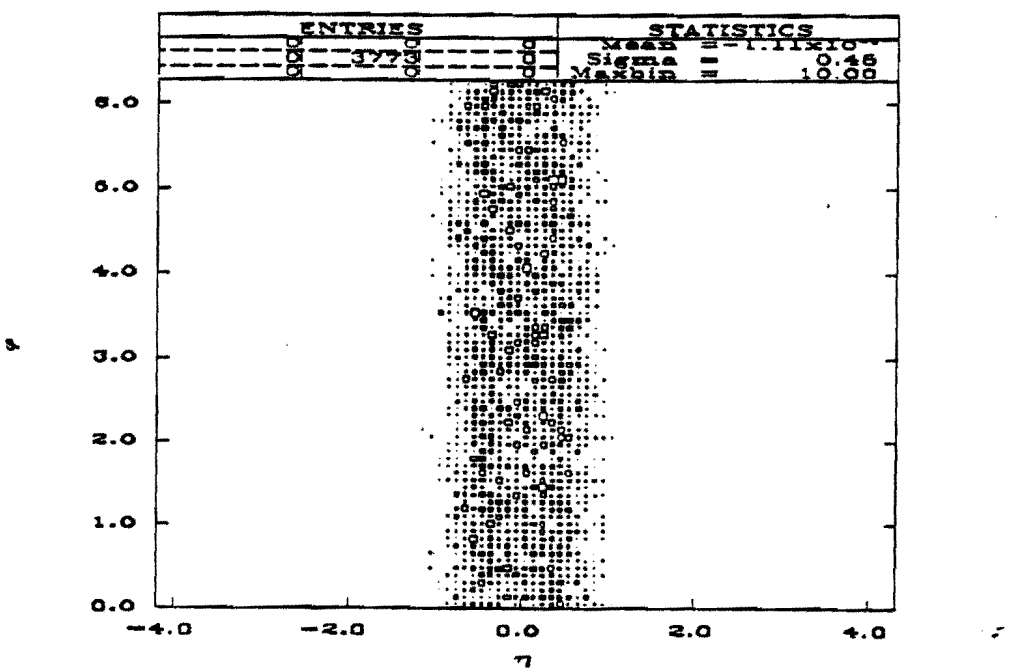

Figure 5.4: η-ϕ distribution of jets. Eta has been calculated using the vertex position.

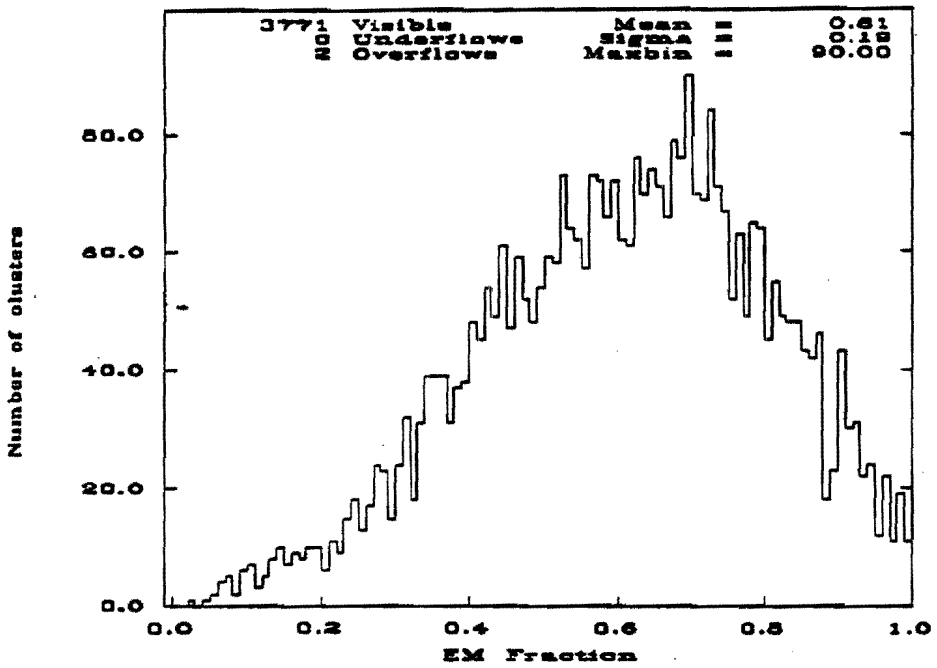

Figure 5.5: The fraction of energy deposited in the electromagnetic calorimeter is shown here for the jet.

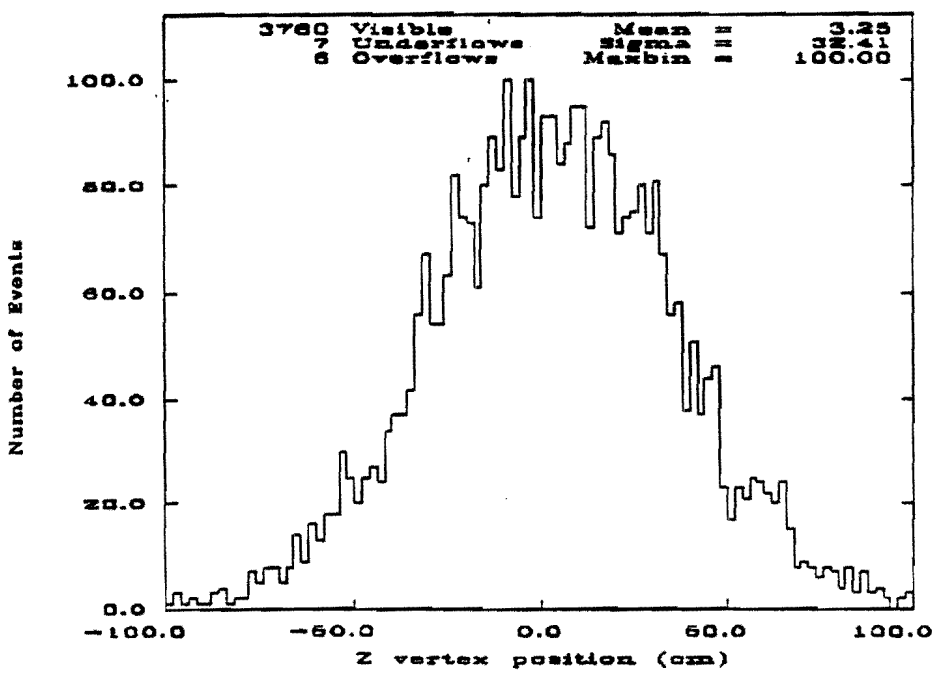

Figure 5.6: Z-vertex distribution for events used to measure the central calorimeter resolution.

Chapter 6

Central Jet Energy Resolution

This chapter describes a technique for measuring the dijet energy resolution and extracting the contribution due to calorimeter resolution. It is based on a method introduced by the UA2 collaboration [28]. One examines the dijet k_t, defined as the vector sum of the transverse momenta of the two jets, in terms of components sensitive to different sources of imbalance in the dijet system. This method has been extended to allow for energy *scale* calibrations of the different calorimeter systems relative to the central calorimeter. This is described in Appendix D.

The chapter begins with a description of the components of the dijet k_t. The behavior of these components is summarized. The application of the analysis to the central calorimeter is described.

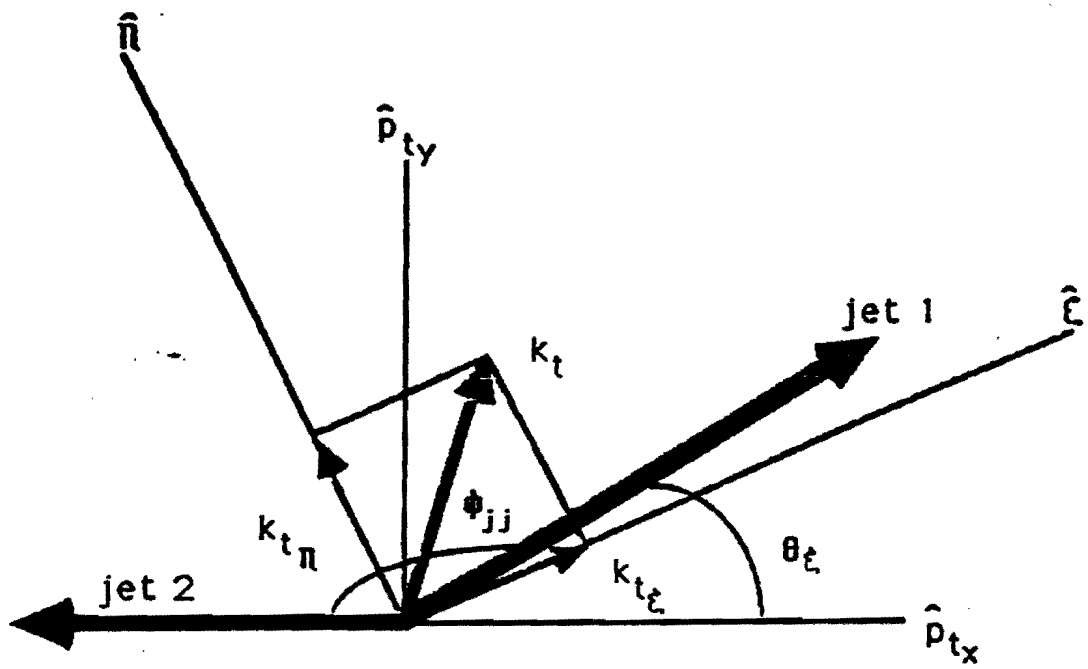

Figure 6.1: Schematic view of two jets. The transverse momentum components of the jets are shown. They have been decomposed into two components, k_{t_ξ} and k_{t_η}. These components are sensitive to different effects responsible for generating the overall dijet k_t.

6.1 Dijet k_t Description

The dijet system is described here in terms of two components of the transverse momentum of the jets. The advantages of using these components are described.

6.1.1 The Components of the Dijet k_t

Figure 6.1 shows a schematic representation of the transverse momentum vectors of two jets. One of the jets is chosen to lie along the negative x-axis. The azimuthal angular separation of these jets is called ϕ_{jj}. A pair of orthogonal coordinates have been drawn such that one axis, called the η-axis*, is defined as the azimuthal angular bisector of the dijet system. The other axis, the ξ-axis, is orthogonal to the η-axis and defined such that

*UA2 uses a convention that labels these axes with η and ξ. It is important to note the differences in meaning for the symbol η. One is used to define pseudorapidity, the other refers to a component of dijet k_t.

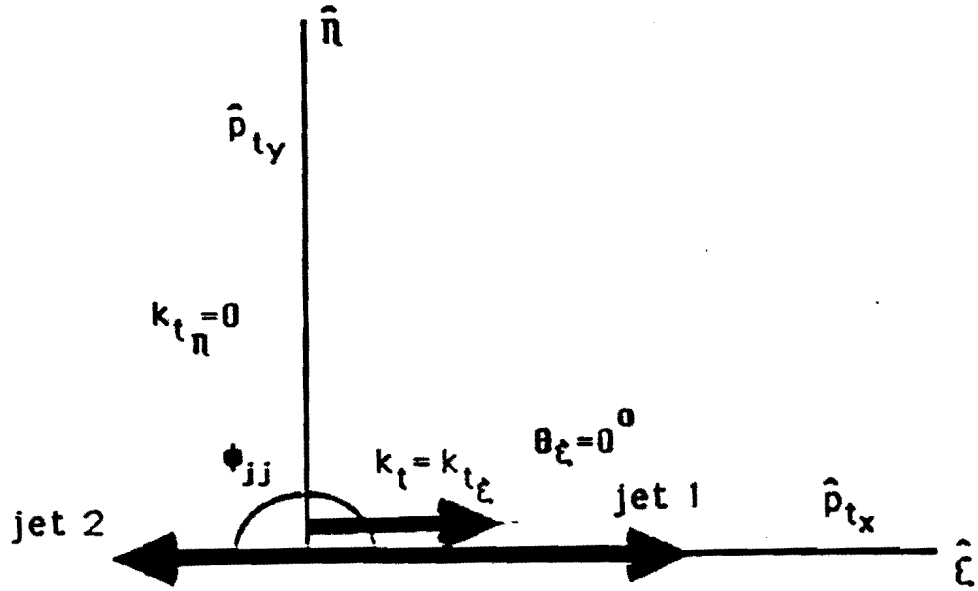

Figure 6.2: The interpretation of k_{t_ξ} is depicted here. It is assumed there is no angular error so that the entire dijet k_t is due to an energy imbalance which is picked up by the k_{t_ξ} component.

the cross product of their unit vectors points along the z-axis: $\hat{\xi} \times \hat{\eta} = \hat{z}$. The (p_{t_ξ}, p_{t_η}) coordinate system is chosen because measurements of distributions in these coordinates reveal difference aspects of the causes of the dijet k_t. These causes include effects due to QCD and effects due to instrumentation and are manifested in two ways. First, they cause imbalances in the magnitudes of the transverse energies of the jets. Secondly, they cause angular deviations of the jets from being exactly back-to-back. Simply speaking, the k_{t_ξ} component is caused by energy imbalance and the k_{t_η} component is caused by angular measurement errors. This can be seen if one takes each of these effects in turn. Consider a dijet system in which $\phi_{jj} = 180^o$. This is illustrated in Figure 6.2. In this case, the k_t points entirely in the $\hat{\xi}$ direction. If one considers an ensemble of such events, then the width of the $k_{t_{zi}}$ distribution reflects the energy measurement error. Next, consider the situation illustrated in Figure 6.3. In this case, the magnitudes of

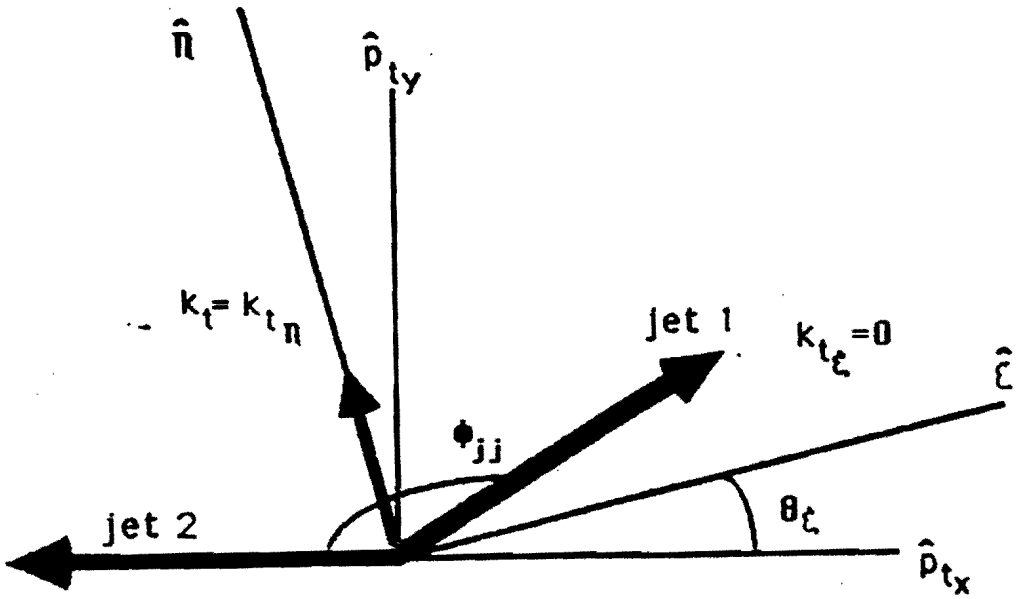

Figure 6.3: The interpretation of k_{t_η} is depicted here. It is assumed there is no energy measurement error so that the entire dijet k_t is due to an angular mismeasurement which is picked up by the k_{t_η} component.

the transverse momenta of the jets are identical, but the jets are not back-to-back. It is clear that the k_t points entirely in the $\hat{\eta}$ direction. An ensemble of such events would give one a measurement of the angular error.

6.2 Measured behavior of the dijet k_t

It is shown in Appendix C that the components of the dijet k_t are given by the simple relations:

$$k_{t_\eta} \simeq [|p_{t1}| + |p_{t2}|] \left[\frac{\pi - \phi_{jj}}{2}\right], \tag{6.5}$$

$$k_{t_\xi} \simeq |p_{t1}| - |p_{t2}|. \tag{6.6}$$

The difference in $|p_t|$ is shown to be approximately the same as the difference in $|E_t|$ and for a calorimeter resolution parameterized as $\sigma/E = A/\sqrt{E}$ where E is measured

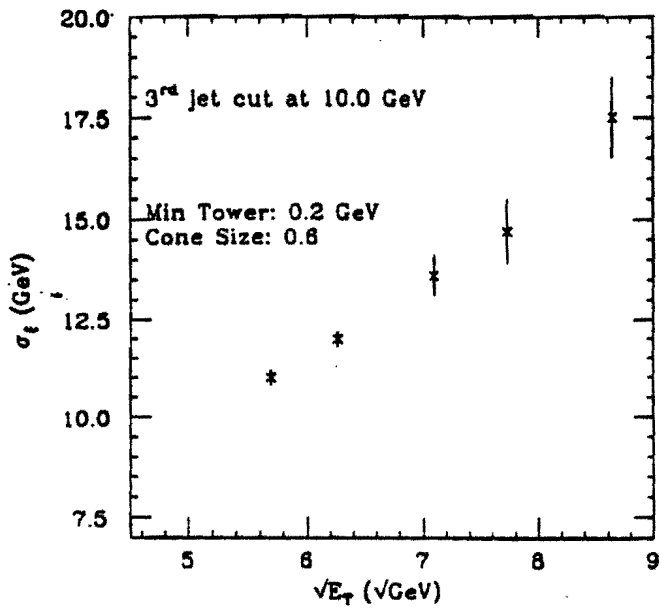

Figure 6.4: This shows σ_ξ is linear in $E_t^{\frac{1}{2}}$. These points are taken for a cluster size of 0.6, minimum tower of 0.2 GeV, and a cut on third jets of 10 GeV.

in GeV, it is shown that $\sigma(k_{t_\xi}) = A\sqrt{2\langle E_t \rangle}$ for central jets. This is demonstrated in Figure 6.4. Consideration of the origin of the components of the dijet k_t suggests that since σ_η is independent of E_t (see Figure 6.5), the jet calorimeter resolution, $\sigma'(E_t)$, may be extracted as $\sigma'(E_t) = \sqrt{\sigma_\xi^2 - \sigma_\eta^2}$ The dependence of σ' on the jet cone and energy of other jets is studied and for a cone size of $\sqrt{\Delta\eta^2 + \Delta\phi^2} = 1.0$, the central detector jet resolution can be taken as $\sigma/E = (0.83 \pm 0.10\ GeV^{1/2})/\sqrt{E}$, where the error is systematic and due to uncertainty in third jet activity.

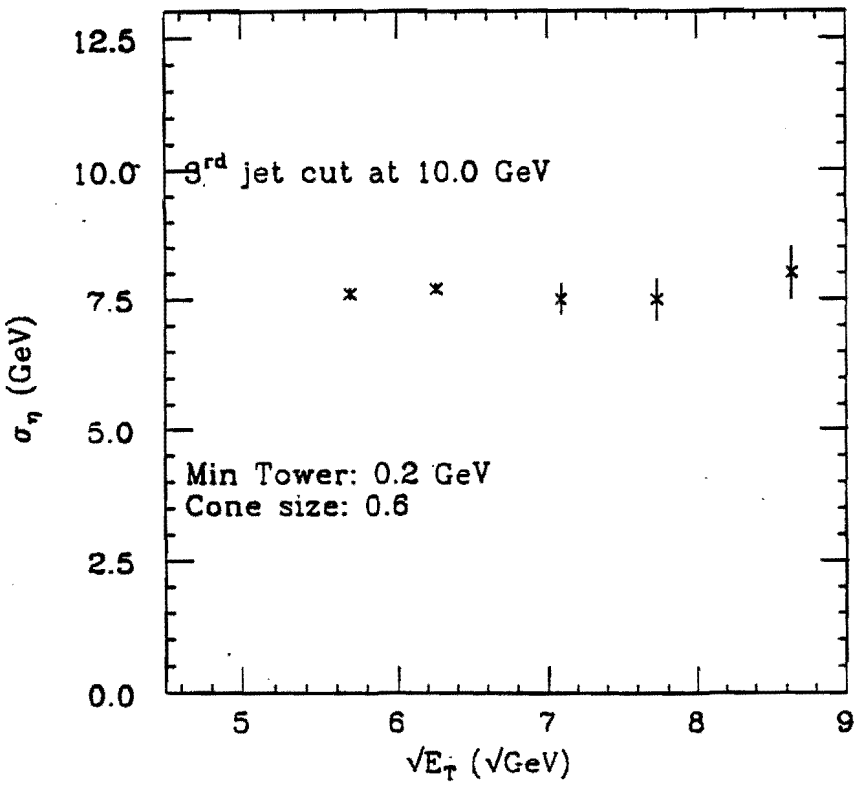

Figure 6.5: This shows σ_η does not depend on $E_t^{\frac{1}{2}}$. These points are taken for a cluster size of 0.6, minimum tower of 0.2 GeV, and a cut on third jets of 10 GeV.

Chapter 7

Measurement of $\frac{dN}{d\cos\theta^*}$

This chapter describes the analysis that was done to obtain the measurement of the angular distribution, $dN/d\cos\theta^*$, for two jet events. It begins with a discussion of the constraints imposed by the 1987 configuration of the CDF detector hardware. Given these conditions, the transformation of detector acceptance from the lab frame to the parton center of mass is described. Specific effects that influence the acceptance are enumerated. The dijet angular distribution is obtained in two phases. In the first phase, a region of uniform acceptance is described and the angular distribution is shown. The region is then extended by applying corrections to the data using a simple Monte Carlo calculation. In the second phase, a more sophisticated Monte Carlo generator and simulator are used. Comparisons of distributions characterizing the jet data are made for the Monte Carlo and the data. Having established this Monte Carlo as a good representation of the data, corrections to $dN/d\cos\theta^*$ are calculated and applied to the data. Systematic errors on these corrections are derived by varying the conditions in a combination of the Monte Carlos. A final set of angular distributions is presented and

compared to QCD.

7.1 Acceptance Issues

The conditions imposed by the hardware trigger and the state of understanding of the calorimeter behavior are described. The trigger efficiency is established. The region of acceptance in the parton center of mass is discussed. Issues concerning calculation of the acceptance are enumerated.

7.1.1 The Event Sample

For the measurement of the dijet angular distribution, one wants a sample of dijet events whose energy satisfies the hardware constraints with high efficiency, and one wishes for these dijets to cover a large angular range. These desires are considered in light of the following:

- Uncertainties in the jet energy scale in the gas calorimetry (see Chapter 4) allow one to use only the transverse momentum (p_t) measurement of the jets in the central detector. The angular measurement of jets can be taken from any portion of the detector.

- The effects of biases introduced by triggering on only the electromagnetic energy for clusters in the gas calorimeters are not understood; therefore, the total transverse energy trigger was used for both electromagnetic and hadronic compartments of the calorimeter in the central detector only.

- The collision vertex has $\sigma = 35$ cm. Jets can be lost between the plug and forward gas calorimeters if the vertex is too far from the center of the detector.

The last item is handled by placing a 50 cm cut on the vertex position. The first two constraints have been satisfied by choosing a sample where one jet, called the *trigger jet*, satisfies the total transverse energy trigger ($E_{t_{sum}}$) in the central detector. This places no trigger constraints on other jets. If more than one jet satisfies trigger jet requirement, a random choice is made.

From measurements of the single jet inclusive cross section in the central detector [16], the highest total transverse energy trigger of $E_{t_{sum}} \geq 45$ GeV is satisfied when a single central jet is above 45 GeV. The data from the $E_{t_{sum}} \geq 20$ or 30 GeV hardware triggers were examined to check this trigger efficiency. Events from the jet sample described in Chapter 5 with one central jet having a cone size of $\sqrt{\Delta\eta^2 + \Delta\phi^2} \leq 1.0$, a $p_t \geq 45$ GeV, and having its axis no closer than 0.2 units of pseudorapidity to the plug boundary were chosen. The z coordinate of the collision vertex in these events was required to be less than 50 cm. Of the 2441 events passing this requirement, 47 events had $E_{t_{sum}}$ less than 45 GeV. This indicates that the entire sample may be used with 98% triggering efficiency. When these requirements are applied to the full sample, 6000 events remain from the 32000 events having $E_{t_{sum}} \geq 45$ GeV.

7.1.2 Description of the Acceptance Geometry

The angular distribution is expressed in terms of three center of mass variables: p^*, the momentum of the jet in the center of mass, η^*, the pseudorapidity of the jet in the center of mass, and η_{boost}, the boost required to go from the lab frame to the center of mass

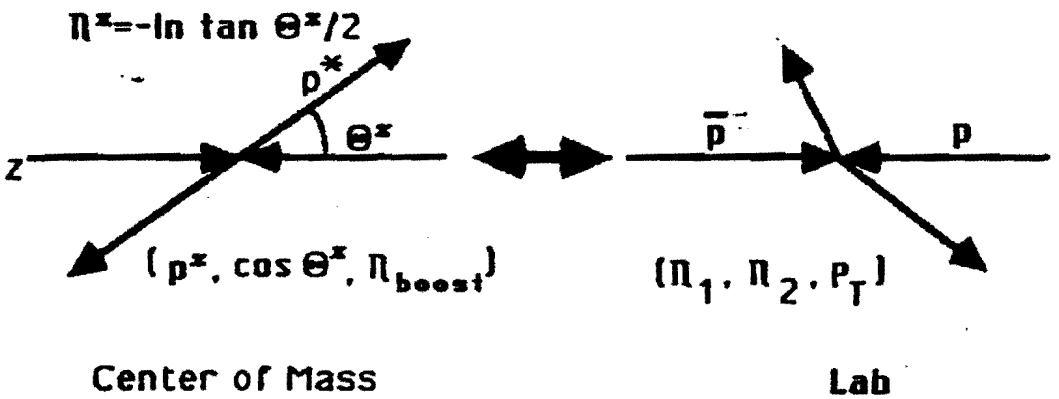

Figure 7.1: Sketch of the dijet system in the lab and center of mass frames

frame. The dijet invariant mass is given by $M_{jj} = 2p^*$. The relationship between these variables and the lab variables (η_1, η_2, p_t) is illustrated in Figure 7.1 and given here:

$$\eta^* = \frac{\eta_1 - \eta_2}{2}, \tag{7.7}$$

$$\eta_{boost} = \frac{\eta_1 + \eta_2}{2}, \tag{7.8}$$

$$p^* = p_t \cosh \frac{\eta_1 - \eta_2}{2}$$

$$= p_t \cosh \eta^*. \tag{7.9}$$

The pseudorapidity of the either jet in the center of mass is related to the center of mass scattering angle since:

$$\eta^* \equiv -\log \tan \frac{\theta^*}{2}, \tag{7.10}$$

$$\cos \theta^* = \tanh \eta^*. \tag{7.11}$$

Figure 7.2 illustrates the mapping of the acceptance region of the detector as one does

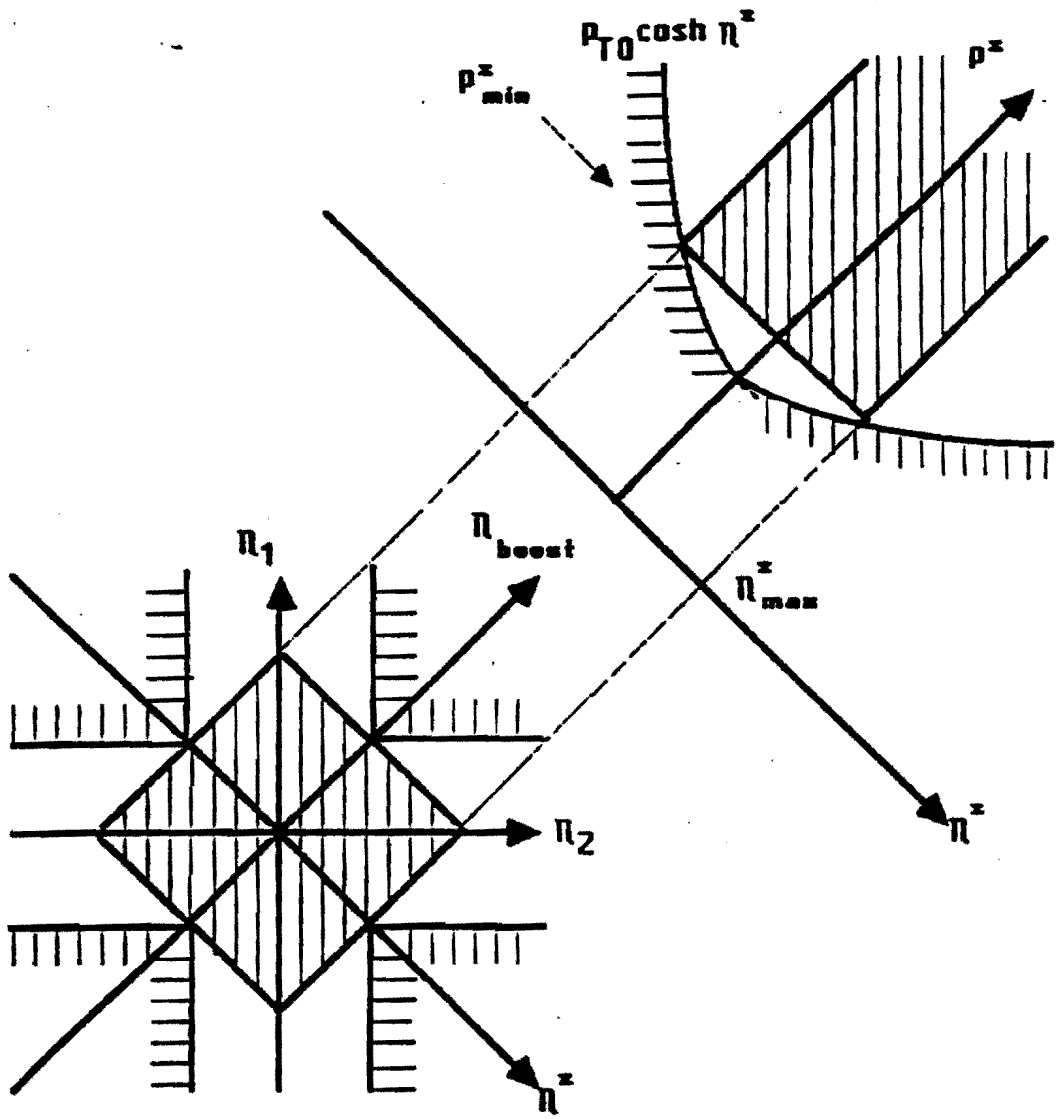

Figure 7.2: Transformation of the sensitive region of the detector from the lab to center of mass frame

this transformation. The sensitive region is a set of overlapping boxes (shown as rectangles in the figure) inside which jets described by (η_1, η_2, p_t) or (η_2, η_1, p_t) may lie. The width of the rectangle is determined by the pseudorapidity coverage of the central detector and the length by the pseudorapidity coverage of the remaining calorimeters. The minimum transverse energy of the jets, p_{t_0}, determines the bottom of these rectangular boxes. This volume of phase space is transformed to the center of mass via the mappings in Equations 7.7 to 7.9. In this transformation a 45 degree rotation and factor of 2 compression in the η_1-η_2 plane occurs for fixed p_t. A plane of constant p_t takes on a curvature in p^*-η^*-η_{boost} space because of the relationship $p^* = p_t \cosh \eta^*$. This relationship means that boundaries of minimum transverse momentum, p_{t_0}, set by the trigger conditions must be translated simultaneously to minimum cuts on the momentum of the trigger jet, p^*_{min}, and maximum choice of the pseudorapidity of the dijet system, η^*_{max}. The implications of this are important in both phases of analysis.

7.1.3 Variables Affecting Acceptance

Consider now the specific quantities affecting acceptance. First, for the trigger jet, there are a number of effects:

1. Variations in the response of the detector across its face, especially those introduced by cracks, will cause fluctuations in the trigger rate across the η-ϕ space of the central detector. This was examined in Chapter 6 and Appendix D. The conclusions were that the only significant variation in rate occurred near the 90° crack. In the measurement of the dijet angular distribution, this crack appears at all values of $\cos\theta^*$ and will amount to a uniform reduction in rate but will not

change the shape. This will be considered in the phase II of the analysis.

2. Since the jet axis is determined from a transverse energy weighted sum, cracks can cause systematic effects in the jet axis position determination. This will be considered in phase II of the analysis.

3. The finite resolution of the calorimeter combines with the rapidly falling jet rate to generate a *feeddown* effect. This may cause events with low energy to undergo a measurement fluctuation and be present in the sample. An unfolding of the resolution is required to scale back the number of events erroneously introduced in this manner. Since the absolute rate is not being measured in this analysis, feeddown is important only if there is a $\cos\theta^*$-dependence. Its effects it will be studied in both phases of analysis. Feeddown is complicated further by the relationship of parton to jet energies. This has been studied extensively [16] for the central calorimeter where, for example, a 45 GeV cluster corresponds to approximately a 60 GeV parton. A number of factors cause this effect: nonlinear low energy response of hadron calorimeters, energy leakage outside of the calorimeter, particles lost outside of the cluster cone, particles included in the jet from the underlying event, and particles lost in cracks. The relationship will be rederived in terms of the trigger jet center of mass momentum in phase II of the analysis.

4. The collisions do not involve only dijets. There are other jets present and they contribute to a transverse momentum of the dijet system (see Chapter 6). This has the effect of smearing the cutoff of the transverse momentum of the jets relative to the partons. A combination of fiducial cuts and Monte Carlo calculations are

used to account for this. It is considered in phase II of the analysis.

For the other jets, many of the acceptance issues are eased. Only the angular position of the other jets need be measured and as described in Chapter 6, the jet axis resolution seems to be about 0.05 units of pseudorapidity. This will be checked in phase II of the analysis.

A final consideration affecting the dijet system is the convolution of the geometric cuts with the vertex distribution. This transforms the sharply defined volumes of acceptance into more complicated contours. These are calculated using the Monte Carlos in both phases of analysis.

7.2 Phase I: Preliminary Measurement of $dN/d\cos\theta^*$

This section describes the first phase of the measurement of the dijet angular distribution. The raw data are examined for a region of uniform acceptance. A simple Monte Carlo calculation is that accounts for geometric and feeddown effects is described. The corrections derived from this calculation are applied to the data to obtain a preliminary measure of the dijet angular distribution.

7.2.1 Uniform Acceptance Measurement of $dN/d\cos\theta^*$

The measurement of the angular distribution can be made without any acceptance correction calculations if the region of uniform acceptance is used. By applying Equation 7.9 with $p_t = 45\ GeV$ and $\eta^* = 0.7$ one finds that the minimum value of p^* is 57 GeV. The 6000 event data sample described in Section 7.1.1 will be examined under these circum-

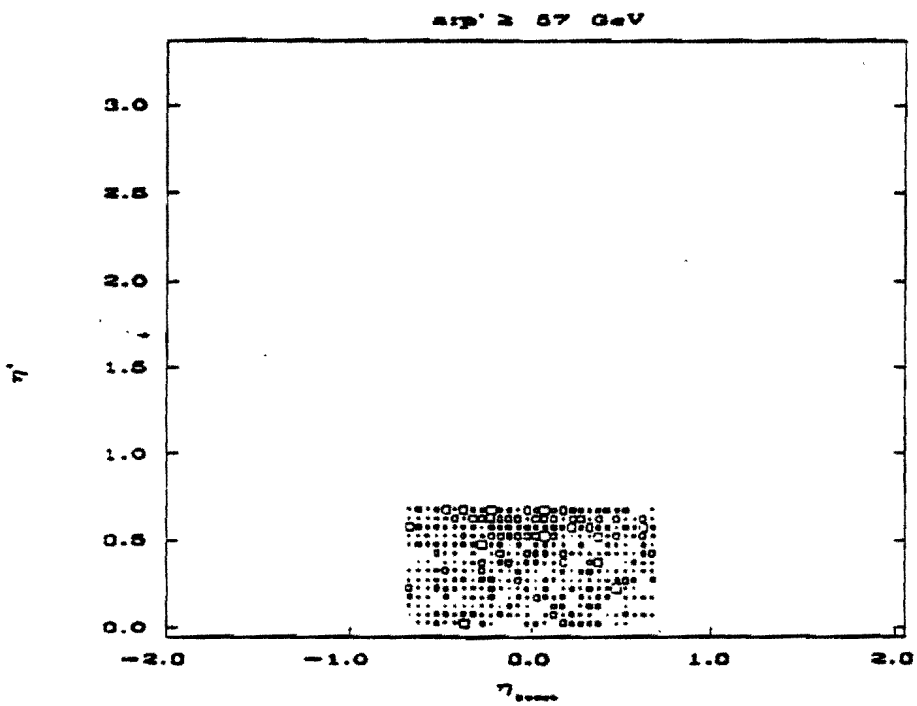

Figure 7.3: Population of data in η_{boost}-η^* plane.

stances. In this data sample, the values of η^*, η_{boost}, and p^* were derived by defining the first jet as the trigger jet and the second jet as the leading jet $180^o \pm 20^o$ opposite the trigger jet in azimuth. Cuts of $|\eta^*|,|\eta_{boost}| \leq 0.7$ and $p^* \geq 57\ GeV$ are placed on the 6000 event sample. This is shown schematically in Figure 7.2. After application of these cuts, 1000 events remain. A plot of η_{boost} vs. η^* is shown in Figure 7.3 and a plot of p^* vs. η^* is shown in Figure 7.4. These events are then projected onto the η^* axis and shown as a function of $\cos\theta^*$ in Figure 7.5. A theoretical calculation of the $2 \rightarrow 2$ parton scattering (see Appendix G) has been placed on the plot as well. An integration of both the theory and the data over the region $0.0 \leq \cos\theta^* \leq 0.6$ provides the normalization.

The extension of the plot to large values of $\cos\theta^*$ has been cut off by the conservative fiducial cuts. From Appendix G, one expects a rapid rise in the number of events at large $\cos\theta^*$; to see this rise, it is necessary to extend the measurement with a correction

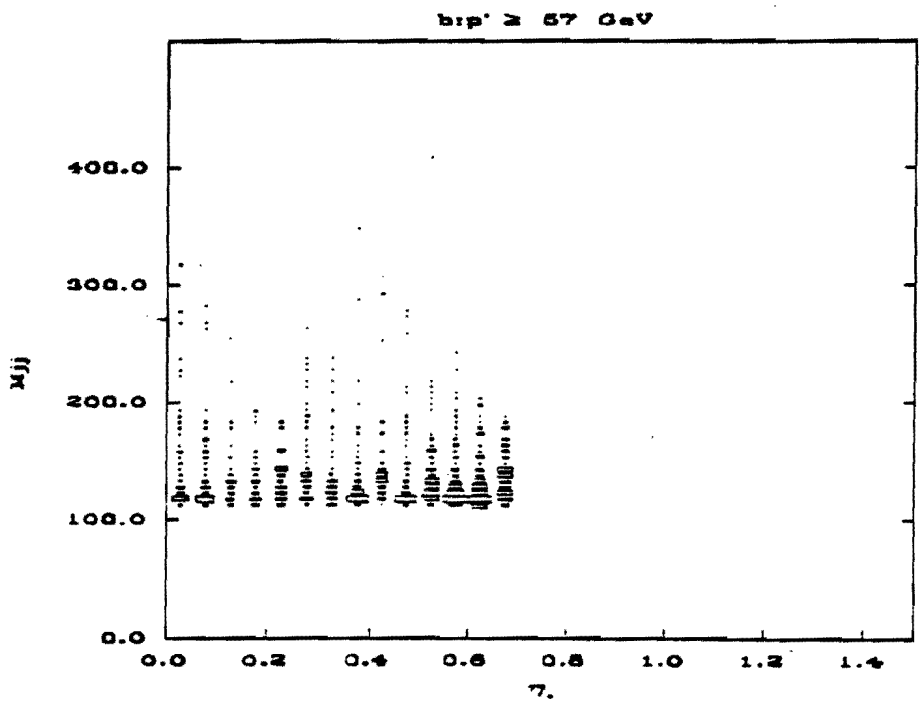

Figure 7.4: Population of data in the p^*-η^* plane.

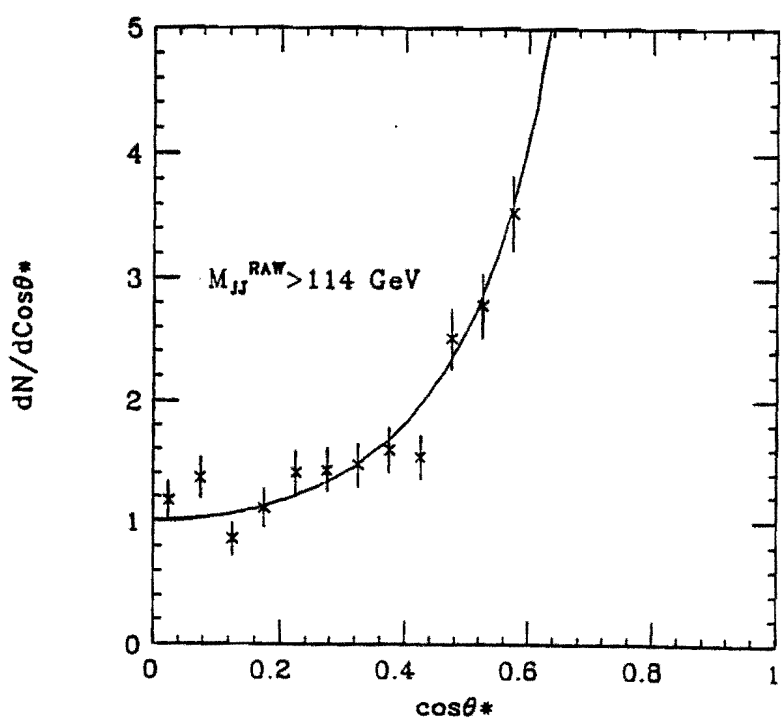

Figure 7.5: Dijet angular distribution uncorrected for acceptance. A 2→2 parton level QCD calculation is also shown. The "raw" designation emphasizes that the mass is derived from the raw cluster energy define in Section 5.2.3.4

for acceptance.

7.2.2 Extension of the Angular distribution

The basic region outlined in Figure 7.2 has been moved out steps to $|\eta^*|,|\eta_{boost}| \leq 1.0$ and then to $|\eta^*|,|\eta_{boost}| \leq 1.2$. Again, the coupling of p^* to η^* via p_t forces choices of minimum p^* to 70 and 82 GeV for these choices of η^*. There are 800 and 600 events in the $|\eta^*|,|\eta_{boost}| \leq 1.0$, 1.2 samples respectively. A simple Monte Carlo was used to calculate the acceptance corrections. These corrections and a description of the Monte Carlo are in Appendix E.

The corrected data are shown in Figure 7.6. The data for $|\eta^*|,|\eta_{boost}| \leq 0.7$ have been normalized to the theoretical curve between $0.2 \leq \cos\theta^* \leq 0.5$. The data for $|\eta^*|,|\eta_{boost}| \leq 1.0$ have been normalized to the data for $|\eta^*|,|\eta_{boost}| \leq 0.7$. The data for $|\eta^*|,|\eta_{boost}| \leq 1.2$ have been normalized to the data for $|\eta^*|,|\eta_{boost}| \leq 1.0$.

The data and correction factors have been calculated for the dijet angular distribution as expressed in terms of the χ variable. As was described in Section 2.4.1, the qcd parton subprocess cross sections take on a general form that is essentially flat as a function of the χ variable when $\chi \geq 2$. The simple parton form of the angular distribution is convolved with the evolution of both the strong coupling, $\alpha_s\left(Q^2\right)$, and of the momentum distribution functions. (See Appendix G.) This curve is shown in Figure 7.7 for the corrected data and for the $2 \rightarrow 2$ calculation of Appendix G. The normalization is similar to that for the distribution in $\cos\theta^*$. The data for $|\eta^*|,|\eta_{boost}| \leq 0.7$ have been normalized to the theoretical curve between $2 \leq \chi \leq 4$. The data for $|\eta^*|,|\eta_{boost}| \leq 1.0$ have been normalized to the data for $|\eta^*|,|\eta_{boost}| \leq 0.7$. The data for $|\eta^*|,|\eta_{boost}| \leq 1.2$

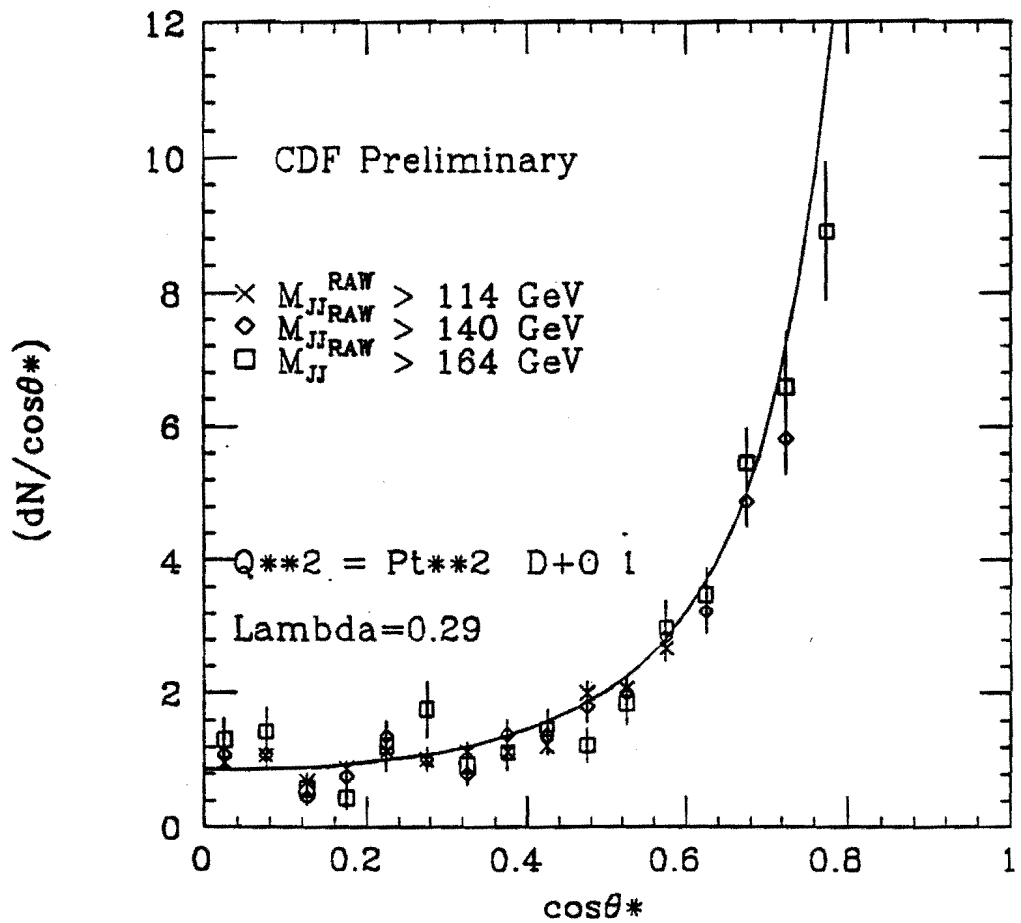

Figure 7.6: Acceptance corrected dijet angular distributions. The curve is a theoretical calculation of the $2 \rightarrow 2$ QCD calculation of the process.

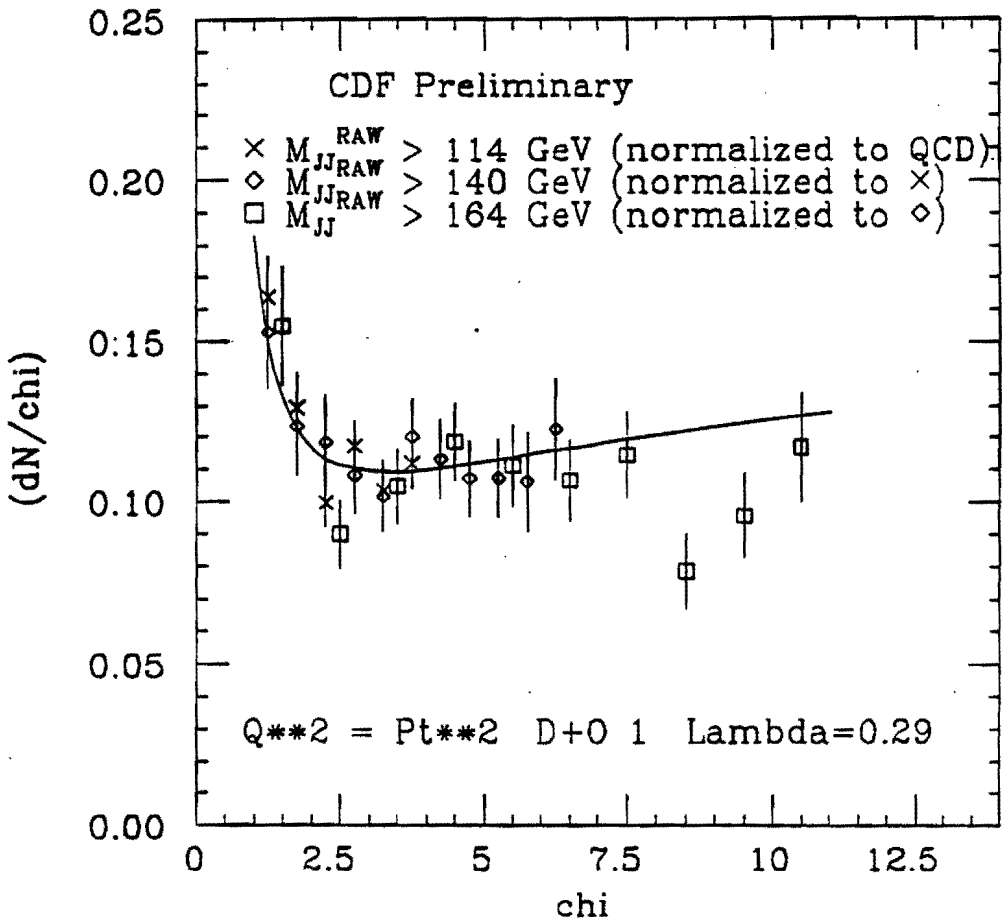

Figure 7.7: Acceptance corrected distribution for $dN/d\chi$. The curve is a theoretical calculation of the $2 \rightarrow 2$ QCD calculation of the process.

η^* cut	η_{boost} cut	p^* cut	Events
$\lvert\eta^*\rvert \leq 0.7$	$\lvert\eta_{boost}\rvert \leq 0.7$	$p^* \geq 57$ GeV	1010
$\lvert\eta^*\rvert \leq 1.0$	$\lvert\eta_{boost}\rvert \leq 1.0$	$p^* \geq 70$ GeV	552
$\lvert\eta^*\rvert \leq 1.2$	$\lvert\eta_{boost}\rvert \leq 1.2$	$p^* \geq 82$ GeV	640

Table 7.1: Cuts and number of events in Phase I $dN/d\cos\theta^*$ analysis.

have been normalized to the data for $|\eta^*|,|\eta_{boost}| \leq 1.0$.

7.3 Phase II: Sophisticated Measurement of $dN/d\cos\theta^*$

Sophisticated Monte Carlos are used and figures of merit are compared to the data. A new set of cuts on the data is described. The Monte Carlos are used to calculate the acceptance. A combination of these Monte Carlos and modifications of the previously described set is used to derive systematic errors. The final measurements of the dijet angular distribution are presented and a limit on quark compositeness is established.

7.3.1 Tests of the Monte Carlos

The effects of cracks and dijet k_t were studied using a more sophisticated simulation of the CDF detector. This simulation, called QFL [29], accepts jet particles as generated from a QCD Monte Carlo, (ISAJET [30] was used here) and produces calorimetric responses that are derived from average behavior of single particles in the test beam data for each detector.

The distributions directly affecting acceptance have been checked in ISAJET/QFL and the data. In these distributions, the leading jet in the hemisphere opposite the trigger jet is called the *probe jet*. The angular distribution is derived from these two jets.

The remaining jets in the detector are called *other jets*. The effects and the associated distributions are described here:

1. **Feeddown** - Since this is a combination of a falling spectrum and resolution, the p^* spectra (Figure 7.8) in bins of $\cos\theta^*$ and the k_{t_ℓ} component (Figure 7.9) of the dijet k_t have been examined. (See Chapter 6 for a description of k_{t_ℓ}.) Good agreement was found between the data and Monte Carlo if the minimum p^* was raised by 5 GeV above that specified by $p^*_{min} = p_{t_0} \cosh \eta^*_{max}$. The division of events in bins of $\cos\theta^*$ allows one to investigate $\cos\theta^*$-dependence of the feeddown. There is no such dependence indicated here.

2. **Soft effects and intrinsic k_t** - These have been tested by comparing the k_{t_η} distributions for data and ISAJET/QFL in Figure 7.10. (Soft effects are discussed in Appendix C.)

3. **Vertex** - The z component of the collision vertex distribution has been represented by a gaussian truncated at ±50 cm. This distribution affects the corrections for regions where the detector is insensitive in the $\eta*$-η_{boost} plane. The data and Monte Carlo results are shown in Figure 7.11.

These tests show excellent reproduction of the data by ISAJET/QFL. Further tests of the Monte Carlo are described in Appendix F.

7.3.2 Determination of the Acceptance

The relationship of the generated parton p^* to the observed dijet p^* is shown for various values of $\cos\theta^*$ in Figure 7.12. From this relationship one establishes the definition of

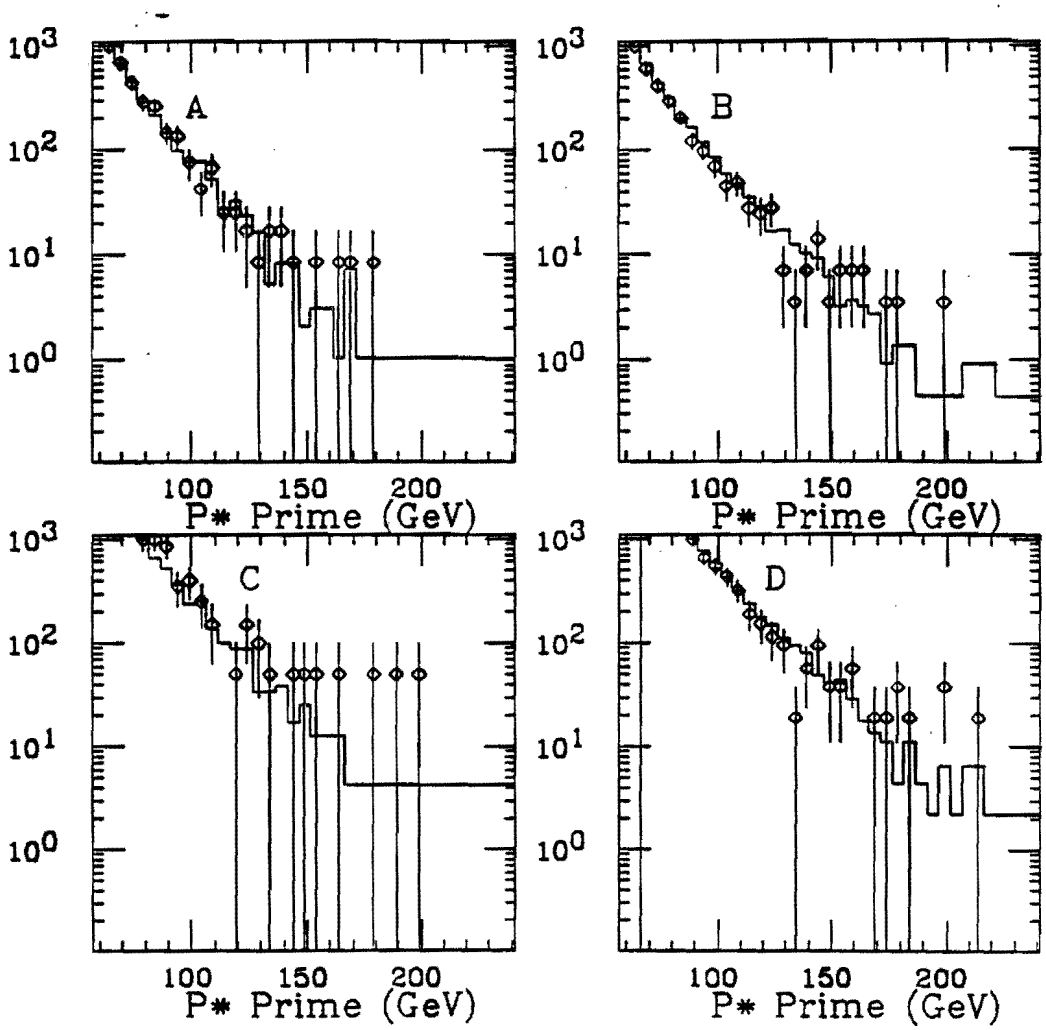

Figure 7.8: Phase II p^* spectra in bins of $\cos\theta^*$. The histogram is the ISAJET/QFL calculation and the points are data: A. $0.0 \leq \cos\theta^* \leq 0.3$ B. $0.3 \leq \cos\theta^* \leq 0.6$ C. $0.6 \leq \cos\theta^* \leq 0.7$ D. $0.7 \leq \cos\theta^* \leq 0.8$

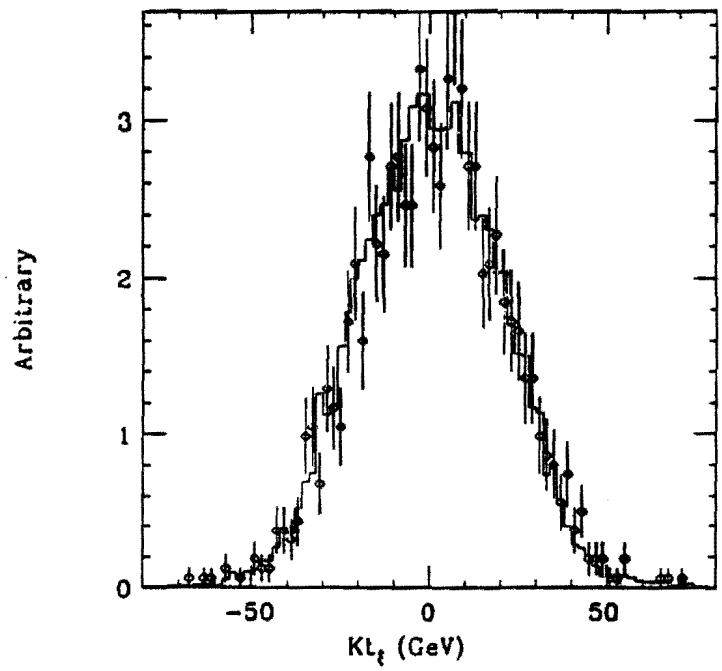

Figure 7.9: k_{t_ℓ} distribution for ISAJET/QFL(histogram) and data(points).

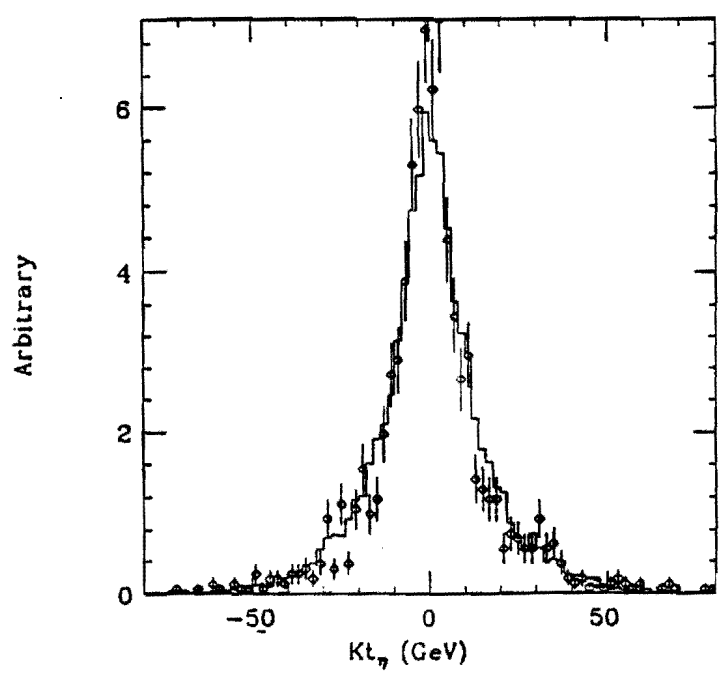

Figure 7.10: k_{t_η} distribution for ISAJET/QFL(histogram) and data(points).

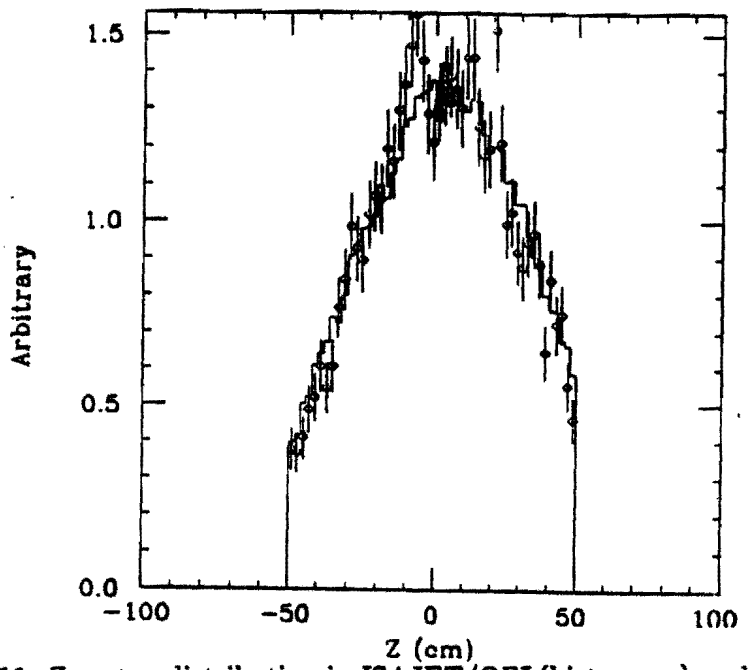

Figure 7.11: Z-vertex distribution in ISAJET/QFL(histogram) and data(points).

the generated and observed $\cos\theta^*$ distributions. As was mentioned above, the original p^* cuts have been increased to be certain that the Monte Carlo was accurately reproducing the detector behavior and the influence of dijet k_t. These cuts must be translated to the appropriate p^* for the partons. The translations and number of events remaining from the 6000 event sample are shown in Table 7.2. In this analysis, the cut on η_{boost} has been extended to 1.2 for all cases and geometric corrections made to the data with the lowest p^* cut.

The corrections are calculated by taking the ratio of the number of events above the observed jet $p_0^{*\prime}$, $N'(p^{*\prime} \geq p_0^{*\prime}, \cos\theta^*)$ to the number observed above the corresponding cut on the parton center of mass momentum, p_0^*, $N(p^* \geq p_0^*, \cos\theta^*)$. The inverse of these corrections, the acceptance, is shown in Figure 7.13 for $\cos\theta^*$ and in Figure 7.14 for χ. In both cases a smoothing function has been used on the results to specify the

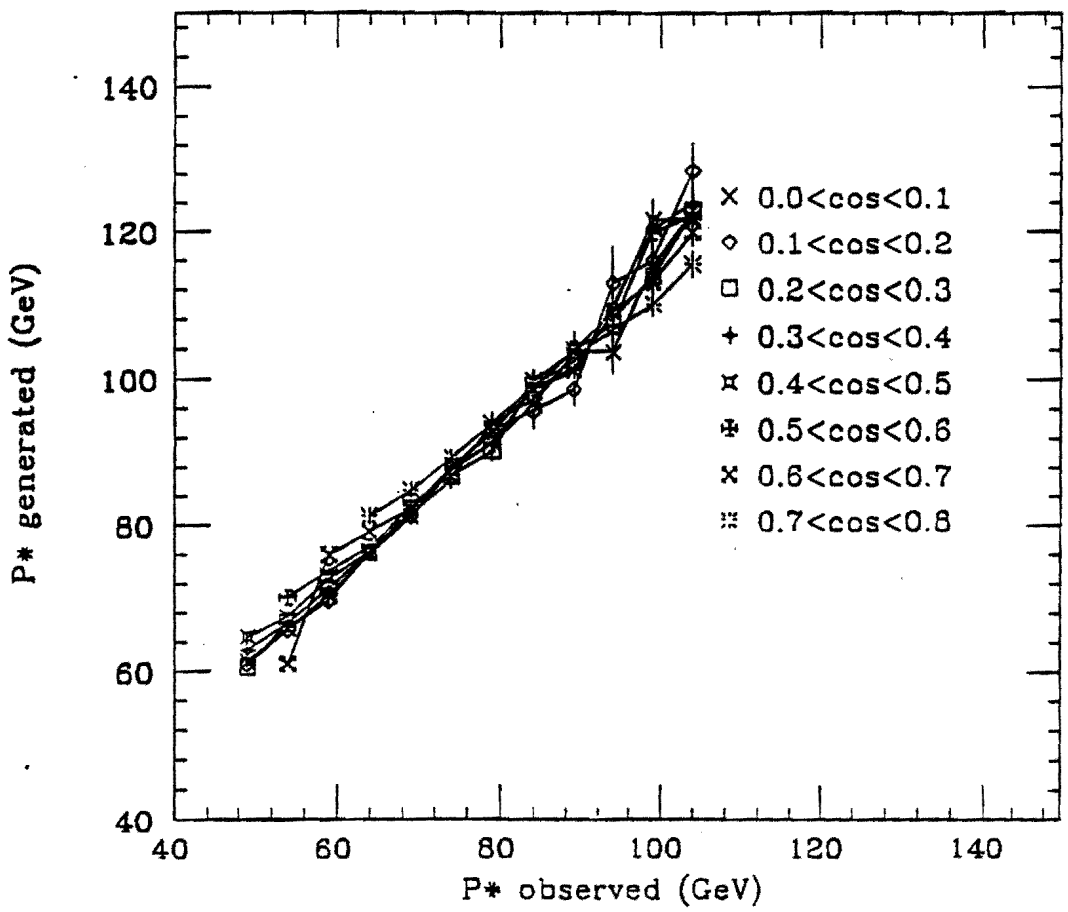

Figure 7.12: Relation of parton p^* to jet p^* shown for various bins of $\cos\theta^*$.

η^* cut	p_0^* cut	$p^{*\prime}$ cut	Events
$\lvert\eta^*\rvert \leq 0.7$	$p_0^* \geq 82$ GeV	$p_0^{*\prime} \geq 61.5$ GeV	1263
$\lvert\eta^*\rvert \leq 1.0$	$p_0^* \geq 106$ GeV	$p_0^{*\prime} \geq 76.5$ GeV	819
$\lvert\eta^*\rvert \leq 1.2$	$p_0^* \geq 118$ GeV	$p_0^{*\prime} \geq 86.5$ GeV	557

Table 7.2: Cuts and number of events in Phase II $dN/d\cos\theta^*$ analysis. The cut values of p_0^* for the partons and the $p_0^{*\prime}$ for the jets are also specified.

final acceptance.

Although they are accounted for in the determination of the acceptance, it is interesting to look at the relationship between the parton pseudorapidity and the jet pseudorapidity directly and then to look at the relationship between parton values of η^*, η_{boost} and the jet values of these quantities. The difference between the initial parton and the final jet axis is shown as a function of the calorimeter pseudorapidity in Figures 7.15 and 7.16 for the trigger and probe jets. The resolution is 0.05 units of pseudorapidity for both η and ϕ and agrees quite well with the determination from tracking (see Chapter 6). There is no deterioration of the jet axis determination in the crack regions. The relationship between η^*, η_{boost} of the partons and jets is shown in Figure 7.17. There is clear indication of a good matching of the calorimeter resolution to the chosen bin size for the measurement of the dijet angular distribution.

7.3.3 Systematic error calculations

The calculation of systematic errors in the acceptance corrections is done by varying parameters in the simple Monte Carlo generator and simulator. The situations being compared are:

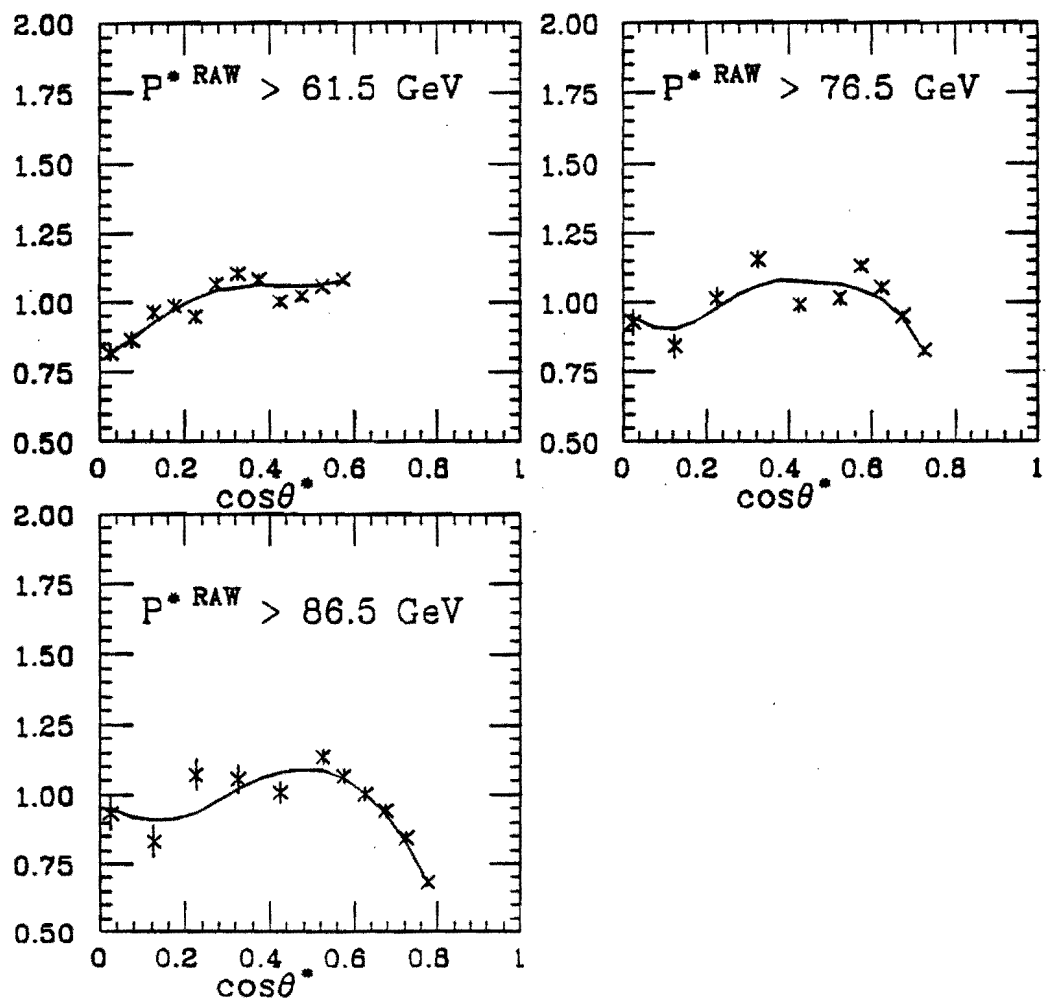

Figure 7.13: Phase II acceptance corrections for $dN/d\cos\theta^*$. The lines are the smoothed corrections derived from the points.

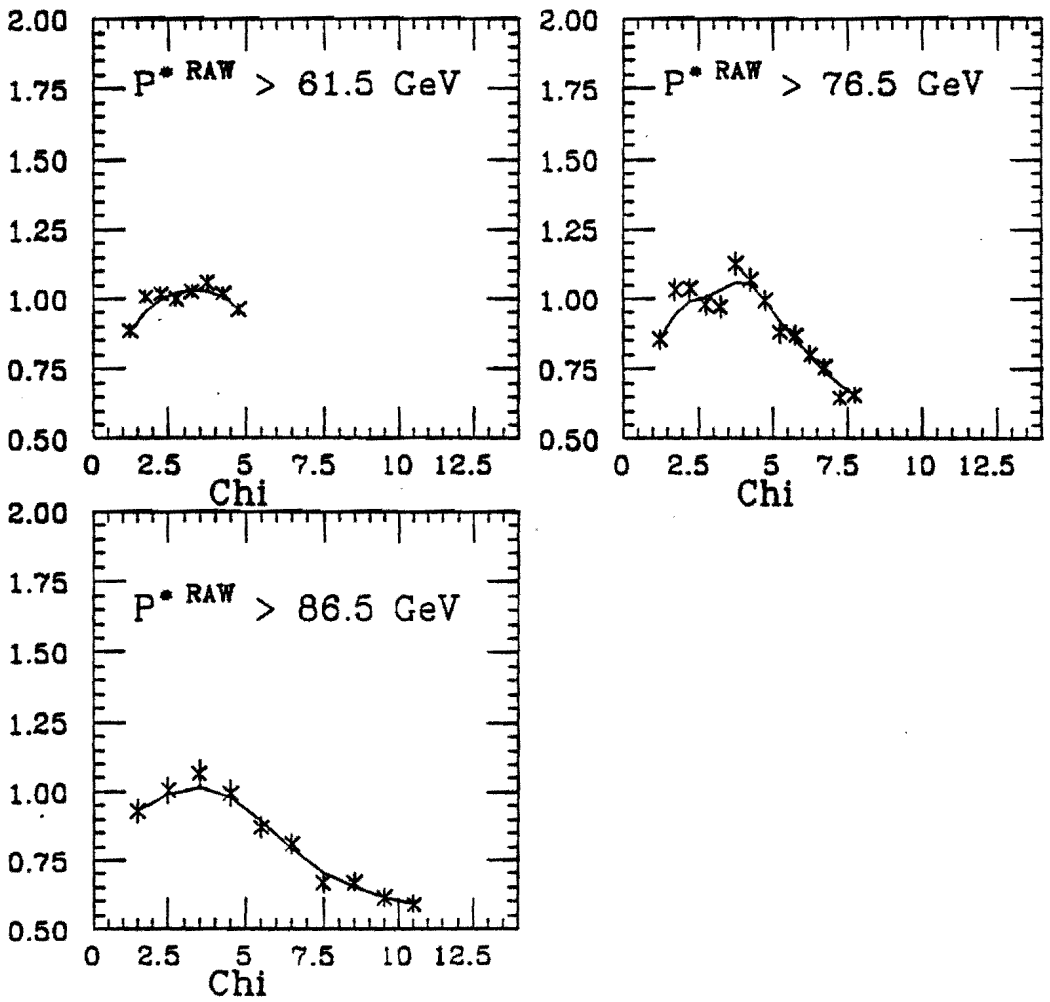

Figure 7.14: Phase II acceptance corrections for $dN/d\chi$. The lines are the smoothed corrections derived from the points.

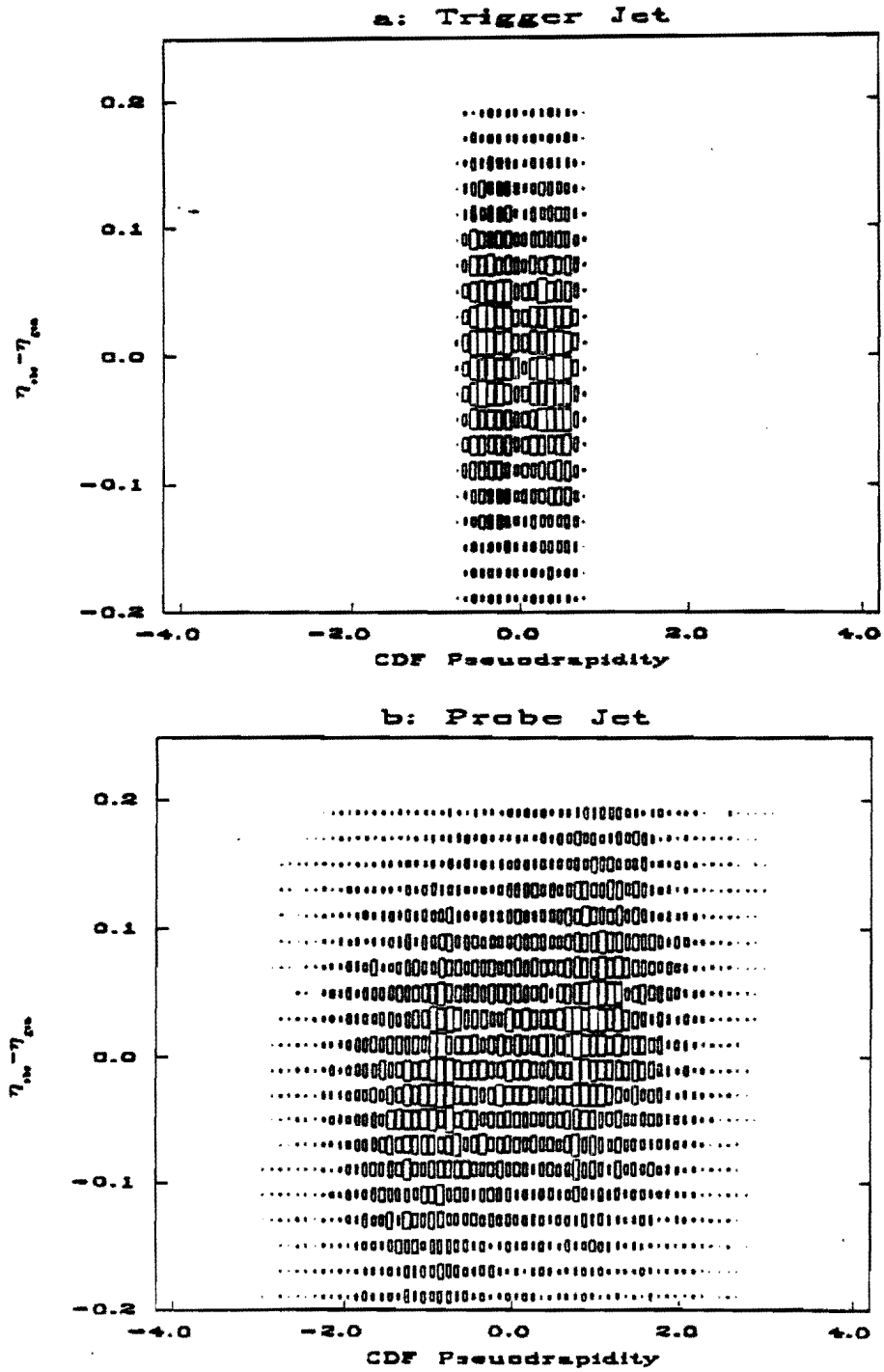

Figure 7.15: Phase II calculation of the relation of the pseudorapidity of the parton axis to the jet axis for a. Trigger η b. Probe η shown as a function of detector tower.

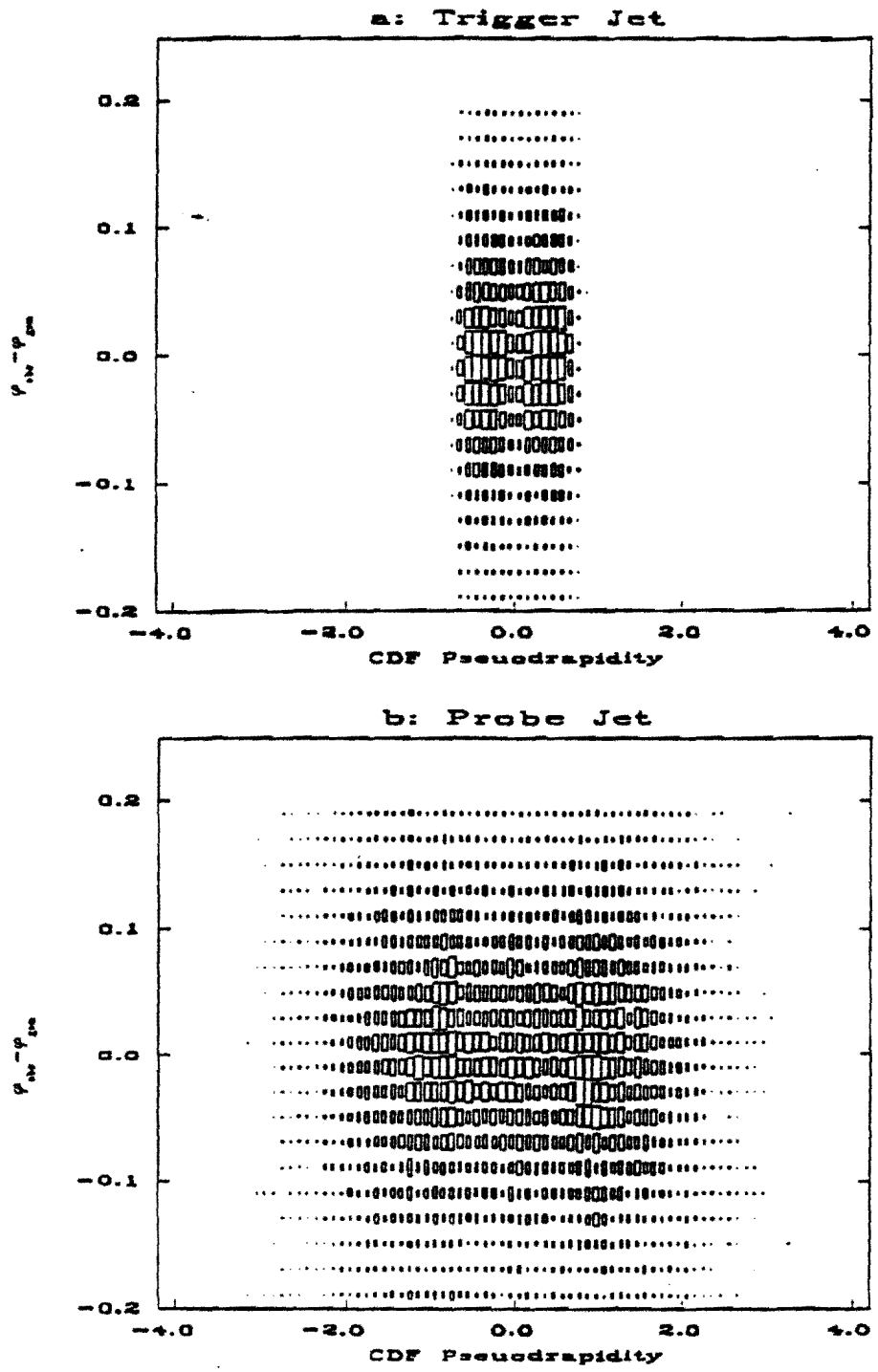

Figure 7.16: Phase II calculation of the relation of the azimuth of the parton axis to the jet axis for a. Trigger ϕ b. Probe ϕ shown as a function of detector tower.

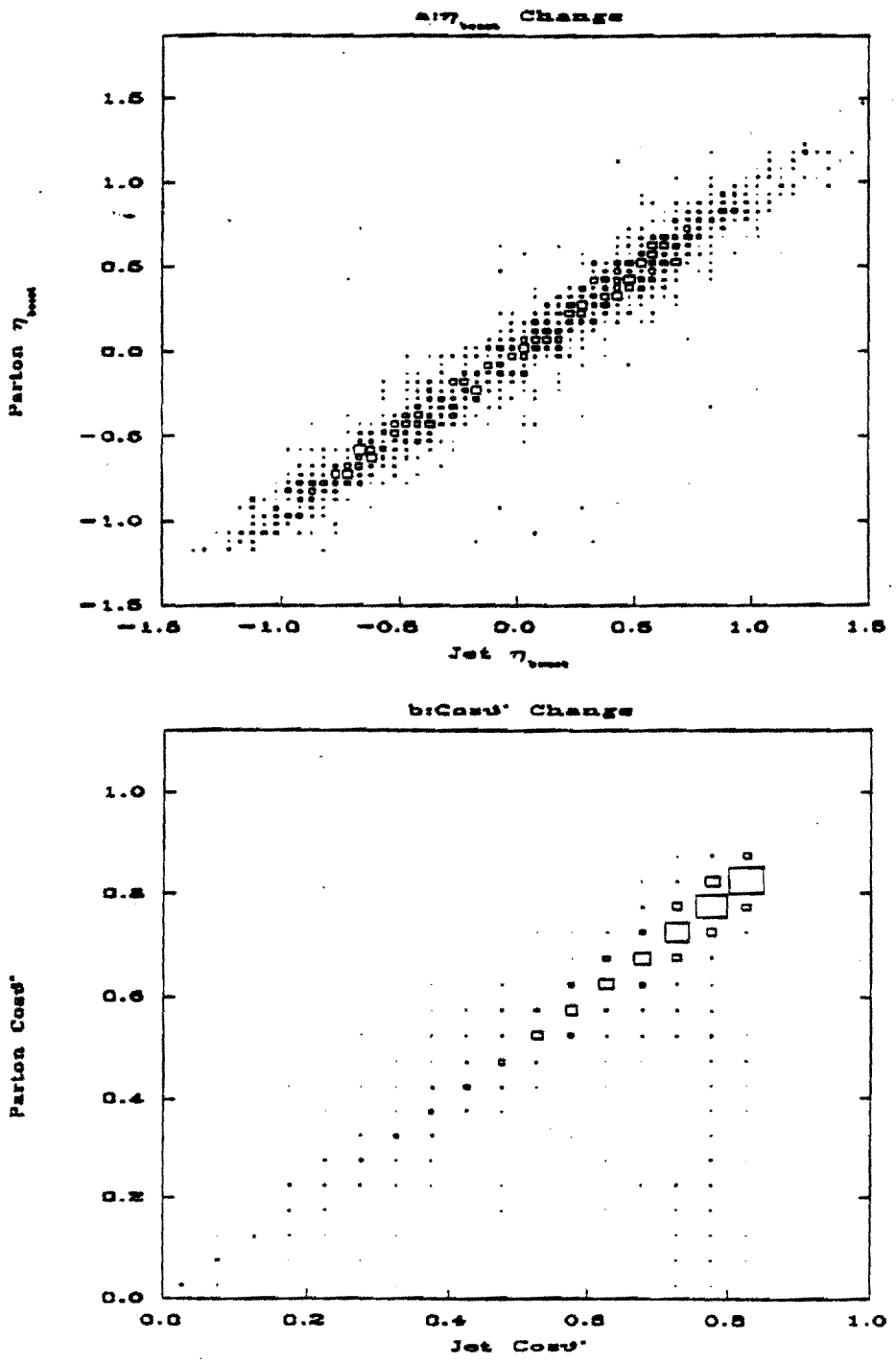

Figure 7.17: Phase II result for then a. η_{boost} and b. $\cos\theta^*$ parton-jet relation.

1: Simple Generator → Simple Simulator

2: ISAJET partons → Simple Simulator

3: ISAJET → QFL

The variations in the generators allow for systematic studies in the changes in the p^* spectrum. The simple simulator described in Appendix E has been modified to allow for a gaussian k_t smearing to be added to the event and uses the relationship of parton p^* to the jet $p*'$. This allows variations in the calorimeter resolution and the k_t to be examined.

The simple Monte Carlos are not expected to reproduce the results of QFL; rather, the variations in the corrections are studied as the conditions of the Monte Carlo are varied. The central detector resolution has been set to 0.50 $GeV^{1/2}/\sqrt{E_t}$, 0.83 $GeV^{1/2}/\sqrt{E_t}$, and 1.10 $GeV^{1/2}/\sqrt{E_t}$. In each case the σ of the dijet k_t has been set to 10, 15, 20, 25 and 30 GeV for the simple generator and to 20, 25, and 30 GeV for the ISAJET hard partons. The valid range of parameter values is checked using the p^*, k_{t_η}, and k_{t_ξ} spectra for comparison of data and Monte Carlo. From the k_{t_η} distribution, the range of k_t's agrees for 20 to 30 GeV with the data and is independent of the choice of calorimeter resolution. The k_{t_ξ} distribution includes a combination of plug and central resolution as well as effects that generated the k_{t_η} distribution. Using a value of k_t = 25 GeV indicates a central resolution of 1.10 $GeV^{1/2}/\sqrt{E_t}$ (see Figure 7.18) when the plug resolution is set at 1.50 $GeV^{1/2}/\sqrt{E_t}$. Given the measurement of 0.83 $GeV^{1/2}/\sqrt{E_t}$ of the central resolution in Chapter 6, it is likely that the choice of plug resolution is too low or that the plug energy scales were not yet fully controlled. Here, the uncertainty in the gas calorimeter behavior enters as secondary effect, and given this uncertainty, the

variation in acceptance as the central calorimeter resolution values run from from 0.50 to 1.10 $GeV^{1/2}/\sqrt{E}$ will be used in calculating the systematic error.

The p^* spectra for the combination of ISAJET partons and simple simulation change slightly when one varies either k_t or the resolution, but the change is not large enough to create inconsistency with the data. The p^* spectrum for the simple generator/simple simulation is quite different than that for ISAJET partons/simple simulator. It is much harder than the data. This is consistent with the assumptions in the generator since the pseudorapidity of the jets is not limited as it is in ISAJET. This means that too many events are being created with large pseudorapidity separation and therefore masses that are large. Although variation of the acceptance of the p^* spectrum is 10%, it is discounted as a systematic error since it is not considered a reasonable reproduction of the data. In conclusion, from the variations of the k_t and the resolution shown in Figure 7.19 a systematic error of 5% is assigned.

7.3.4 Results

The dijet angular distributions are shown again in Figure 7.20 with the QCD prediction. This prediction has been normalized to its integral from $\cos\theta^* = 0.0$ to $\cos\theta^* = 0.6$. The normalizations have been varied in a χ^2 fit where the systematic and statistical error are added in quadrature. The resulting χ^2/DOF are 14.5/11 for $M_{jj}^{parton} \geq 148$ GeV, 18.2/14 for $M_{jj}^{parton} \geq 180$ GeV, and 14.6/15 for $M_{jj}^{parton} \geq 200$ GeV. The corresponding distributions for $dN/d\chi$ are shown in Figure 7.21. The dijet invariant masses have been corrected for the parton to jet relationship and carry a 7 % systematic error [31].

Previous measurements of the dijet angular distribution were made by the UA1

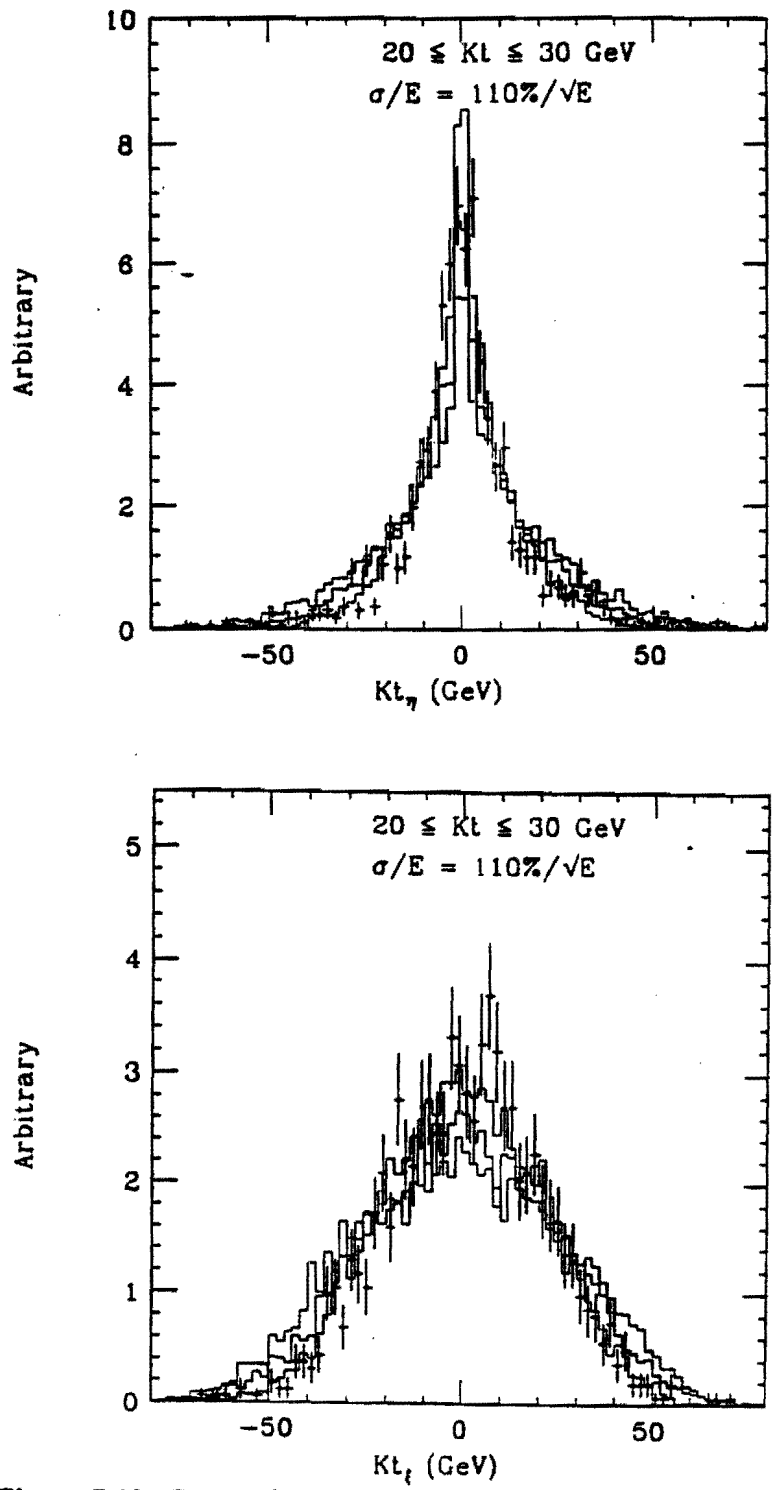

Figure 7.18: Comparison of k_{t_η} and k_{t_ξ} between Monte Carlo and data for $k_t = 20, 25$, and 30 GeV and a resolution of $\sigma/E = 110\%/\sqrt{E}$.

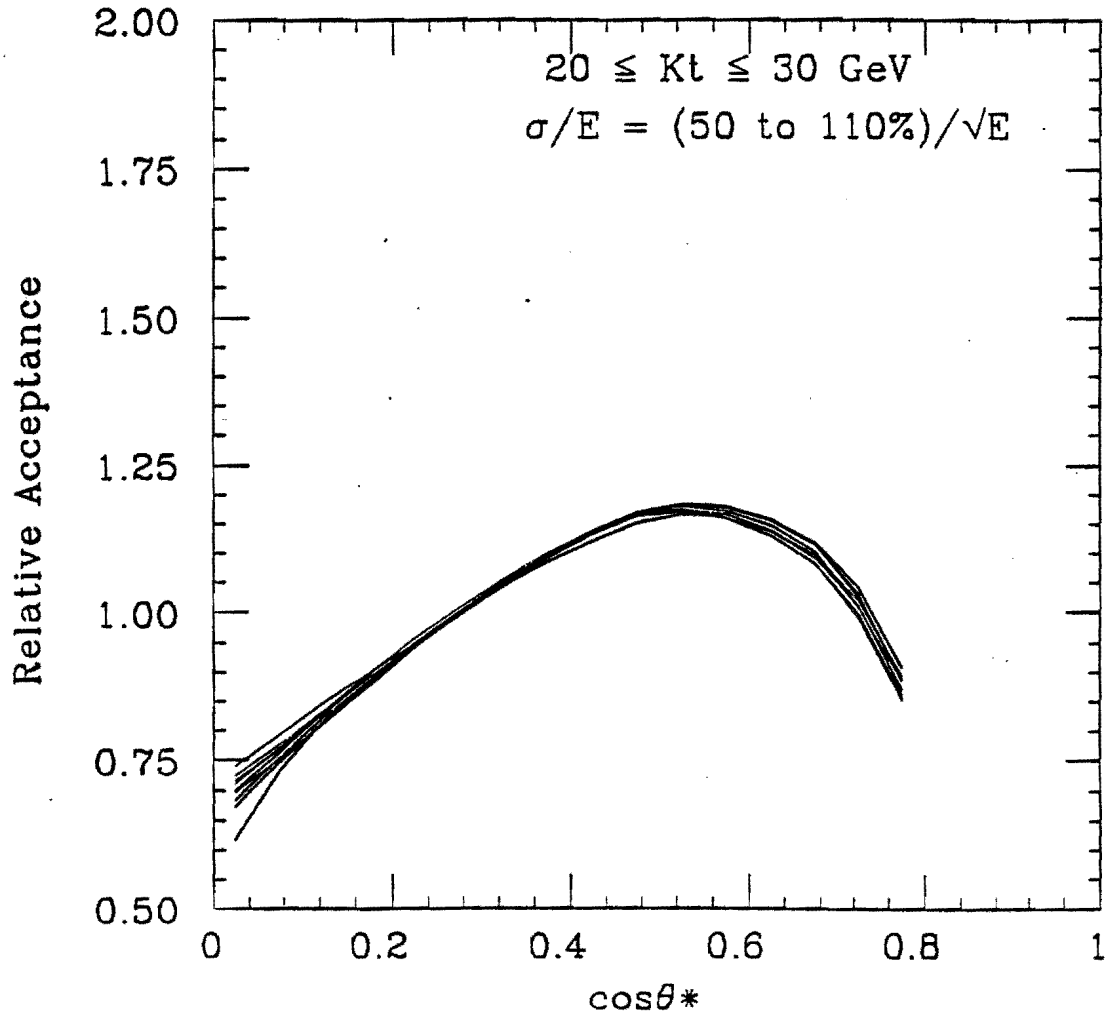

Figure 7.19: Phase II result calculation of the systematic variation of acceptance. The curves represent the acceptance for k_t = 20,25, and 30 GeV and $\sigma/E = (110\%, 83\%, \textit{and } 50\%)/\sqrt{E}$.

collaboration [32] at $\sqrt{s} = 630$ GeV and by the UA2 collaboration [28] at $\sqrt{s} = 540$ GeV. The UA2 group found QCD described the distribution well for $0.0 \leq \cos\theta^* \leq 0.55$. The UA1 group has shown QCD fits the data well for dijet mass intervals of 180 to 200 GeV, 200 to 240 GeV, 240 to 300 GeV, and 300 to 350 GeV and up to $\chi = 19$.

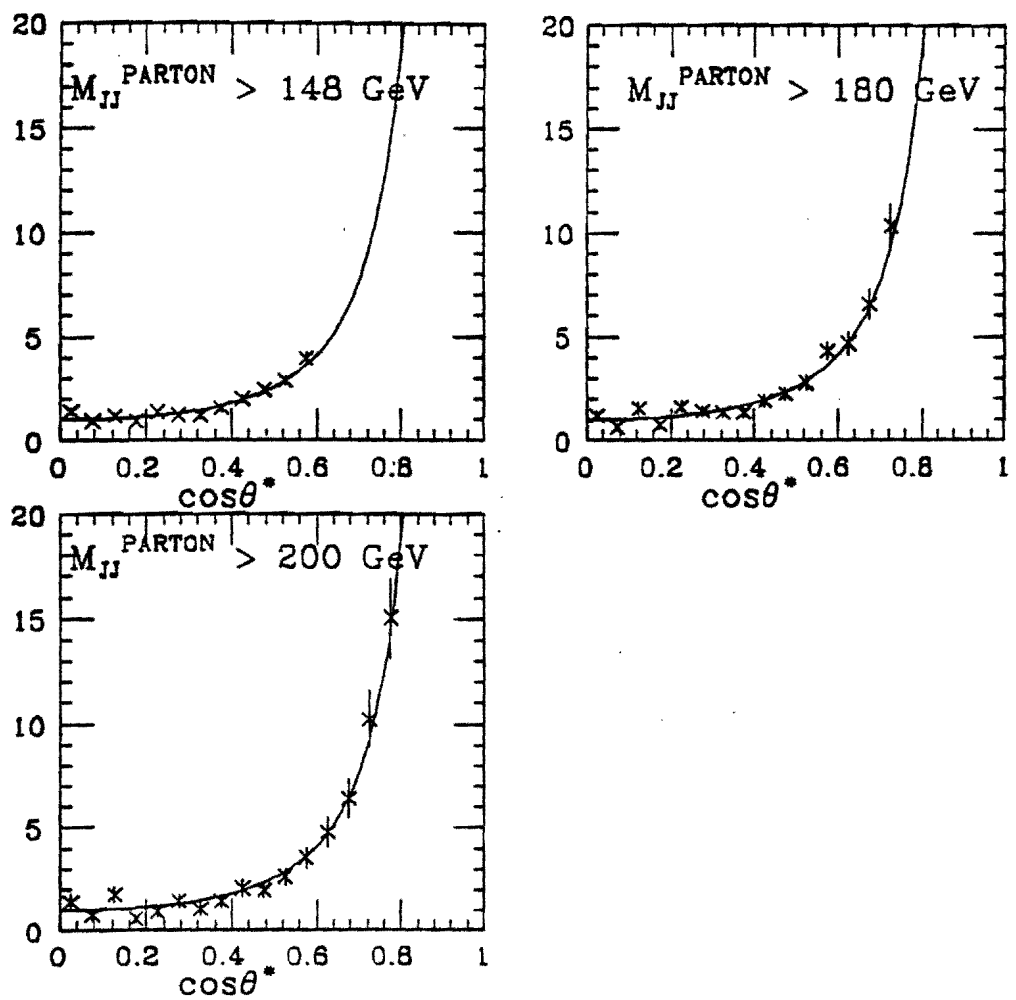

Figure 7.20: Phase II results for $dN/d\cos\theta^*$. The solid curve is the QCD calculation from Appendix G.

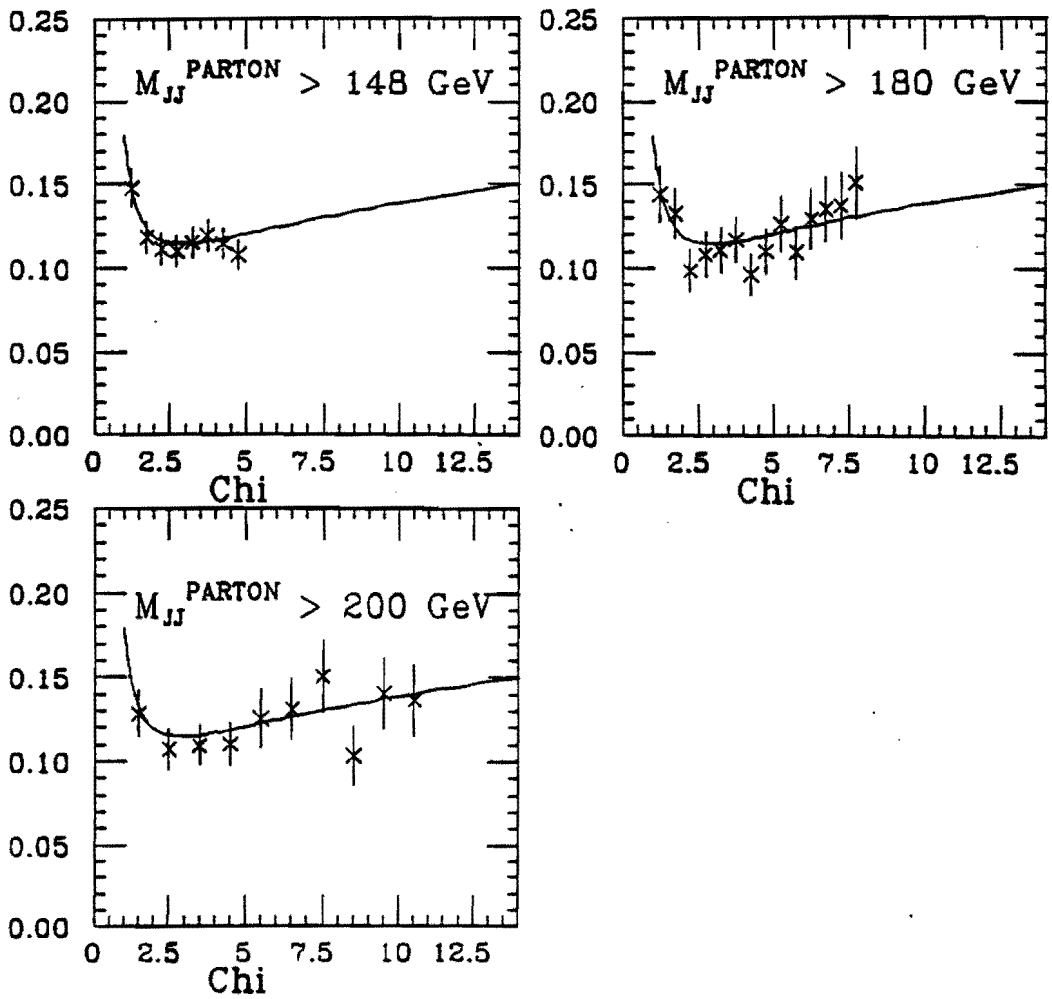

Figure 7.21: Phase II results for $dN/d\chi$. The solid curve is the QCD calculation from Appendix G.

Chapter 8

Summary

The observation of jets produced in collisions of protons with antiprotons at $\sqrt{s} = 1.8$ TeV using the CDF detector at the Fermilab collider is common. The collection of jet events for the 1987 collider run has been used to study the performance of the detector and to test QCD.

These events show a rapidly falling transverse momentum spectrum. The distribution of jets in the central detector indicates uniform response except in the region of the 90° crack. The phi distribution is smooth everywhere. Although the gas calorimeters had several problems, especially neutron sensitivity, these were resolved offline for the most part. The main deficiency of the gas calorimetry was the lack of knowledge of the systematic error on the absolute energy scale. The jets in those portions of the detector were used only for angular measurements.

The study of the transverse momentum of dijet events in the central detector has allowed for a measure of the resolution of the detector by examination of the two components: k_{t_ξ} and k_{t_η}. The jet transverse momentum dependence of k_{t_ξ} shows a linear

relationship in $\sqrt{E_t}$ for the measured range of 30 $GeV \leq E_t \leq 100\ GeV$. The slope of the line is dependent on the cut on other jets and on the cone size of the jet algorithm. This width of the distribution of this component is due to a combination of calorimeter energy resolution and soft particle effects. The k_{t_η} component was independent of the jet transverse momentum. Because of its transverse momentum independence, the contribution of soft effects was removed from the k_{t_ξ} component to obtain a measure of the calorimeter jet energy resolution for a given cone size but independent of third jet activity. In the central detector, this resolution function was $\sigma/E_t = (0.83 \pm 0.10\ GeV^{1/2})/\sqrt{E_t}$ where the error is systematic.

The dijet angular distribution was measured in two phases that were distinguished by the complexity of the acceptance calculation. The first phase allowed for the factors influencing acceptance to be explored and a preliminary measurement to be made. In the second phase, the use of identical cuts on η_{boost} and the inclusion of dijet k_t effects increased the size of the acceptance corrections. Distributions of variables directly affecting the acceptance, including the components of the dijet k_t, were compared to the complex Monte Carlo predictions of the same quantities and excellent agreement was found. Direct control over the variables of merit were then used to estimate the systematic error in the acceptance determination. This was accomplished by modifying the simple Monte Carlos to allow for this control. The bounds on the values of these variables were set by comparing the data and the Monte Carlo results and a 5% variation of acceptance was found for a reasonable range over values of the variables.

Application of the final corrections to the data yielded dijet angular distributions for events above three values of dijet invariant mass. The QCD predictions fit the data very

well.

Appendix A

RABBIT calibrations

This appendix describes the determination of the electronics calibration constants for the CDF calorimetry. It begins with a discussion of the front-end electronics system, the RABBIT system. From there, the calibration of each of the electronics components is described and the equations that model their behavior are derived. Finally, a brief description of the storage of these number in the CDF database is given.

A.1 The RABBIT System

The RABBIT system [33] consists of four major components:

1. RABBIT crates;
2. system modules;
3. front-end instrumentation;
4. microprocessors that direct readout.

The RABBIT crates have slots for 25 modules. Of the 25 slots, three are reserved for system modules and the remainder contain printed circuit boards with up to 64 individual front-end amplifiers. There is a backplane with two redundant busses. These busses contain digital and analog lines that allow for communication of the system modules with the front-end charge to voltage converting modules.

There are two types of system modules. The first is called a EWE. It functions as a crate controller and contains the ADC used to digitize the front-end channels. There can be two such EWEs to provide redundancy in case of failure. Only one module was used in the 1987 data taking run. The second system module is called a BAT. Its duties are:

- To provide timing signals that control the sample and hold functions of the front-end amplifiers
- To monitor the power supply voltages in the crate
- To provide a calibration voltage level for use in charge injection calibration of the front-end amplifiers

The front-end amplifiers consist of two portions: a charge to voltage convertor and a sample and hold circuit. A simplified schematic of such a channel is shown in Figure A.1.

The output voltage of the first section is sampled before and after the beam crossing and stored on two capacitors for later digitization. The signal is taken as the difference between the voltages on the capacitors. The front-end instrumentation modules also have a charge injection circuit that is used to calibrate the individual amplifiers.

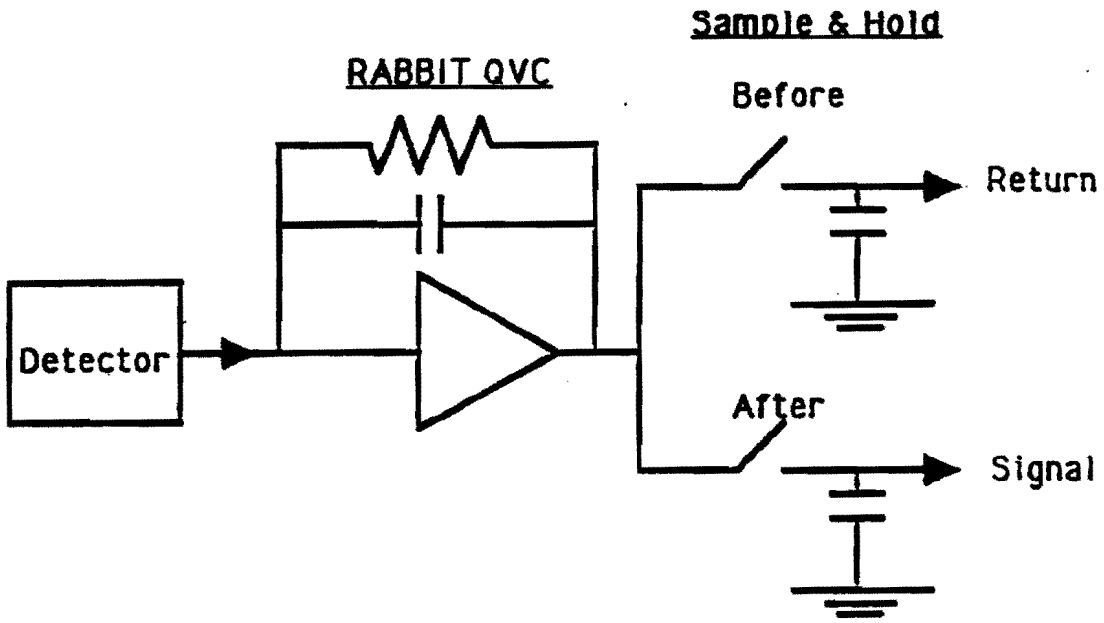

Figure A.1: Simplified schematic of a RABBIT front-end amplifier

The microprocessor, the MX, communicates with the EWE. It commands the EWE to load registers, select channels and digitize.

The calibration of RABBIT electronics is done in three stages. In the first stage, the EWE and BAT components are calibrated. This is described in detail in Section A.2 and A.3.1 respectively. In the second stage, the front-end channels are digitized by the EWE in the absence of signals from the chambers. This procedure determines the pedestal for each channel. It is described in Section A.2.3. In the third stage, the BAT voltage level is varied for each amplifier channel and the response of the channel is digitized by the EWE. Some calibration results from the first stage are then used to determine the amplifier gains. This is described in Section A.3.2.

A.2 EWE Behavior and Calibration

In this section, the general operation of the EWE is described. From this discussion, the detailed equations that model the EWE behavior are derived. The description of how one calibrates and initializes the EWE registers follows from the equations.

A.2.1 Overview of EWE operations

A schematic of the EWE is shown in Figure A.2. When data are being taken, the EWE is commanded to select a channel, subtract the channel pedestal, compare the result to a threshold, and digitize the signal if the threshold is surpassed. These functions may be performed correctly if one has calibrated the threshold and pedestal subtraction circuits on the EWE.

The channel selection is done by setting a card and amplifier address on the digital lines. The EWE then accepts two voltages, V_{signal} and V_{return}, as input from the backplane. These are the voltages on the sample and hold capacitors of the RABBIT amplifiers. The digitization process may be chosen to be accomplished with differences between any combination of V_{signal}, V_{return}, or V_{HQG}, where the last voltage value comes from a high quality ground on the EWE. The difference between these voltages is multiplied by a factor of two. The result is summed with the output of a digital analog convertor, the pedestal DAC. This provides immediate analog pedestal subtraction. The pedestal subtracted signal is split and sent to two portions of the EWE. The first portion, the threshold circuit, is used to determined whether the signal is sufficiently high to digitize. The second portion amplifies the signal by $\times 1$, $\times 2$, $\times 4$, or $\times 8$ and adds $\pm 4V$

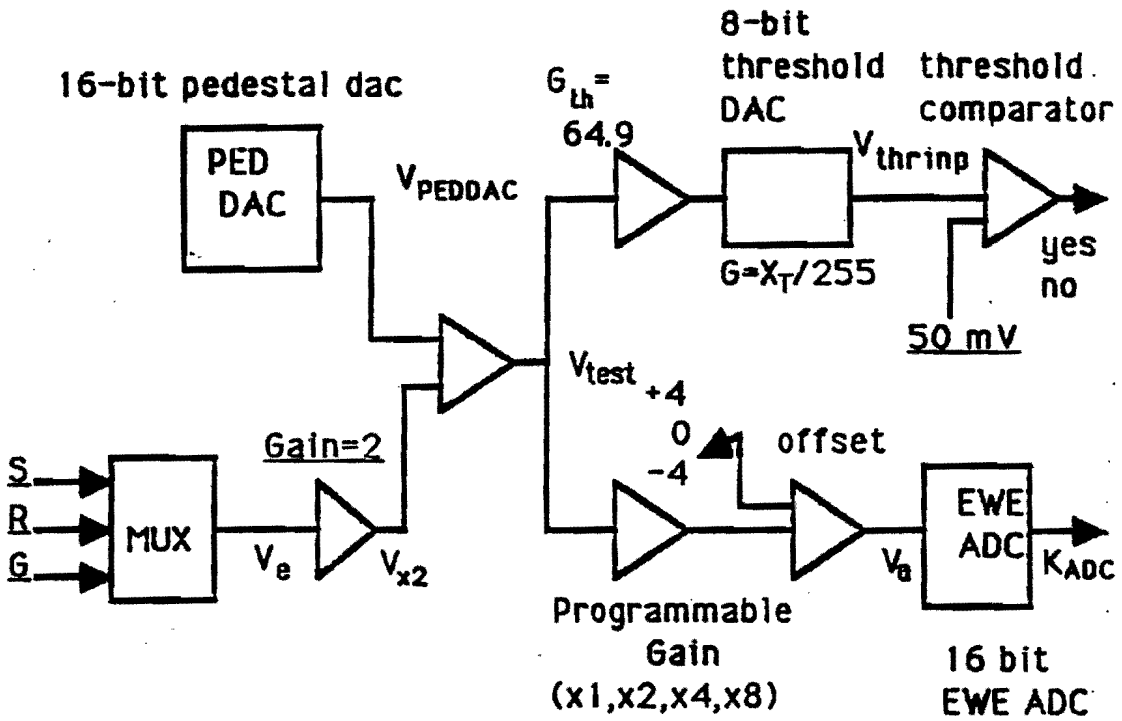

Figure A.2: Simplified schematic of the EWE

or $0V$ to the result before digitizing. The digitization is carried out only if the threshold circuit indicates that the signal is sufficiently high to digitize. This threshold circuit takes the pedestal subtracted value, and scales it by 64.9 and a selectable multiplicative factor. The result is compared to a fixed $50\,mV$ threshold.

Having outlined the operation of the EWE, the specific equations that model this behavior may be derived.

A.2.2 ADC counts in the EWE from the circuit diagram

In following derivation, V stands for voltages, Q for charges, C for capacitor values, X for programmable constants, K for EWE ADC counts, and G for amplifier gains. These symbols will be marked with descriptive subscripts.

Guided by circuit diagram in Figure A.2, one can trace through the behavior of the EWE. Beginning with the MUX and the $\times 2$ op amp, one can define the voltage output as

$$V_{\times 2} = 2 f_{MUX}\left(V_{signal}, V_{return}, V_{HQG}\right), \tag{A.12}$$

where the MUX is assumed to subtract two of the three quantities in parenthesis. Generally, for the sake of reading out a RABBIT channel, one can write Equation A.12 as

$$V_{\times 2} = 2\left(V_{signal} - V_{return}\right), \tag{A.13}$$

or

$$V_{\times 2} = 2\left(V_{return} - V_{signal}\right), \tag{A.14}$$

depending on the design of the amplifier providing the voltages.

It is useful to view the output as consisting of a combination of a chamber signal and a chamber pedestal. Then take

$$V_{\times 2} = 2\left(V_p + V_s\right), \tag{A.15}$$

where

- V_p = Voltage difference between V_{signal} and V_{return} due to channel *pedestal*;

- V_s = Voltage difference between V_{signal} and V_{return} due to the *signal* in the channel.

Continuing the along the circuit, one sees that $V_{\times 2}$ is summed with the output of the pedestal DAC circuit. The result of the addition is:

$$V_{test} = V_{PEDDAC} + V_{\times 2}. \tag{A.16}$$

The voltage from the DAC is considered to be a linear function of the DAC setting:

$$V_{PEDDAC} = X_{PEDDAC} G_{Pedgain} + V_{Pedoff}, \tag{A.17}$$

Where:

- X_{PEDDAC} is pedestal DAC setting;
- $G_{Pedgain}$ and V_{Pedoff} are the slope and intercept of the pedestal DAC behavior V_{Pedoff} and $G_{Pedgain}$ are defined by:

$$+5 \rightarrow -5 \qquad Volts$$

$$0 \rightarrow 65535 \quad Ped\ DAC\ counts$$

so that nominally,

$$G_{Pedgain} = -1/6553.5\ V/Ped\ DAC\ count,$$

$$V_{Pedoff} = +5\ V.$$

Alternatively, one may write:

$$V_{PEDDAC} = G_{Pedgain} \left(X_{PEDDAC} + X_{pedoff} \right),$$

$$X_{Pedoff} = -32767.$$

The V_{test} quantity is examined by two circuits. The first is the threshold circuit. This branch will be discussed in Section A.2.4. The other circuit eventually leads to digitization and is discussed here.

V_{test} is multiplied by a selectable gain. The result is added to programmable offset and finally digitized by the ADC. The voltage seen by the ADC is:

$$V_a = G_s V_{test} + V_{offset}, \tag{A.18}$$

where

- $G_s = selectable\ gain = \times 1,\ \times 2,\ \times 4,\ \times 8;$
- $V_{offset} = \pm 4V,\ 0V.$

One may then write the number of ADC counts as:

$$K_{ADC} = V_a G_{ADC} + K_{offset}, \tag{A.19}$$

where G_{ADC}, K_{offset} are defined nominally by the following relations:

$$+5 \rightarrow -5 \qquad Volts$$

$$0 \rightarrow 65535 \qquad EWE\ counts.$$

So that:

$$G_{ADC} = 6553.5\ EWE\ counts/V,$$

$$K_{offset} = 32767\ EWE\ counts.$$

Thus, Equations A.15 through A.19 describe the conversion of an input voltage to EWE ADC counts.

A.2.3 Application of the EWE Equation to Calibrations

The behaviour of the EWE is described by the equations derived above. The goal of calibration is to specify the pedestal DAC and threshold DAC registers. This requires that the behaviour of these DACs as well as the behaviour of the amplifier channels be specified. In these sections, the pedestal DAC is calibrated, and the setting of the pedestal DAC appropriate to the measured channel pedestal is derived.

A.2.3.1 Combining the EWE Equations into One Master Equation

The EWE equations may be manipulated and applied to the specific situation where one wishes to measure channel pedestals and the response of the pedestal DAC. This begins by successively substituting equations A.15, A.17, A.16, A.18, and A.19 into one another to yield:

$$K_{ADC} = [[2(V_P + V_S) + (X_{PEDDAC} G_{Pedgain} + V_{Pedoff})] G_s + V_{off}] G_{ADC} + K_{offset}. \tag{A.20}$$

Now, expand Equation A.20:

$$\begin{aligned} K_{ADC} &= 2V_p G_s G_{ADC} \\ &+ 2V_s G_s G_{ADC} \\ &+ (X_{PEDDAC} - 32767) G_{Pedgain} G_s G_{ADC} \\ &+ V_{off} G_{ADC} \\ &+ K_{offset}. \end{aligned} \tag{A.21}$$

This rather complicated expression can be simplified by making the following associations:

- $a_1 = G_{Pedgain} G_s G_{ADC}$,

- $b_1 = V_{off} G_{ADC} + K_{offset}$,

- The change in EWE ADC counts due to a channel's pedestal:

$$\begin{aligned} K_{ped} &= 2V_p G_s G_{ADC} \\ &= \frac{2V_p a_1}{G_{PEDGAIN}}; \end{aligned} \tag{A.22}$$

- The change in EWE ADC counts due to an input signal:

$$\begin{aligned} K_{signal} &= 2V_s G_s G_{ADC} \\ &= \frac{2V_s a_1}{G_{PEDGAIN}}. \end{aligned} \tag{A.23}$$

This gives:

$$K_{ADC} = a_1(X_{PEDDAC} - 32767) + b_1 + K_{ped} + K_{signal}. \tag{A.24}$$

Equation A.24 summarizes the behavior of the EWE in terms of numbers that can be measured. It is now possible to consider the calibrations done to determine the constants, a_1, b_1, and K_{ped} as well as the desired value of X_{PEDDAC} in signal readout.

A.2.3.2 EWE PEDDAC Calibration

For a EWE calibration of the pedestal DAC, the input MUX is set to

$$f_{MUX}(V_{signal}, V_{return}, V_{HQG}) = V_{HQG} - V_{HQG} \tag{A.25}$$

which makes $K_{ped} = 0$ and $K_{signal} = 0$. Thus, from Equation A.24, the ADC response is

$$K_{ADC} = a_1 (X_{PEDDAC} - 32767) + b_1 \tag{A.26}$$

and fitting ADC versus ($X_{PEDDAC} - 32767$) yields a_1 and b_1. These values are stored in the CDF database [34].

A.2.3.3 Channel Pedestal Calibration

For a pedestal calibration, the input to the EWE is a channel with no signal ($K_{signal} = 0$), X_{PEDDAC} is set to 32767, and the ADC output is defined to be the pedestal, K_{ped}, for that channel, yielding

$$K_{pedestal} = b_1 + K_{ped}. \tag{A.27}$$

Since b_1 was measured in the EWE calibration (see Equation A.26), this yields K_{ped}.

A.2.3.4 Determination of X_{PEDDAC}

For data acquisition during running of colliding beams, one wants the ADC output to be K_{EWEPED} when there is no signal ($K_{signal} = 0$). K_{EWEPED} is a constant (one for each EWE) to be subtracted from the data by the MX. There is some latitude in defining K_{EWEPED}. The question of exactly what value it has is deferred until after the threshold circuit is discussed in Section A.2.4. Thus, the pedestal DAC is set so that

$$\begin{aligned} K_{EWEPED} &= a_1 (X_{PEDDAC} - 32767) + b_1 + K_{ped} \\ &= a_1 (X_{PEDDAC} - 32767) + K_{pedestal}. \end{aligned} \tag{A.28}$$

This implies the value for X_{PEDDAC}:

$$X_{PEDDAC} = 32767 + \frac{K_{EWEPED} - K_{pedestal}}{a_1}. \tag{A.29}$$

Equation A.29 describes how to calculate X_{PEDDAC} given K_{EWEPED}, $K_{pedestal}$, and a_1. The measurement of $K_{pedestal}$ and a_1 have been described; however, it is necessary

to understand the behavior of the threshold circuit before considering how one chooses K_{EWEPED}.

A.2.4 Threshold circuit equations in the EWE

The goal of this section is to derive equations for the EWE that allow one set a threshold for digitization of a channel. Setting a threshold involves understanding the behavior of the threshold circuit and specifying the value of the threshold. This can be broken into three tasks:

1. **Understanding the Threshold Circuit Behavior** - One must use the schematic in Figure A.2 to write down the conditions under which the threshold is satisfied. The equation that describes this condition is most naturally written in terms of voltages at various points in the EWE circuit.

2. **Calibrate the Threshold DAC** - One must know how the threshold varies as one changes the threshold DAC. This is done by setting the threshold DAC and varying the pedestal DAC until the threshold point is reached. The threshold point is defined as the condition under which the threshold circuit recommends digitization 50% of the time. This calibration is naturally written in terms of the pedestal DAC counts which define the threshold point for some setting of the threshold DAC.

3. **Select a threshold** - One must then select a suitable threshold point. Since one wishes to limit the digitization rate due to noise, the threshold point is constrained by the noise in the channel pedestal; therefore, once one determines the sigma

of the pedestal for a component, the threshold can be specified. This sigma is described naturally in units of EWE ADC counts, so that one will describe the channel threshold value in those same units. For example, if one has a pedestal with a width of 3 EWE ADC counts, then one may wish to set the threshold at 10 EWE ADC counts.

One may note that each of the tasks is accomplished in some set of "natural" units and that these units are different for each task; therefore, specifying a threshold involves describing the behavior of the EWE in a set of common units.

The solution of this problem begins with a derivation of the voltage compared to the threshold. After that, the calibration of the threshold DAC is discussed. This is followed by a derivation of the appropriate setting of the threshold DAC for data acquisition and choosing the free parameter, K_{EWEPED} (see Section A.2.3.4). This section concludes with a summary of the equations one needs in order to configure the EWE for data acquisition.

A.2.4.1 Determination of the Threshold Voltage

In Section A.2.2, Equation A.16 described V_{test}, the voltage into the threshold portion of the EWE. At this point, the remainder of the threshold circuit is considered by tracing through Figure A.2. It can be seen that V_{test} is multiplied by G_{th}, acquires some small offset, V_{toff}. This quantity is then scaled by the value set in the threshold DAC, $X_T/255$. The result may be written:

$$V_{thrinp} = (V_{test}G_{th} + V_{toff})\left(\frac{X_T}{255}\right). \qquad (A.30)$$

V_{thrinp} is compared to a standard comparitor voltage, V_{comp}. If V_{thrinp} exceeds the voltage, V_{comp}, then the threshold is satisfied.

Recall from Section A.2.2 that V_{test} depends on the input voltages and the pedestal DAC behavior. Therefore, it is useful to rewrite Equation A.30 with the value of V_{test} expanded:

$$V_{thrinp} = \left[\left\{2V_p + 2V_s + (X_{PEDDAC} - 32767)\, G_{Pedgain}\right\} G_{th} + V_{toff}\right] \frac{X_T}{255}. \qquad (A.31)$$

From Equations A.22 and A.23, it is possible to rewrite V_p and V_s:

$$2V_p = \frac{K_{ped} G_{Pedgain}}{a_1}, \qquad (A.32)$$

$$2V_s = \frac{K_{signal} G_{Pedgain}}{a_1}. \qquad (A.33)$$

Substitute the definitions of V_p and V_s from equations A.32 and A.33 into A.31.

$$V_{thrinp} = \left\{\left[\left(\frac{K_{ped} + K_{signal}}{a_1}\right) + (X_{PEDDAC} - 32767)\right] G_{Pedgain} G_{th} + V_{toff}\right\} \frac{X_T}{255}, \qquad (A.34)$$

or

$$\left(\frac{K_{ped} + K_{signal}}{a_1}\right) + (X_{PEDDAC} - 32767) = V_{thrinp}\left(\frac{255}{X_T}\right) - \frac{V_{toff}}{G_{Pedgain} G_{th}}. \qquad (A.35)$$

Make the following definitions:

$$V_{thrinp} = a_2,$$

when V_{thrinp} is at the threshold, and

$$b_2 = \frac{-V_{toff}}{G_{Pedgain} G_{th}}.$$

Then rewrite Equation A.35:

$$(X_{PEDDAC} - 32767) + \left(\frac{K_{ped} + K_{signal}}{a_1}\right) = a_2 \frac{255}{X_T} + b_2. \qquad (A.36)$$

A.2.4.2 Calibration of the Threshold DAC

For the threshold DAC calibration, $K_{ped} = 0$ and $K_{signal} = 0$, yielding

$$(X_{PEDDAC} - 32767) = a_2 \left(\frac{255}{X_T}\right) + b_2. \qquad (A.37)$$

Thus, a_2 and b_2 are determined by fitting the value of X_{PEDDAC} at the threshold point versus $255/X_T$.

A.2.4.3 Setting the Threshold DAC for Data Acquisition

Recall now that X_{PEDDAC} as given by equation A.29 above. When one is taking data, this gives the following expression for the threshold criterion:

$$\left(\frac{K_{EWEPED} - K_{pedestal} + K_{ped} + K_{signal}}{a_1}\right) = a_2 \left(\frac{255}{X_T}\right) + b_2, \qquad (A.38)$$

or, using Equation A.27,

$$K_{EWEPED} - b_1 + K_{signal} = a_1 a_2 \left(\frac{255}{X_T}\right) + a_1 b_2. \qquad (A.39)$$

The original desire was to define the threshold in terms of effective EWE counts, K_{Uthr}. This is the case in the previous equation when X_T is set so that $K_{signal} = K_{uthr}$

which implies

$$X_T = \frac{255 a_1 a_2}{(K_{EWEPED} - b_1 + K_{Uthr} - a_1 b_2)}. \qquad (A.40)$$

Thus, once K_{EWEPED} is defined and K_{Uthr} is specified , X_T can be determined.

One consequence of setting X_T to the value in equation A.40 is that there is a limit on the allowed values of K_{Uthr}, since $1 \leq X_T \leq 255$. This corresponds to a limit on K_{Uthr} of

$$a_1 a_2 - K_{EWEPED} + b_1 + a_1 b_2 \leq K_{Uthr} \leq 255 a_1 a_2 - K_{EWEPED} + b_1 + a_1 b_2. \qquad (A.41)$$

This equation is used in directing the choice of K_{EWEPED}.

A.2.4.4 Choosing the Free Parameters

Now, the choice of K_{EWEPED} can be discussed. From equation A.41, it can be seen that certain choices of K_{EWEPED} may lead to limits on K_{Uthr} that are outside of the desired values. There are three choices for K_{EWEPED} that are somewhat sensible:

1. One choice is $K_{EWEPED} = b_1$. This has the advantages that it is a very simple way to set K_{EWEPED} and that the combination $(K_{EWEPED} - b_1)$ cancels out in many of the equations of above. The limits on K_{Uthr} for this choice of K_{EWEPED} are

   $$a_1 a_2 + a_1 b_2 \leq K_{Uthr} \leq 255 a_1 a_2 + a_1 b_2. \qquad (A.42)$$

   Since $a_1 \sim -2$, $a_2 \sim -3$, and b_2 can be between about -20 and $+20$, there are cases where K_{Uthr} must be greater than about 34. This is unacceptable since it corresponds to energies over 100 MeV on most detector components.

2. A second choice is to chose K_{EWEPED} such that the minimum value of K_{Uthr} is some value K_{Uthr0}. This has the advantage that one can always set a certain threshold, since one can define it to be K_{Uthr0}. The disadvantage of this method is that K_{Uthr0} is somewhat arbitrary.

3. A third choice is to set K_{EWEPED} so that it eliminate b_2 from Equation A.40 The value of K_{EWEPED} that does this is

$$K_{EWEPED} = b_1 + a_1 b_2. \tag{A.43}$$

The threshold DAC setting then becomes:

$$X_T = \frac{255 a_1 a_2}{K_{Uthr}}. \tag{A.44}$$

This obviously is a simple equation for X_T; furthermore, if the electronics were perfect, b_2 would be 0 and the choice for K_{EWEPED} in item 1 above would yield the same X_T. Also, the limits on K_{Uthr} are

$$a_1 a_2 \leq K_{Uthr} \leq 255 a_1 a_2, \tag{A.45}$$

which for the usual values gives $6 \leq K_{Uthr} \leq 1580$. This is a very reasonable range with the lower limit corresponding the minimum value of K_{Uthr} that was thought to be reasonable given the noise of the threshold test. This choice is the most reasonable option and the one used.

A.2.5 Summary of EWE calibration choices

In summary, the pedestal DAC, threshold DAC, and K_{EWEPED} are set as follows:

$$K_{EWEPED} = b_1 + a_1 b_2, \tag{A.46}$$

$$X_{PEDDAC} = 32767 + (K_{EWEPED} - K_{pedestal})/a_1, \tag{A.47}$$

$$X_T = 255 a_1 a_2 / K_{Uthr}, \tag{A.48}$$

where K_{Uthr} is the effective threshold on the ADC and is between about 6 and 1580.

A.3 Amplifier Gain Determination

The discussion so far has been aimed at determining the values to be downloaded to the EWE pedestal and threshold DAC's. In this section, the calibration of the EWE ADC, the BAT VCAL voltage and the amplifier channels is discussed.

A.3.1 EWE ADC and BAT VCAL Calibrations

The calibration of the EWE ADC begins by grounding the input to the EWE by setting the MUX to

$$f_{MUX}(V_{signal}, V_{return}, V_{HQG}) = V_{HQG} - V_{HQG}. \tag{A.49}$$

The pedestal DAC is loaded with 32767, and the number of ADC counts is measured for the three voltage settings of the selectable offset. A straight line is fit to these three points to give the number EWE ADC counts per volt:

$$E_m = EWEADC/V_a. \tag{A.50}$$

The standard voltage provided on the RABBIT crate backplane by the BAT is called VCAL. Its calibration begins by placing the BAT VCAL level on the signal line and the BAT ground on the return line. The number of EWE ADC counts is measured for a variety of BAT VCAL DAC settings. The slope of this line is

$$B_m = EWEADC/BATDAC, \tag{A.51}$$

and provides the conversion constant for BAT DAC counts to EWE ADC counts.

A.3.2 Charge injection

The goal of the charge injection calibration is to measure the amplifier gain for each channel. The ratio of the value measured to the nominal value is stored for use by the CDF data acquisition system. The value is taken as a ratio so that it will be a number near one. This constraint arises from consideration of the use of the calibration constant in the MX. The MX is capable of doing online calibration corrections, but since it does sixteen bit integer arithmetic, the highest accuracy and the largest dynamic range can be obtained if the correction factors are near one. In this section then, the calibration is derived with the ultimate goal of determining this number that is close to one.

As was mentioned in Section A.1, there is a single charge injection circuit on each RABBIT card. Such a circuit is shown in Figure A.3. Its main components are an FET switch, a resistor, and a capacitor. The RC time constant is chosen so that the shape of the pulse resembles that coming from the calorimeter. The capacitor is charged by connection to the VCAL voltage on the backplane of the rabbit crate. It is discharged when a timing signal from the BAT, TCAL, closes the FET switch. The charge passes to the input of the amplifier channel that was selected by the EWE. The charge injection occurs after the *before* FET switch is opened. The relative timing of the discharge and the closing of the *before* FET switch is the same as that for signals from a chamber during a beam crossing. The *after* FET switch remains closed for the same amount of time as during normal data acquisition. When the *after* switch is opened, the channel is ready for readout by the EWE.

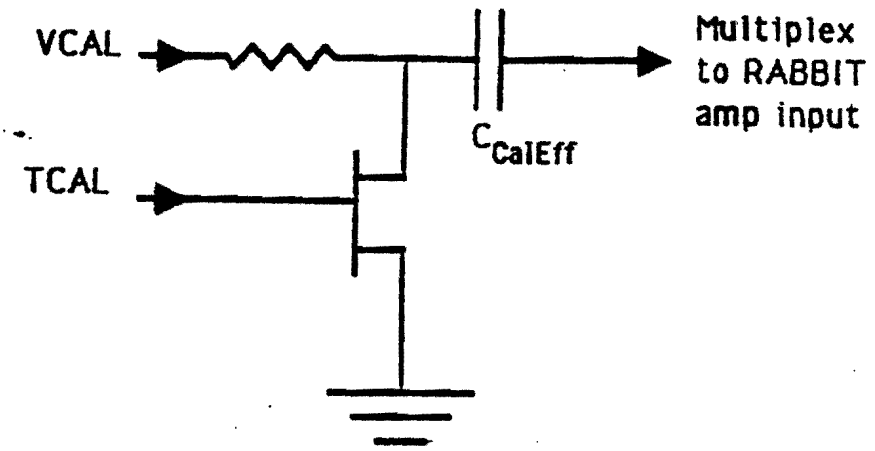

Figure A.3: Simplified schematic of the charge injection circuit

For charge injection calibration readout of a RABBIT amplifier, the EWE has the pedestal DAC set to 32767 and the programmable gain is set to 2. It is assumed on the basis of the use of 0.1% components that the ratio of voltages into the offset op amp, V_a to that at the input of the EWE, V_e, is 4.000. This ratio is defined as

$$F_h = V_a/V_e \equiv 4. \tag{A.52}$$

For any case, if one reads a EWE, one gets some number of counts, K, for a given charge, Q, put into the RABBIT amplifier. There is some linear relationship assumed:

$$K = A + BQ. \tag{A.53}$$

Now consider the specific case of charge injection. The injected charge, Q, is:

$$Q = C_{CalEff}\,(Volts/DAC)\,X_{BATDAC}, \tag{A.54}$$

where C_{CalEff} is the effective charge injection capacitor value and $Volts/DAC$ is the number of volts out of the BAT DAC.

One can express the volts per BAT VCAL DAC count as:

$$Volts/DAC = (V_e/ADC)\,(ADC/DAC)\,. \tag{A.55}$$

The first term takes the voltage into the EWE to ADC counts out of the EWE. This is broken into two steps. One takes the voltage into the EWE to the offset op amp. This is recognized from Equation A.52 as $1/F_h$. The second step takes the voltage into the offset op amp to ADC counts. Its inverse was measured as described above and defined in Equation A.50. One may then write the first term as:

$$(V_e/ADC) = \frac{1}{F_h E_m}. \tag{A.56}$$

This means that Equation A.55 may be written:

$$Volts/DAC = \frac{B_m}{F_h E_m}. \tag{A.57}$$

Combining Equations A.57 and A.54 one arrives at the expression for the charge injected:

$$Q = \frac{C_{CalEff} B_m}{E_m F_h} X_{BATDAC}. \tag{A.58}$$

In doing a charge injection calibration, one measures K in Equation A.53 for several DAC settings, so placing Equation A.58 into Equation A.53 gives:

$$K = A + B\frac{C_{CalEff} B_m}{E_m F_h} X_{BATDAC}. \tag{A.59}$$

One defines the variable QCAL to be the slope of the linear fit of EWE ADC counts versus BAT VCAL DAC settings:

$$QCAL \equiv B\frac{C_{CalEff} B_m}{E_m F_h}. \tag{A.60}$$

The quantity B is the only unknown in Equation A.60 if one uses the charge injection capacitor value for C_{CalEff}. It is useful to rewrite Equation A.60:

$$B = QCAL \times \frac{E_m F_h}{C_{CalEff} B_m}. \tag{A.61}$$

Define the product of B with its nominal value, QNM, to be 1/EQI. Ideally, the value of EQI is one for all channels and all detector components. The explicit expression is:

$$\begin{aligned} EQI &\equiv \frac{1}{B \times QNM} \\ &= \frac{(C_{CalEff} B_m)}{QNM \times QCAL \times E_m F_h}. \end{aligned} \tag{A.62}$$

It can be seen that EQI is the number that one wishes to use to correct for channel to channel gain variations in the MX.

A.4 CDF Database Considerations

The numbers obtained from the RABBIT electronics calibrations are stored on the CDF database. The protocol of this database requires that storage be done in terms of components and attributes of those components. The EWE and BAT modules are considered a component with pneumonic RBC and four attributes:

- The pedestal DAC calibration has attribute UAP and the values a_1 and b_1 from Equation A.26.
- The threshold DAC calibration has attribute UTP and the values of a_2 and b_2 from Equation A.37
- The BAT VCAL DAC calibration value for B_m is referred to as the BVC attribute.

- The EWE ADC calibration value for E_m is referred to as the U4V attribute.

Each calorimeter component has a number of attributes. These include the nominal gain, QNM, the charge injection capacitor value, CNM (referred to as C_{CalEff} above), and the pedestal, PED. For any calorimeter component, Y, one stores the charge injection results in terms of the measured quantity, QCAL, and the attributes mentioned. In this nomenclature, Equation A.62 may be written:

$$EQI\{Y\} = \frac{(CNM\{Y\} \times RBC\{BVC\})}{QNM\{Y\} \times QCAL\{Y\} \times (RBC\{U4V\} \times 4)}, \qquad (A.63)$$

where the attribute-component pairs are given as $ATT\{Comp\}$.

Appendix B

Multiple Collision Estimate

The vertex was reconstructed using the VTPC wire information. The goal of the reconstruction is to determine the vertex and ensure that it is a good beam-beam event. Two kinds of backgrounds to beam-beam events are events where a beam interacts with a gas particle in the beam pipe and events with multiple interactions in a single beam crossing. The beam-gas interaction is considered negligible in the total transverse energy triggers.

An estimation of multiple collisions can be made by taking the probability of an event to be a jet event and folding in the probability of a second jet event occurring within the time of a single crossing. This is

$$N(doubles) = [L_{tot} \times \sigma(jet)][L_{1\ crossing} \times \sigma(jet)]. \qquad (B.64)$$

Here, L_{tot} is the total integrated luminosity for events above some trigger threshold; $\sigma(jet)$ is the cross section for observing a jet event above some transverse energy; $L_{1\ crossing}$ is the integrated luminosity during a single crossing.

One can obtain L_{tot} from the single jet inclusive cross section:

$$\sigma[\bar{p}p \rightarrow \ jet \ + \ X](E_t) = \int_{\Delta y_1} \int_{\Delta y_2} \frac{d\sigma}{dy_1 dy_2 dE_t}. \qquad (B.65)$$

This has been measured for the central pseudorapidity region [16]. One must integrate over this over energy and divide by two to obtain $\sigma(jet)$, assuming that most events contain two jets. This cross section must be calculated for jets at the energy of each of the central thresholds. The choice of jet threshold will be made to coincide with the total transverse energy threshold since it nearly matches the energy of the jet. This is because energy lost by looking only at the cluster is gained back because the cluster will include towers with energy below 1 GeV. The approximate counterbalance of the effects will be assumed for this calculation. The integrated luminosity for one crossing can be given an upper bound by taking the peak machine luminosity, $1.5 \times 10^{29}\ cm^{-2}\ sec^{-1}$, and the time between crossings, 7 microseconds, to get $1.05 \times 10^{-9}\ nb^{-1}$.

The values of L_{tot}, $\sigma(jet)$ and number of doubles are given in Table B.1. It is clear that the number of events with two hard scatterings is negligible. The same chart shows the probability of having a minimum bias event occur in the same crossing as a jet event. The cross section of 44 mb [35] has been used. Approximately 1.5 to 2.5 % of the jet events have an accidental minimum bias event overlapping. The main effect is to change the energy scales and resolutions of the jets and will be considered a component of that measurement.

The distribution of vertices is gaussian, having a mean of 3 cm and a sigma of 35 cm. The vertex must be used in calculating the jet properties since the transverse energy and pseudorapidity calculations change when the vertex moves.

Threshold	20 GeV	30 GeV	40 GeV	45 GeV
Events	15885	98034	17946	15500
Integrated Luminosity	0.419 nb^{-1}	14.9 nb^{-1}	6.30 nb^{-1}	7.24 nb^{-1}
$\sigma(jet)$	25000 nb	4080 nb	1200	625
$N_{jet}(doubles)$	0.0025	0.25	0.01	0.0025
$N_{minbias}(doubles)$	440	2553	317	190
Percent min bias-jet	2.7 %	2.6 %	1.7 %	1.2 %

Table B.1: The number of multiple jet and jet plus min bias events expected for each central jet trigger threshold is given. There is a 15% error on the luminosity numbers and a 70% systematic uncertainty in the cross sections.

Appendix C

Central Jet Energy Resolution

This appendix provides details of the measurements made of dijet energy resolution to extract the contribution due to calorimeter resolution.

The approximations used in subsequent data analysis are derived. Distributions of the components of the dijet k_t are examined. A detailed discussion of the origin of the dijet k_t follows. Next, the application of the analysis to the central calorimeter is described. Finally, the jet resolution for different clustering algorithms and definitions of the dijet system is presented.

C.1 Dijet k_t Description

The general characteristics of the components of the dijet k_t were described in Chapter 6. The behavior of these components is discussed and their relationship to the calorimeter energy resolution derived. The distributions of the components of the dijet k_t are examined and the origin of these components is detailed.

C.1.1 Calculating Dijet k_t

The calculation of the dijet k_t assumes that the 4-vectors of the two jets have been calculated. The jets are defined by a clustering algorithm (Section 5.2.3) characterized by the size of the jet cone in $\eta - \phi$ space and by the minimum energy that a tower may have in order to be included in the cluster. The η and ϕ coordinates of the jet axis are calculated as the transverse energy weighted first moment of the towers in the cluster. The jet 4-vector is calculated by assuming that each tower is a massless particle. The rotation of the k_t components from k_{t_x} and k_{t_y} into k_{t_η} and k_{t_ξ} is described by the angle θ_ξ. Since the η-axis makes an angle $\phi_{jj}/2$ with the negative x-axis, on can write θ_ξ:

$$\begin{aligned} \theta_\xi &= \pi - \left(\frac{\phi_{jj}}{2} + \frac{\pi}{2}\right) \\ &= \frac{\pi - \phi_{jj}}{2}. \end{aligned} \tag{C.66}$$

Using this angle, the rotated components of k_t are

$$\begin{aligned} k_{t_\eta} &= -\left(p_{t1_x} + p_{t2_x}\right)\sin\theta_\xi + p_{t1_y}\cos\theta_\xi \\ &\simeq -\left(p_{t1_x} + p_{t2_x}\right)\left[\frac{\pi - \phi_{jj}}{2}\right] + p_{t1_y}. \end{aligned} \tag{C.67}$$

$$\begin{aligned} k_{t_\xi} &= \left(p_{t1_x} + p_{t2_x}\right)\cos\theta_\xi + p_{t1_y}\sin\theta_\xi \\ &\simeq \left(p_{t1_x} + p_{t2_x}\right) + p_{t1_y}\left[\frac{\pi - \phi_{jj}}{2}\right]. \end{aligned} \tag{C.68}$$

Since ϕ_{jj} is very peaked near 180°, a small angle approximation has been used for θ_ξ (See Section C.1.3 for experimental justification). This approximation applies to the p_t components of the individual jets as well, so one may write:

$$\begin{aligned} p_{t1_x} &\simeq |p_{t1}|, \\ p_{t2_x} &\simeq -|p_{t2}|, \end{aligned}$$

$$
\begin{aligned}
p_{t1_y} &\simeq |p_{t1}|(\pi - \phi_{jj}), \\
p_{t2_y} &= 0.
\end{aligned}
$$

Therefore, to lowest order in $\delta\phi \equiv (\pi - \phi_{jj})$, k_{t_η}, and k_{t_ξ} may be written:

$$
\begin{aligned}
k_{t_\eta} &\simeq -(|p_{t1}| - |p_{t2}|)\left[\frac{\pi - \phi_{jj}}{2}\right] + 2\,|p_{t1}|\left[\frac{\pi - \phi_{jj}}{2}\right] \\
&= [|p_{t1}| + |p_{t2}|]\left[\frac{\pi - \phi_{jj}}{2}\right],
\end{aligned} \tag{C.69}
$$

$$
k_{t_\xi} \simeq |p_{t1}| - |p_{t2}|. \tag{C.70}
$$

These are fairly simple results. The k_{t_ξ} component is approximately the difference in the jet transverse momenta, and the k_{t_η} component is the average transverse momentum times the variation of the dijet azimuthal separation from 180 degrees.

C.1.2 Relating k_t to energies

As was mentioned in Section 6.1, the energy and momenta of jets are taken as the scaler and vector sums of the towers in the cluster:

$$
E^2 = p_x^2 + p_y^2 + p_z^2 + m^2, \tag{C.71}
$$

$$
\begin{aligned}
E_t^2 &= E^2 - p_z^2 \\
&= p_t^2 + m^2.
\end{aligned} \tag{C.72}
$$

Therefore, one may write the difference in jet E_t values as:

$$
\begin{aligned}
E_{t1} - E_{t2} &= \sqrt{p_{t1}^2 + m_1^2} - \sqrt{p_{t2}^2 + m_2^2} \\
&= p_{t1}\sqrt{\left(1 + \frac{m_1^2}{p_{t1}^2}\right)} - p_{t2}\sqrt{\left(1 + \frac{m_2^2}{p_{t2}^2}\right)}
\end{aligned}
$$

$$
\begin{aligned}
&\simeq p_{t1}\left(1+\frac{m_1^2}{2p_{t1}^2}\right)-p_{t2}\left(1+\frac{m_2^2}{2p_{t2}^2}\right)+\mathcal{O}\left(\frac{m^4}{p_t^4}\right)\\
&= p_{t1}-p_{t2}+\frac{1}{2}\left(\frac{m_1^2}{p_{t1}^2}-\frac{m_2^2}{p_{t2}^2}\right)+\mathcal{O}\left(\frac{m^4}{p_t^4}\right). \qquad (C.73)
\end{aligned}
$$

The jet E_t, mass, and p_t was examined in the data in Section 5.3. One observes the distributions in p_t and E_t are identical so that they may be used equivalently in the analysis below. The ratio of mass to p_t is of order 4% and the difference of masses in Equation C.73 is even smaller.

This equivalence of p_t and E_t is important in relating the dijet k_t to calorimeter resolution. One usually models the calorimeter response as:

$$\frac{\sigma(E_i)}{\sqrt{E_i}}=\frac{A_i}{\sqrt{E_i}}, \qquad (C.74)$$

where $i=1,2$ refers to each of the two jets and E is in GeV. Then, since

$$E_{t_i}=E_i\sin\theta, \qquad (C.75)$$

one can write

$$\sigma(E_{t_i})=A\sin\theta\sqrt{E_i}. \qquad (C.76)$$

If one assumes independent errors only, and uses the rms values of E_{ti}, then

$$\sigma(\langle E_{t_1}-E_{t_2}\rangle)=\sqrt{\sigma^2(\langle E_{t_1}\rangle)+\sigma^2(\langle E_{t_2}\rangle)}. \qquad (C.77)$$

Consider one jet constrained to be in the central detector, $\langle E_t\rangle=\langle E_{t_1}\rangle=\langle E_{t_2}\rangle$, $\langle\sin\theta_1\rangle\sim 1$, so

$$\sigma(\langle E_{t_1}-E_{t_2}\rangle)=A_1\sqrt{E_t}\sqrt{1+\left(\frac{A_2\sqrt{\sin\theta_2}}{A_1}\right)^2}. \qquad (C.78)$$

When the second jet is in the central, $A=A_1=A_2$ and $\sin\theta_2\sim 1$ so this becomes:

$$\sigma(\langle E_{t_1}-E_{t_2}\rangle)\simeq A\sqrt{\langle 2E_{t_1}\rangle}. \qquad (C.79)$$

Since $E_t \simeq p_t$ one can combine Equations C.79 and C.70 to obtain:

$$\sigma\left(k_{t_\ell}\right) \simeq A\sqrt{2\langle E_{t_1}\rangle}. \qquad (C.80)$$

One expects the width of the k_{t_ℓ} distribution to grow with the E_t of the jets.

C.1.3 Distributions of Dijet k_t

In order to see what the distributions in the dijet k_t components are like, the characteristics of the events for the sample of data taken with the cluster cone size of 0.6, a minimum tower threshold of 0.2 GeV, and $|\delta\phi_{jj}| \leq 20^o$ will be examined. These are the same data that were examined in Section 5.3:

1. **Dijet k_t vs ϕ_{jj}** - Figure C.1 is a two dimensional histogram of the dijet k_t vs. ϕ_{jj}. This distribution shows the cut at $|\delta\phi_{jj}| \leq 20^o$. It also shows that the jets are peaked around $\phi_{jj} = 180^o$. This justifies the small angle approximation used in calculating the components of the dijet k_t. (See Section C.1.1.) This approximation was important since it allows one to demonstrate the separation of the sensitivity to energy and angular measurement error into the k_{t_ℓ} and k_{t_η} components respectively. Also, since the sum of the transverse energy of two jets must be above 60 GeV, the minimum dijet k_t lies along the line implied by Equation C.69: $k_t \geq 30\,(\pi - \phi_{jj})$. For example, at $\phi_{jj} = 20^o = 0.349$ radians, the minimum k_t should be 10.5 GeV. Indeed, this is indicated by the figure.

2. **Study of k_{t_ℓ}** - The total transverse energy in the two jets is defined as $E_{t_{sum}}$. Figure C.2 shows a plot of k_{t_ℓ} against this quantity. It is important to use the sum of the energy for making the cut so that one jet is not biased to be above

some cut while the other is free to vary. A case in which such a selection bias exists is described in Appendix D. The histogram in Figure C.2 has been sliced in bins of $E_{t_{sum}}$. The results are shown Figures C.3 and C.4. There are a number of important things to note:

- The distributions are all quite gaussian. Had a selection bias of the type described above been introduced, these plots would be offset from zero and the gaussian shape would be truncated.
- One observes that indeed the widths of the distributions increase with increasing energy, as expected from Equation C.80.

3. **Energy of the central jets** - Figure C.5 shows a two dimensional histogram of the energy of the central jet as a function of $E_{t_{sum}}$. This plot has been sliced in the same manner as the k_{t_ξ} plot. The result is shown in Figures C.6 and C.7. The distributions are very gaussian and quite well defined.

4. **Properties of the k_{t_η} distributions** - The data shown were analyzed with a cut on $\delta\phi_{jj}$. This cut was released in order to obtain the k_{t_η} distributions. The plot of k_{t_η} vs $E_{t_{sum}}$ is shown in Figure C.8. Slices of the plot are shown in Figures C.9 and C.10. One observes that these plots are gaussian, have a mean of zero, and the widths of the distributions are constant as a function of the slice.

C.1.4 Origin of the Dijet k_t Components

There are a number of factors that contribute to forming a dijet k_t. These effects influence measurements of distributions in one or both of the components, k_{t_η} and k_{t_ξ}.

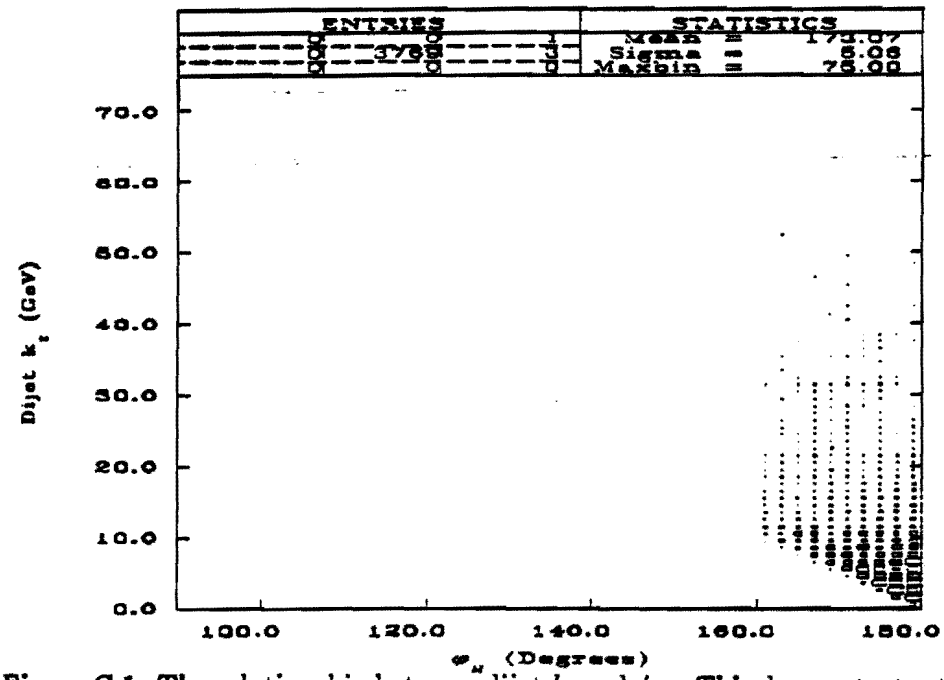

Figure C.1: The relationship between dijet k_t and ϕ_{jj}. This demonstrates the cut applied to ϕ_{jj} and the kinematics of the dijet system. It also shows that the jets tend to be quite back-to-back.

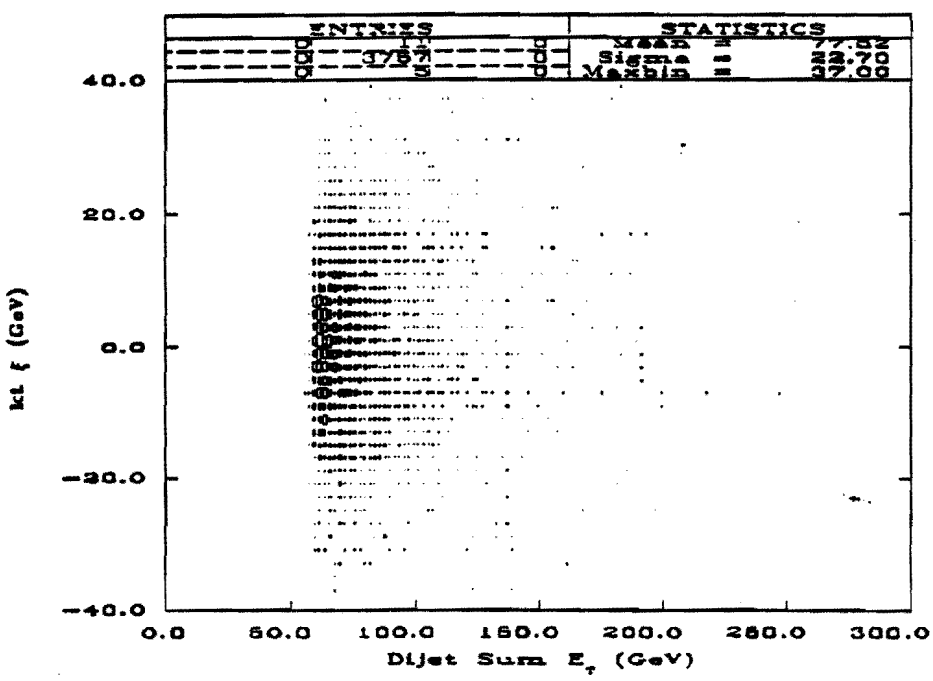

Figure C.2: This shows the energy scale sensitive component of the dijet k_t plotted as a function of the sum of the two jets' transverse energies.

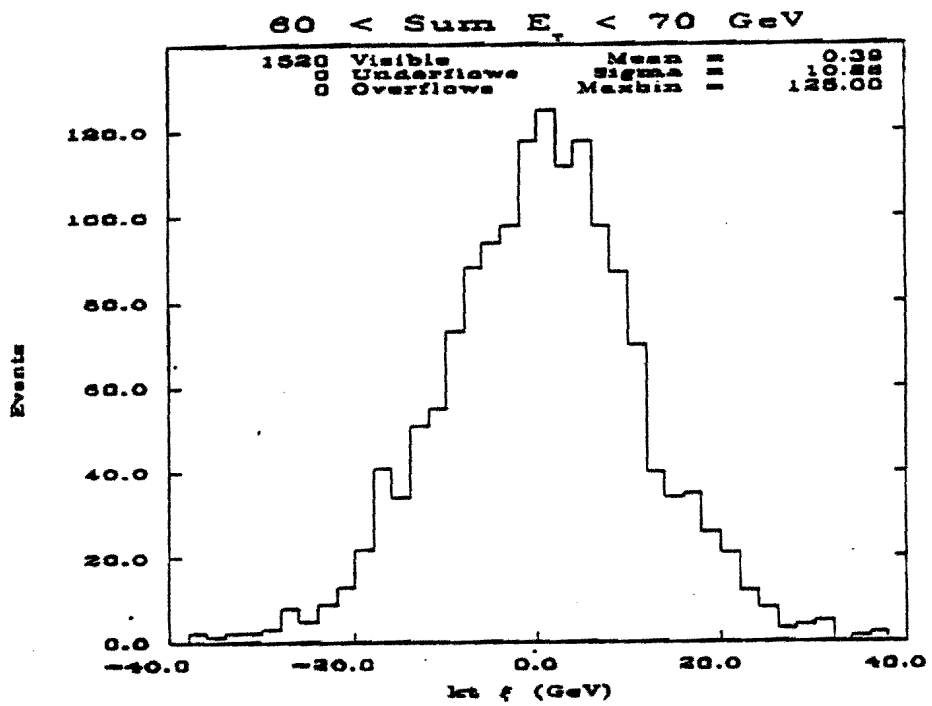

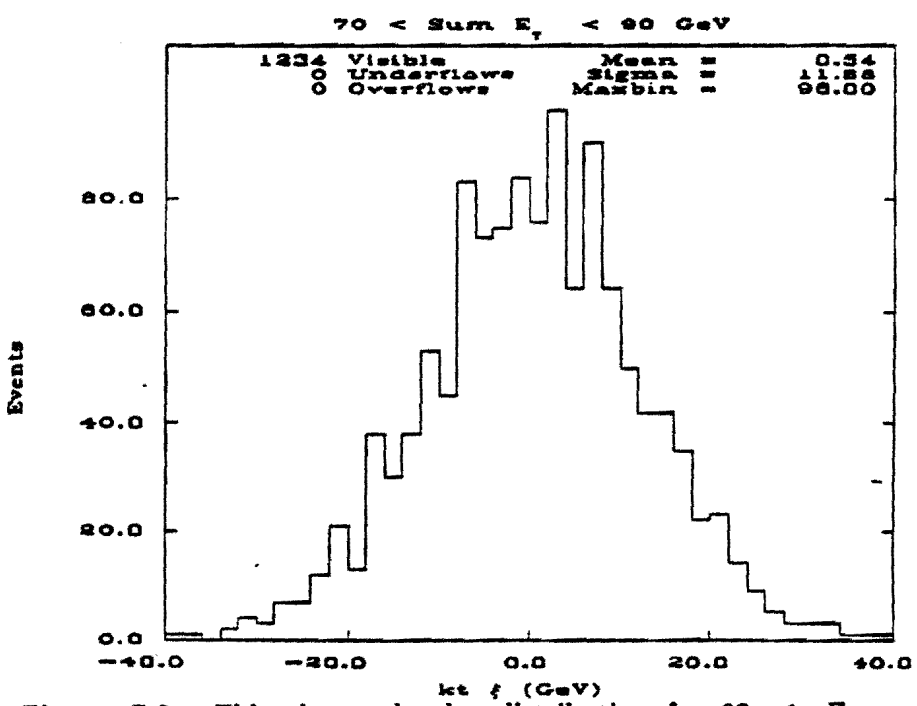

Figure C.3: This shows the k_{t_ℓ} distribution for $60 \leq E_{t_{sum}} \leq 70$ GeV and $70 \leq E_{t_{sum}} \leq 90$ GeV. It demonstrates the gaussian shapes and increase of width with energy.

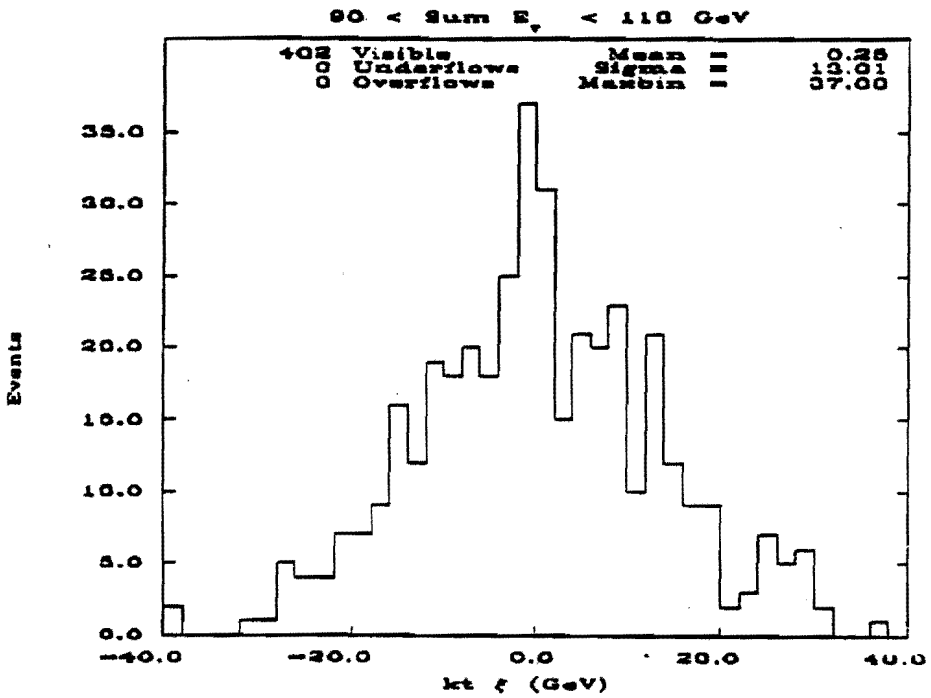

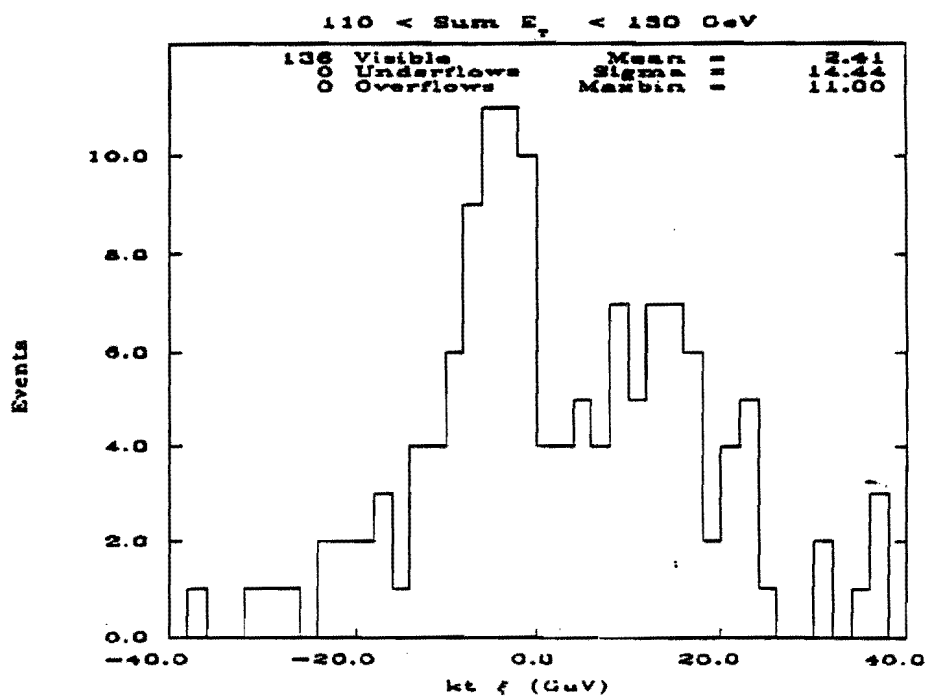

Figure C.4: This shows the k_{t_ξ} distribution for $90 \leq E_{t_{sum}} \leq 110$ GeV and $110 \leq E_{t_{sum}} \leq 130$ GeV. It demonstrates the gaussian shapes and increase of width with energy.

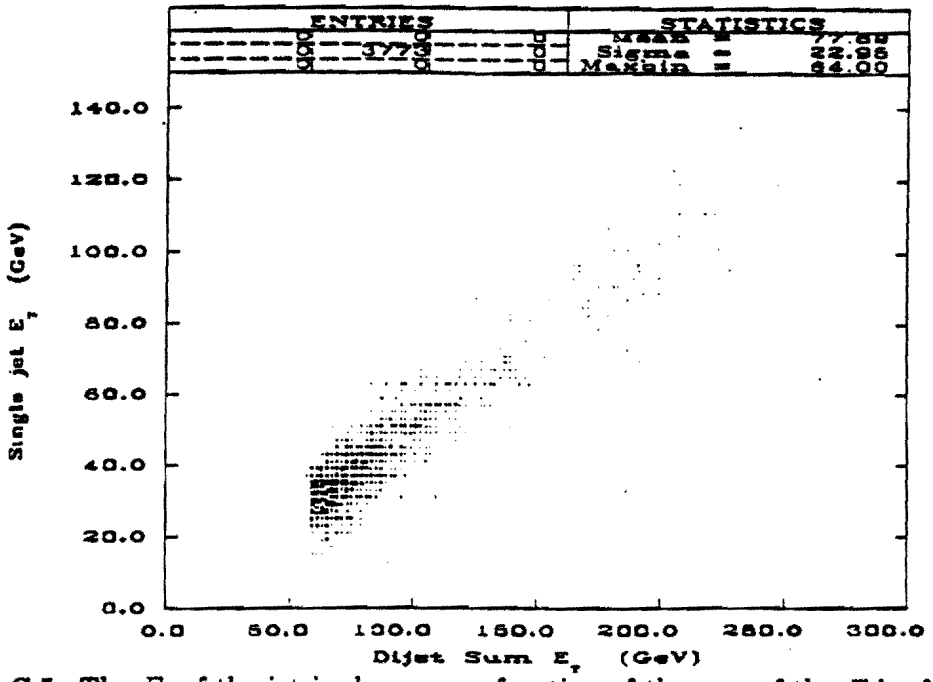

Figure C.5: The E_t of the jet is shown as a function of the sum of the E_t's of the two jets.

They also manifest themselves in other measurements of jet properties. By combining the information in these measurements, the jet energy resolution is extracted.

The causes of the dijet k_t are summarized in Table C.1. It can be seen that there is significant overlap in factors which contribute to each of the components. To consider their relations, one moves on to look at the quantities that can be measured. They are listed here:

1. **Shape of the k_{t_η} distribution**

   - The emission of gluons as well as adding or missing other particles will cause a broadening of this component's distribution.
   - The angular error in measuring the jet axis contributes to the spread in the distribution.
   - Small scale mapping corrections will add to the width of the distribution.

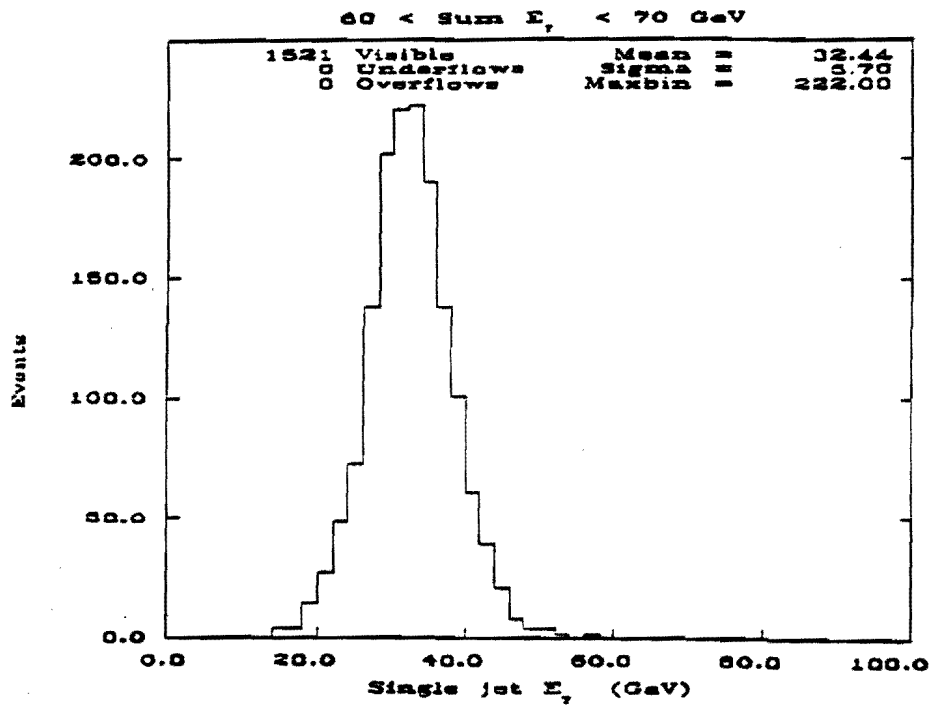

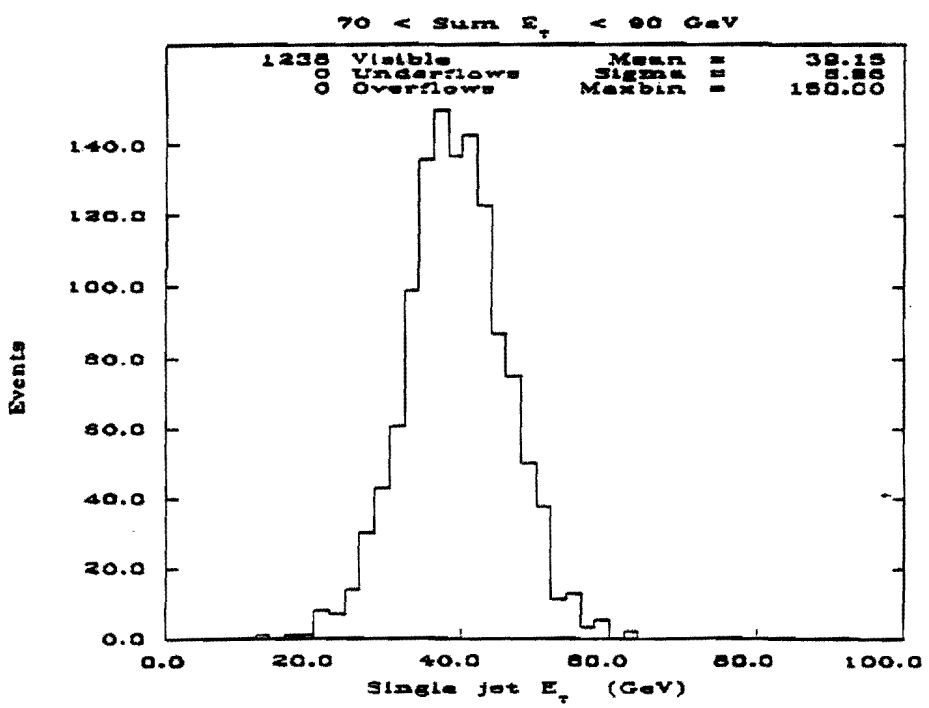

Figure C.6: The E_t distribution of the jet is shown for $60 \leq E_{t_{sum}} \leq 70$ GeV and $70 \leq E_{t_{sum}} \leq 90$ GeV.

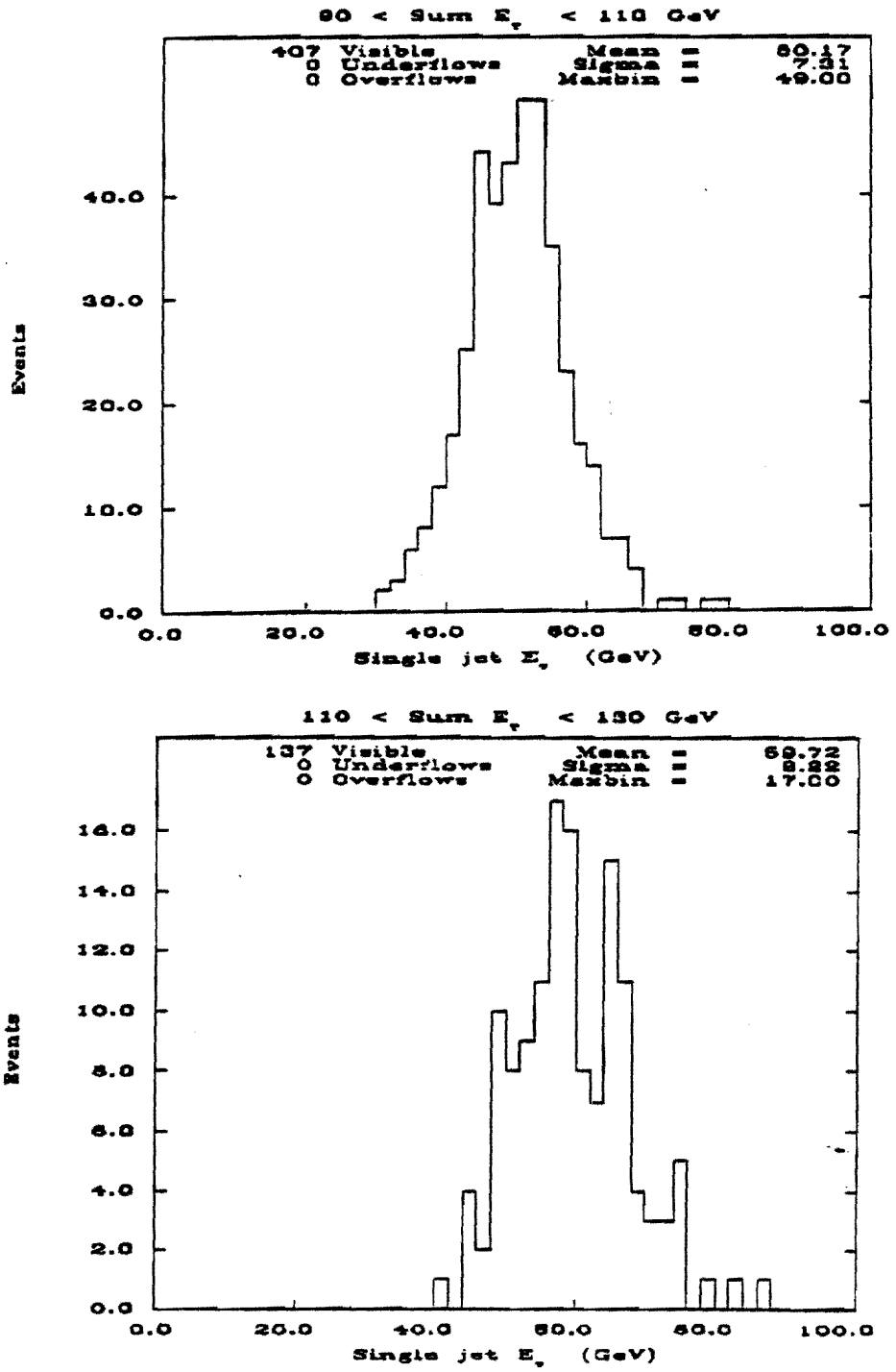

Figure C.7: The E_t distribution of the jet is shown for $90 \leq E_{t_{sum}} \leq 110$ GeV and $110 \leq E_{t_{sum}} \leq 130$ GeV.

Component	Sensitive to:
k_{t_ℓ}	Systematic offset in energy scale: Large scale mapping corrections Fluctuations in energy scale: energy resolution QCD gluon emission (other jets) Misassignment of particles to cluster; $\vec{B}$-field effects
k_{t_η}	QCD soft gluon emission and hard gluon emission (other jets) Jet angular resolution Misassignment of particles to cluster; $\vec{B}$-field effects Small scale mapping corrections

Table C.1: Sources of dijet k_t components

- Hard emission of gluons will increase the width of this component.

2. **Mean of the k_{t_ℓ} distribution** - Systematic offsets in the energy scale will cause a shift in the mean of the dijets. If one jet is tagged by being confined to a specific portion of the calorimeter, then shifts in the mean will imply differences in the absolute jet energy scale between the calorimeters containing the jets; however, if the jets are left untagged, differences in the energy scale would lead to non-gaussian distributions or a larger width.

3. **Shape of the k_{t_ℓ} distribution** -

   - Calorimeter energy resolution is related to that observed in a test beam; however, for jets, one has a collection of different particles that span a range of energies. The resolution of the jet is a convolution of the fragmentation properties of the jet and the response of the detector to the individual particles.
   - The effects that were described for the k_{t_η} distribution apply to this component as well, although they may differ in magnitude.

To summarize, the effects of energy resolution, angular error, mapping corrections, QCD (soft and hard gluons), particle misassignment, and magnetic field effects mix in the width measurement of k_{t_ℓ}. All but one of these factors contribute to the width of the k_{t_η} distribution. That lone effect is the energy resolution. If one can estimate how the pieces that go into the k_{t_η} width are related to those same pieces in the k_{t_ℓ} width, then the jet energy resolution can be extracted.

C.2 Central Detector Resolution Study

In this section, what is known of the causes of the dijet k_t and extraction of calorimeter resolution described. The selection of data for studying the central detector resolution is discussed. This is followed by a presentation of the results for dijet balancing.

C.2.1 Effective Resolution and Extraction of the Causes

There are a number of things one can learn from the data. These are:

1. **Jet p_t spectrum and Dijet η-ϕ distribution** - The jet p_t spectrum describes the rate dependence on energy. From Section 5.3 the rate is known to fall rapidly as a power law of energy; therefore, one can look at the population of jets in the calorimeter to see how uniform the response is. This is quite a sensitive test since the value of the exponent is around six, so that one percent variations in calorimeter mapping response correspond to ten percent changes in the rate. It is important to note that this argument is true only if the calorimeter under question was used in triggering. If one triggers on one calorimeter and looks at the distribution of

jets in another, then the η-ϕ distribution only tells if a second jet can be found. Only very extreme failures of the second calorimeter could lead to nonuniformities in its η-ϕ distribution. The population of jets is uniform in the η-ϕ plot shown in Section 5.3. The mapping corrections can be ignored to the level of about a percent in the energy resolution – since one observes widths $\geq$ 12%, this is negligible.

2. **Calorimeter versus tracking determination of the jet axis** - The tracking chamber can be used to determine the jet axis; however, there are errors in that method due to the inability to observe tracks for neutral particles. Yet this can provide a limit on the error in determining the jet axis. The error in the determination of the jet axis is small relative to the width of the k_{t_η} distribution. The widths of the distributions are of the order of 7 or 8 GeV (Figures C.9 and C.10). Determination of the error in measurement of the jet axis was obtained by comparing the calorimeter clustering jet axis with the axis determined from tracking [36]. The RMS of the mismatch was three degrees. This kind of error on a 50 GeV jet gives only a 2.5 GeV contribution to the width of k_{t_η}. It is a relatively small effect.

This leaves hard and soft gluon emission, misassignment of particles, and magnetic field effects. The hard gluons can be removed from consideration by putting a cut on the third jet energy. This leaves only soft contributions to be considered. The question is whether there are identical contributions in both components of k_t. If the soft effects are isotropic in azimuth, then the contributions are the same; furthermore, if this is so, then one can simply remove the soft contribution by subtracting σ_ξ and σ_η in quadrature.

The validity of the assumption can be checked by looking at k_{t_η} as a function of energy and by noting the following:

- **the energies of the jets** - The energies of the jets correspond to the time scale at which the hard scattering took place. One expects the soft particle effects to be weakly dependent on the hard scattering, since the hard interaction is a phenomenon that occurs on a short time scale relative to the soft particle effects. In the initial state, the soft gluon emission cannot communicate with the hard scattering in lowest order. In the final state, the soft gluons are emitted along the jet axes and are not distinguishable from the jets.

- **the fragmentation function** - The magnetic field and particle misassignment effects will vary with the fragmentation function of the jets. That function varies logarithmically with energy [37]. Therefore, with a hard cut on the third jet, one expects a weak dependence of k_{t_η} on energy. The value of the response will depend on how hard one cuts on the third jet since that limits the soft activity.

The values of the widths of the distributions of the k_{t_ξ} and k_{t_η} distributions (Figures C.3, C.4, Figures C.9, and C.10), σ_ξ and σ_η, are plotted as a function of $\sqrt{E_t}$ where the E_t is taken as the average jet transverse energy (Figures C.6 and C.7). These plots are shown in Figures 6.4 and 6.5. One observes that σ_ξ increases linearly with $\sqrt{E_t}$ and σ_η remains constant. The rise of σ_ξ was expected from calorimeter considerations. The flat response of σ_η is consistent with the picture that it is related to soft particle effects that have logarithmic jet E_t dependence. This is investigated further by examining the relationships shown in Figures 6.4 and 6.5 for various cuts on the third jet.

C.2.2 Dijet k_t Dependence on the Presence of Third Jets

The cut on the third jet, $E_{t_{min}}$, was varied from 5 to 15 GeV in 2.5 GeV steps so that the influence of third jets on the dijet k_t could be investigated. Equations C.69 and C.70 were derived under the assumption that $\delta\phi = \pi - \phi_{jj}$ be small; therefore, since k_{t_ξ} does not depend on this quantity, a cut was placed such that $|\delta\phi_{jj}| \leq 20°$. Also, since k_{t_η} has an explicit dependence on $\delta\phi_{jj}$, no such cut was used. The cuts for the various samples of data are outlined in Table C.2.

The analysis was repeated with different cuts on the minimum jet energy. Points were added for lower energy by using samples of data with total energies in the two jets between 40 and 60 GeV. These were selected from the hardware triggers that required a total transverse energy in the central detector above 20 or 30 GeV. The results for the plots of σ_ξ, σ_η, and $\sigma' \equiv \sqrt{\sigma_\xi^2 - \sigma_\eta^2}$ are shown in Figures C.11a to C.11c. Each is plotted against $\sqrt{E_t}$ for cuts on the third cluster of $E_{t_{min}}$ = 5.0, 7.5, 10.0, 12.5, and 15.0 GeV. There are several striking features:

- The slopes of the σ_ξ lines increase with increasing $E_{t_{min}}$. These slopes are shown for each of the values of $E_{t_{min}}$ in the first column of Table C.3. They are expressed in terms of the value of A that these slopes imply. (A is defined in Equation C.74.)

- For all cuts on $E_{t_{min}}$, σ_η has a flat dependence on $\sqrt{E_t}$. The magnitude of σ_η increases with the cut on $E_{t_{min}}$. This is what one would expect – the increasing activity in the third jet would add to the overall level of the σ_η.

- Finally, when the subtraction in quadrature is performed, the response curves for the various cuts on $E_{t_{min}}$ lie on top of one another. This indicates that the

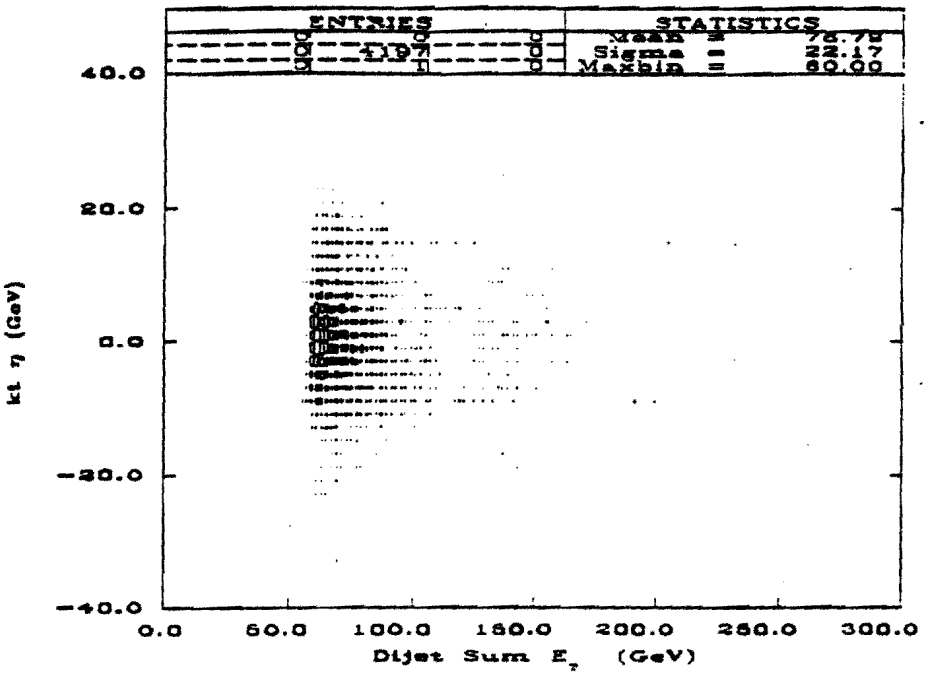

Figure C.8: The dijet k_t component sensitive to QCD and magnetic field effects is plotted as a function of the sum of the E_t in the two jets.

factorization of soft effects from the k_{t_ℓ} component has been successful. The slopes for each value of $E_{t_{min}}$ are listed in column 1 of Table C.4. There is a systematic change in slope, indicating the factorization is not precise; however, the average may be used if one includes this change as a systematic error in the determination of the jet energy resolution.

C.2.2.1 Effects of the Cluster Cone Size

The analysis was repeated twice again for a fixed $E_{t_{min}}$ of 10 GeV, but for the other conditions on the clustering algorithm. The plots of each of the components for these cases are shown in Figures C.12 and C.13. Table C.3 shows the values of A if one includes the effects of soft particle effects as well as calorimeter resolution. This gives the overall "effective" jet resolution. The average slopes of the σ' lines have been computed in order to get numbers that relate more closely to the test beam data. The results are shown in

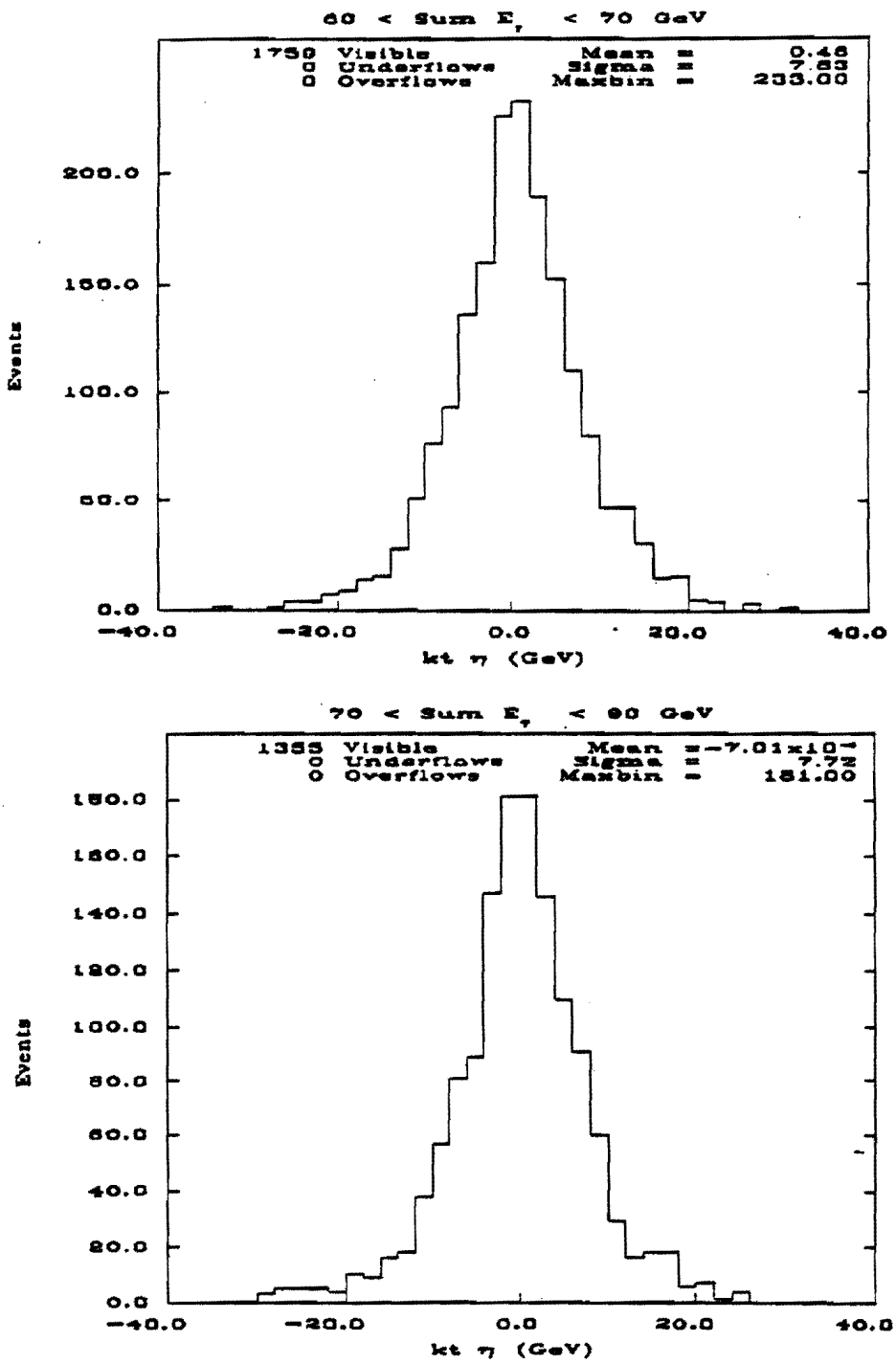

Figure C.9: Distributions of k_{t_η} are shown for $60 \leq E_{t_{sum}} \leq 70$ GeV and $70 \leq E_{t_{sum}} \leq 90$ GeV. Note that the widths of the distributions are constant as the $E_{t_{sum}}$ rises.

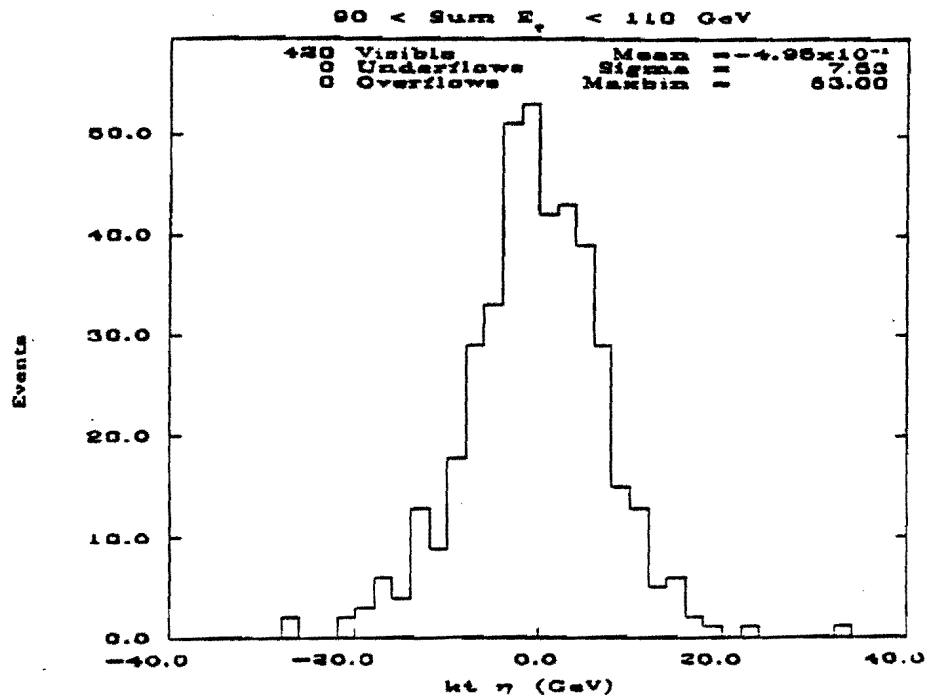

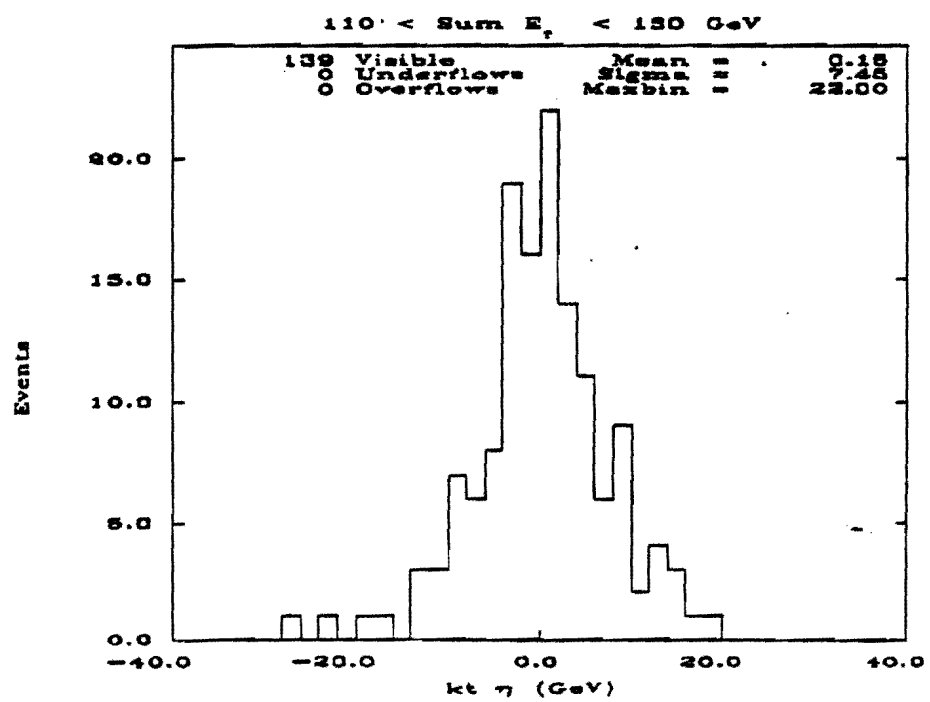

Figure C.10: Distributions of k_{t_η} are shown for $90 \leq E_{t_{sum}} \leq 110$ GeV and $110 \leq E_{t_{sum}} \leq 130$ GeV. Note that the widths of the distributions are constant as the $E_{t_{sum}}$ rises.

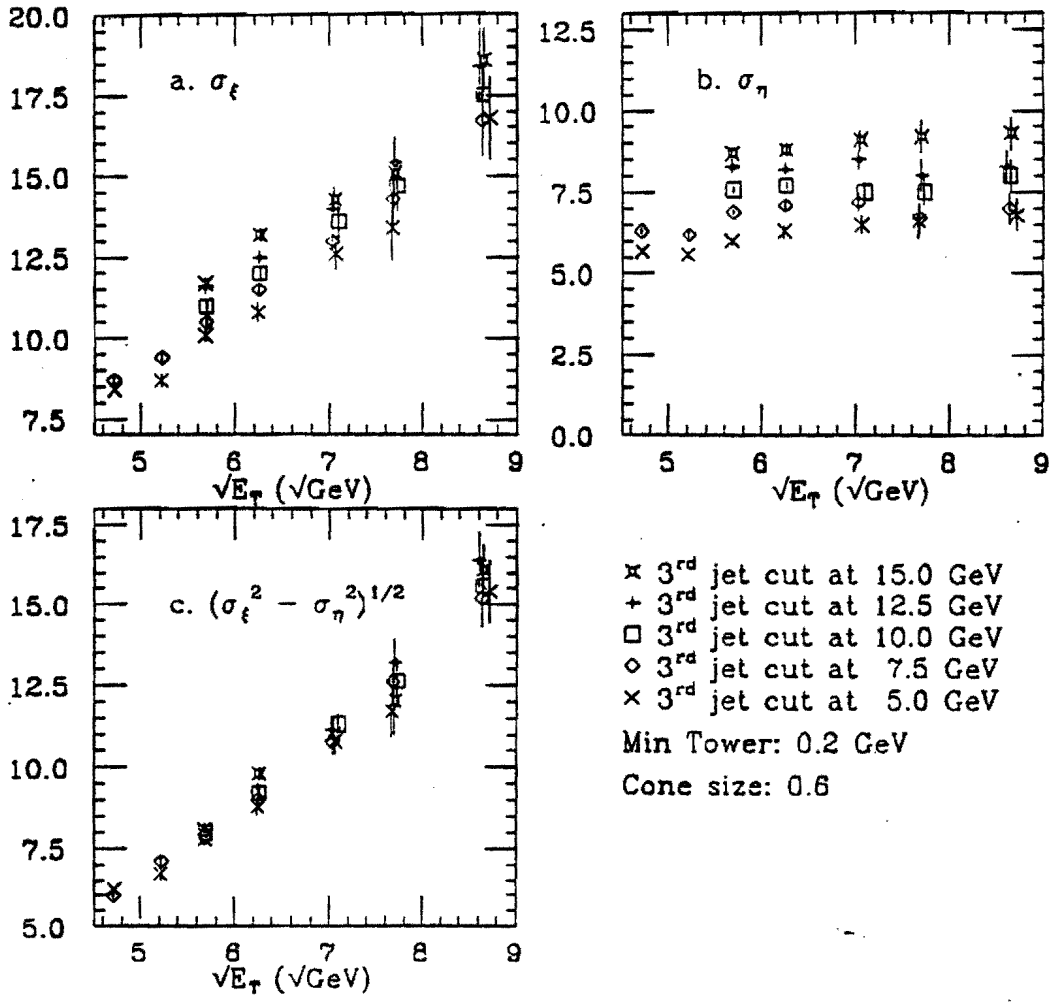

Figure C.11: a: σ_ξ b: σ_η c: σ' plotted as functions of $E_t^{\frac{1}{2}}$ for various $E_{t_{min}}$. The cluster cone size is 0.6 and the minimum tower energy is 0.2 GeV.

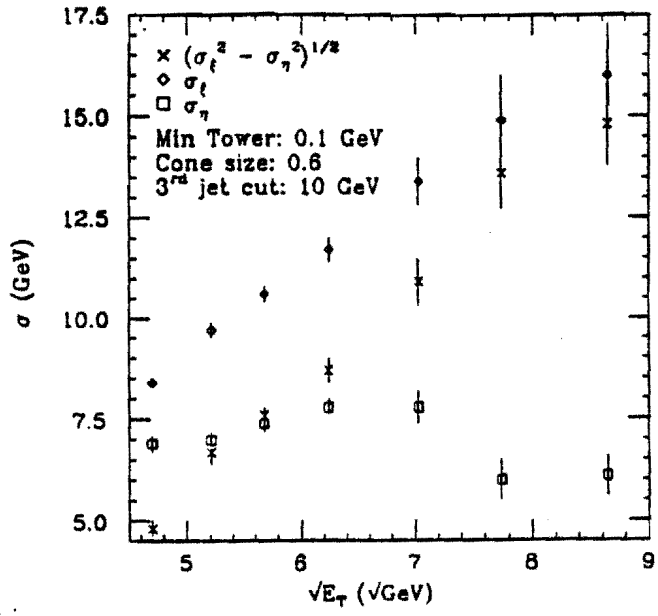

Figure C.12: This figure shows σ_ξ, σ_η, and σ' vs $E_t^{\frac{1}{2}}$ for a cone size of 0.6, minimum tower of 0.1 GeV, and third cluster cut of 10 GeV.

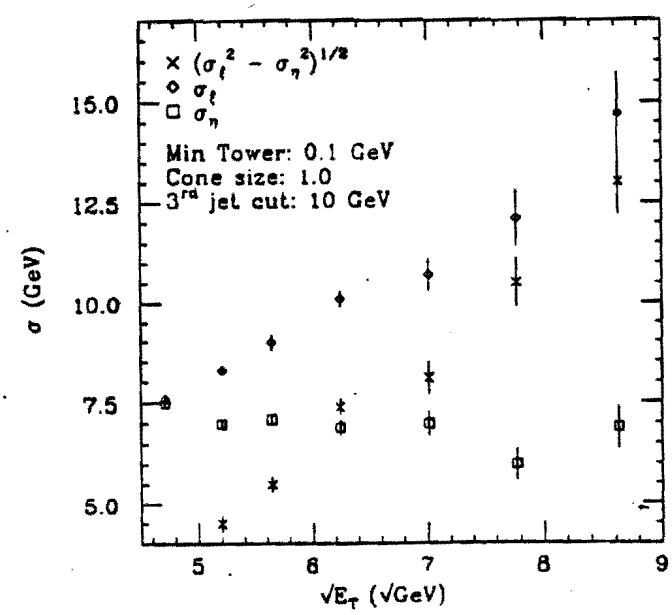

Figure C.13: This figure shows σ_ξ, σ_η, and σ' vs $E_t^{\frac{1}{2}}$ for a cone size of 1.0, minimum tower of 0.1 GeV, and third cluster cut of 10 GeV.

Cone Size	Min Tower (GeV)	$E_{t_{min}}$ (GeV)	$\lvert\delta\phi\rvert_{min}$ (degrees)
0.6	0.2	5.0	20
0.6	0.2	5.0	90
0.6	0.2	7.5	20
0.6	0.2	7.5	90
0.6	0.2	10.0	20
0.6	0.2	10.0	90
0.6	0.2	12.5	20
0.6	0.2	12.5	90
0.6	0.2	15.0	20
0.6	0.2	15.0	90
0.6	0.1	10.0	20
0.6	0.1	10.0	90
1.0	0.1	10.0	20
1.0	0.1	10.0	90

Table C.2: Cuts on the various samples of data

$E_{t_{min}}$ (GeV)	cone 0.6	Min Tower 0.2 GeV	cone 0.6	Min Tower 0.1 GeV	cone 1.0	Min Tower 0.1 GeV
5.0		1.25				
7.5		1.30				
10.0		1.37		1.32		1.12
12.5		1.44				-
15.0		1.47				

(Errors: $\sim \pm 0.05$, statistical)

Table C.3: Effective jet resolution, $\sigma_\xi / (2E_t)^{\frac{1}{2}}$ for various cuts on the third jet and various clustering algorithm parameters

$E_{t_{min}}$ (GeV)	cone 0.6	Min Tower 0.2 GeV	cone 0.6	Min Tower 0.1 GeV	cone 1.0	Min Tower 0.1 GeV
5.0		1.03				
7.5		1.05				
10.0		1.12		1.01		0.83
12.5		1.14				
15.0		1.12				
-	→ ave: 1.09					

Table C.4: Calorimeter resolution, $\sigma'/(2E_t)^{\frac{1}{2}}$ for various cuts on the third jet and for various clustering algorithm parameters.

Table C.4. These slopes are calculated by computing the average value at each energy and drawing a line to the origin, then averaging the results for all the points. There is a nonlinear component to the curve for the σ' plot. As described above, the nonlinear component will contribute a systematic error of $\pm 0.10\ GeV^{1/2}$ to the value of A.

A further estimate of the error on the values of A has been obtained by doing a linear extrapolation of the effective calorimeter resolution in Table C.3 to the expected value for $E_{t_{min}} = 0$ as a check on the subtraction technique. This extrapolation has also been conducted on the data that were analyzed with different clustering parameters. (In that case, one assumes the same linear dependence on $E_{t_{min}}$ for all clustering algorithms.) The results are summarized in Table C.5 and give an indication of the systematic error in the determination of the central jet energy resolution. The indication is that the larger clustering cone enhances the resolution of the dijets. One may worry that spurious particles are included, but studies of the event that underlies the hard scattering [38] indicate that even with a large cone size, the increase in true jet energy outweighs the random collection of background particles.

The conclusion, then, is that for the cone size of 1.0, the resolution of the central

Cluster Parameters		σ^j slope	σ_ξ slope for $E_{t_{min}} = 0$
cone:	0.6	1.09	1.13
min tow:	0.2 GeV		
cone:	0.6	1.01	1.08
min tow:	0.1 GeV		
cone:	1.0	0.83	0.88
min tow:	0.1 GeV		

Table C.5: The value of A is shown for two estimates of the quantity: direct removal of the soft component and extrapolation to no third jet

detector can be taken as $\sigma/E = (0.83 \pm 0.10\ GeV^{1/2})/\sqrt{E}$. This value is useful when one is just using the calorimeter resolution and considers the effects of other jets independently. If one simply wishes to express the combination of calorimeter and soft particle effects, then one may use the values of the effective jet resolution in Table C.3.

Appendix D

Energy Scale Probing

This appendix describes further application of the technique for measuring the dijet energy resolution and extracting the contribution due to calorimeter resolution. This method has been extended to allow for energy *scale* calibrations of the different calorimeter systems relative to the central calorimeter. This is shown schematically in Figure D.1. The cross-calibration of different calorimeter systems is accomplished by examining the dijet k_t when one jet, called a *trigger jet*, is well-contained in the central detector, and the other, called a *probe jet* is well-contained in another calorimeter section. One can also examine the response of areas of CDF where different calorimeter systems meet by requiring that the probe jet be in such boundary regions.

The appendix begins with a probe of the boundary region at $\theta = 90°$. Then, the plug and forward detector analysis is detailed. The work on the gas calorimetry was done at a point in the analysis when the picture concerning the calibration of those detectors was confused and before new test beam information became available. The conclusions of this study were later confirmed by the test beam measurements, systematic Monte Carlo

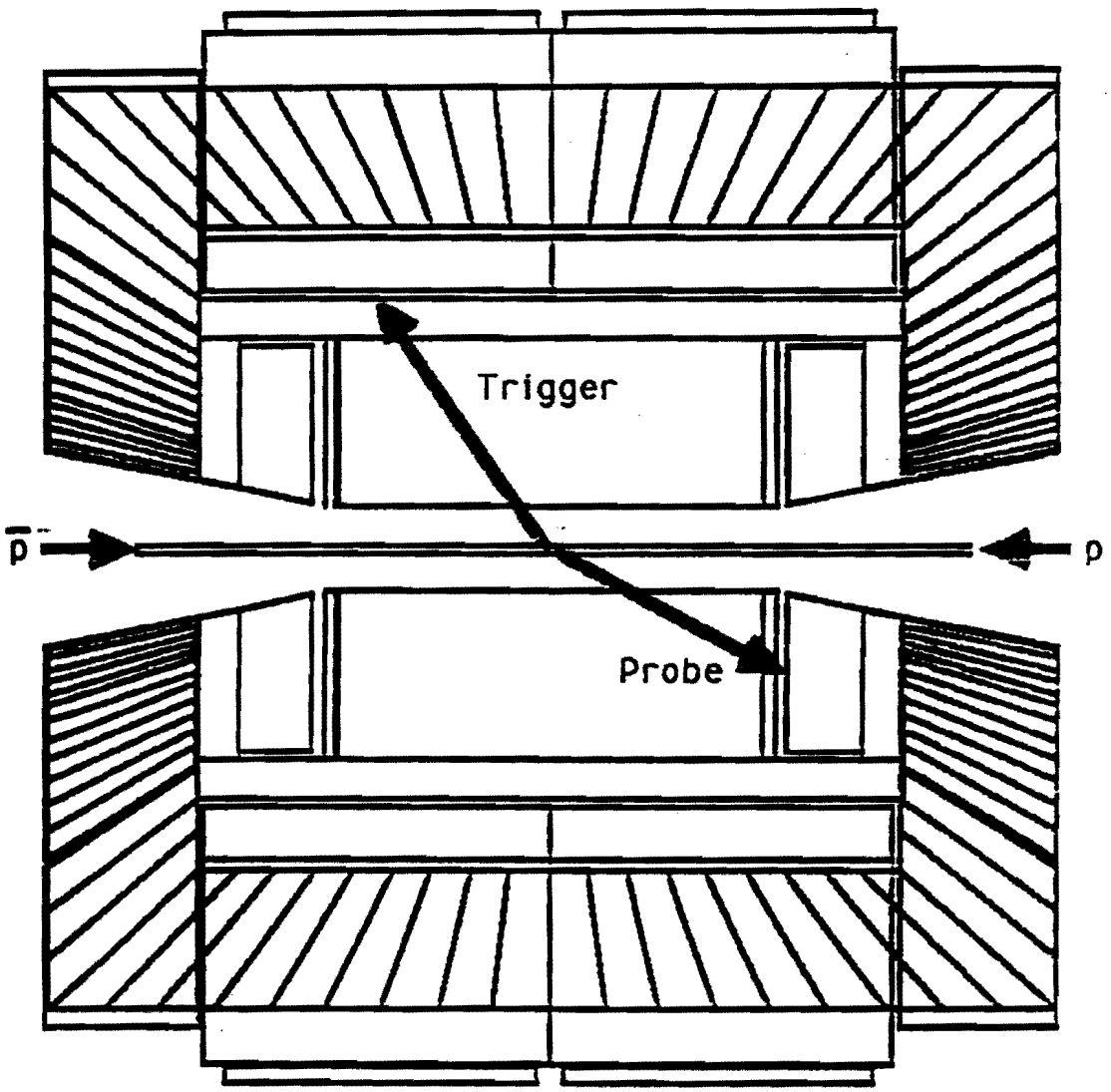

Figure D.1: Schematic view of two jets. The jets are shown in a slice of azimuth. One jet, the trigger jet, is confined to the central detector. The other jet, the probe jet, is used to cross calibrate the different parts of CDF calorimetry. It may be placed in any calorimeter or boundary region to probe the behavior of that portion of the calorimeter.

	Probe in 90°	Probe not in 90° boundary
$\bar{x}$ (GeV)	-3.1 ± 1.4	-0.4 ± 0.3
σ_ξ (GeV)	12.7 ± 0.7	12.0 ± 0.2
$\frac{\sigma_\xi}{\sqrt{E_t}}(GeV^{1/2})$	1.35 ± 0.05	1.41 ± 0.05

Table D.1: The probe jets are compared for $70 \leq E_{t_{sum}} \leq 90\ GeV$

study relating the single particle response to the jet energy scale, and debugging of gas monitoring systems and calibration constants. This technique is valuable in determining the overall performance of the detectors for a given data sample.

D.1 Investigation of the $\theta = 90^o$ Region

A portion of the dijet sample was selected such that one of the two jets in the event had its axis within 0.1 units of pseudorapidity relative to the detector boundary at $\theta = 90^o$. The pseudorapidity difference was calculated for each event so that the effect of the movement of the vertex could be taken into account. The pseudorapidity of the physical crack was calculated and compared to the pseudorapidity of the jet axis. No correction was made for movement of the jet axis by the effects of the crack. Monte Carlo calculations [39] indicate that such effects are small and that the jet axis position resolution is 0.05 units of pseudorapidity .

The distribution in σ_ξ is shown in Figure D.2 for the difference between the trigger and probe jet E_t values. This may be compared to the analogous measurement in Figure C.11c. In both cases, the clustering algorithm was executed with a cone size of 0.6 and a single tower threshold of 0.2 GeV. The cut on the third jet was 10 GeV.

Table D.1 shows a comparison of the mean, sigma and resolution (without soft particle

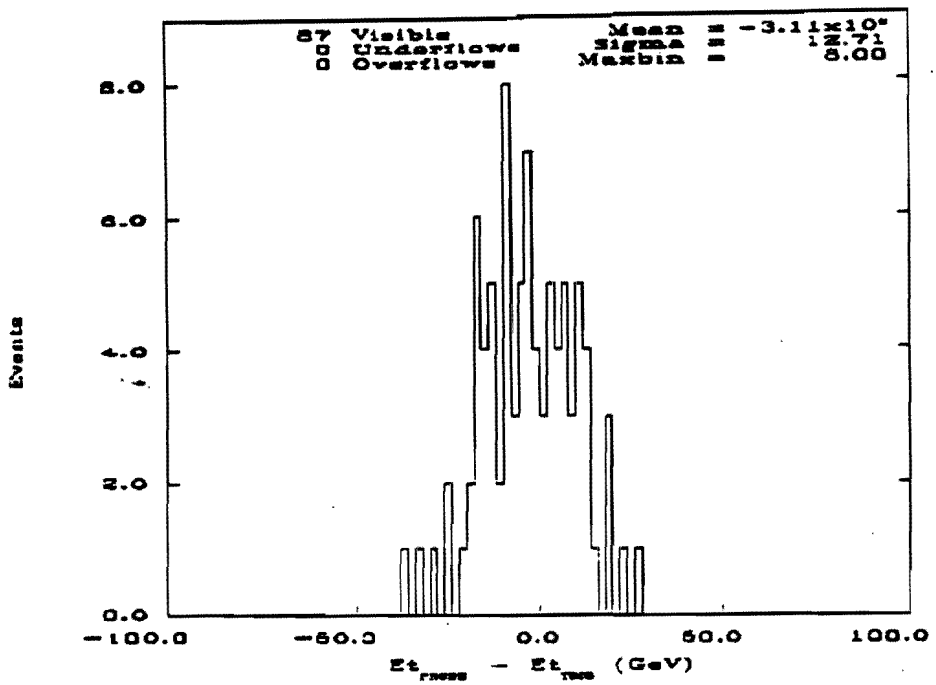

Figure D.2: This figure shows σ_{ξ} for jets probing the 90 degree crack

effects subtracted). It appears that there is some degradation of the energy and the resolution of the probe jet, but the statistical significance is not great. The trigger jet has an average energy of 40 GeV, so the 3 GeV shift implies a ~7 % shift in the energy. Since the jet spectrum falls as $\sim E_t^{-6}$, the shift in energy corresponds to about a 30 % change in rate, consistent with observations made in the single jet inclusive analysis [16].

D.2 Probing Gas Calorimetry

This section describes the results of applying the methods described thus far to probing the energy scale and resolution of the gas calorimetry. This is a difficult task since the hardware trigger was only sensitive in the central detector. This causes a strong bias in the data that will be described. Avoiding the bias limits the statistics; however, with the limited statistics, the analysis will be carried out to determine if there are shifts in the gas calorimeters relative to the central detector and an estimate of the energy resolution

will be made. After this estimate is made, the resolution will be investigated for different choices of relative electromagnetic and hadronic energy scales.

D.2.1 The Data Sample

The offline treatment of the data sample used in this study differs from that described for the central detector analysis. Because the algorithm for removing neutron-induced clusters was not ready at the time of this analysis, the neutron sensitivity was not explicitly removed; however, distributions of the electromagnetic fractions of the clusters indicate no enhancement at low or high values. (See Section 5.2.2 for a description of neutron sensitivity.) This is due to the fact that a transverse energy cut cut of 10 GeV was placed on clusters before they could be considered as jets. The population of neutron-induced clusters above this cut is negligible [21]; however, the clustering algorithm could have contaminated the clusters with neutrons. This is because the algorithm [40] used was different from the one used in the data samples described thus far. It did not use an explicit cone to form the cluster. Instead, it joined together energy clusters that were within a distance of 0.7 units in η-ϕ space. This means that some neutrons could be absorbed into jets during reconstruction. The effect is not large since clusters using this algorithm do not give results that are different [40] from the algorithm described in Section 5.2.3.

D.2.2 Distributions in the Gas Calorimetry

A number of distributions are presented here for the gas calorimetry. The calorimeters are all compared to the central detector. They have been divided into four regions:

forward west, plug west, forward east, and plug east. The jets must be further than 0.2 units of pseudorapidity from a boundary. The plots are discussed here:

1. **η-ϕ distribution of jet clusters** - Figures D.3- D.6 show the distributions of the trigger and probe jet clusters in η-ϕ space for the four regions of gas calorimetry being probed. The average pseudorapidity $|\eta| = 1.5$ in the endplugs and $|\eta| = 2.7$ in the forward detectors. The value of η is measured relative to the event vertex. It can be seen that the distribution is uniform in all portions of the detector. In this case the η-ϕ plot does not provide a sensitive test of the uniformity of calorimeter response. The jet in the gas was not used in triggering. It is accompanying the jet in the central; therefore, a lack of uniformity would indicate only gross failures in the detector. The number of jets does diminish as one goes more forward, but events in the forward calorimetry must have a large boost and a high mass, so one expects some smooth reduction in rate.

2. **Probe cluster electromagnetic fractions** - Figures D.7- D.8 show the electromagnetic energy fractions for the plug and forward calorimeters respectively. The plug has a average of about 51 % whereas the forward is only 36 %. These are lower than the 61 % observed in the trigger jets of the central detector. Since there is about the same amount of material in the various calorimeters, one does not expect the electromagnetic fractions to vary by this much. This is investigated in Section D.2.4 below.

3. σ_{ξ} vs $E_{t_{sum}}$ - Figures D.9- D.10 show the difference in trigger and probe E_t values plotted as a function of the total transverse energy in the trigger and probe

	$90 \leq E_{t_{sum}} \leq 110$		
Detector	Events	k_{t_ℓ}	σ_ξ
Plug East	224	1.9 ± 1.0	14.3 ± 0.7
Plug West	163	-5.8 ± 1.0	12.9 ± 0.7
Forward East	29	12.6 ± 2.9	15.4 ± 2.0
Forward West	21	9.4 ± 3.9	18.1 ± 2.8
	$110 \leq E_{t_{sum}} \leq 130$		
Detector	Events	k_{t_ℓ}	σ_ξ
Plug East	100	-0.2 ± 1.5	15.7 ± 1.1
Plug West	44	-1.1 ± 2.2	14.9 ± 1.6

Table D.2: The σ_ξ values for various $E_{t_{sum}}$

clusters. Theses plots show the bias due to requiring that the trigger jet be above 30 GeV. It is characterized by the diagonal boundary past which the points may not lie. From these figures, it becomes clear that the distribution of k_{t_ℓ} may be examined only for events with an $E_{t_{sum}}$ above 90 GeV.

4. σ_ξ in $E_{t_{sum}}$ bins - Figures D.11- D.12 show the distribution in σ_ξ for $90 \leq E_{t_{sum}} \leq 110\ GeV$. The values of the means and widths of the distributions are in Table D.2. The means and widths of the distribution of the endplug-central events with $110 \leq E_{t_{sum}} \leq 130\ GeV$ have been placed in the table as well. It can be seen that the west end plug appears to have quite a significant shift in energy relative to the central. The East forward detector seems to have quite a shift, although the statistics are quite limited. The West forward detector is difficult to judge, but may be somewhat high as well.

The shifts observed in these data are due to a number of causes:

1. **Dead wire planes** - Some of the wire planes (3-4%) in the plug electromagnetic detector were not functional. Many of these were located at the longitudinal depth at which electromagnetic showers reach a maximum. This contributed to the reduction of the electromagnetic fraction of plug jets and to the shift in the energy scale relative to the central.

2. **Numerical electronics calibration error** - There was an error in the numerical value of the calibration constants for the electronics in the gas calorimeters. This number was very close to one, so its effect is small in most detectors. There were portions of the plug electromagnetic that had the energy scale changed by this error.

3. **Variation in the face response of the plug** - The construction of the plug chambers leads to 20% variations across the face of the detectors [19]. This tends to cause a deterioration of the jet resolution.

4. **Differences in coupling fragmentation to single particle response** - The fragmentation of jets in the gas calorimeters has not been measured. In addition, the low energy response of particles is unknown; however, because of the effect of $\sin\theta$, the transverse energies translate to energies that are three to ten times larger than those of the particles in the central detector. As a result, the effect of the low energy response may be less important in the gas calorimeters than in the central detector. Consequently, the relationship between the absolute energy scale of the jet and the energy measured in the detector is different for the gas calorimeters. One expects the uncorrected gas calorimeter jet E_t's to show a systematic

imbalance with respect to the uncorrected central jet E_t's.

5. **Control of the Gas Gain** - Techniques for maintaining the gas gain calibration for the duration of the running period were not fully established and much work was being done to debug the system after the run was done. The consequence of this is that the means of the σ_ξ distributions for central-gas dijet balancing can wander, producing a composite distribution with a larger width. One sees that this distribution provides a check on maintenance of the calibration and gives a numerical value of the effective resolution for these detectors.

These effects are being studied for the data in the 1988 collider run. The technique of dijet balancing is the benchmark test for understanding if the various components that go into a jet energy scale calibration have been evaluated correctly.

D.2.3 Extraction of Gas Calorimeter Resolutions

The goal here is to extract the resolution of the gas calorimetry, A_2. Equation C.78 gives an expression containing A_2. This can be solved for A_2:

$$A_2 = \sqrt{\frac{(\sigma')^2 / E_t - A_1^2}{\langle \sin\theta_2 \rangle}}. \qquad (D.81)$$

There are a number of assumptions:

1. The energy of the central jet in the $E_{t_{sum}}$ bin is taken from Figure C.5.

2. To calculate σ', the contribution of the soft effects is assumed to be the 7.6 GeV measured in the central detector. (See Figure C.11b.) There is concern that more forward jets may have significant beam-jet contamination, but that systematic error is probably insignificant in light of the poor statistics.

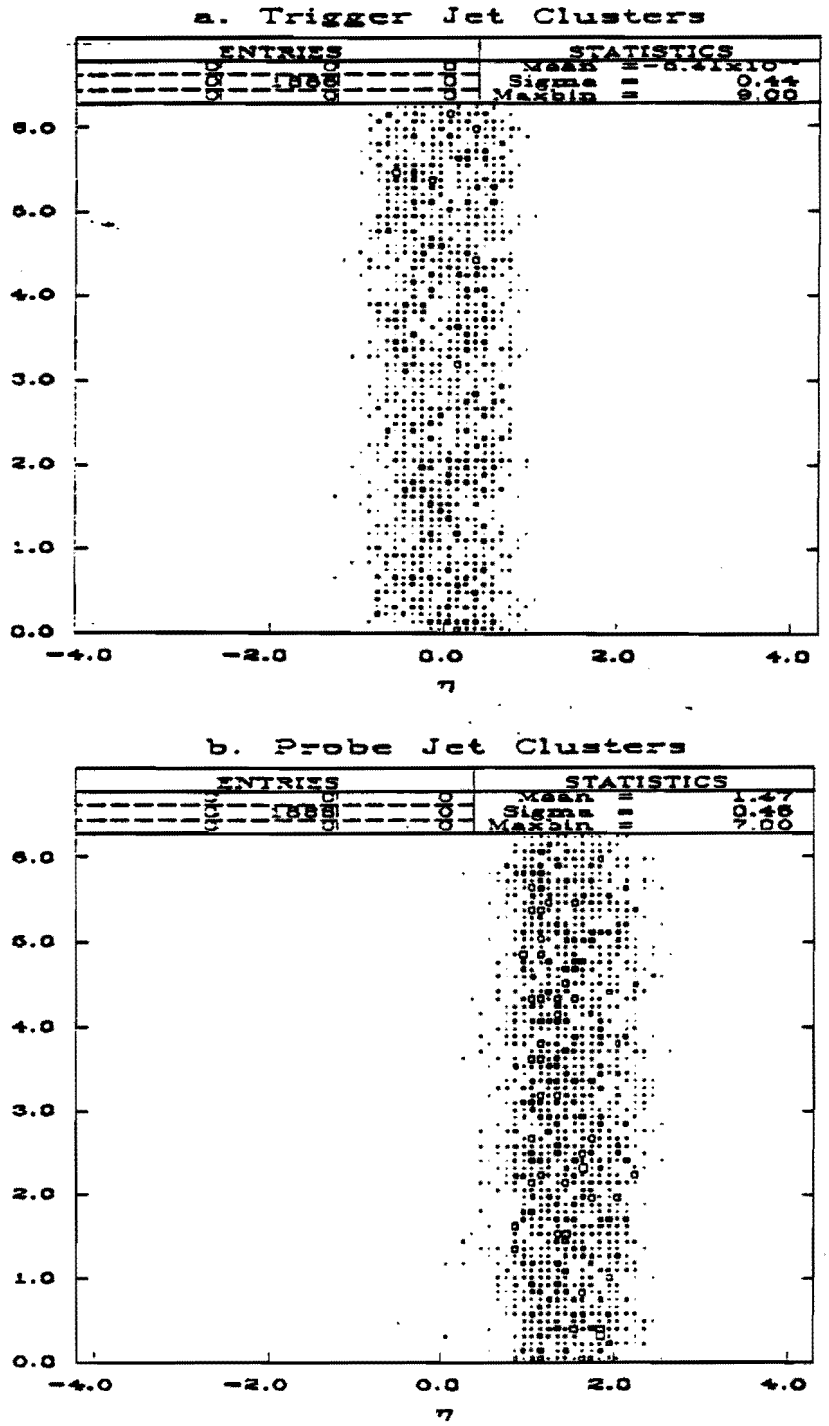

Figure D.3: a: Central and b: East Plug η-ϕ distribution of jets

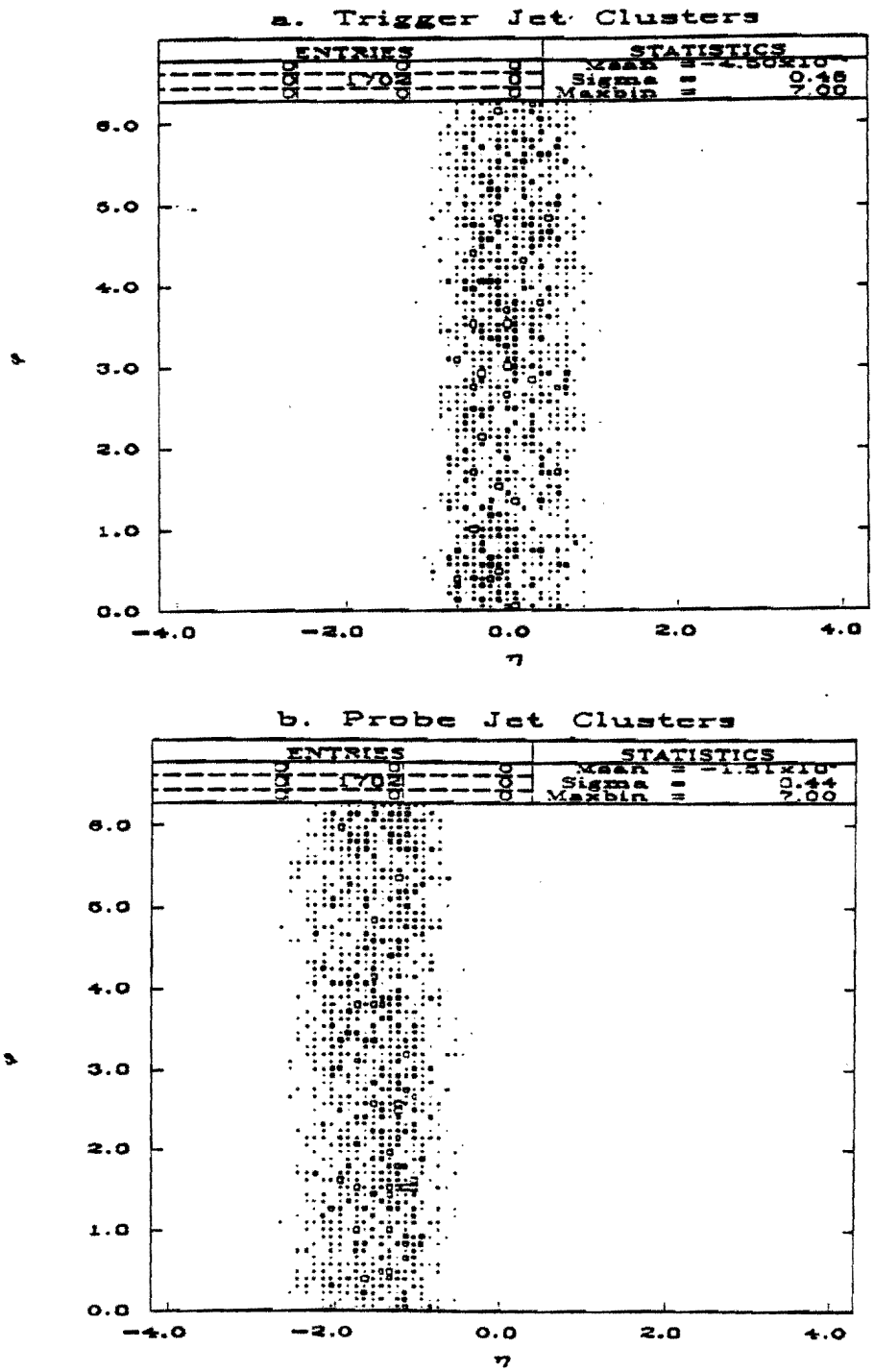

Figure D.4: a: Central and b: West Plug η-ϕ distribution of jets

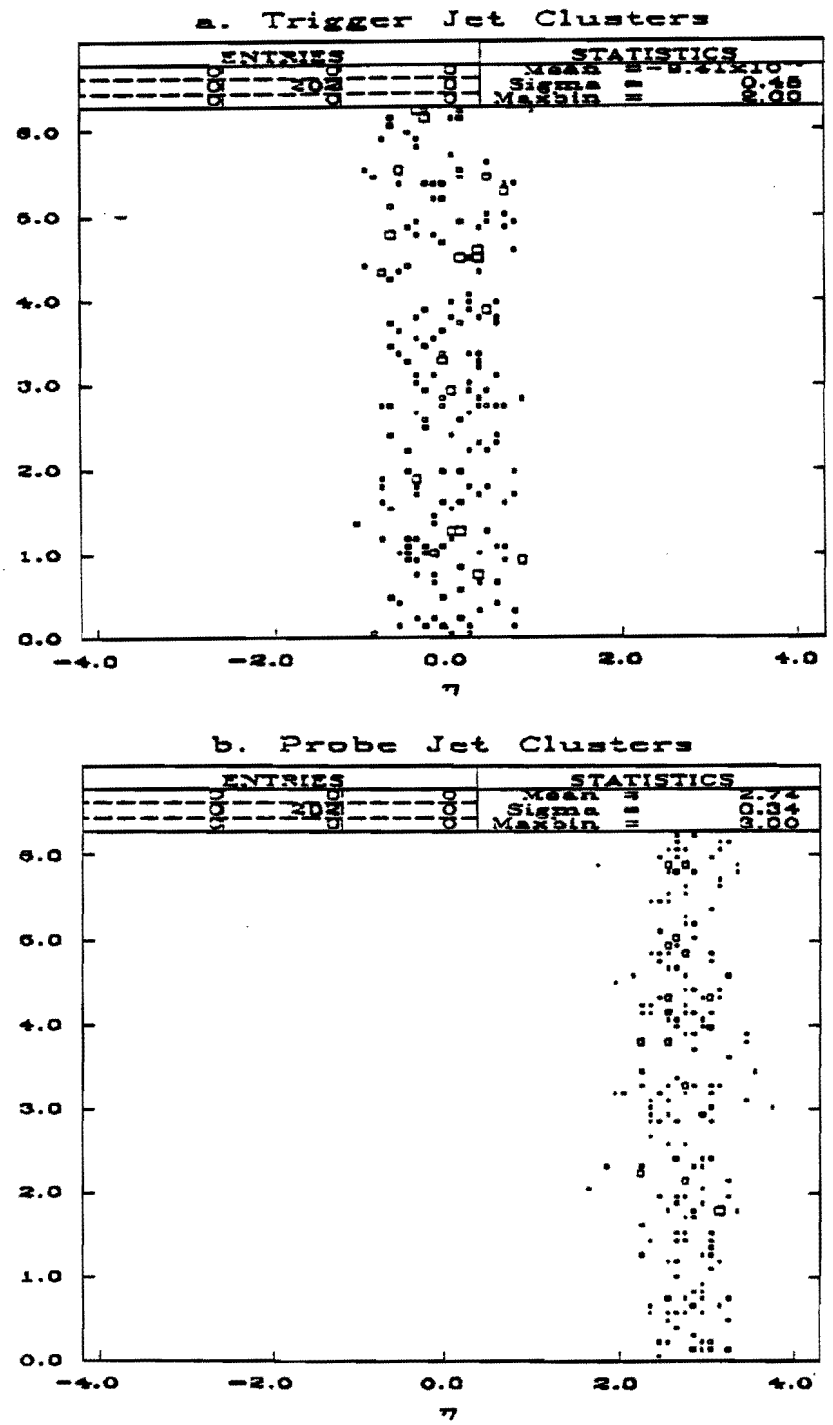

Figure D.5: a: Central and b: East Forward η-ϕ distribution of jets

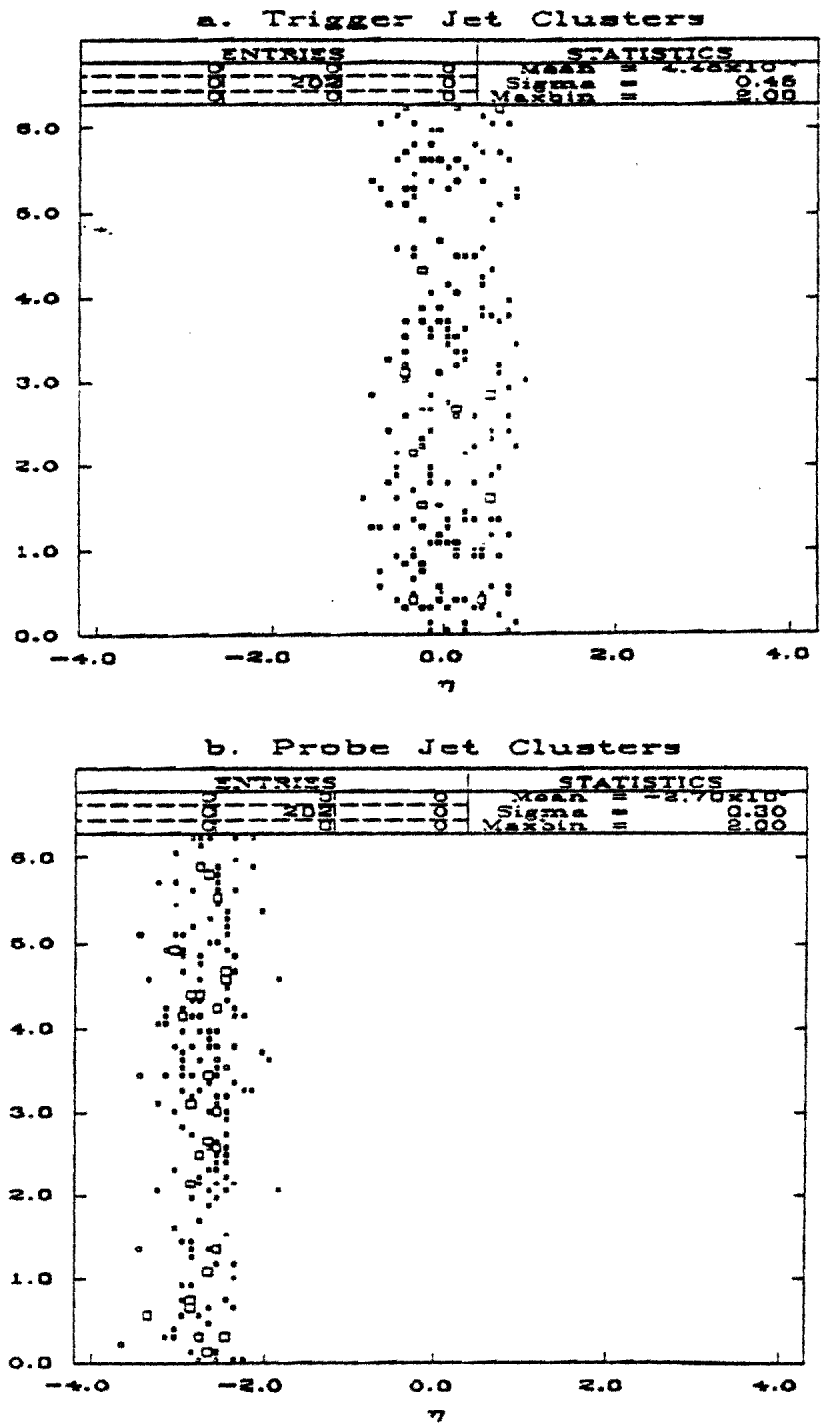

Figure D.6: a: Central and b: West Forward η-ϕ distribution of jets

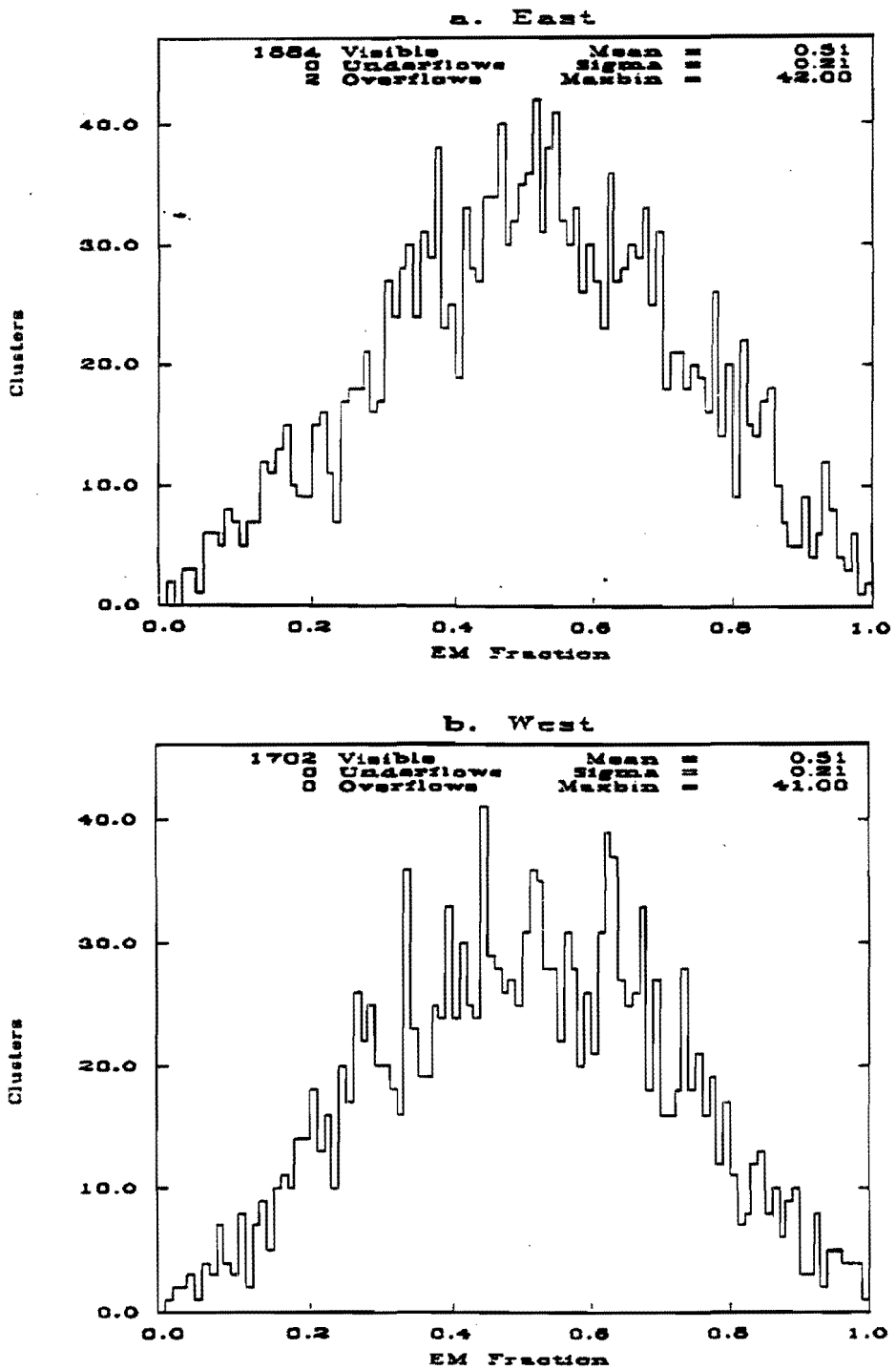

Figure D.7: a: East and b: West plug Cluster Electromagnetic fractions

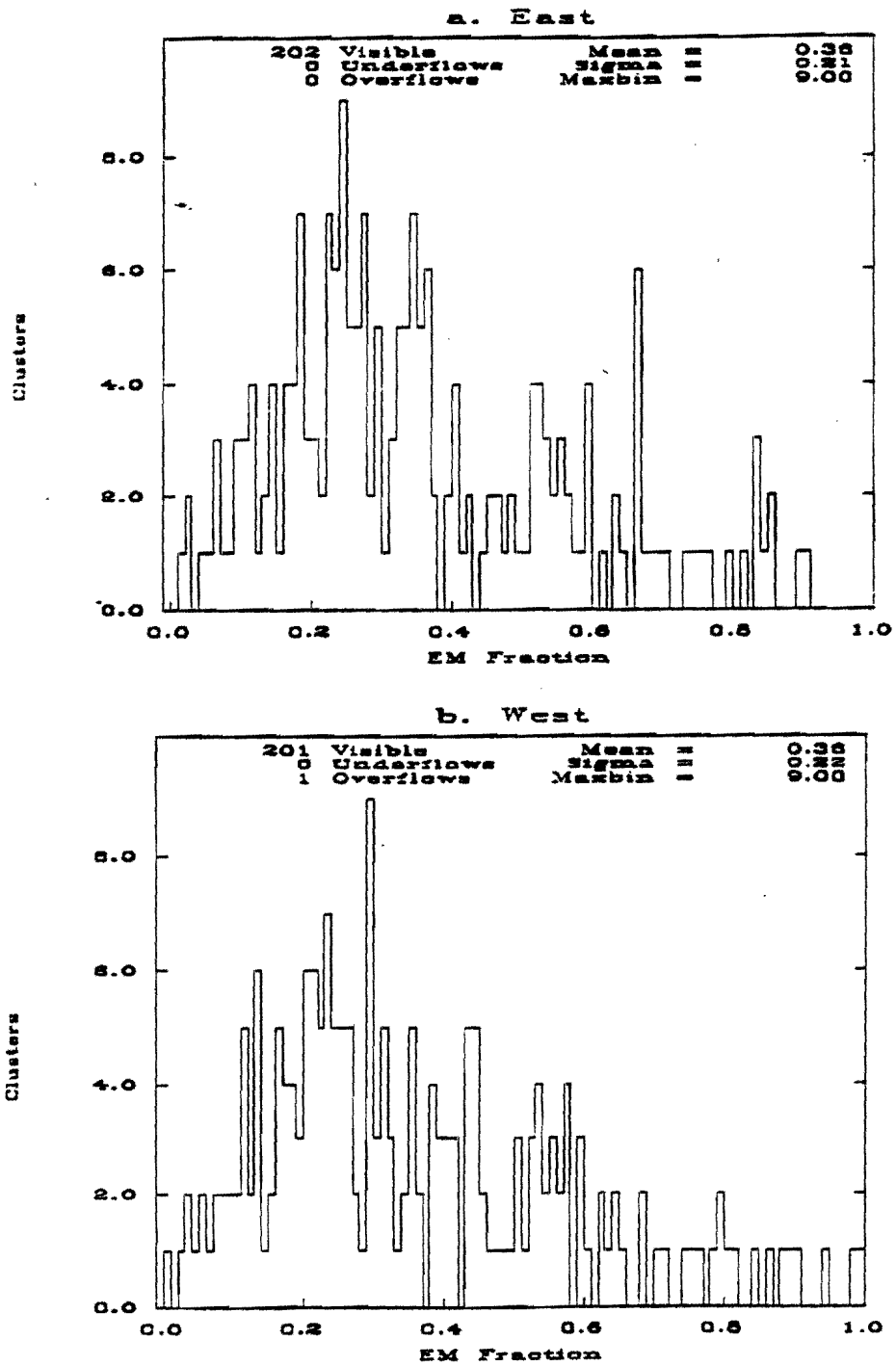

Figure D.8: a: East and b: West Forward Cluster Electromagnetic fractions

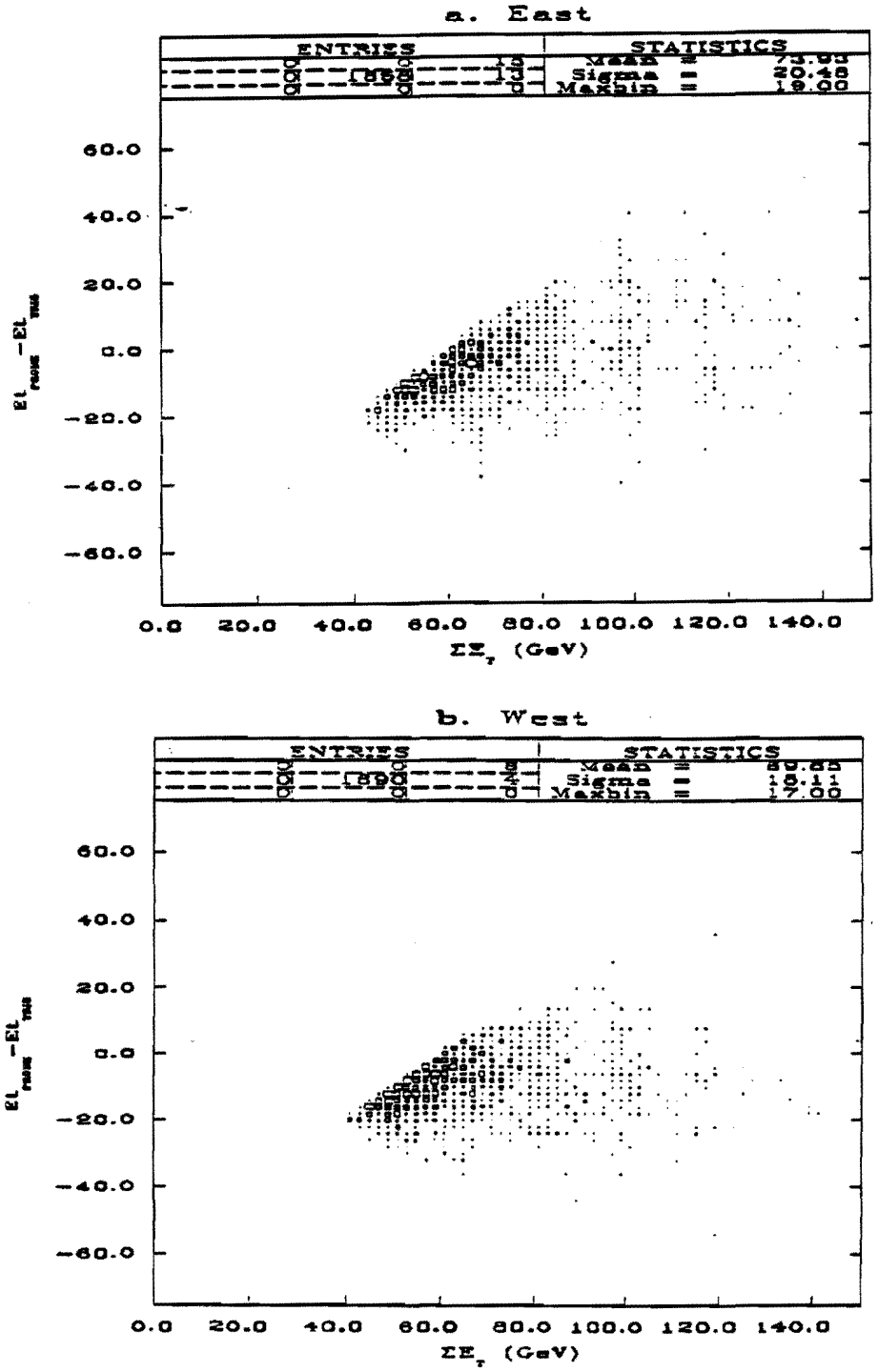

Figure D.9: σ_ξ vs $E_{t_{sum}}$ for the a: East and b: West Plugs

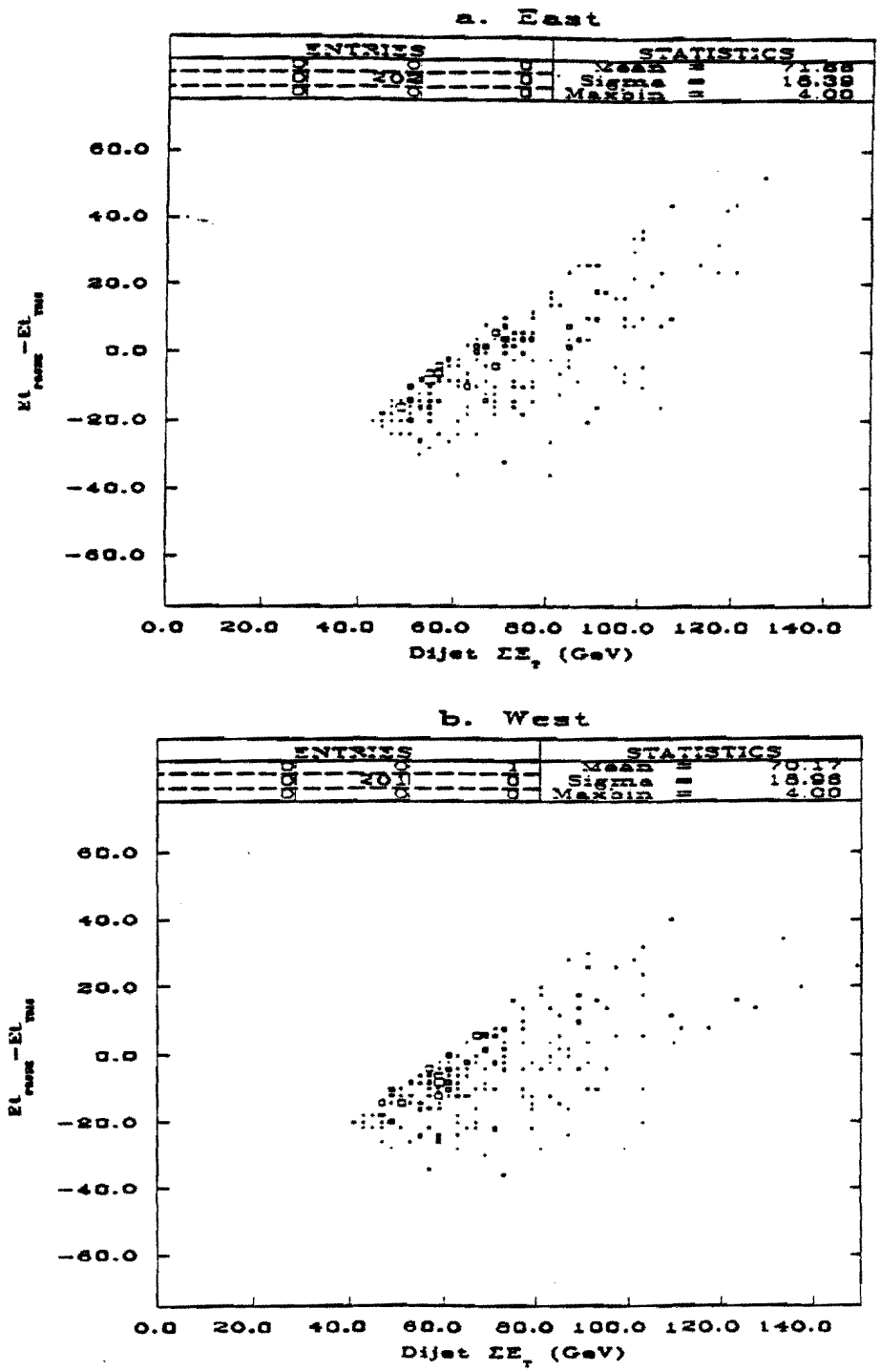

Figure D.10: σ_ξ vs $E_{t_{sum}}$ for the a: East and b: West Forward

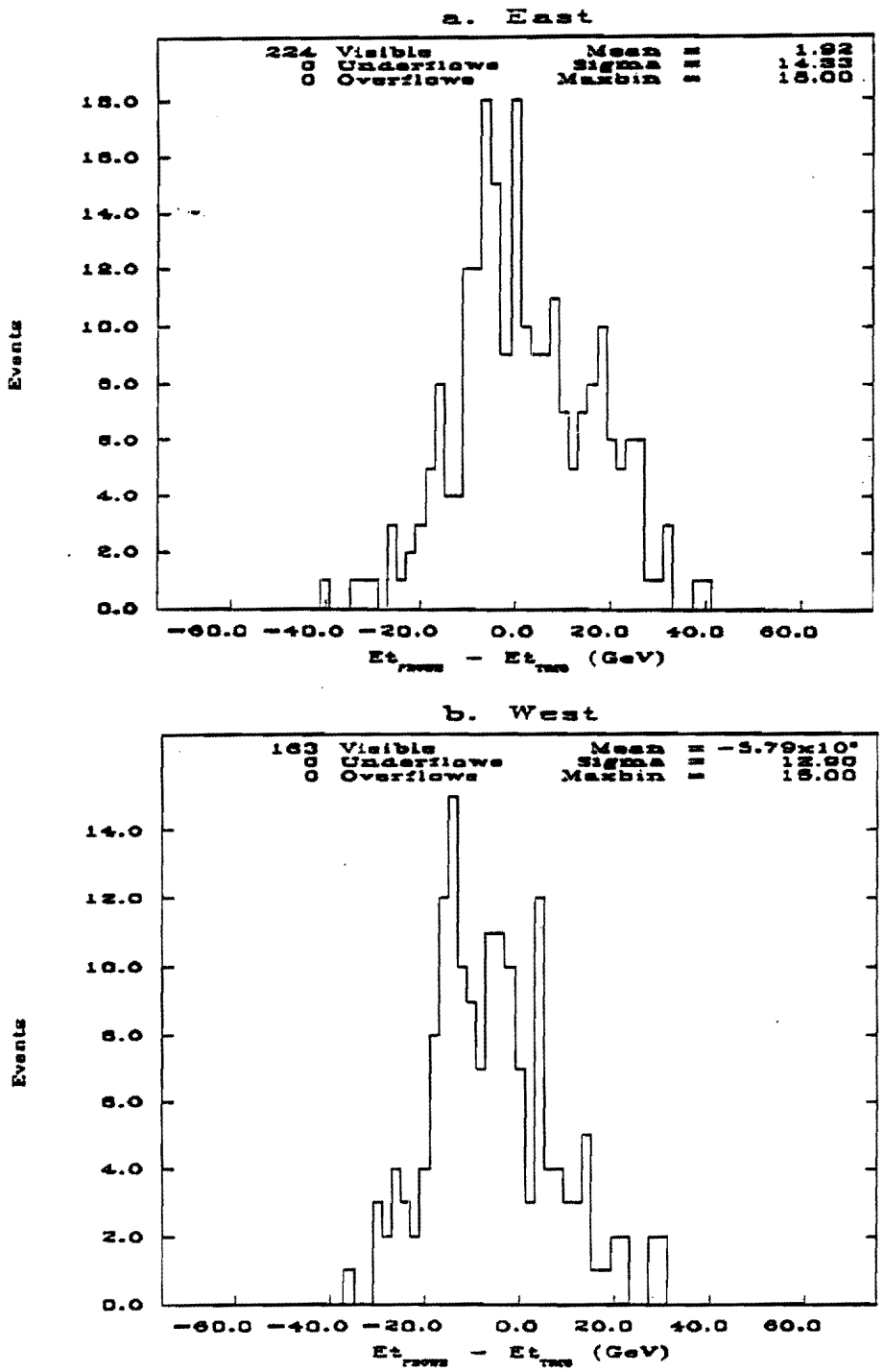

Figure D.11: σ_ξ for $90 \leq E_{t_{sum}} \leq 110\ GeV$ for the a: East and b: West Plug

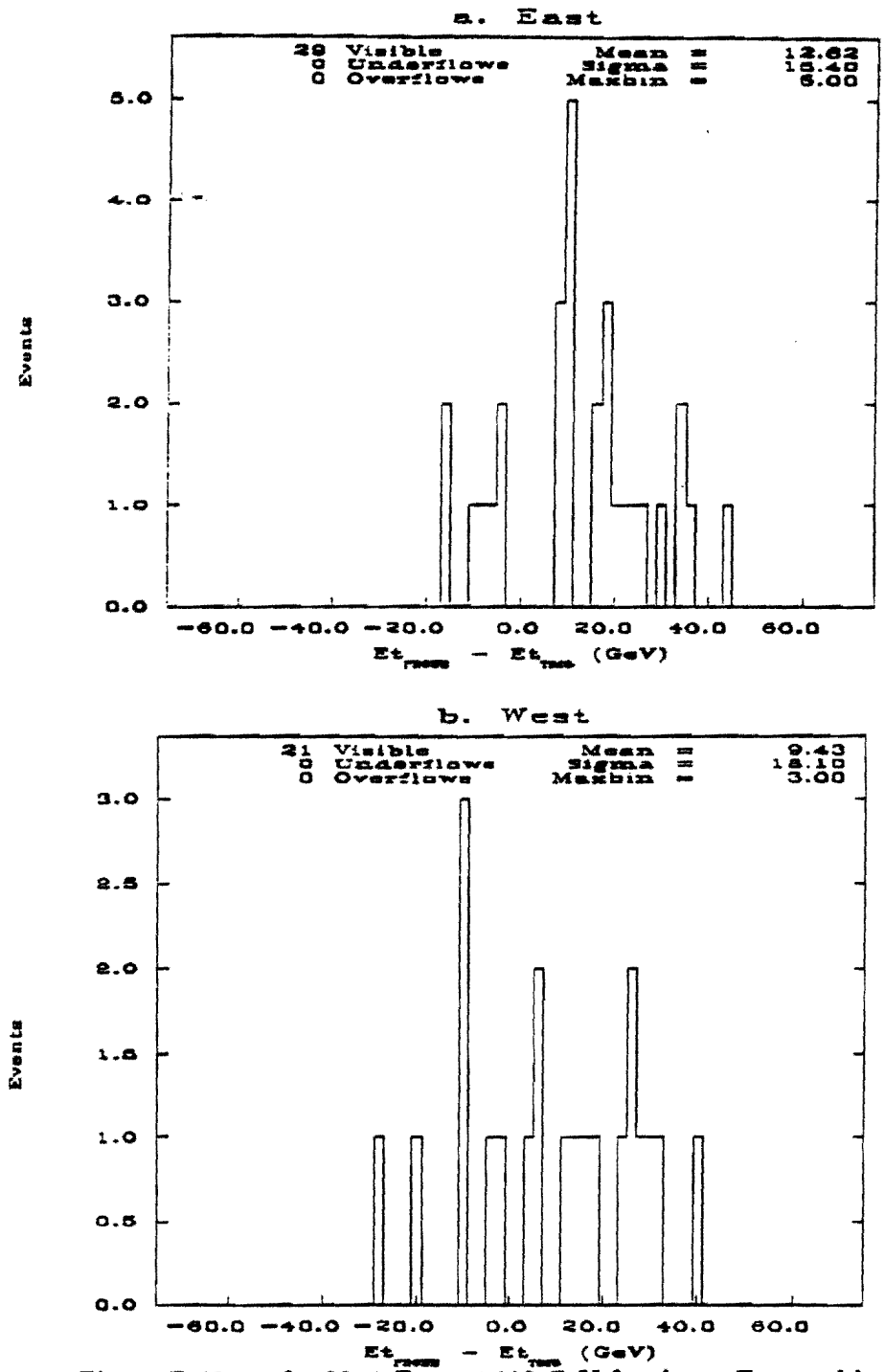

Figure D.12: σ_ξ for $90 \leq E_{t_{sum}} \leq 110\ GeV$ for the a: East and b: West Forward

Detector	A_2 for $90 \leq E_{t_{sum}} \leq 110$	A_2 for $90 \leq E_{t_{sum}} \leq 110$
Plug East	2.25	2.36
Plug West	1.80	2.15
Forward East	4.65	
Forward West	5.95	

Statistical errors $\sim \pm 0.30$

Table D.3: Gas Calorimetry Energy Resolution Coefficients. All coefficients have units of $GeV^{1/2}$.

3. The value of $\sin\theta$ is taken as the average calculated from the measured pseudo-rapidity for the ensemble of jets probing the gas calorimeter. (See Figures D.3 to D.6.)

4. The resolution of the central detector is taken from the same plots (not shown) as were made for the forward detector. The value of $\sigma'/\sqrt{2E_t}$ is found to be 0.88 $GeV^{1/2}$. This is between the values of 0.83 $GeV^{1/2}$ and 1.01 $GeV^{1/2}$ found for the 0.6 and 1.0 cone sizes; therefore, even with only a single bin of $E_{t_{sum}}$, it seems a reasonable estimate of the jet resolution of the central detector.

The results are shown in Table D.3 where the values of the calculated A_2 coefficients are given. They have been calculated independently for two regions of $E_{t_{sum}}$ for the endplug. The statistics are not sufficient to do this in the forward. The resolutions are much worse relative to the central detector. One expects some degradation since the response to pions would indicate a coefficient of 1.5 in the endplug and about 1.8 in the more coarsely segmented forward detector. The resolutions seem to be quite a bit worse

than this and are attributable to the items listed a the end of Section D.2.2.

D.2.4 Changing the Gas Calorimetry Scale

It is possible to change the gas calorimetry scale based on observed values of the electromagnetic fraction and the offset of energies balanced with respect to the central detector. This is derived in the following manner: Consider a calibrated detector response to the probe jet. The energies added to give:

$$f_e = \frac{EM}{EM + HAD}, \tag{D.82}$$

$$1.0 = EM + HAD, \tag{D.83}$$

where f_e is the correct electromagnetic fraction and the total energy adds to 1.0. Notice that this immediately implies $EM = f_e$ and $HAD = 1 - f_e$. In the gas calorimeter, the mix has been scaled differently:

$$E_{rat} = \alpha\, EM + \beta\, HAD, \tag{D.84}$$

$$f_{em} = \frac{\alpha\, EM}{\alpha\, EM + \beta\, HAD}. \tag{D.85}$$

E_{rat} is the ratio of the average probe energy to the trigger energy and f_{em} is the electromagnetic fraction observed for the probe. Here one assumes that the central detector has the correct energy scale. Differences in construction of the detectors may give different values of f_e, so the central detector value is not assumed. Place Equation D.84 into D.85 to get:

$$\alpha\, EM = f_{em} E_{rat},$$

$$\alpha = \frac{f_{em} E_{rat}}{f_e}. \tag{D.86}$$

	East Forward		West Forward		East Plug		West Plug	
f_c	α	β	α	β	α	β	α	β
0.5	0.701	0.635	0.668	1.487	0.937	1.099	0.803	0.943
0.6	0.584	2.043	0.557	1.859	0.780	1.374	0.669	1.179
0.7	0.500	2.724	0.477	2.478	0.669	1.832	0.574	1.572

Table D.4: Gas Calorimetry Energy Correction factors for various assumptions of the electromagnetic fraction

One can also solve for β by using Equation D.84 and the expression for α EM:

$$\beta\, HAD = E_{rat} - f_{em} E_{rat} \tag{D.87}$$

$$\beta = \frac{E_{rat}(1 - f_{em})}{1 - f_c}. \tag{D.88}$$

This gives a solution for α and β in terms of two known quantities, E_{rat} and f_{em}, and one unknown, f_c. The data have been studied by taking the average of the probe jet above 90 GeV to obtain E_{rat}. A choice of three values of f_c was made: 0.5, 0.6, and 0.7. The values of α and β are listed for each calorimeter in Table D.4 The resulting resolutions are summarized in Table D.5 and indicate the various values of A_2 one obtains as a function of f_c. There seems to have been improvements in both forward detectors. One plug is essentially unchanged, the other seems worse. The dependence on f_c is consistent with being flat to within the errors. This indicates that the main change in resolution was due to altering the energy scale used to calculate the widths of the distributions when they were compared to the energy of the central jet.

For the gas calorimeters it is possible to get an estimate of how much one must vary the energy scale to match the central detector. It also provides an estimate of the energy response of the detectors and a monitor of their performance.

Detector	f_e	A_2 for $90 \leq E_{t,sum} \leq 110$	A_2 for $110 \leq E_{t,sum} \leq 130$
Plug East	0.5	2.28	2.07
	0.6	1.98	2.07
	0.7	2.12	2.51
Plug West	0.5	2.04	2.70
	0.6	2.15	2.79
	0.7	2.30	3.09
Forward East	0.5	4.07	
	0.6	4.03	
	0.7	3.42	
Forward West	0.5	4.38	
	0.6	3.91	
	0.7	4.55	

Statistical errors $\sim \pm 0.30\ GeV^{1/2}$

Table D.5: Gas Calorimetry Energy Resolution Coefficients for various assumptions of the electromagnetic fraction. All coefficients are expressed in units of $GeV^{1/2}$.

Appendix E

Phase I Acceptance Calculations

This appendix describes the simple Monte Carlo calculations used in Phase I of the analysis of $dN/d\cos\theta^*$.

E.1 The Simple Monte Carlo

The issues affecting acceptance were described in Section 7.1. The effects of populating the dijet angular distribution with events that creep across the p^* cut and the smearing of the fiducial volume due to vertex movement are calculated from a Monte Carlo that has the following features:

1. **falling p_t spectrum** - The Monte Carlo has been set to generate a parton with a p_t^{-6} spectrum. This agrees with the measured behaviour of the single jet inclusive spectrum [16].

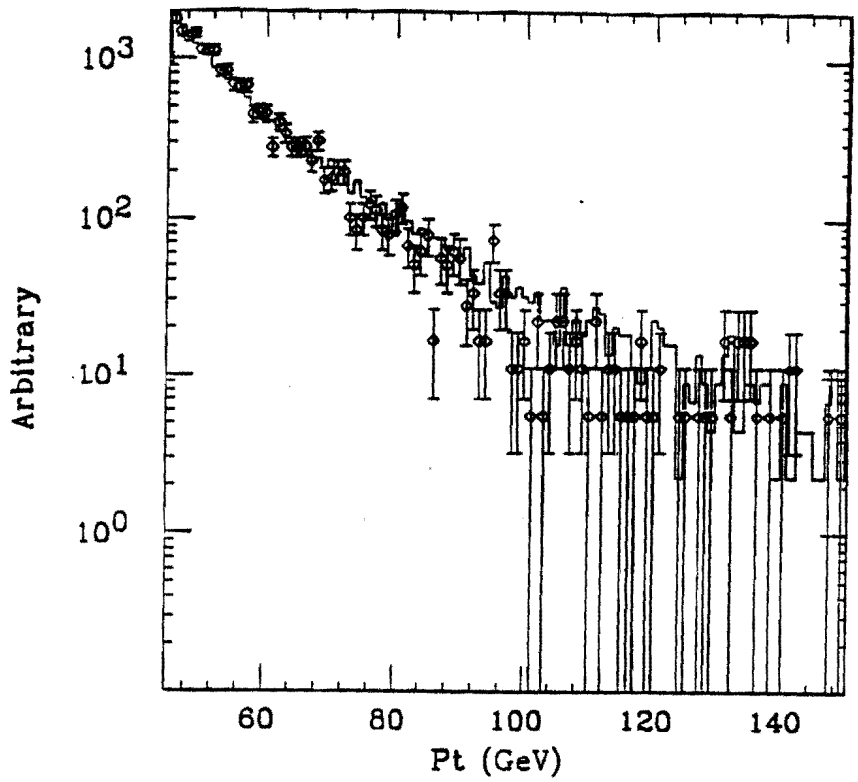

Figure E.1: Comparison of the simple Monte Carlo (histogram) p_t and data (points) spectra.

2. **calorimeter resolution** - The Monte Carlo uses a calorimeter resolution function suggested by the jet energy balancing (Chapter 6) for a cone size of 1.0:

$$\frac{\sigma}{E} = \frac{0.83\ GeV^{1/2}}{\sqrt{E}}. \qquad (E.89)$$

This resolution, plus adjusting the exponent in the falling spectrum compare well with the shape of the observed spectrum as shown in Figure E.1

3. **Vertex smearing** - The gaussian vertex distribution shown in Figure 5.3 was used in generating the events.

4. **pseudorapidity distribution** - The pseudorapidities of the two jets were assumed to be flat to the kinematic limit.

When using this Monte Carlo, it was necessary to begin parton generation at a reasonably low value so that the smearing effects were generated in an unbiased way. For example, given the parameterization of the falling spectrum and jet resolution above, 45 GeV of observed energy gets about a 15% contribution from 35 GeV of generated energy. One must begin to generate events with 30 GeV of energy in order to get a negligible contribution to the 45 GeV observed energy. The consequence is that many events are generated but only about 10% are used.

E.2 Calculation of Acceptance

The basic region outlined in Phase I has been moved out steps to $|\eta^*|,|\eta_{boost}| \leq 1.0$ and then to $|\eta^*|,|\eta_{boost}| \leq 1.2$. Again, the coupling of p^* to η^* via p_t forces choices of minimum p^* to 70 and 82 GeV for these choices of η^*.

The calculation of the acceptance for the various regions is carried out as follows:

1. Events are generated with no vertex smearing and no resolution smearing to establish the baseline for the angular distribution phase space.

2. Events are generated with both vertex smearing and resolution smearing. As described in Section E.1, the generation is done beginning with low energy partons so that the resolution smearing corrections are not improperly truncated.

3. The ratio of the baseline distribution to the simulated distribution is shown in Figure E.2. They have been normalized by the number of events generated and observed. This final distribution contains the correction factors that are applied to the raw angular distribution.

These correction factors have also been calculated for lower values of the p^* than the value implied by the cut on η^* by Equation 7.9. For pseudorapidity values less than 0.7, as the p^* cut was lowered from 57 GeV to 52 then 48 GeV, the correction grew from 1.0 to 1.5 then to 2.0 in the highest bins $\cos\theta^*$. For this Monte Carlo calculation, conservative acceptance corrections were required since there were a number of important effects not simulated. It was decided not to lower the p^* cut. The correction factors due to the geometric effects are much smaller - on the order of 25% for the pseudorapidities that reach out to 1.2. A systematic uncertainty of 5% was obtained by varying the exponent and the assumed resolution used in the Monte Carlo.

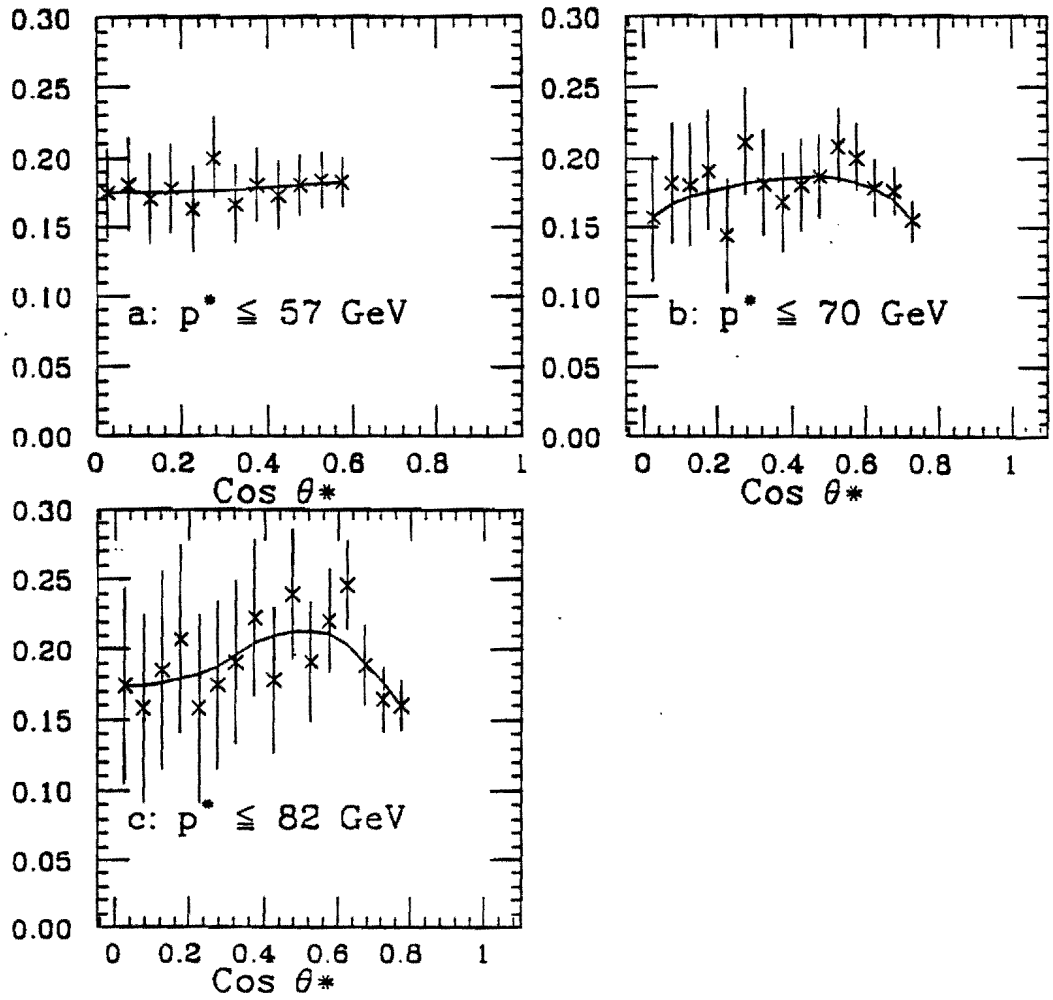

Figure E.2: Acceptance function for $|\eta^*|,|\eta_{boost}| \leq 0.7, 1.0, 1.2$

Appendix F

Tests of QFL

This appendix describes some tests that were made of the ISAJET/QFL Monte Carlo. The sample of Monte Carlo events was described in Section 7.3.1. Various jets distributions are discussed here:

1. **p_t spectra and other cluster multiplicity** - The p_t spectra show excellent agreement for the all three categories of jets in Figures F.1a to F.1c. The other cluster multiplicity is shown in Figure F.1d and indicates the rate of other clusters agrees quite well with the data.

2. **Electromagnetic Fraction** - The electromagnetic fractions in Figure F.2 show fair agreement in the trigger and probe jet spectra and quite good agreement in the other jets. The lack of spikes at either end of the probe and other spectrum indicates that the gas spike removal has worked and, in addition, since QFL does not simulate neutron sensitivity, there is fair indication that the jets are not polluted by neutrons.

3. **mass spectra** - The mass spectra (Figure F.3) show very good agreement. Since jet masses were calculated by assuming the calorimeter cells were massless particles and summing over the momenta and energies of these cells, it is an indication of the size of the jet. Therefore, the mass is related to the fragmentation. The choice of fragmentation used in ISAJET for this exercise was determined from the direct measurement of the fragmentation function [41]. It was found that the best parameterization was that described by Field and Feynman [42] and not that used by default in ISAJET [16].

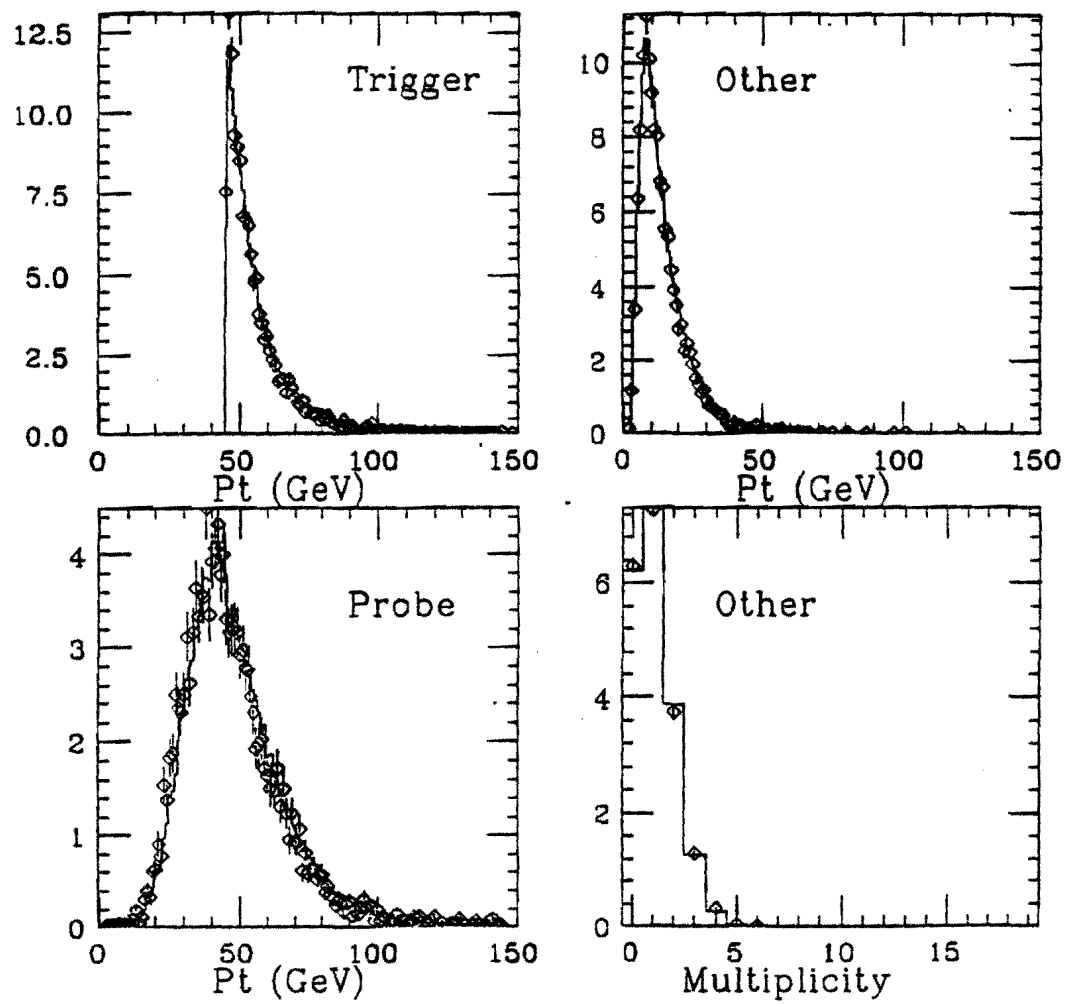

Figure F.1: Jet p_t distributions for ISAJET/QFL(histogram) and data(points).

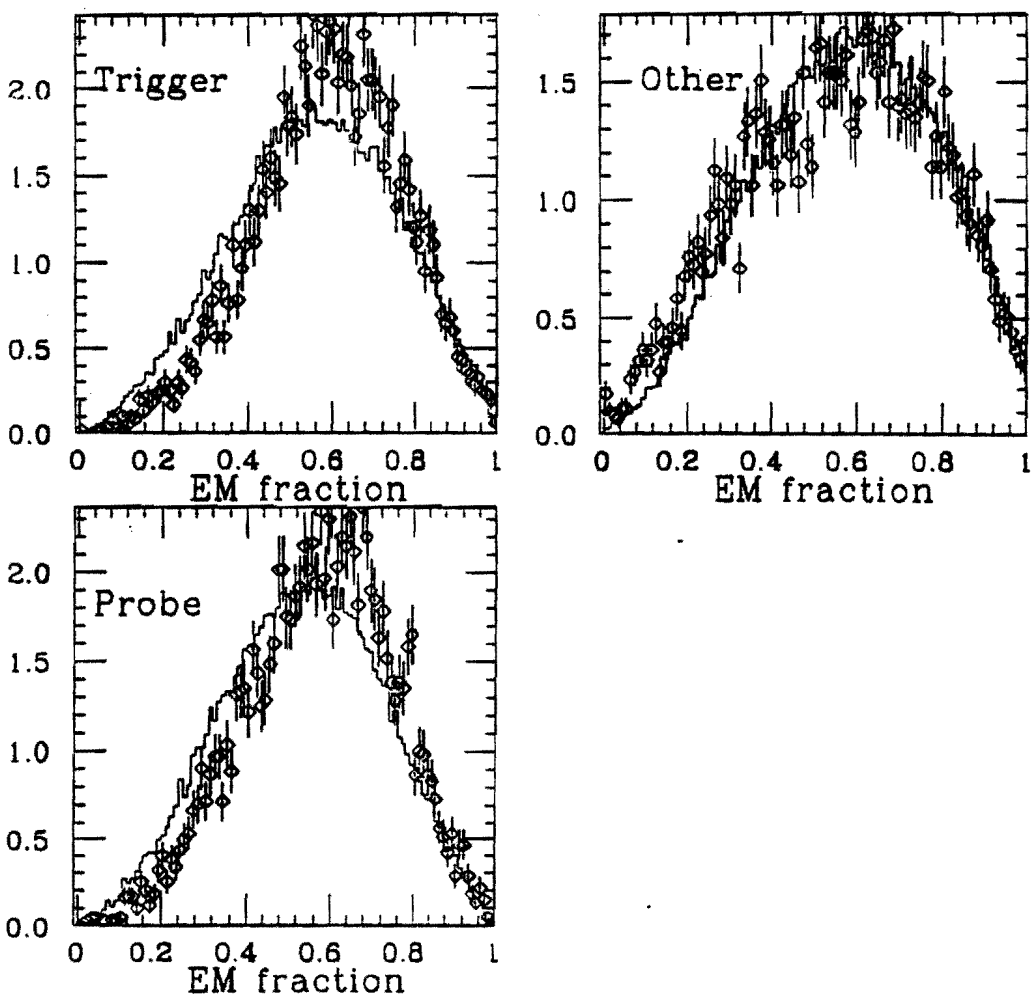

Figure F.2: Jet electromagnetic fraction distributions for ISAJET/QFL(histogram) and data(points).

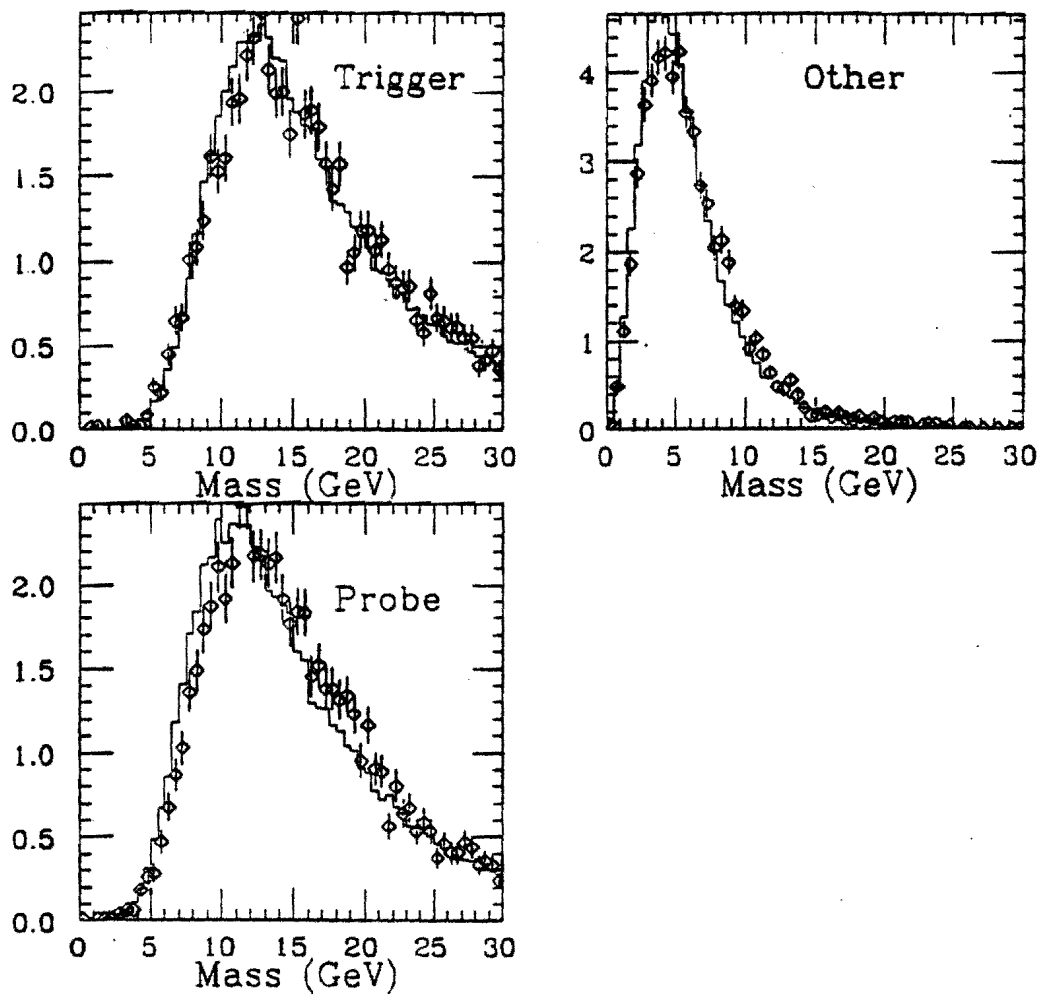

Figure F.3: Single jet mass distributions for ISAJET/QFL(histogram) and data(points).

Appendix G

Theoretical calculations of

$dN/\cos\theta^*$

This appendix presents the method used to obtain the 2→2 QCD calculations. The goal of these calculations is to provide the differential cross section in one variable, such as $\cos\theta^*$, while integrating over all others. These calculations are done using FORTRAN code written by R.K.Ellis, E.Eichten and M.Mangano and a numerical integration program. The QCD quantity that is calculated, $d\sigma/dy_1dy_2dE_\perp$, is presented. The running of α_s with Q^2, the evolution of a choice of parton distribution functions, and the results of the calculation of the parton subprocess cross sections are described. The integration of $d\sigma/dy_1dy_2dE_\perp$ over two of the variables is described. The adaptation of the result for use in the calculation of $dN/d\cos\theta^*$ for various choices of parton distribution functions and Q^2 scales is presented.

G.1 The Quantity that is Calculated

The calculation describes the rate of dijet events in some interval of rapidity for each jet and within some interval of the total transverse energy of the two jets. The expression for this differential cross section is:

$$\frac{d\sigma}{dy_1 dy_2 dE_\perp} = \left(\frac{\pi}{32E_{beam}^4}\right) \underbrace{\alpha_s^2\left(Q^2\right)(E_\perp)\sum_{ab}\left(\frac{f_a\left(x_1,Q^2\right)}{x_1}\right)\left(\frac{f_b\left(x_2,Q^2\right)}{x_2}\right)|M_{ab}|^2}_{TJFUN}. \tag{G.90}$$

In the above equation, E_{beam} is the energy of one of the colliding beams, $f_a(x)$ is the probability of finding parton a with beam momentum fraction x_1, $f_b(x)$ is the probability of finding parton b with beam momentum fraction x_2, y_1 and y_2 are the rapidities of the two jets, and $E_\perp = E_{t_1} + E_{t_2}$ is the total transverse energy of the two jets. The square of the matrix element $|M_{ab}|^2$ is the cross section for the parton subprocess $i + j \rightarrow X$. The produced particles, X, imply a sum over all the final states that may arise from the combination of partons i and j. These final states involve gluons and four flavors of quarks and antiquarks. The sum over the cross sections of the initial partons to interact is then taken over gluons and four flavors of quarks and antiquarks. The specific list of partons considered is: $\bar{c}$,$\bar{s}$,$\bar{d}$,$\bar{u}$,g,u,d,s,c.

G.1.1 Overview of the Procedure

For the purposes of the calculation, it is assumed that the quantity in Equation G.90 will be the integrand of a numerical integration. The variables of integration may be chosen as desired if the function is multiplied by the appropriate Jacobian. This is implemented by making the underbraced portion of $d\sigma/dy_1 dy_2 dE_\perp$ a FORTRAN function,

TJFUN, that is called repeatedly by the numerical integration program, VEGAS [43]. The omitted portion of $d\sigma/dy_1dy_2dE_\perp$ is an overall constant that is multiplied into the result of the integration when VEGAS is done. A main program initializes the bounds of integration in a VEGAS common block and then calls VEGAS with an argument declaring the name of the function to be integrated an the number of dimensions over which to perform the integration. This main program may also set flags that communicate with the FORTRAN function in order to allow for various choices of parton distribution functions and Q^2 scale. The call to VEGAS returns the integral of TJFUN over the specified region.

The function, TJFUN, goes through the following sequence of steps when it is called:

1. It calculates Q^2, x_1, and x_2. These values are derived from the values of the variables over which one integrates. For example, in doing the $dN/d\cos\theta^*$ calculation, one passes a value of $\cos\theta^*$ to TJFUN and asks for an integration over y_{boost} and M_{jj}. (These are the rapidity boost of the dijet system to the center of mass and the invariant mass of the dijet pair.) These three quantities must be used to determine the momentum fractions and Q^2 for the phase space configuration described by y_{boost}, M_{jj}, and $\cos\theta^*$.

2. It obtains the value of the parton distribution for each beam for the parton distribution functions chosen and the calculated value of x and Q^2.

3. It calculates and stores the parton subprocess matrix elements, the $|M_{ab}|^2$.

4. It evolves the strong coupling constant, α_s, with Q^2.

5. It loops over the possible initial state partons, summing over the parton subprocess cross sections weighted by the values of the parton distribution functions.

6. It multiplies the final sum by α_s and stores the result as the function value.

The details of each of these steps are described in the next sections.

G.1.2 Parton Distribution Functions

The parton distribution functions one may choose are: Duke and Owens sets 1 and 2 [44] (DO1 and DO2) and EHLQ sets 1 and 2 [45] (EHLQ1 and EHLQ2). In both DO and EHLQ, the sets are meant to bracket the true values of the parton distribution functions. This is necessary because of uncertainty in the gluon distribution function. The values of Λ used in EHLQ are more consistent with the experimentally measured values than those in DO. EHLQ uses 200 and 290 MeV, while DO uses 200 and 400 MeV for Λ.

The DO1 and DO2 parton distribution functions are parameterized in terms of x and Q^2. A set of coefficients describes the x dependence. These coefficients are evolved by a Q^2-dependant parameterization. A call to the subprogram DENS establishes the evolved coefficients. A subsequent call to the routine FDIST uses the evolved coefficients of the x dependence to return the probability for finding each parton in each beam. The evolution of the up quark and gluon distribution functions is shown in Figure G.1

The EHLQ parton distribution functions are parameterized using Chebyshev polynomials that are functions of x and Q^2. A table of values of the parton distribution functions is stored in a file for $5\ GeV^2 \leq Q^2 \leq 10^8\ GeV^2$ and $0 \leq x \leq 1$. The value of a distribution function is obtained from a linear interpolation of the values in the table.

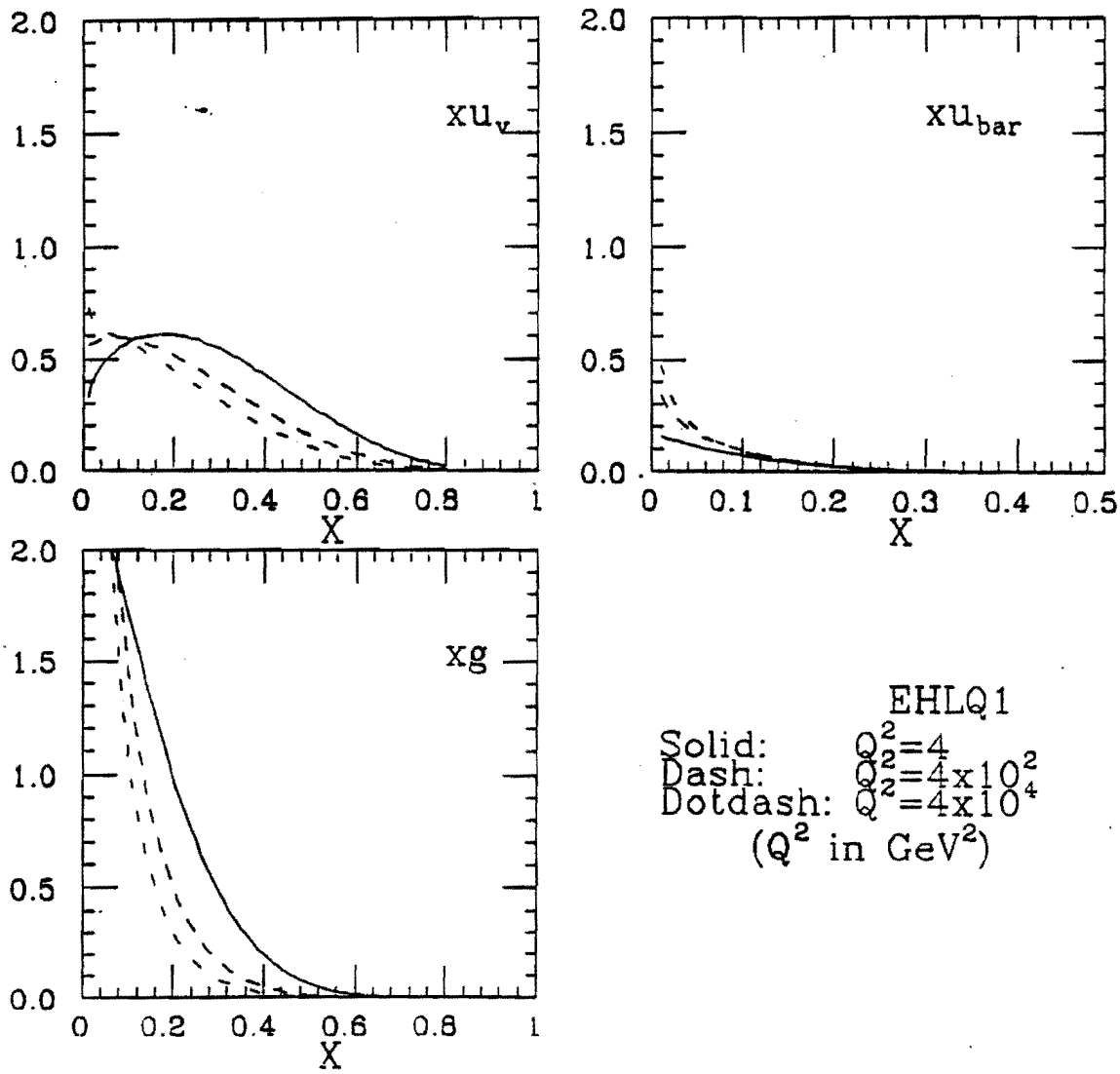

Figure G.1: Q^2**-dependence of up quark and gluon distribution functions in the proton.**

Long and short forms of the tables exist; the short forms were used since it is claimed that they do not degrade the accuracy of the calculation. A call to DENS initializes the value of A for the parton distribution functions. A call to FDIST dispatches one to the appropriate routine, EHLQ1 or EHLQ2, that returns the values of the parton distribution functions. These values are calculated in EHLQ1 and EHLQ2 by interpolating the values in the table.

G.1.3 Evolution of α_s

The evolution of α_s is done using the formulae:

$$
\begin{aligned}
\alpha_s(Q^2) &= \frac{12\pi}{27\log\frac{Q^2+2\Lambda^2}{\Lambda^2}} && \}\, Q^2 \le 4m_b^2, \\
\alpha_s(Q^2) &= \frac{12\pi}{27\log\frac{m_c^2+2\Lambda^2}{\Lambda^2} + 25\log\frac{Q^2}{4m_c^2}} && \}\, 4m_c^2 < Q^2 \le 4m_b^2, \\
\alpha_s(Q^2) &= \frac{12\pi}{27\log\frac{m_c^2+2\Lambda^2}{\Lambda^2} + 25\log\frac{m_b^2}{m_c^2} + 23\log\frac{Q^2}{4m_b^2}} && \}\, 4m_b^2 < Q^2 \le 4m_t^2, \qquad (G.91) \\
\alpha_s(Q^2) &= \frac{12\pi}{27\log\frac{m_c^2+2\Lambda^2}{\Lambda^2} + 25\log\frac{m_b^2}{m_c^2} + 23\log\frac{m_t^2}{m_b^2} + 21\log\frac{Q^2}{4m_t^2}} && \}\, 4m_t^2 < Q^2.
\end{aligned}
$$

The values of the masses of the quarks are $m_c = 1.5\ GeV$, $m_b = 4.5\ GeV$, and $m_t = 40\ GeV$. The first logarithm contains a factor, 2Λ, which is used only to prevent the program from terminating mysteriously if a $Q^2 = 0$ is passed. If such a thing occurs, other parts of the program will terminate the calculation cleanly with a warning.

G.1.4 Parton Subprocess Matrix Elements

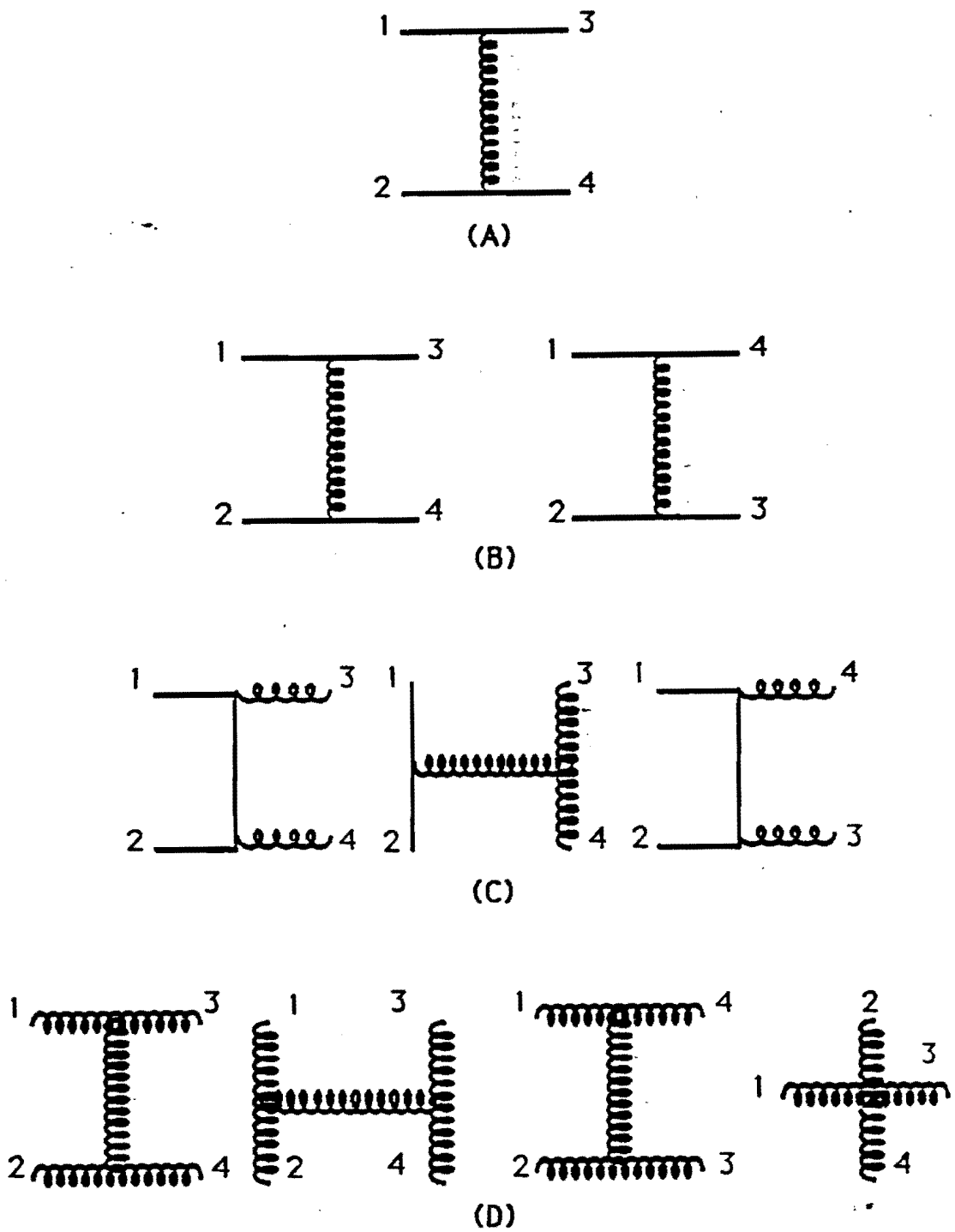

Figure G.2: The four basic parton subprocess cross sections: (A) $QQ'QQ'$ (B) $QQQQ$ (C) $Q\bar{Q}GG$ (D) $GGGG$

Function	Value
$A(1,2,3,4)$	$2V\left(\frac{\hat{s}^2+\hat{u}^2}{\hat{t}^2}\right)$
$B(1,2,3,4)$	$A(1,2,3,4)+A(1,2,4,3)-4V\frac{\hat{s}^2}{N\hat{u}^2}$
$C(1,2,3,4)$	$\frac{2V}{N}\left(\frac{V}{\hat{u}^2}-\frac{2N^2}{\hat{s}^2}\right)\left(\hat{t}^2+\hat{u}^2\right)$
$D(1,2,3,4)$	$16VN^2\left(3-\frac{\hat{u}^2}{\hat{s}^2}-\frac{\hat{u}\hat{s}}{\hat{t}^2}-\frac{\hat{t}\hat{s}}{\hat{u}^2}\right)$

Table G.1: Four basic parton subprocess cross sections. $N = 3$ is the number of colors. $V = N^2 - 1$ is the dimensionality of the $SU(N)$ group.

Figure G.2 shows Feynman diagrams and Table G.1 gives the expressions for the corresponding cross sections of the four 2→2 QCD processes: $QQ'QQ'$, $QQQQ$, $Q\bar{Q}GG$, and $GGGG$ [46]. In the expressions for the four subprocess cross sections, it is assumed that partons with momenta labeled 1, 2, 3, and 4 enter the reaction and conserve energy and momentum. These labels are used in Figure G.2 as well as in Table G.1. In the figures, the crossed channels are denoted by switching the momentum labels. The cross sections in Table G.1 are expressed in terms of the Mandelstam variables, $\hat{s}$, $\hat{t}$, and $\hat{u}$. The hats over the variables indicate that these are defined in terms of the parton 4-momenta:

$$\begin{aligned}\hat{s} &= (1+2)\bullet(1+2),\\ \hat{t} &= (1-3)\bullet(1-3),\\ \hat{u} &= (2-3)\bullet(2-3).\end{aligned} \tag{G.92}$$

The constant, N, is the number of colors; therefore, $N = 3$. The constant, $V = N^2 - 1$, is the dimensionality of the vector representation of $SU(N)$.

All the allowable subprocesses may be derived from these using time reversal and crossing. These subprocesses are listed in Table G.2. They are divided into seven values that represent seven different initial states and the sum of the reaction over all final

$ab \rightarrow X$	$\hat{\sigma}(ab \rightarrow X)$
$QQ' \rightarrow QQ'$	$\frac{1}{4N^2} A(1,2,3,4)$
$QQ \rightarrow QQ$	$\frac{1}{4N^2} \frac{B(1,2,3,4)}{2}$
$Q\bar{Q}' \rightarrow Q\bar{Q}'$	$\frac{1}{4N^2} A(1,4,3,2)$
$Q\bar{Q} \rightarrow Q'\bar{Q}'$ $\rightarrow Q\bar{Q}$ $\rightarrow GG$	$\frac{1}{4N^2}\left[(N_f - 1) A(1,3,2,4) + B(1,4,3,2) + \frac{C(1,2,3,4)}{2}\right]$
$QG \rightarrow QG$	$\frac{1}{4NV}(-1) C(1,3,2,4)$
$GQ \rightarrow GQ$	$\frac{1}{4NV}(-1) C(2,3,1,4)$
$GG \rightarrow GG$ $\rightarrow Q\bar{Q}$	$\frac{1}{4V^2}\left[\frac{D(1,2,3,4)}{2} + N_f C(3,4,1,2)\right]$

Table G.2: Seven basic parton subprocess cross sections for $a + b \rightarrow X$. $N = 3$ is the number of colors. $V = N^2 - 1$ is the dimensionality of the $SU(N)$ group. $N_f = 4$ is the number of quark flavors. The functions A, B, C, D are defined in Table G.1.

states for gluons and N_f flavors of quarks and antiquarks. For each reaction, the values of the parton subprocess cross sections are expressed in terms of the four functions listed in Table G.1.

G.1.5 Summing the Cross Sections and Weighting with Distribution Functions

The routine TJFUN calculates the seven values of the cross sections in Figure G.2 once per call. Then it loops over gluons and the four flavors of quark and antiquark in each incoming beam particle. At each pass of the loop, it fetches the two parton distribution function values that were calculated by the parton distribution function routines, DENS and FDIST. It also looks up the value of the correct parton cross section for the initial state it has at that point in the loop. It multiplies the two parton distribution function values with the parton cross section and adds the result to a running sum.

After the loop is completed, the running sum over the parton distribution function-weighted elementary cross sections is multiplied by the evolved value of α_s and returned as the value of TJFUN. Multiplication of this value by $\pi/\left(32E_{beam}^4\right)$ results in the differential cross section, $d\sigma/dy_1dy_2dE_\perp$. In fact, the multiplication is done by the main program at the end of integration by VEGAS.

G.2 Application to $dN/d\cos\theta^*$

The code above has been used to provide values of $dN/d\cos\theta^*$ by integrating over y_{boost} and M_{jj}. This is done by first using the Jacobian to transform the cross section that is provided to the center of mass coordinates, y_{boost}, M_{jj}, and $\cos\theta^*$. Then the code is run

under a variety of conditions.

G.2.1 Transformation of Variables

The above functions are applied to calculating $dN/d\cos\theta^*$ by using the Jacobian that transforms the volume element $dy_1 dy_2 dE_\perp$ to $dy_{boost} dM_{jj} d(\cos\theta^*)$. Since:

$$\cos\theta^* = \tanh\frac{y_1 - y_2}{2}, \tag{G.93}$$

$$y_{boost} = \frac{y_1 + y_2}{2}, \tag{G.94}$$

$$M_{jj} = E_\perp \cosh\frac{y_1 - y_2}{2}, \tag{G.95}$$

one can write the transformation of each dimension of the volume as:

$$\begin{pmatrix} d\cos\theta^* \\ dy_{boost} \\ dM_{jj} \end{pmatrix} = \begin{pmatrix} \frac{1}{2\cosh^2 y^*} & -\frac{1}{2\cosh^2 y^*} & 0 \\ \frac{1}{2} & \frac{1}{2} & 0 \\ \frac{E_\perp}{2}\sinh y^* & -\frac{E_\perp}{2}\sinh y^* & \cosh y^* \end{pmatrix} \begin{pmatrix} dy_1 \\ dy_2 \\ dE_\perp \end{pmatrix}. \tag{G.96}$$

The determinant of the matrix describes the volume transformation. Equation G.96 may be written

$$\partial(\cos\theta^*, y_{boost}, M_{jj}) = \frac{\partial(\cos\theta^*, y_{boost}, M_{jj})}{\partial(y_1, y_2, E_\perp)} \partial(y_1, y_2, E_\perp), \tag{G.97}$$

where $|M| \equiv \partial(\cos\theta^*, y_{boost}, M_{jj})/\partial(y_1, y_2, E_\perp)$ is the determinant of the matrix in Equation G.96:

$$\frac{\partial(\cos\theta^*, y_{boost}, M_{jj})}{\partial(y_1, y_2, E_\perp)} = \frac{1}{2\cosh y^*}. \tag{G.98}$$

In order to perform the integration over y_{boost} and M_{jj}, one must use the inverse transformation so that the appropriate Jacobian is $1/|M| = 2\cosh y^* = 2M_{jj}/E_\perp$. This

means that one can write Equation G.90 as

$$\frac{d\sigma}{dy_{boost}dM_{jj}d\cos\theta^*} = \left(\frac{\pi\alpha_s^2(Q^2)}{32E_{beam}^4}\right)(2M_{jj})\sum_{ab}\left(\frac{f_a(x_1,Q^2)}{x_1}\right)\left(\frac{f_b(x_2,Q^2)}{x_2}\right)|M_{ab}|^2. \tag{G.99}$$

A similar exercise yields the appropriate Jacobian for $dN/d\chi$ where

$$\chi \equiv \frac{1+\cos\theta^*}{1-\cos\theta^*}.$$

Since

$$d\chi = 2\chi\cosh^2 y^* d\cos\theta^* = 2\chi\frac{M_{jj}^2}{E_\perp^2}d\cos\theta^*,$$

Equation G.99 may be used to write the differential cross section in terms of y_{boost}, M_{jj} and χ:

$$\frac{d\sigma}{dy_{boost}dM_{jj}d\chi} = \left(\frac{\pi\alpha_s^2(Q^2)}{32E_{beam}^4}\right)\left(\frac{E_\perp^2}{\chi M_{jj}}\right)\sum_{ab}\left(\frac{f_a(x_1,Q^2)}{x_1}\right)\left(\frac{f_b(x_2,Q^2)}{x_2}\right)|M_{ab}|^2. \tag{G.100}$$

G.2.2 Results of the Calculation

Figures G.3 shows the curves for $dN/d\cos\theta^*$ for $Q^2 = p_t^2/4$, p_t^2, and $4p_t^2$ and for each of the parton distribution functions, DO1, DO2, EHLQ1, and EHLQ2. The parton distribution functions represent the range of uncertainty in the gluon distribution. The range of Q^2 scale reflects reasonable uncertainty in the choice of scale and is related to the higher order contributions. Consider how the choice of scale is related to higher order calculations. Begin by comparing $\alpha_s(Q^2)$ for $Q^2 = p_t^2$ to that for $Q^2 = (kp_t)^2$. Since

$$\alpha_s\left(Q^2\right) \sim \frac{1}{\log\frac{Q^2}{\Lambda^2}},$$

then

$$\alpha_s\left(k^2Q^2\right) \sim \frac{1}{\log\frac{k^2Q^2}{\Lambda^2}} = \frac{1}{\log\frac{Q^2}{\Lambda^2}\left[1+\frac{\log k^2}{\log\frac{Q^2}{\Lambda^2}}\right]} \simeq \frac{1}{\log\frac{Q^2}{\Lambda^2}} - \underbrace{\frac{\log k^2}{\left(\log\frac{Q^2}{\Lambda^2}\right)^2}}_{O(\alpha_s^2)}.$$

The second term in the final result is of higher order, so that one does not know the scale to that order. Note, however, that the constant, k, cannot become too different from unity or else the coupling strength becomes too large and the perturbation theory becomes invalid.

It is clear from this figure that the shape of the angular distribution is not sensitive to these quantities for the ranges specified.

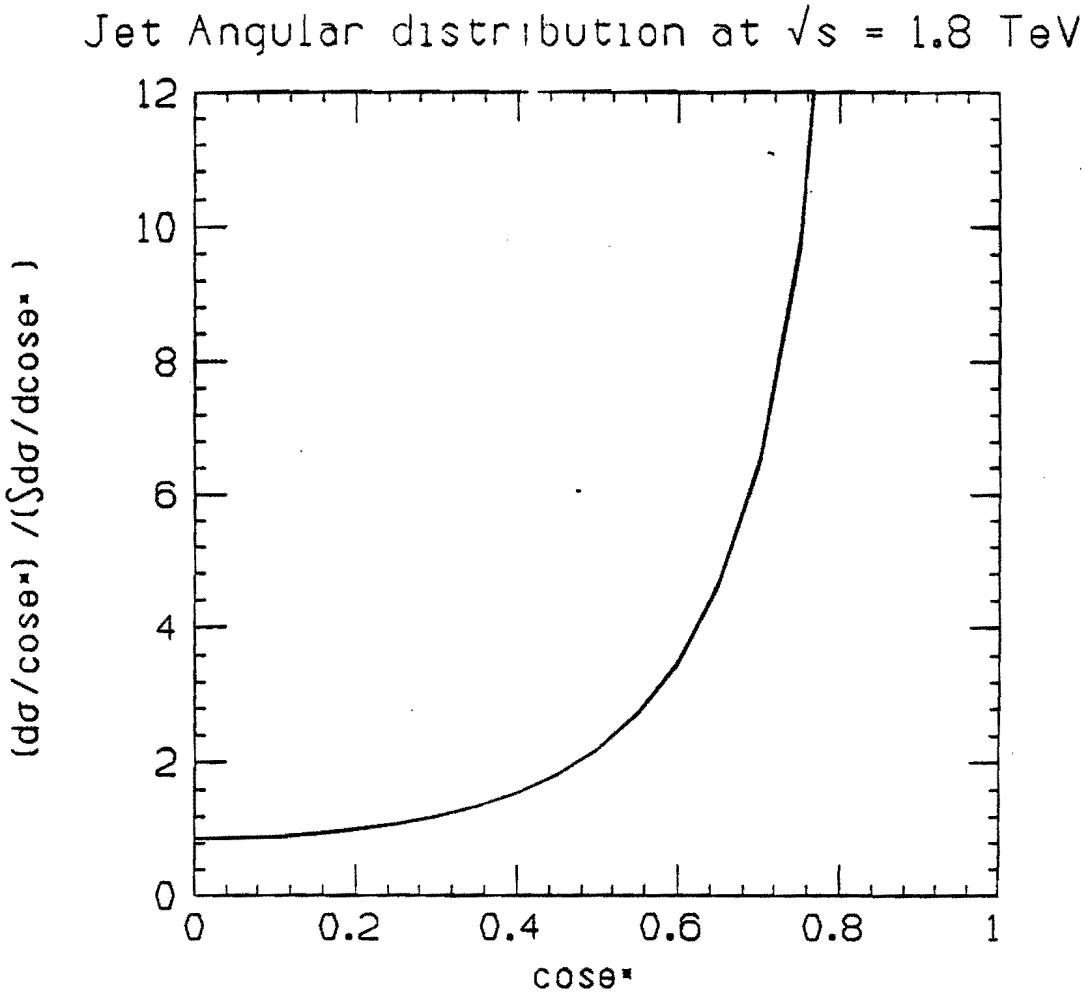

Figure G.3: $dN/d\cos\theta^*$ for DO1,DO2,EHLQ1,EHLQ2 and $Q^2 = p_t^2/4$, p_t^2, and $4p_t^2$. The variation is so small that the curves are indistinguishable.

Bibliography

[1] F. Abe *et al.* Transverse-momentum distributions of charged particles produced in $\bar{p}p$ interactions at $\sqrt{s} = 630$ and 1800 GeV. *Physical Review Letters*, 61(16):1819, 1988.

[2] G. Arnison *et al.* Charged particle multiplicity distributions in proton-antiproton collisions at 540 gev centre of mass energy. *Physics Letters*, B(123):108, 1983.

[3] J. D. Bjorken. Aysmtotic sum rules at infinite momentum. *Physical Review D*, 179(5):1547, 1969.

[4] R. P. Feynman. Very high energy collisions of hadrons. *Physical Review Letters*, 23:1415, 1969.

[5] S. Berman, J. D. Bjorken, and J. Kogut. Inclusive processes at high transverse momentum. *Physical Review D*, 4(11):4, 1971.

[6] H. D. Politzer. Reliable perturbative results for strong interactions? *Physical Review Letters*, 30(26):1346, 1973.

[7] D. J. Gross and F. A. Wilczek. Utraviolet behavior of non-abelian gauge theories. *Physical Review Letters*, 30(26):1343, 1973.

[8] H. Fritzsch, M. Gell-Mann, and H. Leutwyler. Advantages of the color octet gluon picture. *Physics Letters*, B(47):365, 1973.

[9] M. Gell-Mann. *Physics Letters*, (8):214, 1964.

[10] G. Zweig. Technical Report 8419/TH 401, CERN, 1964.

[11] V. Barger and R. Phillips. *Collider Physics*, chapter 7, page 193. Addison-Wesley Publishing Company, 1987.

[12] R.K Ellis *et al.* Perturbation theory and the parton model in QCD. *Nuclear Physics*, B(152):285, 1979.

[13] Combridge and Maxwell. Untangling large-p_t hadronic reactions. *Nuclear Physics*, B(239):429, 1983.

[14] G. Altarelli and G. Parisi. Asymtotic freedom in parton language. *Nuclear Physics*, B(126):298, 1977.

[15] F. Abe *et al.* The CDF detector: an overview. *Nuclear Instruments and Methods*, A(271):287, 1988.

[16] Stephen Eugene Kuhlmann. *Inclusive Central Jet Production at* $\sqrt{s} = 1.8$ *TeV*. PhD thesis, Purdue University, August 1988.

[17] L. Balka *et al.* The CDF central electromagnetic calorimeter. *Nuclear Instruments and Methods*, A(267):272, 1988.

[18] S. R. Hahn *et al.* Calibration systems for the CDF central electromagnetic calorimeter. *Nuclear Instruments and Methods*, A(267):351, 1988.

[19] Hans B. Jensen. CDF calorimetry. In *Proceedings of the International Conference on Advances in Experimental Methods for Colliding Beam Physics*, March 1987.

[20] S.. Behrends *et al.* *Response of the Central Calorimeter to Low Energy Charged Particles.* CDF Note 583.

[21] Melissa Franklin. Peformance of the gas calorimetry at CDF. In *Proceedings of the 7th Topical Workshop on Proton-Antiproton Collider Physics*, June 1988.

[22] G. Brandeburg *et al.* An electromagnetic calorimeter for the small angle regions of the collider detector at fermilab. *Nuclear Instruments and Methods*, A(267):257, 1988.

[23] S. Cihangir *et al.* The CDF forward/backward hadron calorimeter. *Nuclear Instruments and Methods*, A(267):249, 1988.

[24] S. Kuhlmann and J. Yoh. *Filtering Jet Backgrounds in the CDF Central Detector.* CDF Note 548.

[25] G. Redlinger and Y.D.Tsai. *The Hadron TDC Filter for Main Ring and Cosmic Ray Events.* CDF Note 521.

[26] G. Arnison *et al.* Observation of jets in high transverse energy events at the CERN proton antiproton collider. *Physics Letters*, B(123):115, 1983.

[27] P. Bagnaia *et al.* Measurment of very large transverse momentum jet production at the CERN $p\bar{p}$ collider. *Physics Letters*, B(138):430, 1984.

[28] P. Bagnaia *et al.* Measurment of jet production properties at the CERN $p\bar{p}$ collider. *Physics Letters*, B(144):283, 1984.

[29] Cathy Newman-Holmes and Jim Freeman. A fast calorimeter simulation for SSC detector design. In Lawrence E. Price, editor, *Workshop on Detector Simulation for the SSC*, page 285, 1987. Since this publication the simulator geometry has been made realistic for CDF, uninstrumented regions response tuned to test beam data, and gas calorimeter response improved.

[30] F. Paige and S. Protopopescu. Isajet 5.30: a monte carlo event generator for pp and $\bar{p}p$ interactions. In R. Donaldson and J. Marx, editors, *Proceedings of the 1986 Summer Study on the Physics of the Superconducting Supercollider*, page 320, 1986. The event generator used in this Monte Carlo was ISAJET 5.38.

[31] Stephen Kuhlmann *et al.* *Central Jet Energy/Momentum Corrections.* CDF Note 686.

[32] G. Arnison *et al.* Angular distributions for high-mass jet pairs and a limit on the energy scale of compositeness for quarks from the CERN $p\bar{p}$ collider. *Physics Letters*, B(177):244, 1986.

[33] G. Drake *et al.* CDF front end electronics: the rabbit system. *Nuclear Instruments and Methods*, A(273):287, 1988.

[34] Phil Kesten and Jim Proudfoot. *The CDFdb, a Reference Manual for the CDF Database.* CDF Note 473.

[35] T. M. Liss. *Luminosity Monitoring and Beam-Beam Counter Performance.* CDF Note 552.

[36] J. Huth. *Calorimeter Cluster and Track Matching.* CDF Note 809.

[37] S. Kuhlmann. *Central Jet Energy Corrections Due to Clustering Effects.* CDF Note 687.

[38] B. Flaugher and S. Kuhlmann. *Underlying Event Energy in Clusters.* CDF Note 685.

[39] S. Kuhlmann and S. Behrends. *Checks of the CDFSIM Central Calorimeter Simulation.* CDF Note 684.

[40] Robert Carey *et al.* *Clustering Algorithms and Their Performance.* CDF Note 605.

[41] Bradley Hubbard. Jet fragmentation properties at CDF. In *Proceedings of the 7th Topical Workshop on Proton-Antiproton Collider Physics*, June 1988.

[42] R. Field and R. Feynman. A parameterization of the properties of quark jets. *Nuclear Physics*, B(136):1, 1977.

[43] G. P. Lepage. *Journal of Computational Physics*, (27):192, 1978.

[44] D. Duke and J. F. Owens. q^2-dependent parameterizations of parton distribution functions. *Physical Review D*, 30(1):49, 1984.

[45] E. Eichten, I. Hinchliffe, K. Lane, and C. Quigg. *Supercollider Physics.* Technical Report 84/17-T, Fermi National Accelerator Laboratory, February 1984.

[46] R.K. Ellis and J.C. Sexton. QCD radiative corrections to parton-parton scattering. *Nuclear Physics*, B(269):445, 1986.